

Aquaporin-2 trafficking

Studying cellular mechanisms with subcellular aspiration and cryo-electron microscopy

Pronk, Jochem

DOI

[10.4233/uuid:b6c599e8-077c-44f1-bb71-e731bcc7d81f](https://doi.org/10.4233/uuid:b6c599e8-077c-44f1-bb71-e731bcc7d81f)

Publication date

2018

Document Version

Final published version

Citation (APA)

Pronk, J. (2018). *Aquaporin-2 trafficking: Studying cellular mechanisms with subcellular aspiration and cryo-electron microscopy*. [Dissertation (TU Delft), Delft University of Technology].
<https://doi.org/10.4233/uuid:b6c599e8-077c-44f1-bb71-e731bcc7d81f>

Important note

To cite this publication, please use the final published version (if applicable).
Please check the document version above.

Copyright

Other than for strictly personal use, it is not permitted to download, forward or distribute the text or part of it, without the consent of the author(s) and/or copyright holder(s), unless the work is under an open content license such as Creative Commons.

Takedown policy

Please contact us and provide details if you believe this document breaches copyrights.
We will remove access to the work immediately and investigate your claim.

Aquaporin-2 trafficking:

Studying cellular mechanisms with subcellular aspiration and cryo-electron microscopy

Proefschrift

ter verkrijging van de graad van doctor
aan de Technische Universiteit Delft,
op gezag van de Rector Magnificus prof.dr.ir. T.H.J.J. van der Hagen,
voorzitter van het College voor Promoties,
in het openbaar te verdedigen op
woensdag 5 september 2018 om 10:00 uur

Door

Joachim Willem PRONK

Master of Science in Life Science & Technology
Universiteit van Leiden, Nederland
Geboren te Spijkenisse, Nederland

Dit proefschrift is goedgekeurd door de promotoren.

Samenstelling promotiecommissie bestaat uit:

Rector magnificus,	Voorzitter
Prof.dr. A.H. Engel	Technische Universiteit Delft, promotor
Dr. C.J.A. Danelon	Technische Universiteit Delft, copromotor

Onafhankelijke leden:

Prof.dr. U. Stauffer	Technische Universiteit Delft
Prof.dr. R.A. Fenton	Universiteit van Aarhus, Denemarken
Prof.dr.ir. A. J. Koster	Universiteit Leiden
Dr. M. E. Aubin-Tam	Technische Universiteit Delft
Prof.dr. A.M. Dogterom	Technische Universiteit Delft, reservelid

Overig lid:

Dr. A. Jakobi	Technische Universiteit Delft
---------------	-------------------------------



Printed by: Gildeprint

Cover: Martijn Pronk

Casimir PhD series: 2018-30

ISBN: 978.90.8593.360.1

An electronic version of this dissertation is available at <http://repository.tudelft.nl>

Table of Contents:

1: General introduction.....	1
1.1: Aquaporins	2
1.1.1: The general structure of Aquaporins	4
1.1.2: Aquaporins in humans	4
1.2: Aquaporin-2	6
1.2.1: Aquaporin-2 structure and trafficking regulation.....	8
1.2.2: Challenges of studying AQP2 in the cellular context	8
1.3: Microinjection and a hollow cantilever AFM	9
1.3.1: Atomic Force Microscopy	10
1.3.2: Hollow cantilevers for AFM	10
1.4: Cryo Electron Microscopy	10
1.5: Aim of this thesis	12
1.6: Thesis outline	14
1.7: References	16
2: AQP2: Trafficking regulation and Nephrogenic Diabetes Insipidus.....	21
2.1: Introduction	22
2.2: The structure of aquaporin-2	24
2.2.1: AQP2 exhibits the characteristic AQP-fold	24
2.2.2: Structure and water specificity of aquaporin-2	24
2.2.3: The C-terminus and N-terminus of aquaporin-2	24
2.3: Phosphorylation of aquaporin-2	26
2.3.1: Phosphorylation of Ser256.....	27
2.3.2: Phosphorylation of Ser269/Thr269	28
2.3.3: Phosphorylation of Ser264.....	29
2.3.4: (De)Phosphorylation of Ser261	30
2.4: Proteins regulating aquaporin-2 trafficking.....	32
2.4.1: Phosphorylation of Ser256 by PKA guided by AKAP	32
2.4.2: AQP2 trafficking, a role for 14-3-3 proteins.....	34
2.4.3: AQP2 exocytosis, a role for Rab11 and SNARE proteins	35
2.4.4: Clathrin mediated Aquaporin-2 endocytosis and ubiquitination.....	37
2.5: AQP2 and Nephrogenic Diabetes Insipidus	38

2.5.1: X-linked NDI: mutations in the <i>avpr2</i> gene.....	38
2.5.2: Autosomal recessive NDI: AQP2 misfolding	40
2.5.3: Autosomal dominant NDI: AQP2 misrouting.....	40
2.6: Conclusion and Discussion	42
2.7: References	48
3: Comparing actin polymerization in the presence of c-terminal Aquaporin 2 peptides and Thymosin-β-4.....	69
3.1: Abstract	70
3.2: Introduction	71
3.2.1: AQP2	71
3.2.2: The actin cortical network.....	71
3.2.3: Aim of this research	72
3.3: AQP2 and Actin cortex remodelling	72
3.3.1: Aquaporin 2 inhibits actin polymerization.....	73
3.3.2: C-terminal AQP2 interferes with f-actin filament assembly.....	76
3.3.3: AQP2 C-terminal peptides inhibit formation of small actin oligomers.....	76
3.3.4: Actin polymerization reaches equilibrium earlier in the presence of AQP2	79
3.3.5: AQP2 C-terminal peptides do not sever f-actin	81
3.3.6: Do AQP2 C-terminal peptides destabilize actin thin filaments?.....	81
3.3.7: Where do AQP2 C-terminal peptides bind to g-actin?.....	84
3.3.8: The influence of AQP2 R253 and R254 on f-actin formation and stability.....	84
3.3.9: Arginine mutants inhibit AQP2 exocytosis in vivo	89
3.3.10: Arginine mutants can be phosphorylated by PKA	89
3.4: Discussion	91
3.5: Materials and Methods	95
3.6: References	99
3.7: Supplemental figures.....	104
4: Aquaporin-2: Production, purification and reconstitution	107
4.1: Introduction	108
4.2: Aquaporin-2 production	109
4.2.1: Aquaporin-2 expression in <i>Sf9</i> cells by baculovirus expression systems.....	109
4.2.2: Aquaporin-2 expression in <i>P. Pastoris</i>	112
4.3: Aquaporin-2 purification.....	113

4.3.1: Aquaporin-2 purification from <i>Sf9</i> and <i>P. Pastoris</i>	114
4.3.2: Aquaporin-2 purification with Styrene Maleic Acid from <i>Sf9</i> cells.....	119
4.4: Aquaporin-2 reconstitution.....	123
4.4.1: Aquaporin-2 bearing proteoliposomes	124
4.4.2: Aquaporin-2 activity measurements	125
4.5: Conclusion.....	129
4.6: Material and Methods.....	132
4.7: References	138
5: Hollow cantilevers for Cryo-EM sample preparation; the set-up	141
5.1: Introduction	142
5.2: Micro-injections and cryo-EM sample preparation.....	143
5.2.1: Current techniques for cryo-EM sample preparation	143
5.2.2: Micro-injections into single cells	146
5.3: The set-up.....	150
5.3.1: Process flow and set-up overview.....	150
5.3.2: Controlling software	152
5.4: Humidity control	158
5.4.1: Evaporation in an ambient environment	160
5.4.2: The humidity chamber and dewpoint-controller	160
5.5: Grid handling, the sample stage and the AFM	164
5.5.1: The AFM, hollow cantilevers and the sample stage	164
5.5.2: Handling EM-grids in the system	165
5.6: Cryo-EM sample preparation	166
5.6.1: Tweezers and the plunger	166
5.6.2: Handling of the cryogenic liquid.....	169
5.6.3: Preparation of cryo-EM samples.....	170
5.7: Conclusion.....	172
5.8: Materials and methods	176
5.9: References	178
6: Hollow cantilever dispensing and transmission electron microscopy	185
6.1: Introduction	186
6.2: The cantilever and EM-grids	187
6.2.1: Cantilever force and carbon rupture.....	188

6.2.2: The effect of hydrophobicity on dispensing.....	190
6.3: Cells and the cantilever	194
6.3.1: Cantilever coating for cellular interactions	195
6.3.2: Cell targeted dispensing	195
6.3.3: Cellular dissection.....	197
6.4: Transmission electron-microscopy of dispensed picolitre volumes	199
6.4.1: Dispensing Gold-nanoparticles	199
6.4.2: Dispensing Apoferritin.....	201
6.4.3: Dispensing liposomes	202
6.5: Discussion	205
6.6: Materials and Methods	209
6.7: References	211
6.8: Supplemental figures.....	213
Summary:.....	217
Samenvatting:	222
Abbreviations:.....	228
Acknowledgements:.....	230
Curriculum vitae	235
Publications:.....	236

Chapter 1

Introduction

1.1: Aquaporins

All living organisms must be able to deal with osmotic and hydrostatic pressure changes in their environment. Therefore, maintaining water homeostasis plays a central role in all living organisms. Although water can pass through pure lipid bilayers by diffusion, this process is too slow to allow cells to react to environmental changes in time. Aquaporins (AQPs) represent a large, ancient, family of integral membrane proteins that form selective water pores in the membrane (1). AQPs lower the activation energy of a lipid bilayer for water permeation from 10-20 kcal/mol to less than 5 kcal/mol (2).

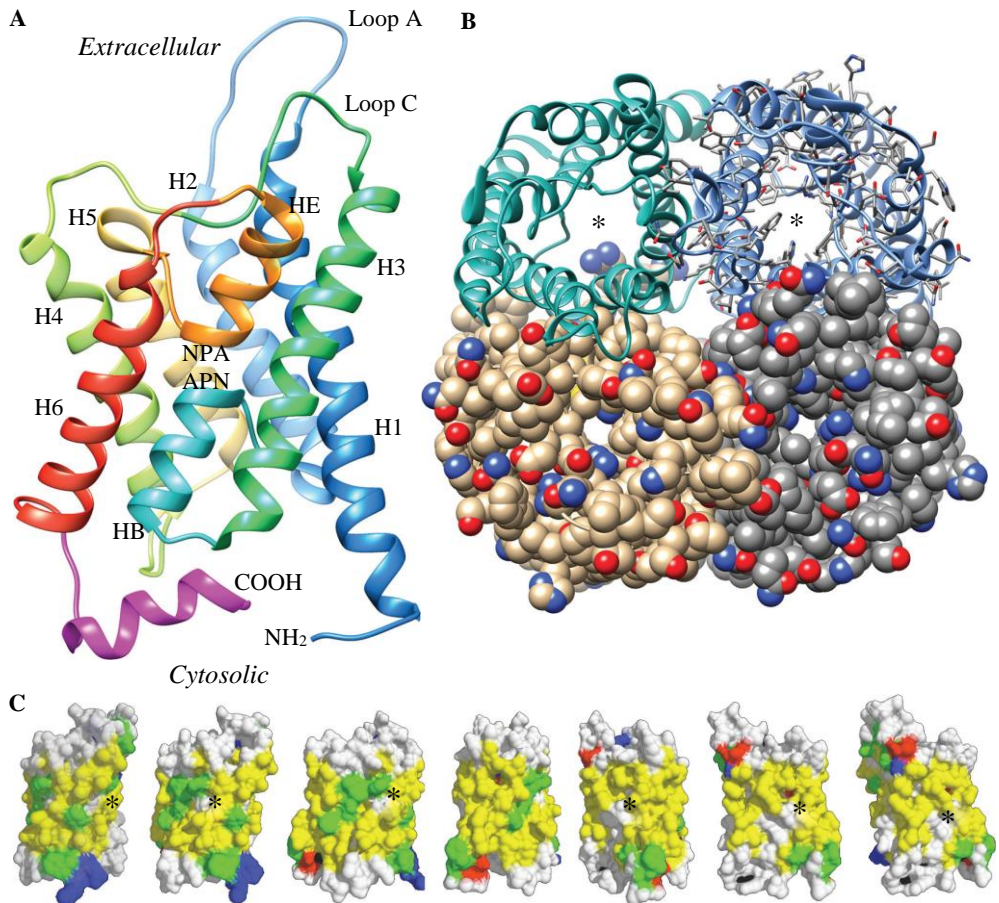


Figure 1.1: The aquaporin fold and its tertiary structure. (A) Bovine AQP1 monomer (PDB entry: 1J4N). The color-codes reveal the typical AQP fold. H1, H2, HB and H3 form the first half of the protein, H4, H5, HE and H6 form the second half. Helices HE and HB emanate outward from the platform formed by the prolines of the NPA motifs in the centre of the pore. (B) Aquaporins and aquaglyceroporins both exist as tetramers, forming four independent pores. Two of the four pores are marked by an asterisk. The tight packaging of the monomers into a tetramer is indicated for two monomers rendered by spheres in Chimera (3). (C) The surface of an AQP monomer consists of mainly hydrophobic (yellow) and aromatic (green) residues. However, polar residues (white/grey) are located between hydrophobic residues as well (indicated by an asterisk) and must be buried in the interfaces between protomers.

1.1.1: The general structure of Aquaporins

When aquaporin 1 (AQP1) was discovered as a major component of the red blood cell membranes, its sequence indicated six membrane spanning hydrophobic regions and a homology between the first and second half of the protein. Each half was found to exhibit an unusually long loop, called loop B and -E, carrying the NPA motif (4,5). Site directed mutagenesis showed that mercurial sensitivity of the AQP1 water activity relates to residue C192 in loop B and that a cysteine engineered at a comparable site in loop E induces mercurial sensibility as well. This led to the hour glass model of the pore (6). Biochemical and electron microscopy (EM) analysis showed that AQP1 exists as a tetramer (7). Figure 1.1 displays the aquaporin fold.

Within a few years, a large number of homologous genes, throughout all kingdoms of life, were identified. Multiple sequence alignments and phylogeny studies revealed the striking conservation of these membrane proteins throughout evolution (Figure 1.2), its presence in all forms of life and its separation in two clusters, (i) the aquaporins and (ii) aquaglyceroporins (GLPs)(Figure 1.3). GLPs are channels that facilitate both the passage of water and small solutes such as glycerol.

This evolutionary conservation of the AQP sequence suggested that all AQPs have a similar protein topology. Indeed, the structure of AQP1, determined by electron crystallography (8), and that of GlpF, the bacterial GLP (9), confirmed the conserved structure of these proteins. Moreover, the determination of these structures made it possible to perform molecular dynamics simulations, rising to deep insights into the water permeation of AQPs and the flow of small solutes in GLPs (10). Accordingly water was found to permeate the water pore at a rate of 3×10^9 H₂O molecules per second, while protons are excluded by an electrostatic potential within the channel (10).

The water channel starts with a width of approximately 10-12Å at the extracellular side leading to a selectivity filter of 3Å, near the NPA motif, in the middle (8).

1.1.2: Aquaporins in humans

Humans express thirteen different AQPs, AQP0-AQP12, that are found in a broad range of tissues, such as the brain, eyes, liver, lungs, intestines and various glands (11). The most important organs in humans for maintaining water homeostasis are the kidneys. It is therefore no surprise that the majority of the mammalian AQPs, eight of the thirteen, are expressed in this organ, namely AQP1-4, 6-8 and 11 (12,13).

The kidney consists of roughly 800,000 to 1.5 million nephrons (14), which are the basic structural and functional units of the kidney. Nephrons consist of the glomeruli and a capillary system (Figure 1.4). They perform the main functions of the kidneys, which includes detoxification and maintenance of water homeostasis. This is achieved by filtering the blood, reabsorption of what is needed and excreting what is not needed as urine (14). Water reabsorption is performed by the AQPs residing at different locations inside the nephrons (12), while salts and organic solutes are actively recovered by specific transporters (15).

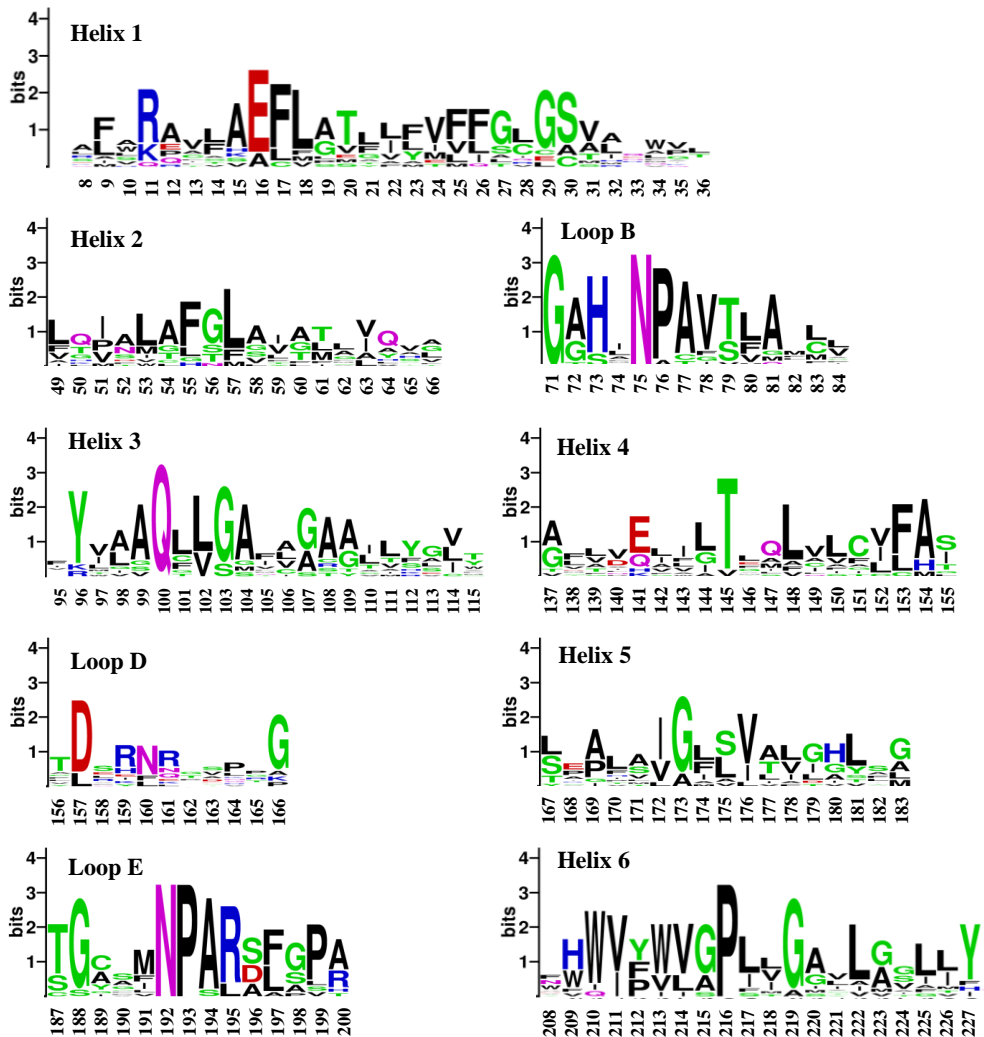


Figure 1.2: Sequence logos (16) of the 13 human aquaporins, visualizing the conservation of residues at particular positions in the sequences. Sequence alignments were executed by Clustal W (17). The aligned sequences were converted to sequence logos using the ‘Weblogo’ facility at weblogo.berkeley.edu/logo.cgi. The logos are displayed with the residue numbers of AQP1. The Y-axis represents the probability of finding a particular amino acid at each position. The transmembrane helices and loops B, D and E show highly conserved residues, whereas loop A and C exhibit a higher variability both in length as in sequence homology (not displayed).

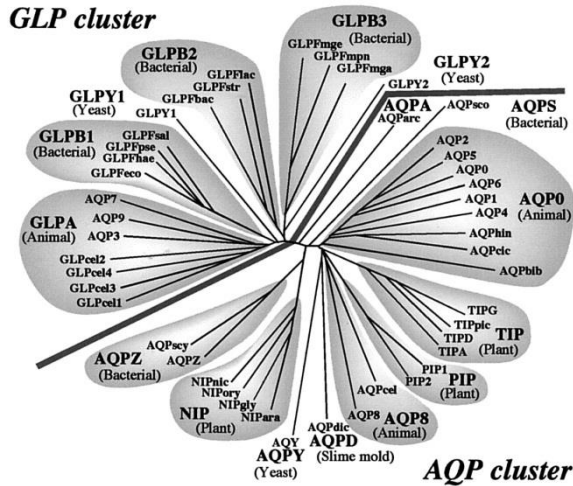


Figure 1.3: Phylogenetic analysis of the aquaporin (AQP) family suggests a classification into two clusters (AQP and glycerol facilitator-like protein (GLP)), 16 subfamilies, and 46 types. The types are considered to be representative of the whole family of 160 sequences obtained from Genbank, SWISS-PROT, EMBL, and the genome databases (18).

The kidney filters 180 liters of plasma per day (19). 90% of water is reabsorbed by AQP1 residing in the proximal tubule and the descending thin limb of Henle (12)(Figure 1.4). No AQPs have been identified in the water-impermeable thin and thick ascending loop of Henle, where the solute transporters are located (15). The terminal part of the renal tubule, the connecting tubules and collecting ducts have variable water permeability, which is controlled by the peptide hormone arginine-vasopressin (AVP) (20). Within the renal tubule segment, three AQPs are expressed: AQP2 (in the apical membrane (21)), AQP3 and AQP4 (in the basolateral membrane (22,23)).

AQP6 is an intracellular water channel located in intracellular vesicles of the acid secreting type-A intercalated cells of the collecting duct and is both a water as well as a chloride channel (24). AQP7 is a GLP and is expressed in the apical membrane of proximal tubules (25,26) and is thought to prevent the excretion of glycerol into urine (27). AQP8 is located in the inner mitochondrial membrane in the proximal tubules (28,29). AQP8 is able to facilitate the diffusional transport of ammonia (NH₃) and is thought to play a role in the adaptive response to metabolic acidosis (30,31). AQP11 is expressed in the proximal tubule as well and is localized in intracellular organelles (32). The exact role AQP11 plays in the kidneys is unknown.

1.2: Aquaporin-2

Aquaporin-2 (AQP2) is expressed in principal epithelium cells of the collecting duct and resides both in cellular vesicles and the apical membrane. AQP2 bearing vesicles traffic

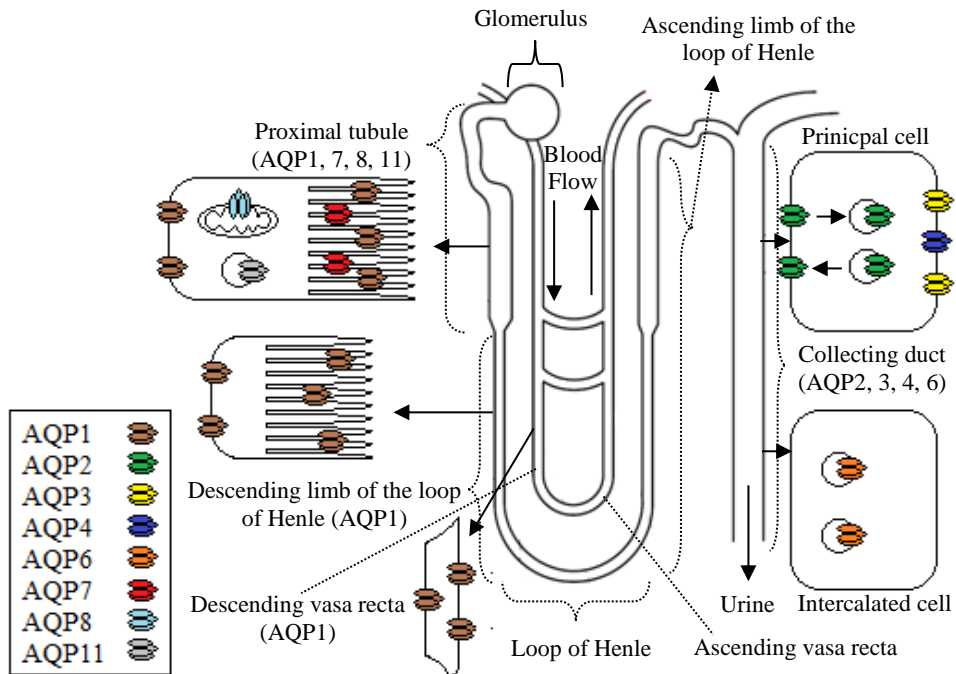


Figure 1.4: Distribution of aquaporins (AQPs) in the nephron. The nephron consists of the glomerulus and two tubular networks. In the first, the blood plasma is filtered. In the second, the blood stream accepts reabsorbed water and specific molecules. At the glomerulus the serum portion of the blood is forced out of the blood vessel and into the renal tubules. 90% of the serum is transported back to the bloodstream by AQP1 (brown) residing in the proximal tubule and the descending limb of the loop of Henle. AQP7 (red), AQP8 (light blue) and AQP11 (grey) also reside in the proximal tubule. In the loop of Henle water and sodium chloride are reabsorbed. The descending limb of the loop of Henle is permeable to water induced by the expression of AQP1. The ascending limb of the loop of Henle is impermeable to water, due to the absence of AQPs, but is permeable for sodium chloride. The sodium chloride passes out of the tubule, into the medullary tissue, the innermost part of the kidney located near the collecting ducts. The high salt concentration causes a concentration gradient between the collecting duct and the medulla, making passive water reabsorption from the collecting duct to the medulla possible (33). AQP2 (green) resides in both internal vesicles and in the apical membrane of collecting duct principal cells. Water permeability in the collecting duct is variable and controlled by vasopressin (AVP). The water permeability of the collecting duct can be enhanced by binding of AVP to the V2 receptor (V2R), leading to AQP2 vesicle transport towards the apical membrane. AQP3 (yellow) and AQP4 (dark blue) reside in the basolateral membrane of the collecting duct principal cell, while AQP6 (orange) resides in internal vesicles in the intercalated cells of the collecting duct.

towards the apical membrane via exocytosis, while exocytosis and endocytosis of AQP2 is in equilibrium. Binding of the peptide hormone (arginine) vasopressin (AVP) to the vasopressin type 2 receptor (V2R) induces expression and exocytosis of AQP2. This results in an increase of water permeability in the collecting duct (34). Release of AVP from the V2R recovers the initial equilibrium between exocytosis and endocytosis of AQP2, leading to a decrease in water permeability.

1.2.1: Aquaporin-2 structure and trafficking regulation

AQP2 has the AQP-fold as discussed in chapter 1.1 and visualized in figure 1.1. However, it exhibits an unusually long C-terminal helix, which plays an important role in trafficking regulation. The end of this helix carries four conserved phosphorylation sites, the state of which is linked to numerous AQP2 trafficking processes (35-39).

Binding of AVP to the V2R induces a hierarchical change of the phosphorylation sites, leading to a controlled displacement of AQP2 bearing vesicles (35,40). Mutations in the C-terminus lead to dominant nephrogenic diabetes insipidus (NDI), a disease characterized by a massive loss of water through the kidney caused by a dysregulation of AQP2 trafficking (12,41,42).

The exact role of these phosphorylation sites in AQP2 trafficking is still under investigation. AQP2 can be phosphorylated on residues Serine-256 (Ser256), Ser261, Ser264 and Threonine-269 (Thr269; Ser269 in rodents), of which Ser256 phosphorylation was found to be the first in the cascade (35,39,43). Furthermore, Ser256 needs to be phosphorylated before the other residues can change their phosphorylated state. Mimicking the phosphorylated state of Ser256, by a S256D mutation, lead to enhanced expression of AQP2-S256D in the apical membrane, while the AQP2-S256A mutant, mimicking the unphosphorylated state of Ser256, resided in intracellular vesicles (44). This documents that phosphorylation of Ser256 is the master switch for the initiation of AQP2 transport.

The function of the other phosphorylation sites have been studied as well, but no clear answers on the exact role of these sites in AQP2 trafficking regulation were obtained (35-39,45). Furthermore, many AQP2 interacting proteins have been identified and studied as well (46). However, the complete protein interaction network, and therefore the complete understanding of NDI, has yet to be resolved. In chapter 2 the structure of AQP2, phosphorylation of the AQP2 C-terminus and proteins regulating AQP2 trafficking will be discussed in more detail.

1.2.2: Challenges of studying AQP2 in the cellular context

Although standard cell research techniques could be used to understand the AQP2 trafficking mechanism, they are also limited. To further enhance our understanding of cellular mechanisms, like the AQP2 transport regulation, at the molecular level, new techniques need to be developed. It is difficult to visualize AQP2 trafficking in real life. To observe exocytosis of AQP2 bearing vesicles to the apical membrane, AQP2 need to be either fluorescently labelled for light microscopy, or identified by immunogold labelling in an electron

microscope (EM). Labelling of AQP2 can either be done directly by adding a green fluorescence protein tag (GFP-tag) to the protein, or indirectly by using immunofluorescence assays. Adding a tag to a protein can alter the structure of the protein or can inhibit the possibility of protein-protein interactions, which may change the function of the protein studied. Immunofluorescence assays and immunogold labelling for EM are only possible with fixated samples, making it impossible to monitor trafficking in real life. Furthermore, although EM can provide us high resolution images, sample preparation is laborious and time consuming.

Other challenges in cell research concern the complexity of living cells. Proteins are able to interact with multiple targets and cellular functions are executed by a complex protein network. *In vivo* studies could give more information on complex protein networks. However, it is difficult to distinguish between direct protein-protein contacts and indirect interactions within this network. *In vitro* studies could make direct interactions clearer. However, because they do not provide the environment of the cell, these studies are limited. Pull down experiments allow AQP2 interaction partners to be identified by mass spectroscopy. However, although pull down experiments could be used to find AQP2-protein interactions, further research is then necessary to unravel the function of these interactions. Injection of labelled AQP2 bearing vesicles may allow observing AQP2 trafficking in real life. The regulatory role of the AQP2 phosphorylation sites in trafficking regulation could be deciphered by the injection of AQP2 phospho-mimics. Furthermore, faster and easier methods to prepare Cryo-EM samples should make it possible to quickly visualize AQP2-protein complexes in high resolution. Developing and optimizing such methods will help us to understand the AQP2 trafficking system at a molecular level.

1.3: Microinjection and a hollow cantilever AFM

To study cells and cell systems it is often necessary to load specific exogenous substances, such as proteins, peptides, cDNA constructs or drugs, into a cell. By introducing these compounds, protein expression can be down- or upregulated, protein mutants can be expressed, specific protein-protein interactions can be inhibited or the effect of certain drugs on cell mechanisms can be tested. Over time many methods have been developed to transfer such compounds into cells and are now widely used. A limiting factor is that such methods cannot be used to address specific cells.

The development of microinjection made it possible to specifically inject certain compounds into individual cells (47). A well known example is the expression of membrane proteins in *Xenopus oocytes* by microinjection of cRNA (reviewed in Dascal *et al.* (48)), used for functional studies of these proteins (1). With the help of micromanipulators the cell membrane can be penetrated by an injection needle and substances can be delivered into desired locations. The advantage of this method is that compounds can be delivered into the nucleus, which is difficult to reach by other methods (49). However, forty years after the development of the first microinjections, the potential of the method has not been completely exploited. Microinjection systems are limited by the delicate manipulation, the relatively

large size of the microneedle, and lack of feedback to monitor the probe insertion. The large size of the needle makes it difficult to inject femtoliter volumes into a cell, to address small cells and cell deaths often occur.

1.3.1: Atomic Force Microscopy

Atomic Force Microscopy (AFM) revolutionized surface science at the nanoscale in the last three decades. By raster-scanning a small probe, namely the tip attached to the end of a cantilever, over a surface, a 3D representation of this surface can be constructed (reviewed in Jalili *et al.* (50)). By precisely measuring the x-, y- and z-movement of the tip and a force feedback control, this method has been used to study membrane morphology, cell division mechanisms, voltage-induced deformation as well as DNA- and protein structures (50,51). Furthermore, the possibility to contour surfaces with sharp tips in buffer solution makes it possible to observe biomolecules at work with sub-nanometer resolution (52).

1.3.2: Hollow cantilevers for AFM

Recently, by exploiting hollow cantilevers and the sensitive force feedback, the AFM was used for intracellular injections (53). This technology and the small tip dimensions made it possible to transfer substances into a cell with minimal damage (53). This, combined with the accurate spatial control, made it possible to insert the AFM cantilever at a certain position into a cell with sub-micrometer accuracy. This method, called Fluid-FM, has been used to inject femtoliters of GFP or DNA specifically into the cytosol or the cell nucleus respectively (54). Therefore, hollow cantilevers are most suitable to inject AQP2 bearing vesicles into principal epithelial cells, to study AQP2 trafficking.

1.4: Cryo Electron Microscopy

The invention of the first microscope by Antoni van Leeuwenhoek (55), made it possible to visualize cells for the first time. Although light can be used as a source to magnify samples, the resolution is limited to half of the wavelength of visible light, typically to 0.2 μm . Studying cells by light microscopy reveals the morphology of the cell and the cell nucleus, but details of the cell structure remain therefore unexplored by light microscopy. Although modern techniques make it possible to visualize single molecules by light microscopy, the complexity of a cell can only be depicted by an electron microscope (EM).

Electron microscopes use electrons as a source to magnify samples. The wavelength of electrons accelerated to 100 keV is 0.037 \AA , which is much smaller than an atom, makes it possible to visualize samples at the atomic level (56). Since the introduction of the EM, in the last century, progress has made it possible to look at single atoms. However, biological samples, unfortunately, are so beam sensitive that many other developments were necessary to record atomic scale images and reconstruct their atomic structure (57,58). Importantly the invention of vitrifying biological samples and observing them at low temperatures, made it possible to visualize the complete interior of the cell at nm resolution (59). The development of fast direct electron detectors allows all scattered electrons to be measured and movies to

be recorded (60-62). These advances make it possible to image beam sensitive biological supramolecular structures at atomic resolution (63).

While electron optics and camera technology are now mature, the major hurdle in cryo-EM is still the sample preparation. The sample size is the limiting factor. Freezing of samples leads to ice-crystal formation, which destroys the sample. For thin samples the cooling rate to prevent ice-crystal formation is achieved by plunging the grid into liquid ethane. Such samples are in a glassy state and thus vitrified (59). For thicker samples, the cooling rate is too small to prevent ice-crystal formation. Even cells can be too thick to be vitrified in a simple manner. To circumvent ice formation, high pressure and fast freezing are necessary (reviewed in Thompson *et al.* (64)).

The next challenge is that electrons have a mean free path of 100-200 nm in biological matter, meaning that electrons only travel this distance without being scattered. The thicker the sample is the more scattering occurs. This leads to an increase in noise and a decrease in image signal and resolution. Normally, samples between 40 and 200 nm are used in cryo-EM, while an average mammalian cell has a diameter of 20 μm . Therefore, to prepare cells for cryo-EM, they need to be sectioned by either using a focussed ion beam (FIB) or an ultramicrotome, while keeping the vitrified sample below -140°C (reviewed in Thompson *et al.* (64)). Both high pressure freezing and cell sectioning are laborious methods, executed by trained professionals, which also limits the utilization of cryo-EM in research.

Limitations related to sample size can be circumvented by using *in vitro* samples. However, these samples lack the environment and complexity of the cell. Recently different preparation methods have been developed to circumvent the laborious preparation steps mentioned above. By unroofing the cells, the actin cortex, a dense network of actin filaments underneath the cell membrane could be studied in great detail (65). Furthermore, easy to prepare single cell cryo-EM samples were produced by lysing specifically targeted cells and dispensing the cell lysate on grids (66). Even cytosol contents extracted by Fluid-FM could be dispensed on EM-grids (67). These techniques make it easier to visualize *in vivo* prepared samples in great detail and will help to resolve biological questions which could not be resolved so far.

1.5: Aim of this thesis

Although AQP2 and AQP2 transport have been extensively studied, the molecular mechanisms behind AQP2 trafficking regulation need yet to be unraveled. Many interacting proteins have been identified and the importance of the C-terminal phosphorylation sites has been acknowledged. However, the exact role of each individual phosphorylation site in AQP2 trafficking regulation and the exact binding partners of AQP2 controlling this mechanism have not been described yet. To understand this process and to unravel the disease called Nephrogenic Diabetes Insipidus, new techniques need to be developed. Therefore, the research question of this thesis is:

How can the use of a hollow cantilever AFM (in combination with cryo-EM sample preparation) resolve the AQP2 trafficking mechanism?

To understand the mechanism underlying the control of AQP2 trafficking and to test this new method, different research questions need to be addressed. First of all, what is already known about AQP2 trafficking? For this, an extensive literature study is summarized in **chapter 2**. **Chapter 3** reports a new analysis of AQP2-actin interactions by using biophysical and biochemical methods. **Chapter 4** describes the purification of AQP2 from different cell types with different solubilization methods, including a novel approach to monitor the reconstitution of AQP2 into proteoliposomes.

The second part of this thesis will focus on the AFM hollow cantilevers and its use in cryo-EM sample preparation. **Chapter 5** will discuss current cryo-EM sample preparation techniques and the developed cryo-EM sample preparation set-up, in **chapter 6** the use of hollow cantilevers for Transmission Electron Microscopy (TEM) and cell manipulation will be discussed. A schematic overview of this thesis is visualized in Figure 1.5.

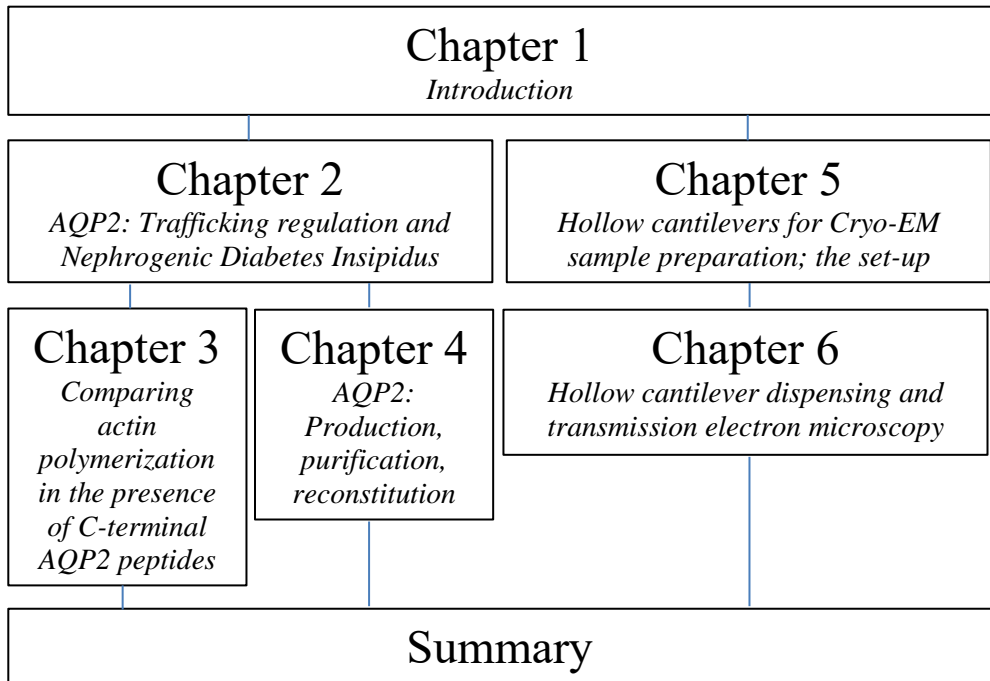


Figure 1.5: Schematic overview of the outline of this thesis. Chapter 2, -3 and -4 will focus on AQP2, while chapter 5 and -6 are focussed on the development and the use of the designed set-up.

1.6: Thesis outline

The outline of the thesis will be as follows:

Chapter 2: On page 21, “AQP2: Trafficking regulation and Nephrogenic Diabetes Insipidus”.

Chapter 2 contains a comprehensive literature study about AQP2. The specific AQP2 structure will be discussed, as well as the importance of the AQP2 C-terminus in trafficking regulation. Changes in C-terminal phosphorylation after AVP stimulation regulate AQP2 trafficking, the effect of these phosphorylation sites on transport regulation will be discussed. Furthermore, a broad range of different proteins are involved in AQP2 apical membrane accumulation and its subsequent endocytosis. The role of these proteins in AQP2 exocytosis and endocytosis will be addressed. In the end, mutations in either the V2R or AQP2 are discussed, for they show the importance of the tight regulation of this transport mechanism.

Chapter 3: On page 69, “Comparing actin polymerization in the presence of c-terminal Aquaporin 2 peptides and Thymosin- β -4”.

In chapter 3 the effect of the AQP2 C-terminal tail on actin cortex remodelling is tested. Before AQP2 can fuse with the apical membrane, it needs to penetrate a tight mesh network of actin filaments, the actin cortex. Structural studies reveal that the C-terminus of AQP2 resembles a structural homology with actin binding peptides. *In vitro* biochemical assays reveal that the AQP2 C-terminus is able to inhibit actin polymerization and destabilize actin thin filaments by interactions with tropomyosin-5b.

Chapter 4: On page 107, “Aquaporin-2: Production, purification and reconstitution”.

In chapter 4, AQP2 is produced, purified and reconstituted in proteoliposomes. Production of mammalian (human) proteins requires dedicated over-expressing organisms. For this both *Sf9* cells infected with *aqp2* carrying baculoviruses and AQP2 producing *Pichia pastoris* were used, both with their own advantages and limitations. Furthermore, purification of membrane proteins is not a triviality and require dedicated compounds to preserve the hydrophobic domains in aqueous solutions. Therefore, AQP2 was purified by solubilisation in detergents or incorporation in nanodiscs. After detergent mediated purification, AQP2 was reconstituted in proteoliposomes. Incorporation of AQP2 in the lipid bilayer was measured by fluorescence microscopy, while AQP2 activity was measured by a homemade rapid mixing set-up.

Chapter 5: On page 141, “Hollow cantilevers for Cryo-EM sample preparation; the set-up”.

In chapter 5, the developed set-up is discussed. The rationale behind certain cryo-EM sample preparation techniques is explored and the current use and development of targeted cell manipulation is reviewed. The combination of cryo-EM sample preparation and targeted cell manipulation based on hollow cantilevers led to the development of a dedicated set-up. With this system complex cellular mechanisms can be explored with cryo-EM, while samples are prepared via the relative straightforward method of plunge freezing. For this a broad range of different components and controlling software is necessary. The use of and the rationale behind these components are discussed in great detail. In the end, the plunger is used to prepare cryo-EM samples.

Chapter 6: On page 185, “Hollow cantilever dispensing and transmission electron microscopy”.

In chapter 6 the use of hollow cantilevers for TEM sample preparation is discussed. Working with picolitre or smaller volumes lead to challenges often not observed when working with larger volumes. The force the cantilever can apply on the EM-grid, hydrophobicity of the EM-grid, cell-cantilever or carbon film-cantilever interactions and sample evaporation after dispensing are all factors that play a role in this set-up. Here, we show the possibility to dispense picolitre volumes on an EM-grid, while the dispensed volume can be imaged with transmission electron microscopy. Furthermore, cell-cantilever interactions were tested, where it was visualized that a hydrophobic cantilever coating limits possible cell-cantilever contact.

1.7: References

1. Preston, G. M., Carroll, T. P., Guggino, W. B., and Agre, P. (1992) Appearance of water channels in *Xenopus* oocytes expressing red cell CHIP28 protein. *Science (New York, N.Y.)* **256**, 385-387
2. Zeidel, M. L., Ambudkar, S. V., Smith, B. L., and Agre, P. (1992) Reconstitution of functional water channels in liposomes containing purified red cell CHIP28 protein. *Biochemistry* **31**, 7436-7440
3. Pettersen, E. F., Goddard, T. D., Huang, C. C., Couch, G. S., Greenblatt, D. M., Meng, E. C., and Ferrin, T. E. (2004) UCSF Chimera--a visualization system for exploratory research and analysis. *Journal of computational chemistry* **25**, 1605-1612
4. Denker, B. M., Smith, B. L., Kuhajda, F. P., and Agre, P. (1988) Identification, purification, and partial characterization of a novel Mr 28,000 integral membrane protein from erythrocytes and renal tubules. *The Journal of biological chemistry* **263**, 15634-15642
5. Smith, B. L., and Agre, P. (1991) Erythrocyte Mr 28,000 transmembrane protein exists as a multisubunit oligomer similar to channel proteins. *The Journal of biological chemistry* **266**, 6407-6415
6. Jung, J. S., Preston, G. M., Smith, B. L., Guggino, W. B., and Agre, P. (1994) Molecular structure of the water channel through aquaporin CHIP. The hourglass model. *The Journal of biological chemistry* **269**, 14648-14654
7. Walz, T., Smith, B. L., Agre, P., and Engel, A. (1994) The three-dimensional structure of human erythrocyte aquaporin CHIP. *The EMBO journal* **13**, 2985-2993
8. Murata, K., Mitsuoka, K., Hirai, T., Walz, T., Agre, P., Heymann, J. B., Engel, A., and Fujiyoshi, Y. (2000) Structural determinants of water permeation through aquaporin-1. *Nature* **407**, 599-605
9. Fu, D., Libson, A., Miercke, L. J., Weitzman, C., Nollert, P., Krucinski, J., and Stroud, R. M. (2000) Structure of a glycerol-conducting channel and the basis for its selectivity. *Science (New York, N.Y.)* **290**, 481-486
10. de Groot, B. L., and Grubmüller, H. (2001) Water Permeation Across Biological Membranes: Mechanism and Dynamics of Aquaporin-1 and GlpF. *Science (New York, N.Y.)* **294**, 2353-2357
11. Ishibashi, K., Hara, S., and Kondo, S. (2009) Aquaporin water channels in mammals. *Clinical and experimental nephrology* **13**, 107-117
12. Nielsen, S., Frokiaer, J., Marples, D., Kwon, T. H., Agre, P., and Knepper, M. A. (2002) Aquaporins in the kidney: from molecules to medicine. *Physiological reviews* **82**, 205-244
13. Rojek, A., Fuchtbauer, E. M., Kwon, T. H., Frokiaer, J., and Nielsen, S. (2006) Severe urinary concentrating defect in renal collecting duct-selective AQP2 conditional-knockout mice. *Proceedings of the National Academy of Sciences of the United States of America* **103**, 6037-6042
14. Hall, J. E., and Guyton, A. C. (2011) *Guyton and Hall textbook of medical physiology*,
15. King, L. S., and Yasui, M. (2002) Aquaporins and disease: lessons from mice to humans. *Trends in endocrinology and metabolism: TEM* **13**, 355-360

16. Schneider, T. D., and Stephens, R. M. (1990) Sequence logos: a new way to display consensus sequences. *Nucleic acids research* **18**, 6097-6100
17. Larkin, M. A., Blackshields, G., Brown, N. P., Chenna, R., McGettigan, P. A., McWilliam, H., Valentin, F., Wallace, I. M., Wilm, A., Lopez, R., Thompson, J. D., Gibson, T. J., and Higgins, D. G. (2007) Clustal W and Clustal X version 2.0. *Bioinformatics (Oxford, England)* **23**, 2947-2948
18. Heymann, J. B., and Engel, A. (1999) Aquaporins: Phylogeny, Structure, and Physiology of Water Channels. *News in physiological sciences : an international journal of physiology produced jointly by the International Union of Physiological Sciences and the American Physiological Society* **14**, 187-193
19. Stanton, B. A., and Koeppe, B. M. (2005) Solute and water transport along the nephron: tubular function. in *Berne & Levy Principles of Physiology*, Mosby Inc., St Louis. pp 699-714
20. Knepper, M. A., Valtin, H., and Sands, J. M. (2010) Renal Actions of Vasopressin. in *Comprehensive Physiology*, John Wiley & Sons, Inc. pp
21. Fushimi, K., Uchida, S., Hara, Y., Hirata, Y., Marumo, F., and Sasaki, S. (1993) Cloning and expression of apical membrane water channel of rat kidney collecting tubule. *Nature* **361**, 549-552
22. Ecelbarger, C. A., Terris, J., Frindt, G., Echevarria, M., Marples, D., Nielsen, S., and Knepper, M. A. (1995) Aquaporin-3 water channel localization and regulation in rat kidney. *The American journal of physiology* **269**, F663-672
23. Terris, J., Ecelbarger, C. A., Marples, D., Knepper, M. A., and Nielsen, S. (1995) Distribution of aquaporin-4 water channel expression within rat kidney. *The American journal of physiology* **269**, F775-785
24. Yasui, M., Hazama, A., Kwon, T. H., Nielsen, S., Guggino, W. B., and Agre, P. (1999) Rapid gating and anion permeability of an intracellular aquaporin. *Nature* **402**, 184-187
25. Ishibashi, K., Imai, M., and Sasaki, S. (2000) Cellular localization of aquaporin 7 in the rat kidney. *Experimental nephrology* **8**, 252-257
26. Nejsum, L. N., Elkjaer, M., Hager, H., Frokiaer, J., Kwon, T. H., and Nielsen, S. (2000) Localization of aquaporin-7 in rat and mouse kidney using RT-PCR, immunoblotting, and immunocytochemistry. *Biochemical and biophysical research communications* **277**, 164-170
27. Sohara, E., Rai, T., Miyazaki, J., Verkman, A. S., Sasaki, S., and Uchida, S. (2005) Defective water and glycerol transport in the proximal tubules of AQP7 knockout mice. *American journal of physiology. Renal physiology* **289**, F1195-1200
28. Elkjaer, M. L., Nejsum, L. N., Gresz, V., Kwon, T. H., Jensen, U. B., Frokiaer, J., and Nielsen, S. (2001) Immunolocalization of aquaporin-8 in rat kidney, gastrointestinal tract, testis, and airways. *American journal of physiology. Renal physiology* **281**, F1047-1057
29. Calamita, G., Ferri, D., Gena, P., Liquori, G. E., Cavalier, A., Thomas, D., and Svelto, M. (2005) The inner mitochondrial membrane has aquaporin-8 water channels and is highly permeable to water. *The Journal of biological chemistry* **280**, 17149-17153

30. Soria, L. R., Fanelli, E., Altamura, N., Svelto, M., Marinelli, R. A., and Calamita, G. (2010) Aquaporin-8-facilitated mitochondrial ammonia transport. *Biochemical and biophysical research communications* **393**, 217-221
31. Molinas, S. M., Trumper, L., and Marinelli, R. A. (2012) Mitochondrial aquaporin-8 in renal proximal tubule cells: evidence for a role in the response to metabolic acidosis. *American journal of physiology. Renal physiology* **303**, F458-466
32. Morishita, Y., Matsuzaki, T., Hara-chikuma, M., Andoo, A., Shimono, M., Matsuki, A., Kobayashi, K., Ikeda, M., Yamamoto, T., Verkman, A., Kusano, E., Ookawara, S., Takata, K., Sasaki, S., and Ishibashi, K. (2005) Disruption of aquaporin-11 produces polycystic kidneys following vacuolization of the proximal tubule. *Molecular and cellular biology* **25**, 7770-7779
33. Mount, D. B. (2014) Thick Ascending Limb of the Loop of Henle. *Clinical Journal of the American Society of Nephrology : CJASN* **9**, 1974-1986
34. Nielsen, S., Chou, C. L., Marples, D., Christensen, E. I., Kishore, B. K., and Knepper, M. A. (1995) Vasopressin increases water permeability of kidney collecting duct by inducing translocation of aquaporin-CD water channels to plasma membrane. *Proc Natl Acad Sci U S A* **92**, 1013-1017
35. Hoffert, J. D., Fenton, R. A., Moeller, H. B., Simons, B., Tchapyjnikov, D., McDill, B. W., Yu, M. J., Pisitkun, T., Chen, F., and Knepper, M. A. (2008) Vasopressin-stimulated Increase in Phosphorylation at Ser269 Potentiates Plasma Membrane Retention of Aquaporin-2. *Journal of Biological Chemistry* **283**, 24617-24627
36. Hoffert, J. D., Nielsen, J., Yu, M. J., Pisitkun, T., Schleicher, S. M., Nielsen, S., and Knepper, M. A. (2007) Dynamics of aquaporin-2 serine-261 phosphorylation in response to short-term vasopressin treatment in collecting duct. *AJP: Renal Physiology* **292**, F691-F700
37. Fenton, R. A., Moeller, H. B., Hoffert, J. D., Yu, M. J., Nielsen, S., and Knepper, M. A. (2008) Acute regulation of aquaporin-2 phosphorylation at Ser-264 by vasopressin. *Proceedings of the National Academy of Sciences* **105**, 3134-3139
38. Moeller, H. B., Praetorius, J., Rutzler, M. R., and Fenton, R. A. (2010) Phosphorylation of aquaporin-2 regulates its endocytosis and protein-protein interactions. *Proc Natl Acad Sci U S A* **107**, 424-429
39. Lu, H. J., Matsuzaki, T., Bouley, R., Hasler, U., Qin, Q. H., and Brown, D. (2008) The phosphorylation state of serine 256 is dominant over that of serine 261 in the regulation of AQP2 trafficking in renal epithelial cells. *AJP: Renal Physiology* **295**, F290-F294
40. Rice, W. L., Zhang, Y., Chen, Y., Matsuzaki, T., Brown, D., and Lu, H. A. J. (2012) Differential, phosphorylation dependent trafficking of AQP2 in LLC-PK1 cells. *PLoS ONE* **7**, e32843
41. Kamsteeg, E. J., Wormhoudt, T. A., Rijss, J. P., van Os, C. H., and Deen, P. M. (1999) An impaired routing of wild-type aquaporin-2 after tetramerization with an aquaporin-2 mutant explains dominant nephrogenic diabetes insipidus. *The EMBO Journal* **18**, 2394-2400
42. Marr, N., Bichet, D. G., Hoefs, S., Savelkoul, P. J., Konings, I. B., De Mattia, F., Graat, M. P., Arthus, M. F., Lonergan, M., Fujiwara, T. M., Knoers, N. V., Landau, D., Balfé, W. J., Oksche, A., Rosenthal, W., Müller, D., Van Os, C. H.,

- and Deen, P. M. (2002) Cell-biologic and functional analyses of five new Aquaporin-2 missense mutations that cause recessive nephrogenic diabetes insipidus. *J Am Soc Nephrol* **13**, 2267-2277
43. Fushimi, K., Sasaki, S., and Marumo, F. (1997) Phosphorylation of serine 256 is required for cAMP-dependent regulatory exocytosis of the aquaporin-2 water channel. *The Journal of biological chemistry* **272**, 14800-14804
 44. van Balkom, B. W., Savelkoul, P. J., Markovich, D., Hofman, E., Nielsen, S., Van der Sluijs, P., and Deen, P. M. (2002) The role of putative phosphorylation sites in the targeting and shuttling of the aquaporin-2 water channel. *The Journal of biological chemistry* **277**, 41473-41479
 45. Moeller, H. B., Knepper, M. A., and Fenton, R. A. (2009) Serine 269 phosphorylated aquaporin-2 is targeted to the apical membrane of collecting duct principal cells. *Kidney International* **75**, 295-303
 46. Barile, M., Pisitkun, T., Yu, M. J., Chou, C. L., Verbalis, M. J., Shen, R. F., and Knepper, M. A. (2005) Large scale protein identification in intracellular aquaporin-2 vesicles from renal inner medullary collecting duct. *Molecular & cellular proteomics : MCP* **4**, 1095-1106
 47. Diacumakos, E. G. (1973) Methods for micromanipulation of human somatic cells in culture. *Methods in cell biology* **7**, 287-311
 48. Dascal, N. (1987) The use of *Xenopus* oocytes for the study of ion channels. *CRC critical reviews in biochemistry* **22**, 317-387
 49. Capecchi, M. R. (1980) High efficiency transformation by direct microinjection of DNA into cultured mammalian cells. *Cell* **22**, 479-488
 50. Jalili, N., and Laxminarayana, K. (2004) A review of atomic force microscopy imaging systems: application to molecular metrology and biological sciences. *Mechatronics* **14**, 907-945
 51. Allison, D. P., Mortensen, N. P., Sullivan, C. J., and Doktycz, M. J. (2010) Atomic force microscopy of biological samples. *Wiley interdisciplinary reviews. Nanomedicine and nanobiotechnology* **2**, 618-634
 52. Tessmer, I. (2014) AFM Studies of Biomolecules. in *Encyclopedia of Applied Electrochemistry* (Kreysa, G., Ota, K.-i., and Savinell, R. F. eds.), Springer New York, New York, NY. pp 15-21
 53. Meister, A., Gabi, M., Behr, P., Studer, P., Voros, J., Niedermann, P., Bitterli, J., Polesel-Maris, J., Liley, M., Heinzelmann, H., and Zambelli, T. (2009) FluidFM: combining atomic force microscopy and nanofluidics in a universal liquid delivery system for single cell applications and beyond. *Nano letters* **9**, 2501-2507
 54. Guillaume-Gentil, O., Potthoff, E., Ossola, D., Dorig, P., Zambelli, T., and Vorholt, J. A. (2013) Force-controlled fluidic injection into single cell nuclei. *Small (Weinheim an der Bergstrasse, Germany)* **9**, 1904-1907
 55. van Leewenhoeck, A. (1677) Observations, Communicated to the Publisher by Mr. Antony van Leewenhoeck, in a Dutch Letter of the 9th of Octob. 1676. Here English'd: concerning Little Animals by Him Observed in Rain-Well-Sea. and Snow Water; as Also in Water Wherein Pepper Had Lain Infused. *Philosophical Transactions of the Royal Society of London* **12**, 821
 56. Ruska, E. (1980) The early development of electron lenses and electron microscopy. *Microscopica acta. Supplement*, 1-140

57. Baker, L. A., and Rubinstein, J. L. (2010) Radiation damage in electron cryomicroscopy. *Methods in enzymology* **481**, 371-388
58. Sayre, D., Kirz, J., Feder, R., Kim, D. M., and Spiller, E. (1977) Transmission microscopy of unmodified biological materials: comparative radiation dosages with electrons and ultrasoft x-ray photons. *Ultramicroscopy* **2**, 337-349
59. Adrian, M., Dubochet, J., Lepault, J., and McDowell, A. W. (1984) Cryo-electron microscopy of viruses. *Nature* **308**, 32-36
60. Deptuch, G., Besson, A., Rehak, P., Szelezniak, M., Wall, J., Winter, M., and Zhu, Y. (2007) Direct electron imaging in electron microscopy with monolithic active pixel sensors. *Ultramicroscopy* **107**, 674-684
61. Milazzo, A. C., Moldovan, G., Lanman, J., Jin, L., Bouwer, J. C., Klienfelder, S., Peltier, S. T., Ellisman, M. H., Kirkland, A. I., and Xuong, N. H. (2010) Characterization of a direct detection device imaging camera for transmission electron microscopy. *Ultramicroscopy* **110**, 744-747
62. Jin, L., Milazzo, A. C., Kleinfelder, S., Li, S., Leblanc, P., Duttweiler, F., Bouwer, J. C., Peltier, S. T., Ellisman, M. H., and Xuong, N. H. (2008) Applications of direct detection device in transmission electron microscopy. *Journal of structural biology* **161**, 352-358
63. Milazzo, A. C., Cheng, A., Moeller, A., Lyumkis, D., Jacovetty, E., Polukas, J., Ellisman, M. H., Xuong, N. H., Carragher, B., and Potter, C. S. (2011) Initial evaluation of a direct detection device detector for single particle cryo-electron microscopy. *Journal of structural biology* **176**, 404-408
64. Thompson, R. F., Walker, M., Siebert, C. A., Muench, S. P., and Ranson, N. A. (2016) An introduction to sample preparation and imaging by cryo-electron microscopy for structural biology. *Methods (San Diego, Calif.)* **100**, 3-15
65. Peitsch, C. F., Beckmann, S., and Zuber, B. (2016) iMEM: Isolation of Plasma Membrane for Cryoelectron Microscopy. *Structure (London, England : 1993)* **24**, 2198-2206
66. Arnold, S. A., Albiez, S., Bieri, A., Syntychaki, A., Adaixo, R., McLeod, R. A., Goldie, K. N., Stahlberg, H., and Braun, T. (2017) Blotting-free and lossless cryo-electron microscopy grid preparation from nanoliter-sized protein samples and single-cell extracts. *Journal of structural biology* **197**, 220-226
67. Guillaume-Gentil, O., Grindberg, R. V., Kooger, R., Dorwling-Carter, L., Martinez, V., Ossola, D., Pilhofer, M., Zambelli, T., and Vorholt, J. A. (2016) Tunable Single-Cell Extraction for Molecular Analyses. *Cell* **166**, 506-516

Chapter 2

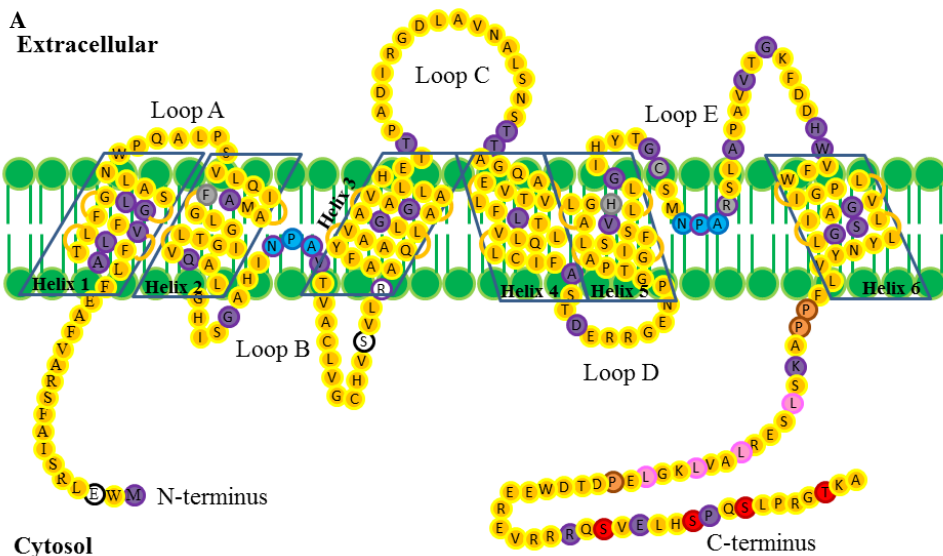
AQP2: Trafficking regulation and Nephrogenic Diabetes Insipidus

2.1: Introduction

To warrant water homeostasis, mammals depend on their kidneys (Figure 1.4). In humans, these organs filter 180 L of blood per day, and maintain tightly controlled blood pressure and osmolarity. While ~90% of the water in the plasma flows back through AQP1 in the descending loop of Henle (Figure 1.4), the major fraction of remaining water is reabsorbed in the collecting ducts of the kidney's nephron by Aquaporin-2 (AQP2). AQP2 is expressed exclusively in principal epithelium cells of the collecting duct and resides both in intracellular vesicles and the apical membrane (1). Binding of the hormone arginine-vasopressin (AVP) to the V2 receptor (V2R) induces a cascade leading to translocation of AQP2 from vesicles to the apical membrane (2). This leads to an increase of water permeability, thereby increasing the water flow through the collecting duct back to the bloodstream. Malfunction of AQP2 trafficking causes the disease Nephrogenic Diabetes Insipidus (NDI).

Although AQP2 trafficking has been extensively studied, the complete molecular mechanism of AQP2 trafficking regulation has yet to be revealed. In order to fill in the gaps present in the current understanding of AQP2 trafficking, an overview of known AQP2 trafficking mechanisms is necessary.

This chapter presents a literature study, summarizing the research that has been achieved on AQP2 and the underlying control mechanisms.



B

Feature Key	Residues	Description
Topological	1-16	N-terminus, cytoplasmic domain
Transmembrane	17-34	Helix 1, transmembrane domain
Topological	35-40	Loop A, extracellular domain
Transmembrane	41-59	Helix 2, transmembrane domain
Topological	60-85	Loop B, cytoplasmic, half membrane spanning helix
Transmembrane	86-107	Helix 3, transmembrane domain
Topological	108-127	Loop C, extracellular domain
Transmembrane	128-148	Helix 4, transmembrane domain
Topological	149-156	Loop D, cytoplasmic domain
Transmembrane	157-176	Helix 5, transmembrane domain
Topological	177-202	Loop E, cytoplasmic, half membrane spanning helix
Transmembrane	203-224	Helix 6, transmembrane domain
Topological	225-271	C-terminus, cytoplasmic domain

Figure 2.1: (A) Topological overview of AQP2. AQP2 contains 6 membrane spanning helices (helix 1-6) and two half membrane spanning helices (loop B and loop E) which, upon folding, overlap forming a seventh pseudo transmembrane segment leading to the formation of the hour-glass shape. Loop B and E carry the NPA motif (blue) which overlap upon folding. These NPA motifs, together with the residues forming the selectivity filter (grey) determine the water specificity of the AQP. Both the AQP2 N-terminus and C-terminus are located in the cytoplasm. The C-terminus of AQP2 contains four phosphorylation sites (Ser256, Ser261, Ser264 and Thr269 in humans; red), which change their phosphorylation state upon AVP stimulation (chapter 2.3). The flexibility of the AQP2 C-terminus is thought to be caused by two proline residues located at the base of the C-terminus (P225 and P226; orange), while P242 (orange) forms a putative hinge in the 38Å long C-terminal helix (E232-V257). The four C-terminal Leucine residues (L230, L234, L237 and L240; pink) are able to interact with LIP5, guiding lysosomal degradation of AQP2. Residue E3 in the N-terminus of AQP2 is thought to interact with residues S82 and R85 from loop B in one of its conformations (white residues), while AQP2 residues linked to autosomal NDI are indicated by a purple color. (B) Topological overview of AQP2 based on residue numbers.

2.2: The structure of aquaporin-2

To understand the AQP2 trafficking mechanism and the role of AQP2 in NDI, it is important to know the structure of AQP2. AQPs are present in all kingdoms of life, and the structure of these proteins is highly conserved. Although AQP2 shares a pronounced sequence homology with other AQPs (discussed in chapter 1) (3), it differs mainly at its the C-terminus.

2.2.1: AQP2 exhibits the characteristic AQP-fold

AQP2 contains six membrane spanning helices, two half-membrane spanning helices in reentrant loops B and E, and the AQP-hallmark NPA motifs (see Figure 2.1). Upon folding loops B and E overlap resulting in a seventh pseudotransmembrane segment and the formation of an hourglass shaped water pore (4). The two halves of AQP2, each containing three membrane spanning helices and one loop, exhibit distinct sequence homology, and are oriented oppositely in the membrane (3). As all AQPs, AQP2 proteins form homotetramers (5) (Figure 2.2B), where each individual pore lets water permeate on its own (6).

2.2.2: Structure and water specificity of aquaporin-2

X-ray crystallography has provided two structures of AQP2: the first a truncated form (7) and the second the full-length form (8). AQP2 is most closely related in sequence to AQP5, but exhibits high sequence homology to AQP1 as well, the membrane resident core of AQP2 is also structurally close to AQP1. The AQP2 pore exhibits the selectivity filter formed by residues F48, R187, C181 and H172 (F56, R195, C189 and H180 in AQP1, see Figure 2.1) and the NPA region. Mercurial sensitivity is related to C181 in loop E. Therefore, AQP2 allows specifically water molecules to permeate; the rate of $0.93 \pm 0.03 \cdot 10^{-13} \text{ cm}^3/\text{s}$ has been determined experimentally (5).

2.2.3: The C-terminus and N-terminus of aquaporin-2

Like in other AQPs, both the C-terminus and N-terminus of AQP2 are located in the cytoplasm (9,10)(Figure 2.1). However, while in most AQPs the C-terminus lies across the AQP cytoplasmic surface with a limited amount of variations between the structures (11-14), the AQP2 C-terminus is significantly longer and flexible (7). This flexibility hindered formation of well-diffracting 3D crystals. Thus, a truncated AQP2 (residues 1-241) was crystallized and its structure solved (7) (PDB entry 4NEF). Nevertheless, optimized crystallization conditions allowed well-ordered crystals of the full-length AQP2 to be grown and its structure to be solved shortly thereafter (8)(PDB entry 4OJ2)(Figure 2.2A and -B). The full-length structure reveals a 38 Å long C-terminal helix extending from residue E232 to V257, with a putative hinge at P242. With two prolines, P225 and P226, the octapeptide linker FPPAKSLS between transmembrane helix 6 and the C-terminal helix is a flexible loop, explaining the conformational freedom of the AQP2 C-terminus. The importance of this hinge region was previously tested by mutational studies, where the proline was substituted by an alanine. While the P225A mutation did not have any effect on AQP2 trafficking, the

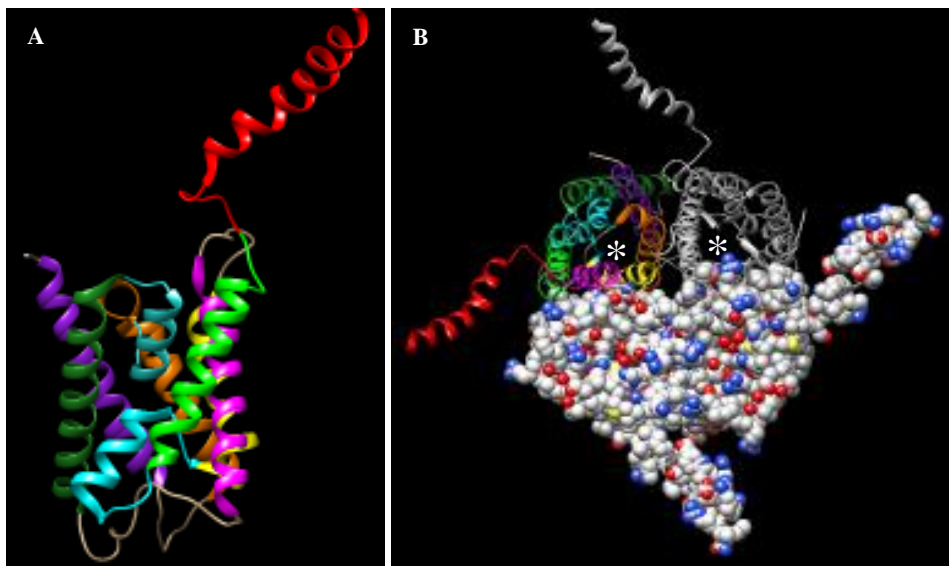


Figure 2.2 (A) Side view of an AQP2 monomer (PDB entry 4OJ2). (B) Top view of on AQP2 tetramer. (A/B) Transmembrane helices are indicated by color. Helix 1 is purple, helix 2 is orange, helix 3 is dark green, helix 4 is pink, helix 5 is yellow and helix 6 is light green. The halfmembrane spanning helices (loop B and -E) are colored blue, while the C-terminus is colored red. (B) individual water channels are indicated by asterisks (top two AQP2 monomers). The tight packaging of the AQP2 monomers into a tetramer is indicated for two monomers (bottom) rendered by spheres in Chimera.

mutation P226A led to retention of AQP2 in the endoplasmic reticulum (ER) in Madin-Darby canine kidney (MDCK) cells (15).

With the truncated form of AQP2, Cd^{2+} was used as crystallization agent. Its location suggested that AQP2 tetramers could bind Ca^{2+} ions, which in turn would modulate the conformation of AQP2 C-termini (7). The molecular mechanism related to this C-terminal positioning remains to be unraveled. However, the link between Ca^{2+} levels in the cell and AQP2 trafficking has been well established. Binding of AVP to the V2R leads to an increase of intracellular Ca^{2+} levels, while inhibition of intracellular Ca^{2+} release lead to a lower plasma membrane sorting of AQP2 after inducing exocytosis (16-22). Furthermore, mutations near the Ca^{2+} binding site have been linked to ER retention of AQP2 and NDI (23-25), both suggesting an importance for the Ca^{2+} induced positioning of the AQP2 C-terminus. The C-terminus of AQP2 is thought to be the main regulator of AQP2 trafficking, because mutations in the C-terminus often lead to the autosomal dominant form of NDI, whereas mutations in the AQP2 core relate to an autosomal recessive form of NDI (26). The AQP2 C-terminus contains four phosphorylation sites, which change their phosphorylation state upon binding of AVP to V2R (27). These residues are located at positions 256, 261, 264 and 269. In rodents, these residues are all serines, while in humans the amino acid located at position 269 is a threonine (27-29)(Figure 2.1). What is currently known about these phosphorylation sites in AQP2 trafficking regulation will be discussed in chapter 2.3.

Besides these phosphorylation sites, the C-terminus of AQP2 contains four hydrophobic leucine residues, located at positions 230, 234, 237 and 240 (Figure 2.1), which are able to interact with lysosomal trafficking regulator interacting protein 5 (LIP5). LIP5 is able to facilitate the lysosomal degradation of AQP2 (30). The presence of the phosphorylation sites and the LIP5 interacting leucines in the C-terminus of AQP2 underlines the importance of the AQP2 C-terminus for transport regulation.

The N-terminus of AQP2 is an undecapeptide (Figure 2.1). Its structure has been resolved by X-ray crystallography and exists in two conformations (7,8). The first conformation compares to a conformation found in human AQP5, where E3 from the AQP2 N-terminus interacts with S82 and R85 from loop B, while the second conformation of the AQP2 N-terminus is similar to the N-terminus of AQP1 (7,11). In the latter conformation, helix 1 extends into the cytoplasm for a full additional turn (12). These two distinct conformations suggest that the N-terminus may play a regulatory role in AQP2 trafficking as well. Indeed, replacing both the N-terminus and the C-terminus of AQP1 with the two termini from AQP2 lead to intracellular localization of AQP1 in MDCK cells, while translocation to the apical membrane could be induced after addition of forskolin. However, replacing just the N-terminus lead to AQP1 localization in both the apical and basolateral membrane, no intracellular AQP1 could be found. Finally, replacement of only the C-terminus lead to expression of AQP1 in the apical membrane, without intracellular localization of AQP1 (15). It is clear that both the C-terminus and N-terminus of AQP2 are important in AQP2 trafficking regulation, but the exact role that both termini may play in this process has yet to be fully understood. Yeast two hybrid assays did not show interactions between both termini, suggesting that AQP2 trafficking regulation by these termini is regulated independently from each other (23).

2.3: Phosphorylation of aquaporin-2

As discussed in chapter 2.2.3, the C-terminal tail of AQP2 plays an important role in AQP2 trafficking regulation. Research showed that just the C-terminal end (S256-A271) of AQP2 is necessary to traffic AQPs specifically to the apical membrane (23), while mutations in the C-terminal helix lead to an autosomal dominant form of NDI (26)(discussed in chapter 2.5.3 and summarized in table 2.4). The four phosphorylation sites (Ser256, Ser261, Ser264 and Thr269 in humans) related to AQP2 trafficking regulation change their phosphorylation state after binding of AVP to the V2R (27). An increase in phosphorylation was measured for Ser256, Ser264 and Thr269 after AVP stimulation, while phosphorylation of Ser261 decreased (27,31-34). The effect of AVP stimulation on the phosphorylative state of these residues is summarized in Table 2.1.

Although the C-terminal tail of AQP2 contains further phosphorylation sites (Ser148, Ser229, Ser231 and Thr244; Figure 2.1A), only the four residues mentioned above are linked to AQP2 trafficking regulation (23).

Table 2.1: The proposed function and the effect of phosphorylation on AQP2 for each residue. Change in phosphorylation after AVP stimulation was measured in both Sprague-Dawley rats (in % of total AQP2)(35) and in Brattleboro rats (in #-fold increase/decrease)(27,32,34).

Residue	t _{1/2} (27)	[phosphorylated AQP2] (%) (35)		Half life (36)	Proposed function
		Before AVP	After AVP		
Ser256	41 s	22.4%	25.6%	5.1h.	“Master switch” in AQP2 trafficking regulation (23,27,37,38)
		2 fold increase (34)			
Ser261	10.6 min	17.7%	1.8%	2.4h.	AQP2 endocytosis/exocytosis control (39,40)
		2.7 fold decrease (34)			
Ser264	4.2 min	1.9%	3.4%	3.8h.	Recycling of AQP2 (32)
		4 fold increase (32)			
Thr269	3.2 min	3%	26%	4.4h.	Retention signal for AQP2 apical membrane accumulation (27,29,33,36)
		14.9 fold increase (27)			

2.3.1: Phosphorylation of Ser256

During the discovery of AQP2 in 1993, Ser256 was immediately recognized as a phosphorylation site thanks to the presence of a cAMP-dependent protein kinase (PKA) consensus sequence (41). Kuwahara *et al.* showed that PKA indeed controls phosphorylation of Ser256 (42), followed by the discovery of its regulatory role in AQP2 exocytosis in 1997 (43). The importance of this residue in AQP2 trafficking regulation was established by mutation experiments, where the Serine at the 256 position was changed into an Alanine (AQP2-S256A). This mutation inhibited the phosphorylation of residue 256 and without phosphorylation, AQP2-S256A was mainly localized in intracellular vesicles even after AVP stimulation (43). Furthermore, a replacement of serine 256 into an aspartic acid (AQP2-S256D), mimicking the phosphorylated state of this residue by charge, resulted in an accumulation of AQP2-S256D in the apical membrane independent of AVP stimulation (23). Expression of AQP2 mutants in *Xenopus oocytes* showed that at least three out of four monomers in the AQP2 tetramer need Ser256 phosphorylation for inducing AQP2 exocytosis (44).

The role of S256 in AQP2 trafficking regulation became more evident once phosphorylation of this residue was compared to the phosphorylated state of the other residues. After AVP stimulation, a sharp increase in phosphorylated Ser256 can be measured by phosphoproteomic methods reaching a maximum at 1 min. after the addition of AVP (27,31). For the other residues a change in phosphorylation state was observed to be, relatively, slower (27). Importantly, Ser264 and Thr269 can only be phosphorylated once Ser256 is phosphorylated (27). Moreover, although Ser261 is dephosphorylated after AVP stimulation, AQP2-S261D was still localized in the apical membrane after Ser256 phosphorylation,

showing that phosphorylation of Ser256 is dominant over the phosphorylated state of Ser261 (37).

PKA is the kinase in the signaling chain switched on by V2R. But although Ser256 is flagged by a PKA consensus sequence and it was shown that this kinase indeed phosphorylates Ser256, PKA is not the only kinase able to phosphorylate this residue. Research showed that PKG (44,45), AKT (46), PKC δ (46) and casein kinase II (47) were able to phosphorylate Ser256 as well. Other kinases are suggested to interact with Ser256 based on consensus sequences surrounding Ser256 (48) or based on LC-MS/MS data (49). Furthermore, Ser256 phosphorylated AQP2 can be detected in both intracellular vesicles and the apical membrane (50) and high quantities of Ser256 phosphorylated AQP2 can be found even without AVP stimulation (35). This suggests that although Ser256 is important in AQP2 trafficking regulation, Ser256 phosphorylation alone is not sufficient for AQP2 bearing vesicles to exocytose into the apical membrane.

2.3.2: Phosphorylation of Ser269/Thr269

The exocytosis and endocytosis of AQP2 is in a constant equilibrium in the absence of AVP (48,51). However, once AVP binds to the V2R, AQP2 accumulates in the apical membrane (52). It was demonstrated by water permeability measurements and mathematical modelling studies that this accumulation in the plasma membrane is caused by two general processes, the first one being the speeding up of the exocytosis rate, complimented by a slowing down of the endocytotic removal of AQP2 (1,53). Indeed, AQP2 accumulation in the apical membrane could be mimicked by inhibiting endocytosis in the cell (54).

Although phosphorylated Ser256 is necessary to regulate phosphorylation of the other residues, its role in AQP2 trafficking control is debatable. Ser256 phosphorylation is only marginally increased after AVP stimulation (22.4% before AVP stimulation, 25.6% after AVP stimulation; Table 2.1)) (35) and Ser256 phosphorylated AQP2 is both localized in the apical membrane and intracellular vesicles (50). However, shortly after Ser256 phosphorylation a second phosphorylation event occurs, located at position 269 (27). In humans, this residue is a threonine, while in rodents this residue is a serine (27-29). (Although most of the experiments performed on residue 269 phosphorylation were done with rat AQP2, and therefore with Ser269, for clarity in this thesis this residue will be denoted as Thr269, for in this thesis a human AQP2 is used.)

After AVP stimulation a 14.9 fold increase in phosphorylated Thr269 can be measured (27), while research done by Xie *et al.* (2010) showed a starting value of 3% phosphorylated Thr269 before AVP treatment and ending with a total of 26% Thr269 phosphorylated AQP2 after AVP was added (35)(Table 2.1). Thr269 is the second residue changing its phosphorylated state after AVP binds to the V2R, with a $t_{1/2}$ of 3.2 min. (Ser256 has a $t_{1/2}$ of 41 s.)(Table 2.1)(27). Furthermore, immunogold labelling studies found that Thr269 phosphorylated AQP2 was exclusively found in the apical membrane in AVP-treated Brattleboro rats, while no Thr269 phosphorylation could be detected in the absence of AVP (27,33). This suggests that Thr269 plays an important role in AQP2 accumulation in the

apical membrane. Indeed, phosphomimetic studies showed that AQP2-T269E, glutamic acid is used to mimic the phosphorylated state of threonine by charge, was predominately present in the apical membrane, even without AVP stimulation, while AQP2-T269A was located intracellularly in the absence of AVP (27). However, after AVP stimulation, AQP2-T269A was partially redistributed to the apical membrane, showing that phosphorylation at this residue is not necessary to initiate AQP2 exocytosis (27).

Although Thr269 does not seem to enhance the rate of exocytosis, it could play a role in endocytosis inhibition. Indeed, biotin internalization studies in MDCK cells showed that the internalization rate of AQP2-T269E was remarkably slower as compared to wildtype AQP2 (AQP2-WT), while internalization rates of AQP2-T269A were comparable to AQP2-WT (36). Furthermore, by using cold block studies, it was found that a significant amount of AQP2-T269E was not internalized until 150 min. of cold block (29) and that protein interactions between AQP2-T269E and endocytosis associated proteins was reduced (29,36). Although Thr269 phosphorylation seems important to retain AQP2 in the apical membrane, similar results were achieved for AQP2-S256D as well. While AQP2-T269E was eventually internalized during cold block experiments, the majority of AQP2-S256D remained located in the cell membrane during the course of this experiment (29). Furthermore, biotin internalization studies in MDCK cells showed AQP2-S256D to exhibit a slightly higher internalization inhibition as compared to AQP2-T269E (36). The half-life of AQP2-S256D was also slightly higher as compared to AQP2-T269E ($t_{1/2}=5.1\text{h.}$ and $t_{1/2}=4.4\text{h.}$, respectively)(Table 2.1)(36). This shows that although Thr269 phosphorylation is important to inhibit endocytosis of AQP2, Ser256 phosphorylation is important as well.

2.3.3: Phosphorylation of Ser264

Shortly after Thr269 phosphorylation, Ser264 is phosphorylated ($t_{1/2}=4.2$ min; Table 2.1)(27). Just like phosphorylation of Thr269, phosphorylation of Ser264 is controlled by the phosphorylated state of Ser256 (27). After AVP stimulation, a four-fold increase in phosphorylated Ser264 could be measured (32)(Table 2.1). However, immunolabeling of normal rat kidney sections showed only a weak labeling of Ser264 phosphorylated AQP2 (32). Indeed, a quantitative analysis of Ser264 phosphorylation showed that only a small percentage of Ser264 is phosphorylated after AVP stimulation (1.9% of total AQP2 before AVP stimulation, 3.4% of total AQP2 after AVP stimulation; Table 2.1)(35).

Although Ser264 phosphorylation is regulated by AVP stimulation, its exact role in AQP2 trafficking regulation remains unclear. There is no apparent link between phosphorylated Ser264 and AQP2 apical membrane retention. In fact, internalization assays did not show a difference in internalization rates between AQP2-WT, AQP2-S264A and AQP2-S264D (36), while Ser264 phosphorylated AQP2 could be found in both the apical membrane and early endosomes after AVP stimulation (32). A regulatory role in enhanced exocytosis of AQP2 seems unlikely, for Ser264 is phosphorylated at a relatively late time point (as compared to Ser256 and Thr269)(27) and the change in the ratio of phosphorylated to unphosphorylated state is relatively small (35).

Ser264 phosphorylation does not seem to influence AQP2 accumulation in the apical membrane. Nevertheless, phosphorylation of this residue is linked to AQP2 trafficking regulation. Before AVP stimulation, a weak signal for Ser264 phosphorylated AQP2 could be found in the intracellular region. Shortly after addition of AVP, Ser264 phosphorylated AQP2 could be found in both the basolateral and apical membrane, while 60 min after AVP stimulation phosphorylated AQP2 was predominantly found in the apical membrane and the signal of phosphorylated Ser264 was increased 4-fold (32). Although Ser264 phosphorylated AQP2 could be found in the apical membrane, small quantities of Ser264 phosphorylated AQP2 colocalized with clathrin-coated vesicle markers (after 15 min), early endosome markers and recycling endosome markers (after 60 min)(32). These findings suggest that Ser264 phosphorylation could play a regulatory role in AQP2 endocytosis, however needs to be studied further.

After AQP2 endocytosis, the protein is either degraded or recycled. Protein degradation is executed in lysosomes. Although Ser264 phosphorylation is linked to AQP2 endocytosis, no colocalization of Ser264 phosphorylated AQP2 and lysosomes could be found at any time point, suggesting that phosphorylation of this residue could play a role in AQP2 recycling (32). Indeed the half-life of AQP2-S264D is slightly higher as compared to AQP2-WT (3.8h. and 2.9h., respectively; Table 2.1), but substantially lower than the half-life of AQP2-S256D and AQP2-T269E (5.1h. and 4.4h., respectively; Table 2.1)(36). Further research should shed more light on the role of Ser264 phosphorylation on AQP2 recycling.

2.3.4: (De)Phosphorylation of Ser261

Ser261, as a phosphorylation site, differs strikingly from the other phosphorylation sites (Ser256, Ser264 and Thr269), for it is dephosphorylated as a response to AVP stimulation (34). Quantitative analysis on inner medullas of Sprague-Dawley rats showed an initial Ser261 phosphorylation of 17.7%, as compared to total AQP2, before AVP treatment, this value decreased to 1.8% after AVP stimulation (Table 2.1)(35). Dephosphorylation of Ser261 is relatively slow with a $t_{1/2}$ of 10.6 min (Table 2.1)(34), while phosphorylation of the other residues as a reaction to AVP stimulation is much faster (27). Indeed, mass spectrometry experiments showed that Ser261 phosphorylated AQP2 co-existed with double phosphorylated AQP2, phosphorylated at Ser256 and Ser261 (28), and triple phosphorylated AQP2, phosphorylated at Ser256, Ser261 and Ser264 (55) or Ser261, Ser264 and Thr269 (27). Mass spectrometry data measuring the phosphorylation of all four phosphorylation sites together were not quantifiable (27). However, phosphorylated Ser261 was found in Ser256-Thr269 phosphorylated AQP2 as well (56).

Although the dephosphorylation of Ser261 upon AVP stimulation has been well established, the exact function of this dephosphorylation in AQP2 trafficking regulation is still under debate. Research shows no link with this residue and AQP2 apical membrane accumulation, which is thought to be induced by an increase in exocytosis and an inhibition of endocytosis of AQP2 (1,53). The relatively slow dephosphorylation of Ser261 (a significant decrease could only be measured 30 min after AVP exposure (34)), and the presence of phosphorylated

Ser261 in multiple phosphorylated AQP2 (27,28,55,56) suggests that this residue does not control the enhancement of exocytosis. Indeed, it was shown that phosphorylation of Ser256 was dominant over Ser261 phosphorylation, resulting in the accumulation of AQP2-S256D-S261D in the apical membrane (37,39). This documents that Ser261 dephosphorylation is not necessary to induce AQP2 exocytosis. Furthermore, internalization rates did not differ between AQP2-WT, AQP-S261A and AQP2-S261D, illustrating that the phosphorylation state of this residue does not influence endocytosis of AQP2 either (36,37) eliminating the role of Ser261 dephosphorylation in AQP2 apical membrane accumulation.

Despite a lack in AQP2 apical membrane accumulation control, Ser261 phosphorylation could play a role in other AQP2 trafficking regulation pathways. Colocalization studies did not show a presence of Ser261 phosphorylated AQP2 in the plasma membrane, the endoplasmic reticulum (ER), the Golgi or lysosomes, suggesting that AQP2 resides in vesicles independent of big membrane structures of the cell (34). The lack in lysosome colocalization suggests that Ser261 plays a role in AQP2 recycling. However, the half-lives of AQP2-S261A and AQP2-S261D are comparable to AQP2-WT (2.6h., 2.4h. and 2.9h., respectively; Table 2.1)(36) contradicting the proposed role of Ser261 in AQP2 recycling.

Another control mechanism for Ser261 phosphorylation could still rely in AQP2 exocytosis. Although AQP2 exocytosis can be initiated despite the phosphorylative state of Ser261 (37,39), this residue does play an indirect role in exocytosis regulation. Phosphomimetic studies in madin darby canine kidney (MDCK) cells showed that AQP2-S261A and AQP2-S261D resided in intracellular vesicles, even after AVP stimulation in combination with 12-*O*-Tetradecanoylphorbol-13-acetate (TPA) (39). Both AQP2-S261A and AQP2-S261D showed an increase in ubiquitinated K270 as compared to AQP2-WT (39). Ubiquitination of K270 is thought to be the initiator of AQP2 endocytosis (57) as will be discussed in chapter 2.4.3. Indeed, a K270R mutation inhibited the ubiquitination of this residue (57) and both AQP2-S261A-K270R and AQP2-S261D-K270R were transported to the apical membrane after AVP stimulation (39). However, AQP2-S261A exocytosis inhibition could not be reproduced in mouse polarized kidney cortical collecting duct (mpkCCD) cells (40), contradicting previous results (39). Further evidence in Ser261 exocytosis control was found in MDCK cells expressing AQP2-S261D. Although AQP2-S261D showed an increase in S256 phosphorylation after AVP treatment, the phosphorylation of Ser256 decreased over time. In AQP2-WT the level of phosphorylated Ser256 stays constant after AVP stimulation (39). Furthermore, an increase in Ser261 phosphorylation after AVP stimulation was found in MDCK cells expressing AQP2-P262L, a mutation carrying the traits of dominant NDI with an impaired reaction on AVP stimulation (58), suggesting that AQP2 translocation is inhibited by the enhanced phosphorylation of Ser261. However, AQP2 exocytosis could not be restored by expression of either AQP2-S261A-P262L or AQP2-S256D-S261A-P262L-S264D-T269E (40). Despite extensive research on Ser261 phosphorylation and the finding of an apparent link between the phosphorylation state of this residue and AQP2 exocytosis regulation, further research is necessary to unravel the exact role of Ser261 in AQP2 trafficking control.

2.4: Proteins regulating aquaporin-2 trafficking

Besides changes in phosphorylation states of the AQP2 C-terminus, a broad range of different proteins controlling the transport of membrane proteins from the ER to their final destination are also involved in AQP2 trafficking regulation. Although AQP2 trafficking has been extensively studied, many of the AQP2 transport controlling proteins have yet to be identified. Furthermore, multiple proteins interacting with AQP2 have been found, but their exact role in AQP2 trafficking regulation is yet to be unraveled.

AQP2 trafficking is a complex cellular process, controlled by a broad variety of proteins. Proteins involved are for instance: PKA-anchoring proteins (AKAPs)(59-63), phosphodiesterases (PDEs)(64-67), actin filaments (discussed in chapter 3)(68-70), microtubules (71), small guanosine triphosphatases (GTPases) of the Rho family (72,73), motor proteins transporting AQP2 bearing vesicles, soluble *N*-ethylmaleimide-sensitive factor attachment protein receptors or SNAREs (74-77), and 70 kDa heat-shock proteins (78,79). An overview of proteins found to be involved in AQP2 trafficking regulation is given in Table 2.2.

The complexity of this regulatory pathway becomes evident from the long list of proteins involved, and a detailed discussion of all these proteins goes beyond the scope of this thesis. Here the best studied proteins playing a role in the most fundamental parts of the AQP2 trafficking pathway, will be discussed.

2.4.1: Phosphorylation of Ser256 by PKA guided by AKAP

Phosphorylation of S256 residue is executed by PKA, while other kinases have been linked to Ser256 phosphorylation as well (Table 2.2, (44-47)), which is activated by a multi-step process upon AVP binding to V2R. The vasopressin receptor V2R is a G protein-coupled receptor linked to the heterotrimeric GTP-binding protein G_s . AVP binding to the extracellular surface of V2R leads an allosteric conformational change of its cytosolic surfaces that fosters binding of G_s . This event catalyses the exchange of GDP to GTP, which leads to the release of the α -subunit, $G_s\alpha$ -GTP, from the β and γ subunit of G_s and the binding of $G_s\alpha$ -GTP to adenylate cyclase. Adenylate cyclase converses ATP in the cell to 3',5'-cyclic AMP (cAMP), leading to a rise of cAMP levels in the cell, which activates PKA.

PKA is a heterotetrameric protein, which comprises two regulatory subunits noncovalently bound to two catalytic subunits (80,81). cAMP can bind to the regulatory subunit on two sites, termed A and B. The B-site is exposed in the tetrameric form of PKA, while the A-site is protected. Binding of cAMP to the B-site leads to an intramolecular steric change and the opening of the A-site, followed by binding of cAMP at this site. Binding of four cAMP molecules, two to each regulatory subunit, leads to the dissociation of the regulatory subunits from the catalytic subunits induced by a conformational change (82). The release of the regulatory subunits leads to active PKA, which can then phosphorylate Ser256 of AQP2.

Table 2.2: Overview of proteins linked to AQP2 trafficking regulation and their (proposed) role. Proteins discussed in this chapter are in *italics*.

Function	Proteins	References
Cytoskeleton	Actin, MLCK, Moesin, Myosin, RhoA, TM5b, Tubulin	(68-71,73,76,79,83-96)
PKA platform phosphorylation	<i>AKAP18δ</i> , <i>AKAP220</i> , CSNK, <i>PKA</i>	(31,38,44,45,48,61,63,97-100)
Other kinases linked to Ser256 phosphorylation	AKT, PKCδ, casein kinase II, PKG	(44-47)
Exocytosis	Annexin, Calcitonin, Epac, Integrin, <i>MUNC18b</i> , PKB, PP1/PP2A, <i>RAB</i> , <i>SNAP</i> , SPA-1, Synaptotagmin, <i>Syntaxin</i> , <i>VAMP</i> , <i>Snapin</i>	(69,71,74-77,86,94,101-127)
Endocytosis	AP1/2, Caveolin-1, Clathrin, Dynactin, Dynamin, Dynein, GSK3β, <i>HSC70</i> , HSP70, MAL, PKC, <i>Ubiquitin</i> , <i>14-3-3θ</i> , <i>14-3-3ζ</i>	(23,28,36,46,48,54,57,71,76,78,79,91,93,95,102,128-144)
Unknown	BiP, RAN, TRPC3, TRPV4	(102,145-148)
AQP2 transcription	AP-1, Calcineurin, CREB, ERK, NFκB, PI3K, TonEBP	(28,104,110-112,114,149-167)
Ser261 phosphorylation	CDK, JNK, p38-MAPK	(28,48,111,158,159,168)
AQP2 degradation	LIP5, VACM-1	(30,142,169,170)

Although PKA phosphorylates Ser256 of AQP2, it is able to phosphorylate a wide variety of different proteins. A peptide array screening found 29 possible substrates for PKA phosphorylation, while it was found that PKA plays a role in lipid metabolism, glycogenesis, glycolysis and protein synthesis as well (171). Specificity of PKA can be enhanced by expression of different PKA subunits. Four different isoforms of the regulatory subunits (RIα, RIβ, RIIα and RIIβ) and three isoforms of the catalytic subunits (Cα, Cβ and Cγ) are known, each isoform contains distinct physical and biological properties and isoforms are differentially expressed (172). By expression of the right subunits, compartmentalization can be reached, however, phosphorylation of specific substrates requires A kinase association proteins (AKAPs).

AKAPs interact with both PKA and a specific PKA target. A broad variety of AKAPs have been discovered and although they are diverse in structure, they share the same function. All AKAPs contain a PKA-binding domain and a unique domain targeting the PKA-AKAP complex to defined subcellular structures, membranes or organelles (173-175). Both AKAP18δ (61) and AKAP220 (63) were reported to interact with AQP2, while other AKAPs may be involved as well (59,60).

AKAP18 δ is one of the splice variants of AKAP18 and was discovered in 2004 (61). AKAP18 δ binds to the RII domain of PKA with a high affinity (20-31nM) and colocalizes with AQP2, both in the cytosol as well in the apical membrane (61). Furthermore, multiple proteins are associated with AQP2-bearing vesicles, but only AKAP18 δ co-translocates with AQP2 to the plasma membrane, suggesting that this protein facilitates AQP2 trafficking (61). AKAP18 δ lacks a membrane targeting domain, although AKAP18 δ does contain a myristoylation consensus site and a leucine zipper motif which could mediate membrane localization of AKAP18 δ . However, both the role of AKAP18 δ in AQP2 phosphorylation and the mechanism of AKAP18 δ association with AQP2 are not fully understood (61). AKAP220 is the most abundantly expressed AKAP in the inner medullary collecting ducts (176) and has been linked to AQP2 phosphorylation (63). COS cells co-expressing AQP2 and AKAP220 showed a 1.98 \pm 0.07 fold increase in AQP2 phosphorylation as compared to cells without AKAP220 expression (63). Furthermore, yeast two-hybrid studies showed that the C-terminus of AQP2 binds to AKAP220 between residues 1098 and 1186 of AKAP220. Both immunofluorescence and immunoelectron microscopy in rat kidney showed colocalization between AQP2 and AKAP220. However, in both COS cells and in the rat kidney, binding of AKAP220 to AQP2 could not be demonstrated by immunoprecipitation, suggesting that interactions between both proteins are weak (63). Besides guiding the phosphorylation of AQP2, AKAP220 is linked to other parts in the AQP2 trafficking regulation pathway. It was shown that AQP2 accumulates in the apical membrane in both mIMCD3 spheroids and in principal cells of the kidney-collecting ducts from AKAP220-null mice caused by a disruption of the actin cortex (177). This suggests that AKAP220 plays a role in actin cortex remodeling. However, the exact role of AKAP220 in actin cortex remodeling has yet to be determined.

2.4.2: AQP2 trafficking, a role for 14-3-3 proteins

14-3-3 proteins represent a highly conserved family involved in fundamental cellular processes, such as metabolism, protein trafficking, signal transduction, apoptosis and cell-cycle regulation. 14-3-3 proteins bind to phosphoserine/phospho-threonine proteins depending on their state of phosphorylation. Therefore, 14-3-3 proteins are important members of the core phosphoregulatory pathways that are crucial for normal growth and cellular development. Ubiquitination of AQP2 is regulated by two distinctive isoforms of the 14-3-3 proteins (144). To date seven isoforms have been identified in mammalian cells: 14-3-3 β , - ϵ , - γ , - η , - σ , - θ , and - ζ , of which 14-3-3 θ and 14-3-3 ζ are directly linked to AQP2 (76,144). Lentiviral mediated knock-down of 14-3-3 ζ expression in mpkCCD cells lead to a decreased half-life of AQP2, an increase in ubiquitinated AQP2 and a reduction of AQP2 levels. This suggests that 14-3-3 ζ is able to inhibit AQP2 endocytosis by inhibiting ubiquitination. Indeed, 14-3-3 ζ was found to colocalize with AQP2 near the apical membrane and direct AQP2-14-3-3 ζ interactions were found by using pull-down assays. The strength of these interactions depends on the phosphorylated state of AQP2, where these interactions were drastically reduced in S256A and T269A mutants of AQP2 (144). 14-3-3 θ is thought to

play an opposite role in AQP2 endocytosis regulation. 14-3-3 θ knock-down resulted in an increased AQP2 half-life, a decreased ubiquitination of AQP2 and enhanced AQP2 levels in the plasma membrane. Furthermore, AQP2-14-3-3 θ interactions are controlled by the phosphorylated state of AQP2 residue Thr269 (144). The importance of Thr269 phosphorylation in AQP2 apical membrane retention was discussed in chapter 2.3.2, showing that internalization rates of AQP2-T269A were much faster as compared to AQP2-T269E (36). The reduced interaction between AQP2-T269A and 14-3-3 θ together with enhanced AQP2 apical membrane retention in 14-3-3 θ knock-down cells suggests that 14-3-3 θ plays a role in Thr269 dephosphorylation. Research showed that protein phosphatase 1 and -2A are both able to dephosphorylate AQP2 at residue 269 (178), while they are also able to interact with 14-3-3 proteins (179,180), suggesting that 14-3-3 θ recruits or stabilizes the protein phosphatase complex able to dephosphorylate AQP2 at residue 269 (144).

2.4.3: AQP2 exocytosis, a role for Rab11 and SNARE proteins

After AVP stimulation, exocytosis of AQP2 bearing vesicles is increased, a process that is tightly regulated and executed by a broad range of proteins. For exocytosis of proteins to the plasma membrane, different pathways are known. (i) Secretory vesicles from the trans-Golgi network (TGN) can travel directly to the plasma membrane via the secretory pathway. (ii) Membrane proteins can be transported to the apical membrane via recycling endosomes. Recycling endosomes can be formed from either early endosomes or from the TGN. (iii) Proteins located in the basolateral membrane can be transported to the apical membrane via transcytosis (181-183). It is thought that AQP2 utilizes one or more of these pathways for its exocytosis.

Rab11 is a member of the rab family of small GTPases and regulates membrane trafficking by interacting with different effector proteins (184,185). Rab11 is found primarily in recycling endosomes and regulates the recycling of endocytosed proteins (185). AQP2 colocalizes with Rab11, suggesting that the majority of AQP2 is exocytosed via pathway (ii) described above (76). Indeed, stimulation of AQP2 exocytosis by forskolin treatment led to a decrease in AQP2-Rab11 colocalization, while the colocalization was restored after forskolin was washed out (94). Furthermore, Nedvetsky *et al.* (2007) reported that Rab11 either directly or indirectly binds to Myosin Vb, a motor protein linked to vesicular trafficking (86). Expression of a dominant-negative construct of myosin Vb led to AQP2 retention in the subapical region, even after forskolin treatment, showing that the interaction between Rab11 and Myosin Vb is critical for AQP2 exocytosis (86). In contradiction, depletion of Rab11 led to apical membrane accumulation of AQP2 (94), suggesting that although Rab11 is an important factor in the AQP2 exocytosis pathway, other proteins may play a role as well. Indeed, LC-MS/MS data revealed a broad range of different proteins located in AQP2 bearing vesicles. Besides Rab11, Rab4, -5, -7, -18, -21 and -25 were identified as well (76). In addition, several endosome-associated SNARE proteins were found, as well as markers of the trans-Golgi network, components of the exocyst complex, several motor proteins, multiple endoplasmic reticulum-resident proteins and ribosomal

proteins (76). These findings indicate that AQP2 is located in recycling endosomes, while the colocalization with ER-markers and TGN-markers point towards the translation and maturation pathway of freshly produced AQP2 (76).

After exocytotic transport, AQP2 bearing vesicles need to fuse with the apical membrane. Vesicle fusion is guided by the soluble *N*-ethylmaleimide-sensitive factor attachment protein (SNAP) receptor (SNARE) family of proteins, which consists of membrane proteins on both the vesicle (v-SNARE) as well as the target membrane (t-SNARE)(186,187). Multiple v-SNARE proteins have been identified in AQP2 bearing vesicles, like syntaxin-7, -12 and -13, Vti1a, VAMP2 and VAMP3 (76,116), while Syntaxin-3 (Stx3) and SNAP23 were identified as t-SNARE proteins located in the apical membrane (116,188). Co-immuno precipitations showed a clear interaction between VAMP2, VAMP3, SNAP23 and Stx3 (75), suggesting that these proteins play a key role in AQP2 apical membrane fusion. Knockdown of either VAMP2 or VAMP3 in MCD4 cells reduced the amount of AQP2 in the apical membrane (75,189), while silencing of VAMP2 or VAMP3 had the same effect (75). Furthermore, RNA interference experiments, inhibiting Stx3 expression, resulted in a dramatic decrease of AQP2 bearing vesicle fusion (75). Co-immuno precipitation experiments showed an enhanced formation of Stx3-SNAP23 complexes after forskolin stimulation, linking all these SNARE proteins to AQP2 apical membrane fusion (75).

A regulatory role in membrane fusion was proposed for Munc18b interacting with Stx3. The exact role Munc18b plays in AQP2 apical membrane accumulation is still unclear. However, a decrease in Stx3-Munc18b association was found after forskolin stimulation, while the association between SNAP23 and Stx3 increased. This suggests that Munc18b plays an inhibitory role in the formation of the SNAP23-Stx3 complex, hence regulating the fusion of AQP2 bearing vesicles with the apical membrane (75).

The scaffolding molecule Snapin, reacting as an intermediate protein linking the transported proteins to their specific SNARE machinery, was found to be linked to AQP2 and Stx3 as well, suggesting that this protein plays a role in the apical membrane specificity of AQP2 (122). A direct interaction between AQP2 and Snapin was found by pull down experiments, as well as a direct interaction between Snapin and Stx3. AQP2 pulled down Stx3 in the presence of Snapin, while this interaction was not observed in the absence of Snapin. Furthermore, expression of AQP2, Stx3, SNAP23 and Snapin in oocytes increased the waterflux 4-fold as compared to the oocytes only expressing AQP2, Stx3 and SNAP23 (122), suggesting that Snapin plays a key regulatory role in the specific fusion of AQP2 to the apical membrane.

Although AQP2 exocytosis and membrane fusion have been extensively studied, a significant fraction still remains unknown. Rab11 is found in AQP2 bearing vesicles and linked to AQP2 exocytosis, but some results are contradictory and other proteins are suggested to be involved in AQP2 exocytosis as well. Furthermore, VAMP2, VAMP3, Stx3 and SNAP23 are linked to AQP2 vesicle fusion to the apical membrane. However, the exact role Munc18b and Snapin play in apical membrane targeting and fusion is still unclear. Additionally, a potential role for VAMP8 in AQP2 apical membrane fusion was found in

mice, while deletion of VAMP3 in mice did not affect their urine-concentrating ability (127). Further research is necessary to discover how the known proteins are involved in AQP2 exocytosis and apical membrane fusion and to decipher the role that other proteins play in this process.

2.4.4: Clathrin mediated Aquaporin-2 endocytosis and ubiquitination

After AQP2 is accumulated in the apical membrane and AVP is washed away, AQP2 needs to be internalized via endocytosis. Although cargo can be internalized into the cell via different pathways, it was demonstrated that AQP2 is endocytosed via clathrin-coated pits. Sun *et al.* (2002) revealed that AQP2 accumulates into clathrin coated pits in GTPase-deficient dynamin expressing cells, inhibiting the release of these pits from the plasma membrane (133). Furthermore, Lu *et al.* (2007) showed that AQP2 directly interacts with clathrin, dynamin, adaptor protein AP2 and Hsc70 (78).

Hsc70 is a clathrin-decoating ATPase and its interaction with AQP2 was found to be crucial for AQP2 endocytosis (78). 30 min. after AVP treatment of Lilly Laboratories Cell Porcine Kidney (LLC-PK1) cells stably expressing AQP2, Hsc70 colocalizes with AQP2 and functional knockdown of Hsc70 activity leads to AQP2 apical membrane retention. AQP2-Hsc70 interactions rely on the dephosphorylated state of Ser256, for it was shown that this interaction was greatly reduced in cells chronically treated with AVP and in cells expressing AQP2-S256D (78). This suggests that endocytosis of AQP2 depends on its phosphorylation state as well.

Besides Hsc70, AQP2 endocytosis is also regulated by the ubiquitinated state of AQP2. Ubiquitin is a highly conserved protein and can be covalently attached to one or more lysine residues of cellular proteins. Ubiquitination of protein can function as a signal for protein degradation or protein localization. Furthermore, it can promote protein interactions and protein activity (190-192). AQP2 can be ubiquitinated on Lysine270 (K270), via K63 linkage, and ubiquitination of AQP2 regulates its endocytosis (57). AQP2 is ubiquitinated while it resides in the apical membrane, suggesting that ubiquitination is a key regulator of AQP2 endocytosis. AQP2-K270R, unable to be ubiquitinated, internalized at a significantly slower rate than AQP2-WT (57). However, AQP2-K270R could still be internalized, suggesting that either K270 is not the only ubiquitination site of AQP2 or ubiquitination is not the only signal for endocytosis.

As discussed previously, the phosphorylated state of AQP2 is thought to play a regulatory role in its endocytosis. Accordingly, AQP2-S256D and AQP2-T269E have a reduced interaction with proteins involved in endocytosis, like clathrin, dynamin and Hsc70, as compared to AQP2-WT (36) and a decreased internalization rate (29,36). Furthermore, endocytosis of ubiquitinated AQP2 can be inhibited by Thr269 phosphorylation of AQP2 even though Thr269 phosphorylation leads to increased ubiquitination of AQP2 (178). However, ubiquitinated AQP2-S256D resided in internal vesicles even after forskolin stimulation in MDCK cells (39), suggesting that, although AQP2-phosphorylation is important in its trafficking regulation, other factors in the cell play an important role as well.

Similar results were obtained with dopamine and PGE₂, showing that both dopamine and PGE₂ can induce AQP2 endocytosis independent of the phosphorylative state of AQP2 (193). Dopamine has a marked diuretic action in humans, rats and other species, while abnormalities in the renal response to dopamine have been associated with certain forms of genetic hypertension in rats (194). Prostaglandins (like PGE₂) inhibit maximal urine concentration in mammalian kidneys and the effect of PGE₂ on AQP2 endocytosis is linked to cellular cAMP levels (193,195,196).

The importance of AQP2 phosphorylation in AQP2 endocytosis regulation, while AQP2 can be endocytosed independent of its phosphorylated state suggests that AQP2 endocytosis requires a tight interplay between its phosphorylation state and the proteins guiding AQP2 endocytosis.

2.5: AQP2 and Nephrogenic Diabetes Insipidus

Diabetes Insipidus (DI) is a disease characterized by an increased urine production (typically 12 L/day) and an increased thirst (water uptake of up to 20 L/day), caused by a disruption in the body water balance (197). This disease affects roughly 1 in 25,000 people (198). The importance of AQP2 in maintaining water homeostasis was discussed in chapter 1. A disruption of the regulated AQP2 translocation mechanism is the leading cause of this disease. DI is either caused by an impaired production or release of AVP, or an impaired effect of AVP in the kidney (199,200). The latter type of this disease is called Nephrogenic Diabetes Insipidus (NDI) and is caused by a decreased or defective action of AVP on the principal cells of the collecting duct.

NDI can either be acquired or hereditary, where hereditary NDI accounts for less than 10% of all cases of DI (201,202). Hereditary NDI is caused by mutations in either the *avpr2* gene (coding for the V2R; X-linked NDI) or the *aqp2* gene (Autosomal NDI)(203). This thesis focuses on AQP2 and its trafficking regulation, therefore the underlying mechanism of X-linked and Autosomal NDI will be discussed.

2.5.1: X-linked NDI: mutations in the *avpr2* gene

X-linked NDI is the most prevalent form of hereditary NDI, accounting for 90% of the cases (204). The *avpr2* gene is located in chromosome region Xq28 and mutations in this gene lead to a recessive X-linked disease (205). Therefore, X-linked NDI mostly affects males, while females are often carriers or suffer from partial NDI caused by skewed X-chromosome inactivation (206-208).

The V2R contains seven membrane-spanning helices and AVP binds within the transmembrane helices II-IV causing allosteric structural rearrangements as discussed above (209-211). More than 200 mutants resulting in X-linked NDI have been identified and the effect these mutations have on V2R expression and functionality can be divided into five classes (212-214). (i) Mutations leading to improperly processed or unstable mRNA, (ii) mutations resulting in the misfolding of the receptor and retention in the ER, (iii) mutations causing an impaired interaction between the V2R and G proteins leading to impaired cAMP

Table 2.3: An overview of the known mutations, causing the autosomal recessive form of NDI and their location in the AQP2 protein. If tested, the functionality of the protein is added.

Mutation	Functionality	Location
MII (215)	Unknown, absence of start codon	N-terminus
A19V (216)	Unknown	Transmembrane domain 1
L22V (217,218)	Partial (60%)	Transmembrane domain 1
V24A (219)	Functional	Transmembrane domain 1
L28P (220)	Not functional	Transmembrane domain 1
G29S (215)	Unknown	Transmembrane domain 1
A47V (220)	Partial (40%)	Transmembrane domain 2
Q57P (25)	Not functional	Transmembrane domain 2
G64R (221-223)	Partial (20%)	Loop B
N68S (24,223)	Not functional	Loop B, NPA motif
A70D (224)	Unknown	Loop B, NPA motif
V71M (220)	Partial	Loop B
R85-terminated (225)		Loop B
G96E (226)	Unknown	Transmembrane domain 3
G100-terminated (227)		Transmembrane domain 3
G100R (228)	Unknown, probably not functional	Transmembrane domain 3
G100V (25)	Not functional	Transmembrane domain 3
T108M (229)	Unknown	Loop C
369delC / Frameshift, terminated after amino acid 131 (221)	Not functional	
T125M (230-232)	Partial (25%)	Loop C
T126M (24,223,230)	Partial (20%)	Loop C
L137P (233)	Unknown	Transmembrane domain 4
A147T (24,223)	Functional	Transmembrane domain 4
D150E (234)	Not functional	Loop D
V168M (225,235)	Partial (60%)	Transmembrane domain 5
G175R (220,230,231)	Not functional	Transmembrane domain 5
G180S (228)	Unknown	Loop E
C181W (217,218,236)	Not functional	Loop E
P185A (220)	Not functional	Loop E
R187C (2,221,223)	Not functional	Loop E
R187H (224)	Unknown	Loop E
A190T (58,231)	Not functional	Loop E
V194I (220)	Functional	Loop E
G196D (237)	Not functional	Loop E
H201Y (238)	Unknown	Loop E
W202C / splice variant (239)		Loop E
C606+1G>A / Splice variant (220)		
G211R (238)	Unknown	Transmembrane domain 6
G215C (234)	Not functional	Transmembrane domain 6
S216P (2,222)	Not functional	Transmembrane domain 6
S216F (240)	Unknown	Transmembrane domain 6
652delC / Frameshift (220)		Transmembrane domain 6

production, (iv) mutations leading to improper interactions between the V2R and AVP, (v) mutations leading to miss-sorting of the V2R to incorrect cellular compartments (212). Class (ii) is the most prevalent type of X-linked NDI (212).

At the moment, there are no cures for X-linked NDI. In some cases, fluid deprivation or AVP administration can release some of the symptoms (199), while pharmacologic chaperones to inhibit ER retention have been proposed as well (241-243). However, the existing methods do not provide a complete cure for X-linked NDI and further research is necessary to develop new drugs for this disease.

2.5.2: Autosomal recessive NDI: AQP2 misfolding

Autosomal recessive NDI accounts for 9% of the hereditary forms of NDI and is mostly caused by a mutation in the pore-forming region. Two C-terminal modifications are linked to autosomal recessive NDI (AQP2-P262L and AQP2-K228E), however, this is due to a compound heterozygote mutation, AQP2-P262L and AQP2-K228E on themselves show the typical characteristics of dominant NDI (58,219). Mutations causing autosomal recessive NDI result in misfolding of AQP2, leading to ER retention and degradation (212). This hereditary form of NDI is a recessive trait, meaning that patients are either homozygous or compound heterozygous for the AQP2 mutations. Therefore, this type of NDI affects males and females equally (199). An overview of the known mutations found in the patients suffering from the autosomal recessive form of NDI is visualized in Table 2.3.

Up till now, more than 40 mutations causing autosomal recessive NDI are known (212). Although these mutations lead to AQP2 misfolding, for some mutations the water permeability of AQP2 is preserved. AQP2-L22V, -A47V, -T125M, -T126M, -A147T all conferred a reduced water permeability as compared to AQP2-WT, which was more likely caused by ER retardation of these mutants, instead of an impaired water channel (217,220,223). The same was found for AQP2-K228E and AQP2-V24A (219). Possible therapies, to recover the water homeostasis misbalance caused by autosomal recessive NDI, could therefore rely on ER retention inhibition or the use of chemical chaperones able to restore the plasma membrane routing (220). However, these therapies are not trivial, for the misfolding of AQP2 often result in impaired tetramerization of AQP2 (244), although tetramerization of AQP2-L22V, -V24A, -A47V, -T126M and -D150E could be restored once expressed in combination with AQP2-WT (245).

2.5.3: Autosomal dominant NDI: AQP2 misrouting

C-terminal mutations shed light on the effect of phosphorylation or ubiquitination on AQP2 endocytosis and exocytosis. Mutations in the C-terminus of AQP2 lead to a disruption of AQP2 trafficking and apical membrane targeting. All autosomal dominant forms of NDI are caused by mutations in the C-terminus of AQP2 (26). Up till now 9 mutations causing autosomal dominant NDI have been found (Table 2.4) (246). Furthermore, two mutations in the C-terminal tail of AQP2 were found showing the cellular phenotype of dominant NDI when expressed alone (AQP2-P262L, AQP2-K228E, Table 2.4 asterisk). These mutations

Table 2.4: An overview of the known AQP2 C-terminal mutations, causing the autosomal dominant form of NDI, the mutation type and its molecular diagnosis in cells. The asterisk indicates the mutations found in heterozygote expressing recessive NDI patients visualizing autosomal dominant NDI traits during cellular studies.

Mutations	Mutation type	Molecular diagnosis
K228E*	Substitution	Found in heterozygote recessive NDI, weakly responded to forskolin treatment in MDCK cells (20%) (219)
E258K	Substitution	Retained in the Golgi, this mutation does not affect the phosphorylation of Ser256 in oocytes (247)
721delG	Frameshift, elongated protein	Defective trafficking in oocytes (248)
763-772del	Frameshift, elongated protein	Defective trafficking in oocytes (248)
812-818del	Frameshift, elongated protein	Defective trafficking in oocytes (248)
R254L	Substitution	Defective Ser256 phosphorylation leading to impaired trafficking in oocytes and MDCK cells (249)
R254Q	Substitution	Defective Ser256 phosphorylation leading to impaired trafficking in oocytes and MDCK cells (250)
R254W	Substitution	Defective Ser256 phosphorylation leading to impaired trafficking in MDCK cells (251)
AQP2-insA (frameshift c779-780insA)	Frameshift	Misrouting to basolateral membrane in polarized renal cells (252)
727 δ G	Frameshift, elongated protein	Located in endosomes and lysosomes, leading to defective trafficking in oocytes and renal cells (220)
P262L*	Substitution	Found in heterozygote recessive NDI, impaired trafficking to the apical membrane, small fraction trafficked to basolateral and apical membrane upon forskolin stimulation in MDCK cells (58)

are found in patients suffering from heterozygote recessive NDI and are therefore not, directly, linked to patients suffering from the dominant form of NDI (58,219).

In autosomal dominant NDI, heterotetramers of both AQP2-WT and mutants are formed. Both the WT AQP2 and the mutants form functional water channels and are released from the ER. However, the C-terminal mutations lead to misrouting of AQP2, sorting to late endosomes, lysosomes, the basolateral plasma membrane or retention in the Golgi apparatus (252,253). The importance of functional AQP2 C-termini in the AQP2 tetramer was shown by Kamsteeg *et al.* (2000) in *Xenopus oocytes*, where he found that at least three out of four AQP2 monomers need to be phosphorylated at Ser256 to induce AQP2 exocytosis (44). Indeed, mutations found in residue Arg254 were found to cause autosomal dominant NDI, probably caused by the disruption of the PKA consensus site, inhibiting Ser256 phosphorylation (249-251).

Although this type of NDI is a dominant form, the condition is only partial due to expression of functional AQP2-WT besides the mutated AQP2, meaning that functional AQP2 tetramers are formed as well (247-250). Therefore, fluid restriction or AVP treatment often releases the symptoms to some extent.

2.6: Conclusion and Discussion

The disease NDI underlines the importance of AQP2 in maintaining body water homeostasis in humans. Mutations in either the *aqp2* gene or the *avpr2* gene lead to a miss-regulation of AQP2 trafficking, causing severe dehydration and excess secretion of urine (197,199,200). Hereditary NDI is either caused by mutations in the V2R (impairing the AVP response), mutations in the water pore (leading to AQP2 degradation) or mutations in the AQP2 C-terminal tail (leading to misrouting of AQP2)(212,252,253).

AQP2 trafficking regulation is a complex mechanism controlled by the structure of AQP2 (chapter 2.2), post translational modifications of AQP2 (phosphorylation; chapter 2.3) and a complex network of different proteins interacting with AQP2 and controlling AQP2 trafficking (chapter 2.4; Table 2.2). Since the discovery of AQP2 in 1993 (41), AQP2 and its transport mechanism have been extensively studied. This research led to new insights in the understanding of NDI and the mechanism controlling AQP2 trafficking. A summary of the AQP2 trafficking pathway and its controlling proteins is visualized in Figure 2.3.

Although AQP2 trafficking regulation has been extensively studied, the machinery is very complex and not all facets of this system are thoroughly understood. The importance of AQP2-phosphorylation was discussed in chapter 2.3. Here it was shown that Ser256 is the first residue to be phosphorylated after AVP stimulation (27,31) and that this phosphorylation is both necessary to transport AQP2 towards the apical membrane (23) and to induce phosphorylation of downstream residues (Ser264 and Thr269) (27). Phosphorylation of Ser256 is directly linked to AVP stimulation, for AVP binding to the V2R leads to an increase in cellular cAMP levels followed by the activation of PKA and subsequent phosphorylation of Ser256 (42). Furthermore, the importance of Ser256 phosphorylation in AQP2 apical membrane accumulation was confirmed in *Xenopus oocytes*, for at least three out of four

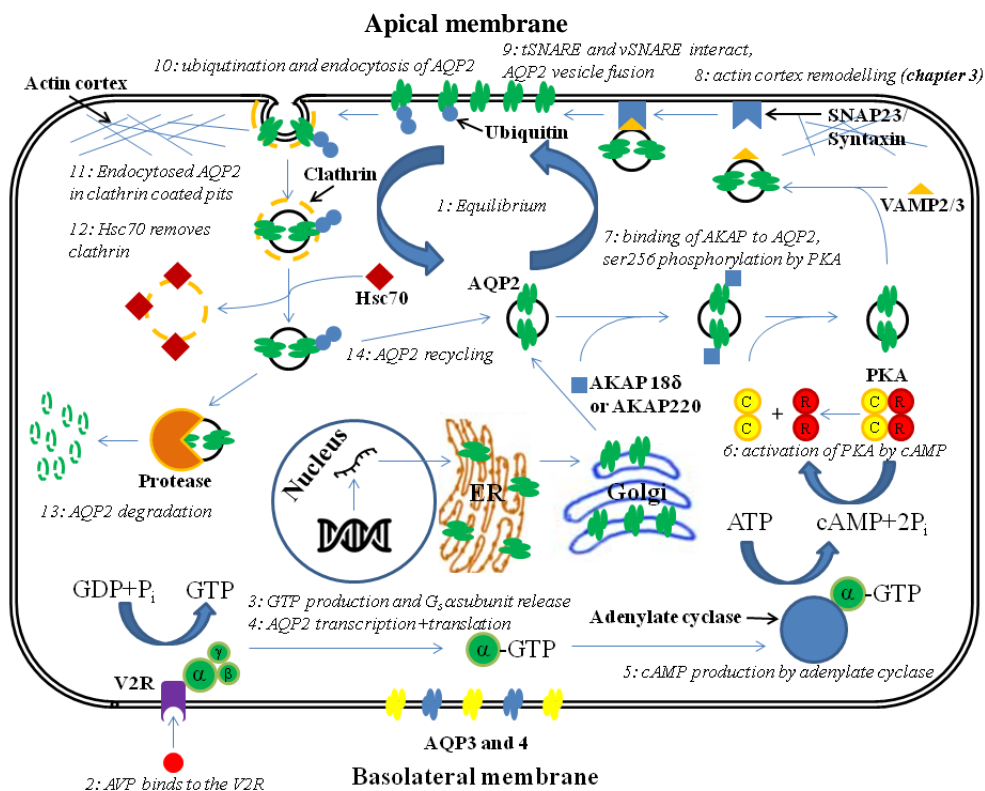


Figure 2.3: Schematic overview of AQP2 trafficking. 1) AQP2 exocytosis and endocytosis is in equilibrium. 2) Enhanced fluid-flow in the collecting duct, detected by osmosensors and blood pressure sensors, leads to the production of vasopressin (AVP), which binds to the Vasopressin-2 receptor (V2R) leading to the production of GTP. 3) GTP binds to the α subunit of the G_s protein complex leading to the release of $G_s\alpha$ -GTP. 4) Binding of AVP to the V2R induces enhanced transcription and translation of AQP2. 5) $G_s\alpha$ -GTP binds to adenylate cyclase inducing the production of cAMP. 6) cAMP reacts with the regulatory subunits (R) of PKA, releasing the catalytic subunits (C). 7) AKAP18 δ or AKAP220 interacts with AQP2 (bearing vesicles), guiding the phosphorylation of residue Ser256 by PKA. 8) AQP2 is transported towards the apical membrane; a tight network of actin filaments prevents AQP2 exocytosis. The actin cortex needs to be remodeled; this is discussed in chapter 3. 9) The vSNAREs in the AQP2 bearing vesicle, VAMP2 and 3, and the tSNAREs located in the apical membrane, SNAP23 and syntaxin, interact leading to the fusion of the apical membrane with AQP2 bearing vesicles. 10) AQP2 is ubiquitinated and endocytosis is initiated. AQP2 endocytosis without ubiquitination is also possible. 11) AQP is endocytosed via clathrin coated pits. 12) Clathrin is removed via the clathrin decoating ATPase Hsc70. After internalization AQP2 is either degraded 13) or recycled 14) in recycling endosomes.

AQP2's need to be phosphorylated at this residue to induce AQP2 exocytosis (44). However, research done in Sprague-Dawley rats only showed a marginal increase in phosphorylated Ser256 after AVP stimulation (Table 2.1) (35). While in Brattleboro rats, lacking AVP production, only a 2-fold increase in Ser256 phosphorylated AQP2 was found after AVP stimulation (34). The relatively small increase in phosphorylation of this residue suggests that already large quantities of Ser256 phosphorylated AQP2 should exist independent of AVP stimulation. Although Ser256 phosphorylation is clearly linked to AVP induced activation of PKA (42), other kinases are linked to Ser256 phosphorylation as well (44-49)(Table 2.2) and the relatively large quantities of phosphorylated Ser256 in the absence of AVP can be explained by phosphorylation of this residue by other kinases. This was confirmed by the fact that Ser256 phosphorylated AQP2 can be found in both the apical membrane as well as in internal vesicles (35,50). The presence of, relatively, large quantities of Ser256 phosphorylated AQP2 in the absence of AVP and the possibility to phosphorylate Ser256 independent of AVP stimulation suggests that either phosphorylated Ser256 plays other regulatory rolls for AQP2, besides being a “master switch” for AQP2 exocytosis, or a base level of Ser256 phosphorylated AQP2 is necessary to induce AQP2 exocytosis during the equilibrium state. The discrepancy between the results obtained from Brattleboro rats (27,32,34) and Sprague-Dawley (35) rats is highly likely caused by the absence of AVP expression in Brattleboro rats, meaning that Ser256 phosphorylated AQP2 found in Brattleboro rats before AVP stimulation is mainly formed by PKA independent phosphorylation of this residue, while in Sprague-Dawley rats a mixture of both PKA phosphorylated AQP2, caused by base levels of AVP, and AQP2 phosphorylated by other kinases coexist.

After Ser256 phosphorylation, other AQP2 residues (Ser261, Ser264 and Thr269) change their phosphorylative state. Thr269 is clearly linked to AQP2 apical membrane retention, for phosphorylation of this residue increases its half-life and decreased the internalization rate of AQP2 and interactions with endocytosis linked proteins (29,36). Furthermore, endocytosis of Thr269 phosphorylated AQP2 was inhibited due to a decreased ubiquitination of AQP2 caused by the interaction of Thr269 phosphorylated AQP2 with 14-3-3 ζ (144), even when AQP2 was ubiquitinated endocytosis was inhibited once this residue was phosphorylated (178). Endocytosis of AQP2 is likely initiated by 14-3-3 θ , guiding the dephosphorylation of Thr269 (144). Although Thr269 is thought to be the apical retention signal for AQP2, a higher half-life and lower internalization rate was found for AQP2-S256D as compared to AQP2-T269E (Table 2.1) (29,36). Meaning that besides Thr269 phosphorylation, Ser256 phosphorylation is important as well to retain AQP2 in the apical membrane. The increased half-life and decreased internalization rate for AQP2-S256D could rely on a, relatively, constant phosphorylation of Thr269 in this mutant, due to the “master switch” role of Ser256, while Ser256 is dephosphorylated over time when studying AQP2-T269E, suggesting that both residues are equally important for AQP2 apical membrane retention.

Ser264 phosphorylation is relatively slow as compared to Ser256 phosphorylation ($t_{1/2} = 4.2$ min and $t_{1/2} = 42$ sec respectively; Table 2.1) (27). The relative late phosphorylation response

and the apparent link between Thr269 phosphorylation and AQP2 apical membrane retention suggests that Ser264 phosphorylation plays a role in AQP2 internalization and perhaps recycling. Furthermore, research done in *Xenopus oocytes* showed that 3 out of 4 Ser256 residues need to be phosphorylated to induce AQP2 exocytosis (44), meaning that relatively large quantities of phosphorylated AQP2 are necessary to induce apical membrane accumulation. The relative low percentage of Ser264 phosphorylated AQP2 after AVP stimulation (3.4% of total AQP2 as compared to 25.6% of total AQP2 for Ser256 phosphorylation; Table 2.1) (35), suggests that Ser264 phosphorylation does not play a role in apical membrane retention. Indeed, Ser264 phosphorylated AQP2 was found to colocalize with clathrin coated pits, which are linked to AQP2 endocytosis as discussed in chapter 2.4.4, early endosomes and recycling endosomes (32), where recycled AQP2 resides (chapter 2.4.3). This suggests that Ser264 phosphorylation functions as an AQP2 recycling signal. The apparent low phosphorylation rate suggests that either only a small portion of AQP2 is recycled after endocytosis, or that only a small fraction of Ser264 phosphorylation is necessary to induce AQP2 recycling. Perhaps phosphorylation of only one AQP2 monomer is enough to recycle the complete tetramer. Indeed AQP2-S264D showed an increased half-life as compared to AQP2-WT (3.8 hrs and 2.9 hrs respectively; Table 2.1) (36). Although both AQP2-S256D and AQP2-T269E show even higher half-lives (5.1 hrs and 4.4 hrs respectively; Table 2.1) (36), the increased half-lives of these mutants could be caused by the decreased internalization rate, while the internalization rate for AQP2-S264D was comparable to AQP2-WT (36).

Ser261 dephosphorylation is relatively slow, with a $t_{1/2}$ of 10.6 min (Table 2.1) (27), as compared to the phosphorylation of the other residues. The relatively late response on AVP stimulation suggests that the phosphorylation state of this residue is linked to one of the late stages of the AQP2 trafficking cycle. Indeed, Ser261 phosphorylation was found in combination with all other phosphorylated residues (27,28,55,56). A controlling role in exocytosis and AQP2 recycling seems unlikely, for AQP2-S261D and AQP2-S261A both show equal internalization rates as compared to AQP2-WT and the half-lives of these mutants were equal to AQP2-WT as well (36). However, although AQP2-S256D-S261D accumulated in the apical membrane (37,39), showing that Ser256 phosphorylation is dominant over Ser261 phosphorylation, prolonged forskolin stimulation of AQP2-S261D expressing MDCK cells showed an initial increase in Ser256 phosphorylation followed by a decrease in phosphorylation of Ser256 (39). This suggests that Ser261 phosphorylation, indirectly, controls the phosphorylated state of Ser256. Indeed, MDCK cells expressing AQP2-WT showed an increase in Ser256 phosphorylated AQP2, while this signal stayed constant over time (39). Without AVP stimulation, AQP2 exocytosis and endocytosis are in equilibrium. This means that AQP2 should be phosphorylated at Ser256 to reach the apical membrane, but AQP2 should not accumulate in the apical membrane. Therefore, relatively low quantities of Ser256 phosphorylated AQP2 are necessary at this state. As discussed, different kinases can phosphorylate AQP2, even in the absence of AVP, meaning that Ser256 phosphorylation needs to be controlled in the equilibrium state. The above mentioned results therefore suggest

that phosphorylated Ser261 controls the quantity of Ser256 phosphorylated AQP2 at equilibrium. Once cells are stimulated by AVP, AQP2 should accumulate in the apical membrane, meaning that Ser256 phosphorylation inhibition is not necessary. By dephosphorylating Ser261, the Ser256 phosphorylation control is released and AQP2 can continuously be transported towards the apical membrane.

Although key parts in the AQP2 trafficking mechanism have been unraveled, results can differ while using different model organisms. Changes in phosphorylation state of AQP2 after AVP stimulation differed per organism, where in Brattleboro rats a 2-fold increase in Ser256 phosphorylation was measured after AVP stimulation (34), the Ser256 phosphorylation only marginally increased in Sprague-Dawley rats (35). Although these differences can be explained by the absence of AVP production in Brattleboro rats, one must be careful which model-organism is used during AQP2 trafficking experiments. Indeed, expression of recessive NDI AQP2 mutants in Oocytes, showed that some mutants still retain their water transport capabilities (217,219,220,223), while these results could not be repeated when these mutants are expressed in kidney cells. Furthermore, VAMP3 plays an important role in AQP2 membrane fusion in MDCK cells (75,116,189), while a VAMP3 deletion in mice did not seem to influence their urine-concentrating abilities (127). Moreover, one should be careful when using phospho-mimics in AQP2 trafficking regulation research. Although these mutants unraveled the role of AQP2 phosphorylation in transport control to a great extent, these mutants differ from native AQP2. By using these mutants, the always phosphorylated state of these residues is mimicked, while in the native conditions, the change in phosphorylation state plays a rudimental role in AQP2 trafficking regulation. Furthermore, mutating Ser261 from AQP2 into an alanine or aspartic acid increased the ubiquitination of AQP2 at K270 after AVP stimulation leading to AQP2 exocytosis inhibition (56). These results indicate that the serine itself, at position 261, plays an important role in ubiquitination inhibition, and residue mutations could therefore induce cellular processes independent of the intended phosphomimetic purpose.

In Figure 2.3 a proposed overview of AQP2 trafficking is visualized. Although this overview is quite comprehensive, showing the main components of the AQP2 trafficking pathway, a lot of aspects remain unknown. The controlling mechanism behind AQP2 recycling still needs to be deciphered, while the exact role of Ser261 phosphorylation in Ser256 phosphorylation regulation is still unclear as well. Determining the exact kinases and phosphatases controlling AQP2 phosphorylation could shed more light on this mechanism, while structural studies could aid in the determination of C-terminal positioning depending on its phosphorylation state. The flexibility of the AQP2 C-terminus (8), hindering the formation of well diffracting 3D crystals (7), suggest a regulatory role for the C-terminus depending on its conformation, which could be controlled by the phosphorylation state of AQP2. Indeed, the importance of the AQP2 C-terminal conformational freedom was confirmed by mutating the proline at residue 226, in the hinge region of the AQP2 C-terminus, to an alanine, leading to AQP2 ER retention (15). Further research on the flexibility of the C-terminus could therefore shed more light on AQP2 trafficking regulation. The same

counts for AQP2's N-terminus. Although the N-terminus of AQP2 is less flexible, only 2 conformations were found (7), this terminus does play a regulatory role in AQP2 trafficking (15,23) and further research, linking specific conformations to AQP2 trafficking regulation, could shed more light on this transport mechanism.

The development of new methods could aid in elucidating the complete AQP2 trafficking regulation mechanism. One of these methods relies on optimization of cryo-EM sample preparation, making it possible to study complex cellular mechanisms at a high magnification with a relatively easy sample preparation method. The development of such a method will be discussed in chapter 5 and 6.

2.7: References

1. Nielsen, S., and Knepper, M. A. (1993) Vasopressin activates collecting duct urea transporters and water channels by distinct physical processes. *American Journal of Physiology - Renal Physiology* **265**, F204-F213
2. Deen, P. M., Verdijk, M. A., Knoers, N. V., Wieringa, B., Monnens, L. A., van Os, C. H., and van Oost, B. A. (1994) Requirement of human renal water channel aquaporin-2 for vasopressin-dependent concentration of urine. *Science (New York, N.Y.)* **264**, 92-95
3. Knepper, M. A. (1994) The aquaporin family of molecular water channels. *Proceedings of the National Academy of Sciences of the United States of America* **91**, 6255-6258
4. Jung, J. S., Preston, G. M., Smith, B. L., Guggino, W. B., and Agre, P. (1994) Molecular structure of the water channel through aquaporin CHIP. The hourglass model. *The Journal of biological chemistry* **269**, 14648-14654
5. Wertén, P. J., Hasler, L., Koenderink, J. B., Klaassen, C. H., de Grip, W. J., Engel, A., and Deen, P. M. (2001) Large-scale purification of functional recombinant human aquaporin-2. *FEBS letters* **504**, 200-205
6. Preston, G. M., Jung, J. S., Guggino, W. B., and Agre, P. (1993) The mercury-sensitive residue at cysteine 189 in the CHIP28 water channel. *The Journal of biological chemistry* **268**, 17-20
7. Frick, A., Eriksson, U. K., de Mattia, F., Oberg, F., Hedfalk, K., Neutze, R., de Grip, W. J., Deen, P. M., and Tornroth-Horsefield, S. (2014) X-ray structure of human aquaporin 2 and its implications for nephrogenic diabetes insipidus and trafficking. *Proc Natl Acad Sci U S A* **111**, 6305-6310
8. Vahedi-Faridi, A., Lodowski, D., Schenk, A., Kaptan, S., de Groot, B. L., Walz, T., and Engel, A. (2014) The structure of Aquaporin. *To be published*
9. Smith, B. L., and Agre, P. (1991) Erythrocyte Mr 28,000 transmembrane protein exists as a multisubunit oligomer similar to channel proteins. *The Journal of biological chemistry* **266**, 6407-6415
10. Sasaki, S., Fushimi, K., Saito, H., Saito, F., Uchida, S., Ishibashi, K., Kuwahara, M., Ikeuchi, T., Inui, K., Nakajima, K., and et al. (1994) Cloning, characterization, and chromosomal mapping of human aquaporin of collecting duct. *The Journal of clinical investigation* **93**, 1250-1256
11. Horsefield, R., Nordén, K., Fellert, M., Backmark, A., Törnroth-Horsefield, S., Terwisscha van Scheltinga, A. C., Kvassman, J., Kjellbom, P., Johanson, U., and Neutze, R. (2008) High-resolution x-ray structure of human aquaporin 5. *Proceedings of the National Academy of Sciences* **105**, 13327-13332
12. Sui, H., Han, B. G., Lee, J. K., Walian, P., and Jap, B. K. (2001) Structural basis of water-specific transport through the AQP1 water channel. *Nature* **414**, 872-878
13. Gonen, T., Cheng, Y., Sliz, P., Hiroaki, Y., Fujiyoshi, Y., Harrison, S. C., and Walz, T. (2005) Lipid-protein interactions in double-layered two-dimensional AQP0 crystals. *Nature* **438**, 633-638
14. Harries, W. E., Akhavan, D., J., M. L., Khademi, S., and Stroud, R. M. (2004) The channel architecture of aquaporin 0 at a 2.2-Å resolution. *Proceedings of the National Academy of Sciences* **101**, 14045-14050

15. Balkom, B. W. M., Graat, M. P. J., van Raak, M., Hofman, E., van der Sluijs, P., and Deen, P. M. (2004) Role of cytoplasmic termini in sorting and shuttling of the aquaporin-2 water channel. *Cell Physiology* **286**, C372-C379
16. Champigneulle, A., Siga, E., Vassent, G., and Imbert-Teboul, M. (1993) V2-like vasopressin receptor mobilizes intracellular Ca²⁺ in rat medullary collecting tubules. *The American journal of physiology* **265**, F35-F45
17. Ecelbarger, C. A., Chou, C. L., Lolait, S. J., and Knepper, M. A. (1996) Evidence for dual signaling pathways for V2 vasopressin receptor in rat inner medullary collecting duct. *The American journal of physiology* **270**, F623-F633
18. Maeda, Y., S., H. J., Gibson, C. C., and Knepper, M. A. (1993) Vasopressin and oxytocin receptors coupled to Ca²⁺ mobilization in rat inner medullary collecting duct. *The American journal of physiology* **265**, F15-F25
19. Star, R. A., Nonoguchi, H., Balaban, R., and Knepper, M. A. (1988) Calcium and cyclic adenosine monophosphate as second messengers for vasopressin in the rat inner medullary collecting duct. *The Journal of clinical investigation* **81**, 1879-1888
20. Yip, K. P. (2002) Coupling of vasopressin-induced intracellular Ca²⁺ mobilization and apical exocytosis in perfused rat kidney collecting duct. *J Physiol* **538**, 891-899
21. Levine, S. D., Kachadorian, W. A., Levin, D. N., and Schlondorff, D. (1981) Effects of trifluoperazine on function and structure of toad urinary bladder. Role of calmodulin vasopressin-stimulation of water permeability. *The Journal of clinical investigation* **67**, 662-672
22. Chou, C. L., Yip, K. P., Michea, L., Kador, K., Ferraris, J. D., Wade, J. B., and Knepper, M. A. (2000) Regulation of aquaporin-2 trafficking by vasopressin in the renal collecting duct. Roles of ryanodine-sensitive Ca²⁺ stores and calmodulin. *The Journal of biological chemistry* **275**, 36839-36846
23. van Balkom, B. W., Savelkoul, P. J., Markovich, D., Hofman, E., Nielsen, S., Van der Sluijs, P., and Deen, P. M. (2002) The role of putative phosphorylation sites in the targeting and shuttling of the aquaporin-2 water channel. *The Journal of biological chemistry* **277**, 41473-41479
24. Mulders, S. M., Knoers, N. V., van Lieburg, A. F., Monnens, L. A., Leumann, E., Wühl, E., Schober, E., Rijss, J. P., Van Os, C. H., and Deen, P. M. (1997) New mutations in the AQP2 gene in nephrogenic diabetes insipidus resulting in functional but misrouted water channels. *J Am Soc Nephrol* **8**, 242-248
25. Lin, S. H., Bichet, D. G., Sasaki, S., Kuwahara, M., Arthus, M. F., Lonergan, M., and Lin, Y. F. (2002) Two novel aquaporin-2 mutations responsible for congenital nephrogenic diabetes insipidus in Chinese families. *J Clin Endocrinol Metab* **87**, 2694-2700
26. Bichet, D. G., and Bockenhauer, D. (2016) Genetic forms of nephrogenic diabetes insipidus (NDI): vasopressin receptor defect (X-linked) and aquaporin defect (autosomal recessive and dominant). *Best Pract Res Clin Endocrinol Metab* **30**, 263-276
27. Hoffert, J. D., Fenton, R. A., Moeller, H. B., Simons, B., Tchapyjnikov, D., McDill, B. W., Yu, M. J., Pisitkun, T., Chen, F., and Knepper, M. A. (2008) Vasopressin-stimulated Increase in Phosphorylation at Ser269 Potentiates Plasma

- Membrane Retention of Aquaporin-2. *Journal of Biological Chemistry* **283**, 24617-24627
28. Hoffert, J. D., Pisitkun, T., Wang, G., Shen, R. F., and Knepper, M. A. (2006) Quantitative phosphoproteomics of vasopressin-sensitive renal cells: regulation of aquaporin-2 phosphorylation at two sites. *Proceedings of the National Academy of Sciences* **103**, 7159-7164
 29. Rice, W. L., Zhang, Y., Chen, Y., Matsuzaki, T., Brown, D., and Lu, H. A. J. (2012) Differential, phosphorylation dependent trafficking of AQP2 in LLC-PK1 cells. *PLoS ONE* **7**, e32843
 30. Van Balkom, B. W., Boone, M., Hendriks, G., Kamsteeg, E., Robben, J. H., Stronks, H. C., van der Voorde, A., van Herp, F., Van der Sluijs, P., and Deen, P. M. (2008) LIP5 interacts with aquaporin 2 and facilitates its lysosomal degradation. *J Am Soc Nephrol* **20**, 990-1001
 31. Nishimoto, G., Zelenina, M., Li, D., Yasui, M., Aperia, A., Nielsen, S., and Nairn, A. C. (1999) Arginine vasopressin stimulates phosphorylation of aquaporin-2 in rat renal tissue. *The American journal of physiology* **276**, F254-259
 32. Fenton, R. A., Moeller, H. B., Hoffert, J. D., Yu, M. J., Nielsen, S., and Knepper, M. A. (2008) Acute regulation of aquaporin-2 phosphorylation at Ser-264 by vasopressin. *Proceedings of the National Academy of Sciences* **105**, 3134-3139
 33. Moeller, H. B., Knepper, M. A., and Fenton, R. A. (2009) Serine 269 phosphorylated aquaporin-2 is targeted to the apical membrane of collecting duct principal cells. *Kidney International* **75**, 295-303
 34. Hoffert, J. D., Nielsen, J., Yu, M. J., Pisitkun, T., Schleicher, S. M., Nielsen, S., and Knepper, M. A. (2007) Dynamics of aquaporin-2 serine-261 phosphorylation in response to short-term vasopressin treatment in collecting duct. *AJP: Renal Physiology* **292**, F691-F700
 35. Xie, L., Hoffert, J. D., Chou, C. L., Yu, M. J., Pisitkun, T., Knepper, M. A., and Fenton, R. A. (2010) Quantitative analysis of aquaporin-2 phosphorylation. *AJP: Renal Physiology* **298**, F1018-F1023
 36. Moeller, H. B., Praetorius, J., Rutzler, M. R., and Fenton, R. A. (2010) Phosphorylation of aquaporin-2 regulates its endocytosis and protein-protein interactions. *Proc Natl Acad Sci U S A* **107**, 424-429
 37. Lu, H. J., Matsuzaki, T., Bouley, R., Hasler, U., Qin, Q. H., and Brown, D. (2008) The phosphorylation state of serine 256 is dominant over that of serine 261 in the regulation of AQP2 trafficking in renal epithelial cells. *AJP: Renal Physiology* **295**, F290-F294
 38. Katsura, T., Gustafson, C. E., Ausiello, D. A., and Brown, D. (1997) Protein kinase A phosphorylation is involved in regulated exocytosis of aquaporin-2 in transfected LLC-PK1 cells. *American Journal of Physiology - Renal Physiology* **272**, F816-F822
 39. Tamma, G., Robben, J. H., Trimpert, C., Boone, M., and Deen, P. M. (2011) Regulation of AQP2 localization by S256 and S261 phosphorylation and ubiquitination. *American journal of physiology. Cell physiology* **300**, C636-646
 40. Trimpert, C., van den Berg, D. T., Fenton, R. A., Klussmann, E., and Deen, P. M. (2012) Vasopressin increases S261 phosphorylation in AQP2-P262L, a mutant in recessive nephrogenic diabetes insipidus. *Nephrology, dialysis, transplantation* :

official publication of the European Dialysis and Transplant Association - European Renal Association **27**, 4389-4397

41. Fushimi, K., Uchida, S., Hara, Y., Hirata, Y., Marumo, F., and Sasaki, S. (1993) Cloning and expression of apical membrane water channel of rat kidney collecting tubule. *Nature* **361**, 549-552
42. Kuwahara, M., Fushimi, K., Terada, Y., Bai, L., Marumo, F., and Sasaki, S. (1995) cAMP-dependent phosphorylation stimulates water permeability of aquaporin-collecting duct water channel protein expressed in *Xenopus* oocytes. *J. Biol. Chem.*, 10384-10387
43. Katsura, T., Gustafson, C. E., Ausiello, D. A., and Brown, D. (1997) Protein kinase A phosphorylation is involved in regulated exocytosis of aquaporin-2 in transfected LLC-PK1 cells. *Am. J. Physiol.*, F817-F822
44. Kamsteeg, E. J., Heijnen, I., van Os, C. H., and Deen, P. M. T. (2000) The Subcellular Localization of an Aquaporin-2 Tetramer Depends on the Stoichiometry of Phosphorylated and Nonphosphorylated Monomers. *The Journal of cell biology* **151**, 919-930
45. Bouley, R., Breton, S., Sun, T.-x., McLaughlin, M., Nsumu, N. N., Lin, H. Y., Ausiello, D. A., and Brown, D. (2000) Nitric oxide and atrial natriuretic factor stimulate cGMP-dependent membrane insertion of aquaporin 2 in renal epithelial cells. *Journal of Clinical Investigation* **106**, 1115-1126
46. Douglass, J., Gunaratne, R., Bradford, D., Saeed, F., Hoffert, J. D., Steinbach, P. J., Knepper, M. A., and Pisitkun, T. (2012) Identifying protein kinase target preferences using mass spectrometry. *AJP: Cell Physiology* **303**, C715-C727
47. Brunati, A. M., Marin, O., Bisinella, A., Salviati, A., and Pinna, L. A. (2000) Novel consensus sequence for the golgi apparatus casein kinase, revealed using proline-rich protein-1 (PRP1)-derived peptide substrates. *Biochem. J.*, 765-768
48. Brown, D., Hasler, U., Nunes, P., Bouley, R., and Lu, H. A. J. (2008) Phosphorylation events and the modulation of aquaporin 2 cell surface expression. *Current Opinion in Nephrology and Hypertension* **17**, 491-498
49. Bradford, D., Raghuram, V., Wilson, J. L. L., Chou, C., Hoffert, J. D., Knepper, M. A., and Pisitkun, T. (2014) Use of LC-MS/MS and Bayes' theorem to identify protein kinases that phosphorylate aquaporin-2 at Ser256. *Am. J. Physiol. Cell Physiol.*, C123-C139
50. Christensen, B. M., Zelenina, M., Aperia, A., and Nielsen, S. (2000) Localization and regulation of PKA-phosphorylated AQP2 in response to V(2)-receptor agonist/antagonist treatment. *American journal of physiology. Renal physiology* **278**, F29-42
51. Brown, D. (2003) The ins and outs of aquaporin-2 trafficking. *American journal of physiology. Renal physiology* **284**, F893-901
52. Nielsen, S., Chou, C. L., Marples, D., Christensen, E. I., Kishore, B. K., and Knepper, M. A. (1995) Vasopressin increases water permeability of kidney collecting duct by inducing translocation of aquaporin-CD water channels to plasma membrane. *Proc Natl Acad Sci U S A* **92**, 1013-1017
53. Knepper, M. A., and Nielsen, S. (1993) Kinetic model of water and urea permeability regulation by vasopressin in collecting duct. *American Journal of Physiology - Renal Physiology* **265**, F214-F224

54. Lu, H., Sun, T. X., Bouley, R., Blackburn, K., McLaughlin, M., and Brown, D. (2004) Inhibition of endocytosis causes phosphorylation (S256)-independent plasma membrane accumulation of AQP2. *American journal of physiology. Renal physiology* **286**, F233-243
55. Hoffert, J. D., Wang, G., Pisitkun, T., Shen, R. F., and Knepper, M. A. (2007) An automated platform for analysis of phosphoproteomic datasets: application to kidney collecting duct phosphoproteins. *Journal of proteome research* **6**, 3501-3508
56. Yui, N., Sasaki, S., and Uchida, S. (2017) Aquaporin-2 Ser-261 phosphorylation is regulated in combination with Ser-256 and Ser-269 phosphorylation. *Biochemical and biophysical research communications* **482**, 524-529
57. Kamsteeg, E. J., Hendriks, G., Boone, M., Konings, I. B., Oorschot, V., van der Sluijs, P., Klumperman, J., and Deen, P. M. (2006) Short-chain ubiquitination mediates the regulated endocytosis of the aquaporin-2 water channel. *Proc Natl Acad Sci U S A* **103**, 18344-18349
58. de Mattia, F., Savelkoul, P. J., Bichet, D. G., Kamsteeg, E. J., Konings, I. B., Marr, N., Arthus, M. F., Lonergan, M., van Os, C. H., van der Sluijs, P., Robertson, G., and Deen, P. M. (2004) A novel mechanism in recessive nephrogenic diabetes insipidus: wild-type aquaporin-2 rescues the apical membrane expression of intracellularly retained AQP2-P262L. *Human molecular genetics* **13**, 3045-3056
59. Klussmann, E., Maric, K., Wiesner, B., Beyermann, M., and Rosenthal, W. (1999) Protein kinase A anchoring proteins are required for vasopressin-mediated translocation of aquaporin-2 into cell membranes of renal principal cells. *The Journal of biological chemistry* **274**, 4934-4938
60. Klussmann, E., and Rosenthal, W. (2001) Role and identification of protein kinase A anchoring proteins in vasopressin-mediated aquaporin-2 translocation. *Kidney International* **60**, 446-449
61. Henn, V., Edemir, B., Stefan, E., Wiesner, B., Lorenz, D., Theilig, F., Schmitt, R., Vossebein, L., Tamma, G., Beyermann, M., Krause, E., Herberg, F. W., Valenti, G., Bachmann, S., Rosenthal, W., and Klussmann, E. (2004) Identification of a novel A-kinase anchoring protein 18 isoform and evidence for its role in the vasopressin-induced aquaporin-2 shuttle in renal principal cells. *The Journal of biological chemistry* **279**, 26654-26665
62. McSorley, T., Stefan, E., Henn, V., Wiesner, B., Baillie, G. S., Houslay, M. D., Rosenthal, W., and Klussmann, E. (2006) Spatial organisation of AKAP18 and PDE4 isoforms in renal collecting duct principal cells. *European journal of cell biology* **85**, 673-678
63. Okutsu, R., Rai, T., Kikuchi, A., Ohno, M., Uchida, K., Sasaki, S., and Uchida, S. (2008) AKAP220 colocalizes with AQP2 in the inner medullary collecting ducts. *Kidney International* **74**, 1429-1433
64. Stefan, E., Wiesner, B., Baillie, G. S., Mollajew, R., Henn, V., Lorenz, D., Furkert, J., Santamaria, K., Nedvetsky, P., Hundsrucker, C., Beyermann, M., Krause, E., Pohl, P., Gall, I., MacIntyre, A. N., Bachmann, S., Houslay, M. D., Rosenthal, W., and Klussmann, E. (2007) Compartmentalization of cAMP-dependent signaling by phosphodiesterase-4D is involved in the regulation of vasopressin-mediated water reabsorption in renal principal cells. *J Am Soc Nephrol* **18**, 199-212

65. Szaszak, M., Christian, F., Rosenthal, W., and Klussmann, E. (2008) Compartmentalized cAMP signalling in regulated exocytic processes in non-neuronal cells. *Cellular signalling* **20**, 590-601
66. Valtin, H., Coffey, A. K., O'Sullivan, D. J., Homma, S., and Dousa, T. P. (1990) Causes of the urinary concentrating defect in mice with nephrogenic diabetes insipidus. *Physiologia Bohemoslovaca* **39**, 103-111
67. Takeda, S., Lin, C. T., Morgano, P. G., McIntyre, S. J., and Dousa, T. P. (1991) High activity of low-Michaelis-Menten constant 3', 5'-cyclic adenosine monophosphate-phosphodiesterase isozymes in renal inner medulla of mice with hereditary nephrogenic diabetes insipidus. *Endocrinology* **129**, 287-294
68. Noda, Y., Horikawa, S., Katayama, Y., and Sasaki, S. (2004) Water channel aquaporin-2 directly binds to actin. *Biochem. Biophys. Res. Commun.* **322**, 740-745
69. Noda, Y., Horikawa, S., Katayama, Y., and Sasaki, S. (2005) Identification of a multiprotein "motor" complex binding to water channel aquaporin-2. *Biochemical and Biophysical Research Communications* **330**, 1041-1047
70. Noda, Y., Horikawa, S., Kanda, E., Yamashita, M., Meng, H., Eto, K., Li, Y., Kuwahara, M., Hirai, K., Pack, C., Kinjo, M., Okabe, S., and Sasaki, S. (2008) Reciprocal interaction with G-actin and tropomyosin is essential for aquaporin-2 trafficking. *The Journal of Cell Biology* **182**, 587-601
71. Vossenkamper, A., Nedvetsky, P. I., Wiesner, B., Furkert, J., Rosenthal, W., and Klussmann, E. (2007) Microtubules are needed for the perinuclear positioning of aquaporin-2 after its endocytic retrieval in renal principal cells. *American journal of physiology. Cell physiology* **293**, C1129-1138
72. Tamma, G. (2003) cAMP-induced AQP2 translocation is associated with RhoA inhibition through RhoA phosphorylation and interaction with RhoGDI. *Journal of Cell Science* **116**, 1519-1525
73. Klussmann, E., Tamma, G., Lorenz, D., Wiesner, B., Maric, K., Hofmann, F., Aktories, K., Valenti, G., and Rosenthal, W. (2001) An inhibitory role of Rho in the vasopressin-mediated translocation of aquaporin-2 into cell membranes of renal principal cells. *The Journal of biological chemistry* **276**, 20451-20457
74. Gouraud, S., Laera, A., Calamita, G., Carmosino, M., Procino, G., Rossetto, O., Mannucci, R., Rosenthal, W., Svelto, M., and Valenti, G. (2002) Functional involvement of VAMP/synaptobrevin-2 in cAMP-stimulated aquaporin 2 translocation in renal collecting duct cells. *Journal of cell science* **115**, 3667-3674
75. Procino, G., Barbieri, C., Tamma, G., De Benedictis, L., Pessin, J. E., Svelto, M., and Valenti, G. (2008) AQP2 exocytosis in the renal collecting duct -- involvement of SNARE isoforms and the regulatory role of Munc18b. *Journal of cell science* **121**, 2097-2106
76. Barile, M., Pisitkun, T., Yu, M. J., Chou, C. L., Verbalis, M. J., Shen, R. F., and Knepper, M. A. (2005) Large scale protein identification in intracellular aquaporin-2 vesicles from renal inner medullary collecting duct. *Molecular & cellular proteomics : MCP* **4**, 1095-1106
77. Liebenhoff, U., and Rosenthal, W. (1995) Identification of Rab3-, Rab5a- and synaptobrevin II-like proteins in a preparation of rat kidney vesicles containing the vasopressin-regulated water channel. *FEBS letters* **365**, 209-213

78. Lu, H. A., Sun, T. X., Matsuzaki, T., Yi, X. H., Eswara, J., Bouley, R., McKee, M., and Brown, D. (2007) Heat shock protein 70 interacts with aquaporin-2 and regulates its trafficking. *The Journal of biological chemistry* **282**, 28721-28732
79. Park, E.-J., Lim, J.-S., Jung, H. J., Kim, E., Han, K.-H., and Kwon, T.-H. (2013) The role of 70-kDa heat shock protein in dDAVP-induced AQP2 trafficking in kidney collecting duct cells. *American Journal of Physiology - Renal Physiology* **304**, F958-F971
80. Krebs, E. G., and Beavo, J. A. (1979) Phosphorylation-dephosphorylation of enzymes. *Annual review of biochemistry* **48**, 923-959
81. Taylor, S. S., Buechler, J. A., and Yonemoto, W. (1990) cAMP-dependent protein kinase: framework for a diverse family of regulatory enzymes. *Annual review of biochemistry* **59**, 971-1005
82. Kopperud, R., Christensen, A. E., Kjarland, E., Viste, K., Kleivdal, H., and Doskeland, S. O. (2002) Formation of inactive cAMP-saturated holoenzyme of cAMP-dependent protein kinase under physiological conditions. *The Journal of biological chemistry* **277**, 13443-13448
83. Simon, H., Gao, Y., Franki, N., and Hays, R. M. (1993) Vasopressin Depolymerizes Apical F-actin in Rat Inner Medullary Collecting Duct. *Am. J. Physiol.* **265**, C757-762
84. Chou, C. L., Christensen, B. M., Frische, S., Vorum, H., Desai, R. A., Hoffert, J. D., de Lanerolle, P., Nielsen, S., and Knepper, M. A. (2004) Non-muscle myosin II and myosin light chain kinase are downstream targets for vasopressin signaling in the renal collecting duct. *The Journal of biological chemistry* **279**, 49026-49035
85. Tamma, G., Klussmann, E., Oehlke, J., Krause, E., Rosenthal, W., Svelto, M., and Valenti, G. (2005) Actin remodeling requires ERM function to facilitate AQP2 apical targeting. *Journal of cell science* **118**, 3623-3630
86. Nedvetsky, P. I., Stefan, E., Frische, S., Santamaria, K., Wiesner, B., Valenti, G., Hammer, J. A., 3rd, Nielsen, S., Goldenring, J. R., Rosenthal, W., and Klussmann, E. (2007) A Role of myosin Vb and Rab11-FIP2 in the aquaporin-2 shuttle. *Traffic (Copenhagen, Denmark)* **8**, 110-123
87. Tamma, G., Klussmann, E., Procino, G., Svelto, M., Rosenthal, W., and Valenti, G. (2003) cAMP-induced AQP2 translocation is associated with RhoA inhibition through RhoA phosphorylation and interaction with RhoGDI. *Journal of cell science* **116**, 1519-1525
88. Li, Y. H., Eto, K., Horikawa, S., Uchida, S., Sasaki, S., Li, X. J., and Noda, Y. (2009) Aquaporin-2 regulates cell volume recovery via tropomyosin. *The international journal of biochemistry & cell biology* **41**, 2466-2476
89. Sabolic, I., Katsura, T., Verbavatz, J. M., and Brown, D. (1995) The AQP2 water channel: effect of vasopressin treatment, microtubule disruption, and distribution in neonatal rats. *The Journal of membrane biology* **143**, 165-175
90. Breton, S., and Brown, D. (1998) Cold-induced microtubule disruption and relocalization of membrane proteins in kidney epithelial cells. *J Am Soc Nephrol* **9**, 155-166
91. Marples, D., Schroer, T. A., Ahrens, N., Taylor, A., Knepper, M. A., and Nielsen, S. (1998) Dynein and dynactin colocalize with AQP2 water channels in intracellular vesicles from kidney collecting duct. *The American journal of physiology* **274**, F384-394

92. Shaw, S., and Marples, D. (2002) A rat kidney tubule suspension for the study of vasopressin-induced shuttling of AQP2 water channels. *American journal of physiology. Renal physiology* **283**, F1160-1166
93. Kang, D. Y., Park, J. I., Cho, W. S., Jeong, M. H., Cho, G. W., Park, H. T., and Bae, H. R. (2004) Identification of vasopressin-induced genes in AQP2-transfected MDCK cells by suppression subtractive hybridization. *Biochemical and biophysical research communications* **324**, 1234-1241
94. Tajika, Y., Matsuzaki, T., Suzuki, T., Ablimit, A., Aoki, T., Hagiwara, H., Kuwahara, M., Sasaki, S., and Takata, K. (2005) Differential regulation of AQP2 trafficking in endosomes by microtubules and actin filaments. *Histochemistry and cell biology* **124**, 1-12
95. Zhao, H., Yao, X., Wang, T. X., Jin, W. M., Ji, Q. Q., Yang, X., Duan, Q. H., and Yao, L. J. (2012) PKC α regulates vasopressin-induced aquaporin-2 trafficking in mouse kidney collecting duct cells in vitro via altering microtubule assembly. *Acta pharmacologica Sinica* **33**, 230-236
96. Yui, N., Lu, H. A., Chen, Y., Nomura, N., Bouley, R., and Brown, D. (2013) Basolateral targeting and microtubule-dependent transcytosis of the aquaporin-2 water channel. *American journal of physiology. Cell physiology* **304**, C38-48
97. Brunati, A. M., Marin, O., Bisinella, A., Salviati, A., and Pinna, L. A. (2000) Novel consensus sequence for the Golgi apparatus casein kinase, revealed using proline-rich protein-1 (PRP1)-derived peptide substrates. *Biochemical Journal* **351**, 765-768
98. Procino, G., Carmosino, M., Marin, O., Brunati, A. M., Contri, A., Pinna, L. A., Mannucci, R., Nielsen, S., Kwon, T. H., Svelto, M., and Valenti, G. (2003) Ser-256 phosphorylation dynamics of Aquaporin 2 during maturation from the ER to the vesicular compartment in renal cells. *FASEB journal : official publication of the Federation of American Societies for Experimental Biology* **17**, 1886-1888
99. Fushimi, K., Kuwahara, M., Terada, Y., Bai, L., Marumo, F., and Sasaki, S. (1995) cAMP-dependent Phosphorylation Stimulates Water Permeability of Aquaporin-collecting Duct Water Channel Protein Expressed in Xenopus Oocytes. *Journal of Biological Chemistry* **270**, 10384-10387
100. Klokkers, J., Langehanenberg, P., Kemper, B., Kosmeier, S., von Bally, G., Riethmuller, C., Wunder, F., Sindic, A., Pavenstadt, H., Schlatter, E., and Edemir, B. (2009) Atrial natriuretic peptide and nitric oxide signaling antagonizes vasopressin-mediated water permeability in inner medullary collecting duct cells. *American journal of physiology. Renal physiology* **297**, F693-703
101. Tamma, G., Procino, G., Mola, M. G., Svelto, M., and Valenti, G. (2008) Functional involvement of Annexin-2 in cAMP induced AQP2 trafficking. *Pflugers Archiv : European journal of physiology* **456**, 729-736
102. Zwang, N. A., Hoffert, J. D., Pisitkun, T., Moeller, H. B., Fenton, R. A., and Knepper, M. A. (2009) Identification of phosphorylation-dependent binding partners of aquaporin-2 using protein mass spectrometry. *Journal of proteome research* **8**, 1540-1554
103. Bouley, R., Lu, H. A., Nunes, P., Da Silva, N., McLaughlin, M., Chen, Y., and Brown, D. (2011) Calcitonin has a vasopressin-like effect on aquaporin-2 trafficking and urinary concentration. *J Am Soc Nephrol* **22**, 59-72

104. Umenishi, F., Narikiyo, T., Vandewalle, A., and Schrier, R. W. (2006) cAMP regulates vasopressin-induced AQP2 expression via protein kinase A-independent pathway. *Biochimica et biophysica acta* **1758**, 1100-1105
105. Yip, K. P. (2006) Epac-mediated Ca(2+) mobilization and exocytosis in inner medullary collecting duct. *American journal of physiology. Renal physiology* **291**, F882-890
106. Kortenoeven, M. L., Trimpert, C., van den Brand, M., Li, Y., Wetzels, J. F., and Deen, P. M. (2012) In mpkCCD cells, long-term regulation of aquaporin-2 by vasopressin occurs independent of protein kinase A and CREB but may involve Epac. *American journal of physiology. Renal physiology* **302**, F1395-1401
107. Wu, W., Kitamura, S., Truong, D. M., Rieg, T., Vallon, V., Sakurai, H., Bush, K. T., Vera, D. R., Ross, R. S., and Nigam, S. K. (2009) Beta1-integrin is required for kidney collecting duct morphogenesis and maintenance of renal function. *American journal of physiology. Renal physiology* **297**, F210-217
108. Tamma, G., Lasorsa, D., Ranieri, M., Mastrofrancesco, L., Valenti, G., and Svelto, M. (2011) Integrin signaling modulates AQP2 trafficking via Arg-Gly-Asp (RGD) motif. *Cellular physiology and biochemistry : international journal of experimental cellular physiology, biochemistry, and pharmacology* **27**, 739-748
109. Chen, Y., Rice, W., Gu, Z., Li, J., Huang, J., Brenner, M. B., Van Hoek, A., Xiong, J., Gundersen, G. G., Norman, J. C., Hsu, V. W., Fenton, R. A., Brown, D., and Lu, H. A. (2012) Aquaporin 2 promotes cell migration and epithelial morphogenesis. *J Am Soc Nephrol* **23**, 1506-1517
110. Bustamante, M., Hasler, U., Kotova, O., Chibalin, A. V., Mordasini, D., Rousselot, M., Vandewalle, A., Martin, P. Y., and Feraille, E. (2005) Insulin potentiates AVP-induced AQP2 expression in cultured renal collecting duct principal cells. *American journal of physiology. Renal physiology* **288**, F334-344
111. Nielsen, J., Hoffert, J. D., Knepper, M. A., Agre, P., Nielsen, S., and Fenton, R. A. (2008) Proteomic analysis of lithium-induced nephrogenic diabetes insipidus: mechanisms for aquaporin 2 down-regulation and cellular proliferation. *Proc Natl Acad Sci U S A* **105**, 3634-3639
112. Pisitkun, T., Jacob, V., Schleicher, S. M., Chou, C. L., Yu, M. J., and Knepper, M. A. (2008) Akt and ERK1/2 pathways are components of the vasopressin signaling network in rat native IMCD. *American journal of physiology. Renal physiology* **295**, F1030-1043
113. Kim, H. Y., Choi, H. J., Lim, J. S., Park, E. J., Jung, H. J., Lee, Y. J., Kim, S. Y., and Kwon, T. H. (2011) Emerging role of Akt substrate protein AS160 in the regulation of AQP2 translocation. *American journal of physiology. Renal physiology* **301**, F151-161
114. Valenti, G., Procino, G., Carmosino, M., Frigeri, A., Mannucci, R., Nicoletti, I., and Svelto, M. (2000) The phosphatase inhibitor okadaic acid induces AQP2 translocation independently from AQP2 phosphorylation in renal collecting duct cells. *Journal of cell science* **113 (Pt 11)**, 1985-1992
115. Procino, G., Barbieri, C., Carmosino, M., Tamma, G., Milano, S., De Benedictis, L., Mola, M. G., Lazo-Fernandez, Y., Valenti, G., and Svelto, M. (2011) Fluvastatin modulates renal water reabsorption in vivo through increased AQP2 availability at the apical plasma membrane of collecting duct cells. *Pflugers Archiv : European journal of physiology* **462**, 753-766

116. Inoue, T., Nielsen, S., Mandon, B., Terris, J., Kishore, B. K., and Knepper, M. A. (1998) SNAP-23 in rat kidney: colocalization with aquaporin-2 in collecting duct vesicles. *The American journal of physiology* **275**, F752-760
117. Shukla, A., Hager, H., Corydon, T. J., Bean, A. J., Dahl, R., Vajda, Z., Li, H., Hoffmann, H. J., and Nielsen, S. (2001) SNAP-25-associated Hrs-2 protein colocalizes with AQP2 in rat kidney collecting duct principal cells. *American journal of physiology. Renal physiology* **281**, F546-556
118. Noda, Y., Horikawa, S., Furukawa, T., Hirai, K., Katayama, Y., Asai, T., Kuwahara, M., Katagiri, K., Kinashi, T., Hattori, M., Minato, N., and Sasaki, S. (2004) Aquaporin-2 trafficking is regulated by PDZ-domain containing protein SPA-1. *FEBS letters* **568**, 139-145
119. Kishore, B. K., Wade, J. B., Schorr, K., Inoue, T., Mandon, B., and Knepper, M. A. (1998) Expression of synaptotagmin VIII in rat kidney. *The American journal of physiology* **275**, F131-142
120. Mandon, B., Chou, C. L., Nielsen, S., and Knepper, M. A. (1996) Syntaxin-4 is localized to the apical plasma membrane of rat renal collecting duct cells: possible role in aquaporin-2 trafficking. *The Journal of clinical investigation* **98**, 906-913
121. Brooks, H. L., Ageloff, S., Kwon, T. H., Brandt, W., Terris, J. M., Seth, A., Michea, L., Nielsen, S., Fenton, R., and Knepper, M. A. (2003) cDNA array identification of genes regulated in rat renal medulla in response to vasopressin infusion. *American journal of physiology. Renal physiology* **284**, F218-228
122. Mistry, A. C., Mallick, R., Klein, J. D., Weimbs, T., Sands, J. M., and Frohlich, O. (2009) Syntaxin specificity of aquaporins in the inner medullary collecting duct. *American journal of physiology. Renal physiology* **297**, F292-300
123. Franki, N., Macaluso, F., Schubert, W., Gunther, L., and Hays, R. M. (1995) Water channel-carrying vesicles in the rat IMCD contain cellubrevin. *The American journal of physiology* **269**, C797-801
124. Jo, I., Harris, H. W., Amendt-Raduege, A. M., Majewski, R. R., and Hammond, T. G. (1995) Rat kidney papilla contains abundant synaptobrevin protein that participates in the fusion of antidiuretic hormone-regulated water channel-containing endosomes in vitro. *Proc Natl Acad Sci U S A* **92**, 1876-1880
125. Marples, D., Knepper, M. A., Christensen, E. I., and Nielsen, S. (1995) Redistribution of aquaporin-2 water channels induced by vasopressin in rat kidney inner medullary collecting duct. *The American journal of physiology* **269**, C655-664
126. Nielsen, S., Marples, D., Birn, H., Mohtashami, M., Dalby, N. O., Trimble, M., and Knepper, M. (1995) Expression of VAMP-2-like protein in kidney collecting duct intracellular vesicles. Colocalization with Aquaporin-2 water channels. *The Journal of clinical investigation* **96**, 1834-1844
127. Wang, C. C., Ng, C. P., Shi, H., Liew, H. C., Guo, K., Zeng, Q., and Hong, W. (2010) A role for VAMP8/endobrevin in surface deployment of the water channel aquaporin 2. *Molecular and cellular biology* **30**, 333-343
128. Bouley, R., Hawthorn, G., Russo, L. M., Lin, H. Y., Ausiello, D. A., and Brown, D. (2006) Aquaporin 2 (AQP2) and vasopressin type 2 receptor (V2R) endocytosis in kidney epithelial cells: AQP2 is located in 'endocytosis-resistant' membrane domains after vasopressin treatment. *Biology of the cell* **98**, 215-232

129. Aoki, T., Suzuki, T., Hagiwara, H., Kuwahara, M., Sasaki, S., Takata, K., and Matsuzaki, T. (2012) Close Association of Aquaporin-2 Internalization with Caveolin-1. *Acta Histochemica et Cytochemica* **45**, 139-146
130. Strange, K., Willingham, M. C., Handler, J. S., and Harris, H. W., Jr. (1988) Apical membrane endocytosis via coated pits is stimulated by removal of antidiuretic hormone from isolated, perfused rabbit cortical collecting tubule. *The Journal of membrane biology* **103**, 17-28
131. Verkman, A. S., Lencer, W. I., Brown, D., and Ausiello, D. A. (1988) Endosomes from kidney collecting tubule cells contain the vasopressin-sensitive water channel. *Nature* **333**, 268-269
132. Katsura, T., Verbavatz, J. M., Farinas, J., Ma, T., Ausiello, D. A., Verkman, A. S., and Brown, D. (1995) Constitutive and regulated membrane expression of aquaporin 1 and aquaporin 2 water channels in stably transfected LLC-PK1 epithelial cells. *Proc Natl Acad Sci U S A* **92**, 7212-7216
133. Sun, T. X., Van Hoek, A., Huang, Y., Bouley, R., McLaughlin, M., and Brown, D. (2002) Aquaporin-2 localization in clathrin-coated pits: inhibition of endocytosis by dominant-negative dynamin. *American journal of physiology. Renal physiology* **282**, F998-1011
134. Rao, R., Zhang, M. Z., Zhao, M., Cai, H., Harris, R. C., Breyer, M. D., and Hao, C. M. (2005) Lithium treatment inhibits renal GSK-3 activity and promotes cyclooxygenase 2-dependent polyuria. *American journal of physiology. Renal physiology* **288**, F642-649
135. Rao, R., Patel, S., Hao, C., Woodgett, J., and Harris, R. (2010) GSK3beta mediates renal response to vasopressin by modulating adenylate cyclase activity. *J Am Soc Nephrol* **21**, 428-437
136. Nielsen, J., Kwon, T. H., Christensen, B. M., Frokiaer, J., and Nielsen, S. (2008) Dysregulation of renal aquaporins and epithelial sodium channel in lithium-induced nephrogenic diabetes insipidus. *Seminars in nephrology* **28**, 227-244
137. Rice, W. L., Zhang, Y., Chen, Y., Matsuzaki, T., Brown, D., and Lu, H. A. J. (2012) Differential, Phosphorylation Dependent Trafficking of AQP2 in LLC-PK1 Cells. *PLoS One* **7**, e32843
138. Kamsteeg, E. J., Duffield, A. S., Konings, I. B., Spencer, J., Pagel, P., Deen, P. M., and Caplan, M. J. (2007) MAL decreases the internalization of the aquaporin-2 water channel. *Proc Natl Acad Sci U S A* **104**, 16696-16701
139. Bagnasco, S. M. (2012) Protein kinase C-alpha comes to the rescue of aquaporin-2. *American journal of physiology. Renal physiology* **303**, F35-36
140. Thai, T. L., Blount, M. A., Klein, J. D., and Sands, J. M. (2012) Lack of protein kinase C-alpha leads to impaired urine concentrating ability and decreased aquaporin-2 in angiotensin II-induced hypertension. *American journal of physiology. Renal physiology* **303**, F37-44
141. Lee, Y. J., and Kwon, T. H. (2009) Ubiquitination of aquaporin-2 in the kidney. *Electrolyte & blood pressure : E & BP* **7**, 1-4
142. Lee, Y. J., Lee, J. E., Choi, H. J., Lim, J. S., Jung, H. J., Baek, M. C., Frokiaer, J., Nielsen, S., and Kwon, T. H. (2011) E3 ubiquitin-protein ligases in rat kidney collecting duct: response to vasopressin stimulation and withdrawal. *American journal of physiology. Renal physiology* **301**, F883-896

143. Boone, M., Kortenoeven, M. L., Robben, J. H., Tamma, G., and Deen, P. M. (2011) Counteracting vasopressin-mediated water reabsorption by ATP, dopamine, and phorbol esters: mechanisms of action. *American journal of physiology. Renal physiology* **300**, F761-771
144. Moeller, H. B., Slengerik-Hansen, J., Aroankins, T., Assentoft, M., MacAulay, N., Moestrup, S. K., Bhalla, V., and Fenton, R. A. (2016) Regulation of the Water Channel Aquaporin-2 via 14-3-3theta and -zeta. *The Journal of biological chemistry* **291**, 2469-2484
145. Cai, Q., Nelson, S. K., McReynolds, M. R., Diamond-Stanic, M. K., Elliott, D., and Brooks, H. L. (2010) Vasopressin increases expression of UT-A1, UT-A3, and ER chaperone GRP78 in the renal medulla of mice with a urinary concentrating defect. *American journal of physiology. Renal physiology* **299**, F712-719
146. Goel, M., Sinkins, W. G., Zuo, C. D., Hopfer, U., and Schilling, W. P. (2007) Vasopressin-induced membrane trafficking of TRPC3 and AQP2 channels in cells of the rat renal collecting duct. *American journal of physiology. Renal physiology* **293**, F1476-1488
147. Goel, M., Zuo, C. D., and Schilling, W. P. (2010) Role of cAMP/PKA signaling cascade in vasopressin-induced trafficking of TRPC3 channels in principal cells of the collecting duct. *American journal of physiology. Renal physiology* **298**, F988-996
148. Galizia, L., Pizzoni, A., Fernandez, J., Rivarola, V., Capurro, C., and Ford, P. (2012) Functional interaction between AQP2 and TRPV4 in renal cells. *Journal of cellular biochemistry* **113**, 580-589
149. Yasui, M., Zelenin, S. M., Celsi, G., and Aperia, A. (1997) Adenylate cyclase-coupled vasopressin receptor activates AQP2 promoter via a dual effect on CRE and AP1 elements. *The American journal of physiology* **272**, F443-450
150. Irrazabal, C. E., Williams, C. K., Ely, M. A., Birrer, M. J., Garcia-Perez, A., Burg, M. B., and Ferraris, J. D. (2008) Activator protein-1 contributes to high NaCl-induced increase in tonicity-responsive enhancer/osmotic response element-binding protein transactivating activity. *The Journal of biological chemistry* **283**, 2554-2563
151. Jo, I., Ward, D. T., Baum, M. A., Scott, J. D., Coghlan, V. M., Hammond, T. G., and Harris, H. W. (2001) AQP2 is a substrate for endogenous PP2B activity within an inner medullary AKAP-signaling complex. *American journal of physiology. Renal physiology* **281**, F958-965
152. Gooch, J. L., Guler, R. L., Barnes, J. L., and Toro, J. J. (2006) Loss of calcineurin Aalpha results in altered trafficking of AQP2 and in nephrogenic diabetes insipidus. *Journal of cell science* **119**, 2468-2476
153. Li, S. Z., McDill, B. W., Kovach, P. A., Ding, L., Go, W. Y., Ho, S. N., and Chen, F. (2007) Calcineurin-NFATc signaling pathway regulates AQP2 expression in response to calcium signals and osmotic stress. *American journal of physiology. Cell physiology* **292**, C1606-1616
154. Rinschen, M. M., Klokckers, J., Pavenstadt, H., Neugebauer, U., Schlatter, E., and Edemir, B. (2011) Different effects of CsA and FK506 on aquaporin-2 abundance in rat primary cultured collecting duct cells. *Pflugers Archiv : European journal of physiology* **462**, 611-622

155. Hozawa, S., Holtzman, E. J., and Ausiello, D. A. (1996) cAMP motifs regulating transcription in the aquaporin 2 gene. *The American journal of physiology* **270**, C1695-1702
156. Matsumura, Y., Uchida, S., Rai, T., Sasaki, S., and Marumo, F. (1997) Transcriptional regulation of aquaporin-2 water channel gene by cAMP. *J Am Soc Nephrol* **8**, 861-867
157. Yu, M. J., Miller, R. L., Uawithya, P., Rinschen, M. M., Khositseth, S., Braucht, D. W., Chou, C. L., Pisitkun, T., Nelson, R. D., and Knepper, M. A. (2009) Systems-level analysis of cell-specific AQP2 gene expression in renal collecting duct. *Proc Natl Acad Sci U S A* **106**, 2441-2446
158. Hasler, U., Nunes, P., Bouley, R., Lu, H. A., Matsuzaki, T., and Brown, D. (2008) Acute hypertonicity alters aquaporin-2 trafficking and induces a MAPK-dependent accumulation at the plasma membrane of renal epithelial cells. *The Journal of biological chemistry* **283**, 26643-26661
159. Rinschen, M. M., Yu, M.-J., Wang, G., Boja, E. S., Hoffert, J. D., Pisitkun, T., and Knepper, M. A. (2010) Quantitative phosphoproteomic analysis reveals vasopressin V2-receptor-dependent signaling pathways in renal collecting duct cells. *Proceedings of the National Academy of Sciences* **107**, 3882-3887
160. Hasler, U., Leroy, V., Jeon, U. S., Bouley, R., Dimitrov, M., Kim, J. A., Brown, D., Kwon, H. M., Martin, P. Y., and Feraille, E. (2008) NF-kappaB modulates aquaporin-2 transcription in renal collecting duct principal cells. *The Journal of biological chemistry* **283**, 28095-28105
161. Hocherl, K., Schmidt, C., Kurt, B., and Bucher, M. (2010) Inhibition of NF-kappaB ameliorates sepsis-induced downregulation of aquaporin-2/V2 receptor expression and acute renal failure in vivo. *American journal of physiology. Renal physiology* **298**, F196-204
162. Hasler, U. (2011) An example of functional interaction between NFAT5/TonEBP and nuclear factor-kappaB by hypertonic stress: aquaporin-2 transcription. *Cell cycle (Georgetown, Tex.)* **10**, 364-365
163. Tajika, Y., Matsuzaki, T., Suzuki, T., Aoki, T., Hagiwara, H., Kuwahara, M., Sasaki, S., and Takata, K. (2004) Aquaporin-2 is retrieved to the apical storage compartment via early endosomes and phosphatidylinositol 3-kinase-dependent pathway. *Endocrinology* **145**, 4375-4383
164. Storm, R., Klussmann, E., Geelhaar, A., Rosenthal, W., and Maric, K. (2003) Osmolality and solute composition are strong regulators of AQP2 expression in renal principal cells. *American journal of physiology. Renal physiology* **284**, F189-198
165. Lam, A. K., Ko, B. C., Tam, S., Morris, R., Yang, J. Y., Chung, S. K., and Chung, S. S. (2004) Osmotic response element-binding protein (OREBP) is an essential regulator of the urine concentrating mechanism. *The Journal of biological chemistry* **279**, 48048-48054
166. Lopez-Rodriguez, C., Antos, C. L., Shelton, J. M., Richardson, J. A., Lin, F., Novobrantseva, T. I., Bronson, R. T., Igarashi, P., Rao, A., and Olson, E. N. (2004) Loss of NFAT5 results in renal atrophy and lack of tonicity-responsive gene expression. *Proc Natl Acad Sci U S A* **101**, 2392-2397
167. Hasler, U., Jeon, U. S., Kim, J. A., Mordasini, D., Kwon, H. M., Feraille, E., and Martin, P. Y. (2006) Tonicity-responsive enhancer binding protein is an essential

- regulator of aquaporin-2 expression in renal collecting duct principal cells. *J Am Soc Nephrol* **17**, 1521-1531
168. Nedvetsky, P. I., Tabor, V., Tamma, G., Beulshausen, S., Skroblin, P., Kirschner, A., Mutig, K., Boltzen, M., Petrucci, O., Vossenkamper, A., Wiesner, B., Bachmann, S., Rosenthal, W., and Klussmann, E. (2010) Reciprocal regulation of aquaporin-2 abundance and degradation by protein kinase A and p38-MAP kinase. *J Am Soc Nephrol* **21**, 1645-1656
 169. Boone, M., Mobasheri, A., Fenton, R. A., van Balkom, B. W., Wismans, R., van der Zee, C. E., and Deen, P. M. (2010) The lysosomal trafficking regulator interacting protein-5 localizes mainly in epithelial cells. *Journal of molecular histology* **41**, 61-74
 170. Le, I. P., Schultz, S., Andresen, B. T., Dewey, G. L., Zhao, P., Listenberger, L., Deen, P. M., Buchwalter, A., Barney, C. C., and Burnatowska-Hledin, M. A. (2012) Aquaporin-2 levels in vitro and in vivo are regulated by VACM-1, a cul 5 gene. *Cellular physiology and biochemistry : international journal of experimental cellular physiology, biochemistry, and pharmacology* **30**, 1148-1158
 171. Smith, F. D., Samelson, B. K., and Scott, J. D. (2011) Discovery of cellular substrates for protein kinase A using a peptide array screening protocol. *Biochemical Journal* **438**, 103-110
 172. Skalhegg, B. S., and Tasken, K. (2000) Specificity in the cAMP/PKA signaling pathway. Differential expression, regulation, and subcellular localization of subunits of PKA. *Frontiers in bioscience : a journal and virtual library* **5**, D678-693
 173. Colledge, M., and Scott, J. D. (1999) AKAPs: from structure to function. *Trends in cell biology* **9**, 216-221
 174. Smith, F. D., and Scott, J. D. (2002) Signaling complexes: junctions on the intracellular information super highway. *Current biology : CB* **12**, R32-40
 175. Taskén, K., and Aandahl, E. M. (2004) Localized Effects of cAMP Mediated by Distinct Routes of Protein Kinase A. *Physiological Reviews* **84**, 137-167
 176. Uawithya, P., Pisitkun, T., Ruttenberg, B. E., and Knepper, M. A. (2008) Transcriptional profiling of native inner medullary collecting duct cells from rat kidney. *Physiological genomics* **32**, 229-253
 177. Whiting, J. L., Ogier, L., Forbush, K. A., Bucko, P., Gopalan, J., Seternes, O.-M., Langeberg, L. K., and Scott, J. D. (2016) AKAP220 manages apical actin networks that coordinate aquaporin-2 location and renal water reabsorption. *Proceedings of the National Academy of Sciences* **113**, E4328-E4337
 178. Moeller, H. B., Aroankins, T. S., Slengerik-Hansen, J., Pisitkun, T., and Fenton, R. A. (2014) Phosphorylation and ubiquitylation are opposing processes that regulate endocytosis of the water channel aquaporin-2. *Journal of cell science* **127**, 3174-3183
 179. Liang, S., Yu, Y., Yang, P., Gu, S., Xue, Y., and Chen, X. (2009) Analysis of the protein complex associated with 14-3-3 epsilon by a deuterated-leucine labeling quantitative proteomics strategy. *Journal of chromatography. B, Analytical technologies in the biomedical and life sciences* **877**, 627-634
 180. Angrand, P. O., Segura, I., Volkel, P., Ghidelli, S., Terry, R., Brajenovic, M., Vintersten, K., Klein, R., Superti-Furga, G., Drewes, G., Kuster, B., Bouwmeester, T., and Acker-Palmer, A. (2006) Transgenic mouse proteomics identifies new 14-

- 3-3-associated proteins involved in cytoskeletal rearrangements and cell signaling. *Molecular & cellular proteomics : MCP* **5**, 2211-2227
181. Nelson, W. J., and Yeaman, C. (2001) Protein trafficking in the exocytic pathway of polarized epithelial cells. *Trends in cell biology* **11**, 483-486
 182. Maxfield, F. R., and McGraw, T. E. (2004) Endocytic recycling. *Nature reviews. Molecular cell biology* **5**, 121-132
 183. Polishchuk, R., Di Pentima, A., and Lippincott-Schwartz, J. (2004) Delivery of raft-associated, GPI-anchored proteins to the apical surface of polarized MDCK cells by a transcytotic pathway. *Nature cell biology* **6**, 297-307
 184. Schwartz, S. L., Cao, C., Pylypenko, O., Rak, A., and Wandinger-Ness, A. (2007) Rab GTPases at a glance. *Journal of cell science* **120**, 3905
 185. Stenmark, H. (2009) Rab GTPases as coordinators of vesicle traffic. *Nature reviews. Molecular cell biology* **10**, 513-525
 186. Sollner, T., Bennett, M. K., Whiteheart, S. W., Scheller, R. H., and Rothman, J. E. (1993) A protein assembly-disassembly pathway in vitro that may correspond to sequential steps of synaptic vesicle docking, activation, and fusion. *Cell* **75**, 409-418
 187. Sollner, T., Whiteheart, S. W., Brunner, M., Erdjument-Bromage, H., Geromanos, S., Tempst, P., and Rothman, J. E. (1993) SNAP receptors implicated in vesicle targeting and fusion. *Nature* **362**, 318-324
 188. Li, X., Low, S. H., Miura, M., and Weimbs, T. (2002) SNARE expression and localization in renal epithelial cells suggest mechanism for variability of trafficking phenotypes. *American journal of physiology. Renal physiology* **283**, F1111-1122
 189. Borisovska, M., Zhao, Y., Tsytsyura, Y., Glyvuk, N., Takamori, S., Matti, U., Rettig, J., Südhof, T., and Bruns, D. (2005) v-SNAREs control exocytosis of vesicles from priming to fusion. *The EMBO Journal* **24**, 2114-2126
 190. Glickman, M. H., and Ciechanover, A. (2002) The ubiquitin-proteasome proteolytic pathway: destruction for the sake of construction. *Physiol Rev* **82**, 373-428
 191. Mukhopadhyay, D., and Riezman, H. (2007) Proteasome-independent functions of ubiquitin in endocytosis and signaling. *Science (New York, N.Y.)* **315**, 201-205
 192. Schnell, J. D., and Hicke, L. (2003) Non-traditional functions of ubiquitin and ubiquitin-binding proteins. *The Journal of biological chemistry* **278**, 35857-35860
 193. Nejsum, L. N., Zelenina, M., Aperia, A., Frøkiær, J., and Nielsen, S. (2005) Bidirectional regulation of AQP2 trafficking and recycling: involvement of AQP2-S256 phosphorylation. *American Journal of Physiology - Renal Physiology* **288**, F930-F938
 194. Jose, P. A., Raymond, J. R., Bates, M. D., Aperia, A., Felder, R. A., and Carey, R. M. (1992) The renal dopamine receptors. *J Am Soc Nephrol* **2**, 1265-1278
 195. Nadler, S. P., Zimpelmann, J. A., and Hebert, R. L. (1992) PGE2 inhibits water permeability at a post-cAMP site in rat terminal inner medullary collecting duct. *The American journal of physiology* **262**, F229-235
 196. Anderson, R. J., Berl, T., McDonald, K. D., and Schrier, R. W. (1975) Evidence for an in vivo antagonism between vasopressin and prostaglandin in the mammalian kidney. *The Journal of clinical investigation* **56**, 420-426

197. Kalra, S., Zargar, A. H., Jain, S. M., Sethi, B., Chowdhury, S., Singh, A. K., Thomas, N., Unnikrishnan, A. G., Thakkar, P. B., and Malve, H. (2016) Diabetes insipidus: The other diabetes. *Indian Journal of Endocrinology and Metabolism* **20**, 9-21
198. Robertson, G. L. (1995) Diabetes insipidus. *Endocrinology and metabolism clinics of North America* **24**, 549-572
199. Babey, M., Kopp, P., and Robertson, G. L. (2011) Familial forms of diabetes insipidus: clinical and molecular characteristics. *Nature reviews. Endocrinology* **7**, 701-714
200. Robertson, G. L. (1988) Differential diagnosis of polyuria. *Annual review of medicine* **39**, 425-442
201. Saifan, C., Nasr, R., Mehta, S., Sharma Acharya, P., Perrera, I., Faddoul, G., Nalluri, N., Kesavan, M., Azzi, Y., and El-Sayegh, S. (2013) Diabetes insipidus: a challenging diagnosis with new drug therapies. *ISRN nephrology* **2013**, 797620
202. Di Iorgi, N., Napoli, F., Allegri, A. E., Olivieri, I., Bertelli, E., Gallizia, A., Rossi, A., and Maghnie, M. (2012) Diabetes insipidus--diagnosis and management. *Hormone research in paediatrics* **77**, 69-84
203. Bichet, D. G., Oksche, A., and Rosenthal, W. (1997) Congenital nephrogenic diabetes insipidus. *J Am Soc Nephrol* **8**, 1951-1958
204. Garcia Castano, A., Perez de Nancrales, G., Madariaga, L., Aguirre, M., Chocron, S., Madrid, A., Lafita Tejedor, F. J., Gil Campos, M., Sanchez Del Pozo, J., Ruiz Cano, R., Espino, M., Gomez Vida, J. M., Santos, F., Garcia Nieto, V. M., Loza, R., Rodriguez, L. M., Hidalgo Barquero, E., Printza, N., Camacho, J. A., Castano, L., and Ariceta, G. (2015) Novel mutations associated with nephrogenic diabetes insipidus. A clinical-genetic study. *European journal of pediatrics* **174**, 1373-1385
205. Birnbaumer, M., Seibold, A., Gilbert, S., Ishido, M., Barberis, C., Antaramian, A., Brabet, P., and Rosenthal, W. (1992) Molecular cloning of the receptor for human antidiuretic hormone. *Nature* **357**, 333-335
206. Arthus, M. F., Lonergan, M., Crumley, M. J., Naumova, A. K., Morin, D., De Marco, L. A., Kaplan, B. S., Robertson, G. L., Sasaki, S., Morgan, K., Bichet, D. G., and Fujiwara, T. M. (2000) Report of 33 novel AVPR2 mutations and analysis of 117 families with X-linked nephrogenic diabetes insipidus. *J Am Soc Nephrol* **11**, 1044-1054
207. Satoh, M., Ogikubo, S., and Yoshizawa-Ogasawara, A. (2008) Correlation between clinical phenotypes and X-inactivation patterns in six female carriers with heterozygote vasopressin type 2 receptor gene mutations. *Endocrine journal* **55**, 277-284
208. Faerch, M., Corydon, T. J., Rittig, S., Christensen, J. H., Hertz, J. M., and Jendle, J. (2010) Skewed X-chromosome inactivation causing diagnostic misinterpretation in congenital nephrogenic diabetes insipidus. *Scandinavian journal of urology and nephrology* **44**, 324-330
209. Barberis, C., Mouillac, B., and Durroux, T. (1998) Structural bases of vasopressin/oxytocin receptor function. *The Journal of endocrinology* **156**, 223-229
210. Slusarz, M. J., Gieldon, A., Slusarz, R., and Ciarkowski, J. (2006) Analysis of interactions responsible for vasopressin binding to human neurohypophyseal hormone receptors-molecular dynamics study of the activated receptor-

- vasopressin-G(alpha) systems. *Journal of peptide science : an official publication of the European Peptide Society* **12**, 180-189
211. Slusarz, M. J., Sikorska, E., Slusarz, R., and Ciarkowski, J. (2006) Molecular docking-based study of vasopressin analogues modified at positions 2 and 3 with N-methylphenylalanine: influence on receptor-bound conformations and interactions with vasopressin and oxytocin receptors. *Journal of medicinal chemistry* **49**, 2463-2469
 212. Robben, J. H., Knoers, N. V., and Deen, P. M. (2006) Cell biological aspects of the vasopressin type-2 receptor and aquaporin 2 water channel in nephrogenic diabetes insipidus. *American journal of physiology. Renal physiology* **291**, F257-270
 213. Bichet, D. G. (2008) Vasopressin receptor mutations in nephrogenic diabetes insipidus. *Seminars in nephrology* **28**, 245-251
 214. Spanakis, E., Milord, E., and Gagnoli, C. (2008) AVPR2 variants and mutations in nephrogenic diabetes insipidus: review and missense mutation significance. *Journal of cellular physiology* **217**, 605-617
 215. Sahakitrungruang, T., Wacharasindhu, S., Sinthuwiwat, T., Supornsilchai, V., Suphapeetiporn, K., and Shotelersuk, V. (2008) Identification of two novel aquaporin-2 mutations in a Thai girl with congenital nephrogenic diabetes insipidus. *Endocrine* **33**, 210-214
 216. Sasaki, S., Chiga, M., Kikuchi, E., Rai, T., and Uchida, S. (2013) Hereditary nephrogenic diabetes insipidus in Japanese patients: analysis of 78 families and report of 22 new mutations in AVPR2 and AQP2. *Clinical and experimental nephrology* **17**, 338-344
 217. Canfield, M. C., Tamarappoo, B. K., Moses, A. M., Verkman, A. S., and Holtzman, E. J. (1997) Identification and Characterization of Aquaporin-2 Water Channel Mutations Causing Nephrogenic Diabetes Insipidus with Partial Vasopressin Response. *Human molecular genetics* **6**, 1865-1871
 218. Tamarappoo, B. K., and Verkman, A. S. (1998) Defective aquaporin-2 trafficking in nephrogenic diabetes insipidus and correction by chemical chaperones. *Journal of Clinical Investigation* **101**, 2257-2267
 219. Leduc-Nadeau, A., Lussier, Y., Arthus, M. F., Lonergan, M., Martinez-Aguayo, A., Riveira-Munoz, E., Devuyst, O., Bissonnette, P., and Bichet, D. G. (2010) New autosomal recessive mutations in aquaporin-2 causing nephrogenic diabetes insipidus through deficient targeting display normal expression in *Xenopus* oocytes. *J Physiol* **588**, 2205-2218
 220. Marr, N., Bichet, D. G., Hoefs, S., Savelkoul, P. J., Konings, I. B., De Mattia, F., Graat, M. P., Arthus, M. F., Lonergan, M., Fujiwara, T. M., Knoers, N. V., Landau, D., Balfe, W. J., Oksche, A., Rosenthal, W., Muller, D., Van Os, C. H., and Deen, P. M. (2002) Cell-biologic and functional analyses of five new Aquaporin-2 missense mutations that cause recessive nephrogenic diabetes insipidus. *J Am Soc Nephrol* **13**, 2267-2277
 221. van Lieburg, A. F., Verdijk, M. A., Knoers, V. V., van Essen, A. J., Proesmans, W., Mallmann, R., Monnens, L. A., van Oost, B. A., van Os, C. H., and Deen, P. M. (1994) Patients with autosomal nephrogenic diabetes insipidus homozygous for mutations in the aquaporin 2 water-channel gene. *Am J Hum Genet* **55**, 648-652

222. Deen, P. M., Croes, H., van Aubel, R. A., Ginsel, L. A., and van Os, C. H. (1995) Water channels encoded by mutant aquaporin-2 genes in nephrogenic diabetes insipidus are impaired in their cellular routing. *Journal of Clinical Investigation* **95**, 2291-2296
223. Marr, N., Kamsteeg, E. J., van Raak, M., van Os, C. H., and Deen, P. M. (2001) Functionality of aquaporin-2 missense mutants in recessive nephrogenic diabetes insipidus. *Pflugers Archiv : European journal of physiology* **442**, 73-77
224. Cheong, H. I., Cho, S. J., Zheng, S. H., Cho, H. Y., Ha, I. S., and Choi, Y. (2005) Two novel mutations in the aquaporin 2 gene in a girl with congenital nephrogenic diabetes insipidus. *Journal of Korean medical science* **20**, 1076-1078
225. Vargas-Poussou, R., Forestier, L., Dautzenberg, M. D., Niaudet, P., Dechaux, M., and Antignac, C. (1997) Mutations in the vasopressin V2 receptor and aquaporin-2 genes in 12 families with congenital nephrogenic diabetes insipidus. *J Am Soc Nephrol* **8**, 1855-1862
226. Rugpolmuang, R., Deeb, A., Hassan, Y., Deekajorndech, T., Shotelersuk, V., and Sahakitrungruang, T. (2014) Novel AQP2 mutation causing congenital nephrogenic diabetes insipidus: challenges in management during infancy. *Journal of pediatric endocrinology & metabolism : JPEM* **27**, 193-197
227. Hochberg, Z., Van Lieburg, A., Even, L., Brenner, B., Lanir, N., Van Oost, B. A., and Knoers, N. V. (1997) Autosomal recessive nephrogenic diabetes insipidus caused by an aquaporin-2 mutation. *J Clin Endocrinol Metab* **82**, 686-689
228. Carroll, P., Al-Mojalli, H., Al-Abbad, A., Al-Hassoun, I., Al-Hamed, M., Al-Amr, R., Butt, A. I., and Meyer, B. F. (2006) Novel mutations underlying nephrogenic diabetes insipidus in Arab families. *Genetics in medicine : official journal of the American College of Medical Genetics* **8**, 443-447
229. Park, Y. J., Baik, H. W., Cheong, H. I., and Kang, J. H. (2014) Congenital nephrogenic diabetes insipidus with a novel mutation in the aquaporin 2 gene. *Biomedical reports* **2**, 596-598
230. Goji, K., Kuwahara, M., Gu, Y., Matsuo, M., Marumo, F., and Sasaki, S. (1998) Novel mutations in aquaporin-2 gene in female siblings with nephrogenic diabetes insipidus: evidence of disrupted water channel function. *J Clin Endocrinol Metab* **83**, 3205-3209
231. Kuwahara, M. (1998) Aquaporin-2, a vasopressin-sensitive water channel, and nephrogenic diabetes insipidus. *Internal medicine (Tokyo, Japan)* **37**, 215-217
232. Laursen, U. H., Pihakaski-Maunsbach, K., Kwon, T. H., Ostergaard Jensen, E., Nielsen, S., and Maunsbach, A. B. (2004) Changes of rat kidney AQP2 and Na,K-ATPase mRNA expression in lithium-induced nephrogenic diabetes insipidus. *Nephron. Experimental nephrology* **97**, e1-16
233. Duzenli, D., Saglar, E., Deniz, F., Azal, O., Erdem, B., and Mergen, H. (2012) Mutations in the AVPR2, AVP-NPII, and AQP2 genes in Turkish patients with diabetes insipidus. *Endocrine* **42**, 664-669
234. Iolascon, A., Aglio, V., Tamma, G., D'Apolito, M., Addabbo, F., Procino, G., Simonetti, M. C., Montini, G., Gesualdo, L., Debler, E. W., Svelto, M., and Valenti, G. (2007) Characterization of two novel missense mutations in the AQP2 gene causing nephrogenic diabetes insipidus. *Nephron. Physiology* **105**, p33-41
235. Boccalandro, C., De Mattia, F., Guo, D. C., Xue, L., Orlander, P., King, T. M., Gupta, P., Deen, P. M., Lavis, V. R., and Milewicz, D. M. (2004) Characterization

- of an aquaporin-2 water channel gene mutation causing partial nephrogenic diabetes insipidus in a Mexican family: evidence of increased frequency of the mutation in the town of origin. *J Am Soc Nephrol* **15**, 1223-1231
236. Moses, A. M., Scheinman, S. J., and Oppenheim, A. (1984) Marked hypotonic polyuria resulting from nephrogenic diabetes insipidus with partial sensitivity to vasopressin. *J Clin Endocrinol Metab* **59**, 1044-1049
237. Loonen, A. J., Knoers, N. V., van Os, C. H., and Deen, P. M. (2008) Aquaporin 2 mutations in nephrogenic diabetes insipidus. *Seminars in nephrology* **28**, 252-265
238. Liberatore Junior, R. D., Carneiro, J. G., Leidenz, F. B., Melilo-Carolino, R., Sarubi, H. C., and De Marco, L. (2012) Novel compound aquaporin 2 mutations in nephrogenic diabetes insipidus. *Clinics (Sao Paulo, Brazil)* **67**, 79-82
239. Oksche, A., Moller, A., Dickson, J., Rosendahl, W., Rascher, W., Bichet, D. G., and Rosenthal, W. (1996) Two novel mutations in the aquaporin-2 and the vasopressin V2 receptor genes in patients with congenital nephrogenic diabetes insipidus. *Human genetics* **98**, 587-589
240. Moon, S. S., Kim, H. J., Choi, Y. K., Seo, H. A., Jeon, J. H., Lee, J. E., Lee, J. Y., Kwon, T. H., Kim, J. G., Kim, B. W., and Lee, I. K. (2009) Novel mutation of aquaporin-2 gene in a patient with congenital nephrogenic diabetes insipidus. *Endocrine journal* **56**, 905-910
241. Ulloa-Aguirre, A., Janovick, J. A., Brothers, S. P., and Conn, P. M. (2004) Pharmacologic rescue of conformationally-defective proteins: implications for the treatment of human disease. *Traffic (Copenhagen, Denmark)* **5**, 821-837
242. Romisch, K. (2004) A cure for traffic jams: small molecule chaperones in the endoplasmic reticulum. *Traffic (Copenhagen, Denmark)* **5**, 815-820
243. Bernier, V., Lagace, M., Bichet, D. G., and Bouvier, M. (2004) Pharmacological chaperones: potential treatment for conformational diseases. *Trends in endocrinology and metabolism: TEM* **15**, 222-228
244. Kamsteeg, E. J., Wormhoudt, T. A., Rijss, J. P., van Os, C. H., and Deen, P. M. (1999) An impaired routing of wild-type aquaporin-2 after tetramerization with an aquaporin-2 mutant explains dominant nephrogenic diabetes insipidus. *The EMBO Journal* **18**, 2394-2400
245. El Tarazi, A., Lussier, Y., Da Cal, S., Bissonnette, P., and Bichet, D. G. (2016) Functional Recovery of AQP2 Recessive Mutations Through Hetero-Oligomerization with Wild-Type Counterpart. *Scientific Reports* **6**, 33298
246. Moeller, H. B., Rittig, S., and Fenton, R. A. (2013) Nephrogenic diabetes insipidus: essential insights into the molecular background and potential therapies for treatment. *Endocrine reviews* **34**, 278-301
247. Mulders, S. M., Bichet, D. G., Rijss, J. P., Kamsteeg, E. J., Arthus, M. F., Lonergan, M., Fujiwara, M., Morgan, K., Leijendekker, R., van der Sluijs, P., van Os, C. H., and Deen, P. M. (1998) An aquaporin-2 water channel mutant which causes autosomal dominant nephrogenic diabetes insipidus is retained in the Golgi complex. *Journal of Clinical Investigation* **102**, 57-66
248. Kuwahara, M., Iwai, K., Ooeda, T., Igarashi, T., Ogawa, E., Katsushima, Y., Shinbo, I., Uchida, S., Terada, Y., Arthus, M.-F., Lonergan, M., Fujiwara, T. M., Bichet, D. G., Marumo, F., and Sasaki, S. (2001) Three Families with Autosomal Dominant Nephrogenic Diabetes Insipidus Caused by Aquaporin-2 Mutations in the C-Terminus. *American Journal of Human Genetics* **69**, 738-748

249. de Mattia, F., Savelkoul, P. J., Kamsteeg, E. J., Konings, I. B., van der Sluijs, P., Mallmann, R., Oksche, A., and Deen, P. M. (2005) Lack of arginine vasopressin-induced phosphorylation of aquaporin-2 mutant AQP2-R254L explains dominant nephrogenic diabetes insipidus. *J Am Soc Nephrol* **16**, 2872-2880
250. Savelkoul, P. J., De Mattia, F., Li, Y., Kamsteeg, E. J., Konings, I. B., van der Sluijs, P., and Deen, P. M. (2009) p.R254Q mutation in the aquaporin-2 water channel causing dominant nephrogenic diabetes insipidus is due to a lack of arginine vasopressin-induced phosphorylation. *Human mutation* **30**, E891-903
251. Dollerup, P., Thomsen, T. M., Nejsum, L. N., Faerch, M., Osterbrand, M., Gregersen, N., Rittig, S., Christensen, J. H., and Corydon, T. J. (2015) Partial nephrogenic diabetes insipidus caused by a novel AQP2 variation impairing trafficking of the aquaporin-2 water channel. *BMC nephrology* **16**, 217
252. Kamsteeg, E.-J., Bichet, D. G., Konings, I. B. M., Nivet, H., Lonergan, M., Arthus, M.-F., van Os, C. H., and Deen, P. M. T. (2003) Reversed polarized delivery of an aquaporin-2 mutant causes dominant nephrogenic diabetes insipidus. *The Journal of cell biology* **163**, 1099-1109
253. Boone, M., and Deen, P. M. (2009) Congenital nephrogenic diabetes insipidus: what can we learn from mouse models? *Experimental physiology* **94**, 186-190

Chapter 3

Comparing actin polymerization in the presence of c-terminal Aquaporin 2 peptides and Thymosin- β -4

Pronk, J.W.; Aroankins, T.S.; Fenton, R.A.; Engel, E.H.

This chapter is under revision at Journal of Biological Chemistry.

3.1: Abstract

To maintain water homeostasis in mammals, aquaporin 2 (AQP2) bearing vesicles traffic to the apical membrane of collecting duct principal cells. This process is controlled by arginine-vasopressin (AVP), which activates a signalling network that results in phosphorylation of conserved C-terminal sites in AQP2 and translocation towards the apical membrane. Fusion of AQP2 bearing vesicles is hindered by a sub-apical actin cortex, which needs to be opened before fusion occurs. AVP-induced remodelling of the actin cytoskeleton and the interaction of AQP2 with actin have previously been studied. Here we compare the influence of AQP2 C-terminal peptides, thymosin- β -4, and sermorelin on actin polymerization using polymerization assays, negative stain electron microscopy, and blue native gel electrophoresis. We demonstrate that the C-terminal AQP2 mutant S256D, which mimics the phosphopeptide 256-p, has a gelsolin-like effect on actin nucleation. We show the importance of AQP2 residues R253 and R254 on actin polymerization inhibition and actin cortex opening. In addition, AQP2-S256D destabilizes actin thin filaments and thereby enhances opening of the actin cortex to facilitate fusion of AQP2 vesicles with the apical membrane.

3.2: Introduction

Maintaining water homeostasis is critical in all mammals. Although water can pass through pure lipid bilayers by diffusion, the process is too slow to ensure water homeostasis. Enhanced water permeability is achieved by aquaporins (AQPs), a large family of integral membrane proteins that facilitate water permeation across biological membranes (1-3,4,5-7). In mammals, water homeostasis is mainly maintained by the kidneys, which expresses eight of the thirteen mammalian AQPs (8,9).

Glomeruli in human kidneys filter 180 litres of plasma per day (10). 90% of the filtered water is reabsorbed by AQP1 residing in the proximal tubule and descending thin limb of Henle (8). A large fraction of the remaining water is reabsorbed in the collecting tubule and collecting duct, where the water permeability is variable and controlled by the peptide hormone arginine-vasopressin (AVP) (11). Three AQPs are expressed in tubules and ducts that connect the nephrons to the ureter: AQP2, located in internal vesicles and the apical membrane (12), and AQP3 and AQP4, both located in the basolateral membrane of collecting duct principal cells (13,14).

3.2.1: AQP2

AQP2 consists of 271 residues and exhibits the characteristic aquaporin fold (15). However, AQP2 carries a unique hydrophilic C-terminal helix (16), which contains four phosphorylation sites (Ser256, Ser261, Ser264, Thr269 (Ser269 in rodents)). AVP binding to the AVP receptor (V2R) leads to activation of cAMP-dependent protein kinases, including protein kinase-A (PKA). PKA phosphorylates AQP2 at residue Ser256, inducing transport of AQP2 to the apical membrane (17,18). Phosphorylation of Ser256 is thought to be the master switch regulating AQP2, because it is the first residue to be phosphorylated after AVP stimulation and downstream phosphorylation is limited in the absence of Ser256 (18). Furthermore, AQP2-S256D, mimicking the phosphorylated state of Ser256, accumulated in the apical membrane (19,20), while AQP2-S256A, where no Ser256 phosphorylation is possible, resided in intracellular vesicles (19,20). Co-expression experiments in *Xenopus oocytes* showed that at least 75% of AQP2-S256D was necessary to induce AQP2 apical accumulation (21).

3.2.2: The actin cortical network

Near the apical membrane, a dynamic network of actin filaments, the actin cortical network, is located, providing mechanical stability to the cell but also acting as a barrier to vesicle fusion (22,23). For AQP2 to fuse with the apical membrane, the actin cortex needs to be broken. Indeed, a reduction of cellular f-actin was found to be synchronized with binding of AVP to its receptor in toad bladder epithelial cells (24), rat inner medullary collecting duct cells (25) and murine cortical collecting duct cells (26). Furthermore, actin depolymerization was linked to the fluid shear stress (FSS) in the collecting duct (27) and the activation of PKA by AVP, leading to an inactivation of RhoA (28). Direct interactions between actin and AQP2 were found by surface plasmon resonance experiments, showing that AQP2, reconstituted in

proteoliposomes, specifically binds to g-actin (29,30). Depolymerization of f-actin was linked to AQP2 expression levels in MDCK cells and LLC-PK₁ cells (31). Furthermore, Ser256 phosphorylation increases the affinity of AQP2 to tropomyosin-5b (Tm5b), resulting in a destabilization of actin polymers (30,32). In general, actin seems to interact with a variety of channel proteins during their trafficking to the plasma membrane (reviewed in (33)).

Actin dynamics are regulated by a wide variety of different actin binding proteins, mainly binding to the barbed end of actin in the groove between domains one and three (34). This groove accommodates an α -helix up to 20Å. Interactions include conserved charged and hydrophobic residues forming either salt bridges or hydrogen bonds or leads to hiding in the hydrophobic groove. The α -helical C-terminus of AQP2 could be a regulator of actin dynamics, because it shows a distinct sequence homology to α -helical RPEL and WASP domains (35).

3.2.3: Aim of this research

Here we compare the influence of the C-terminal AQP2 peptides AQP2-WT, AQP2-S256A, AQP2-S256D, AQP2-R253A, AQP2-R253A-R254A, AQP2-R253A-S256D and AQP2-R254A-S256D, with the actin-binding peptide thymosin- β -4 (TM β 4) and the hormone sermorelin on actin polymerization. *In vitro* polymerization assays, negative stain transmission electron microscopy (TEM), blue native PAGE, and fluorescence measurements with pyrene-labelled actin revealed that C-terminal AQP2 peptide isoforms inhibit actin polymerization and destabilize actin thin filaments by their interaction with actin and Tm5b. Furthermore, the propensity of AQP2 C-terminal peptides to inhibit actin polymerization and destabilize actin thin filaments could be diminished by mutations in the residues R253 and R254 of AQP2. However, we could not demonstrate that C-terminal AQP2 peptides sever actin filaments *in vitro*. Our results suggest that the C-terminus of AQP2 plays a role in breaking the actin cortex for fusion of AQP2-bearing vesicles with the apical membrane, but that other factors may be equally important.

3.3: AQP2 and Actin cortex remodelling

The apical actin cortex needs to be remodelled for AQP2-bearing vesicles to reach the apical membrane and to fuse with it. To explore the role of the AQP2 C-terminus we used different synthetic peptides (Table 3.1) and measured their interactions with actin. Because phosphorylation of S256 is thought to be the main switch for AVP-mediated AQP2 trafficking, we concentrated on varying this residue (18,21,36-38). The first peptide differed in length, but shares the wild type residue S256, and is referred to as AQP2-WT. The change in peptide length did not alter the effect of the peptide on actin polymerization (results not shown). The second isoform mimics the phosphorylated state of residue S256, i.e. it carries the mutation S256D, whereas the last peptide with mutation S256A, mimics the dephosphorylated state. These mutants will be referred to as AQP2-S256D and AQP2-S256A, respectively. We used thymosin- β -4 (TM β 4) as a positive control, because it is

Table 3.1. Amino acid sequence of the peptides used in this study, with corresponding molecular weight. In red is residue 256 of AQP2 highlighted indicating the mutation in this peptide, mimicking the phosphorylated state of this residue (D) or dephosphorylated state of this residue (A). In green the mutated arginine residues are highlighted.

Peptide	Amino acid sequence	MW (Da)
AQP2-WT long	FPPAKSLSER LAVLKGLEPD TDWEEREVRR RQSVELHSPQ SLPRG	5197.80
AQP2-WT	DWEEREVRRR QSVELHSPQS LPRG	2975.25
AQP2-S256D	DWEEREVRRR QDVELHSPQS LPRG	3003.26
AQP2-S256A	DWEEREVRRR QAVELHSPQS LPRG	2959.25
AQP2-R253A	DWEEREVRRR QSVELHSPQS LPRG	2862.09
AQP2-R253A-R254A	DWEEREVRAA QSVELHSPQS LPRG	2776.98
AQP2-R253A-S256D	DWEEREVRRR QDVELHSPQS LPRG	2890.10
AQP2-R254A-S256D	DWEEREVRAA QDVELHSPQS LPRG	2890.10
TM β 4	MSDKPDMAEI EKFDKSKLKK TETQEKNPLP SKETIEQEQ AGES	4963.49
Sermorelin	YADAIFTNSY RKVLGQLSAR KLLQDIMNR	3357.88

known to interact with actin and is able to inhibit the formation of f-actin (39), and sermorelin as a negative control.

3.3.1: Aquaporin 2 inhibits actin polymerization

First, we studied the inhibiting effect of C-terminal AQP2 peptides on the formation of f-actin using an actin-binding protein spin-down assay (40). Actin polymerization was initiated in the presence of different molar ratios of peptides (peptide:actin) and f-actin was harvested by ultracentrifugation after 1 hr, leaving g-actin in the supernatant. Figure 3.1A shows that addition of sermorelin leads to an increase of protein concentration in the supernatant up to a normalized signal of 0.16 (± 0.07) for a ratio of 2:1 (sermorelin:actin). However, addition of AQP2-WT leads to a significantly higher protein concentration in the supernatant as compared to sermorelin, reaching a value of 0.37 ± 0.08 ($p=0,04$) (Table 3.2) after addition of AQP2-WT in a molar ratio of 2 (AQP2:actin). AQP2-S256D and AQP2-S256A did not show a significant different effect on actin polymerization as compared to AQP2-WT ($p=0.40$ and $p=0.27$, respectively) (Table 3.2) reaching values of 0.40 ± 0.07 and 0.29 ± 0.08 respectively after addition at a molar ratio of 2 (peptide:actin) (Figure 3.1A). This suggests that the AQP2 C-terminus is indeed able to inhibit actin polymerization to some extent. However, TM β 4 had a stronger effect on actin polymerization inhibition, reaching a normalized actin concentration in the supernatant of 0.70 ± 0.08 using a molar ratio of 2:1 (TM β 4:actin) (Figure 3.1A).

By loading the supernatant (g-actin) and the pellet (f-actin) on SDS-gel (Figure 3.1B), we can visualize the change in actin with increasing amounts of peptide. For AQP2-S256D and TM β 4 a strong increase of g-actin in the supernatant is visible, complemented by a strong decrease of f-actin in the pellet. For AQP2-WT and AQP2-S256A the same is observed, although to a lesser degree. Sermorelin does not affect the signal of g-actin and f-actin. SDS-

Table 3.2. Statistical analysis of actin polymerization assays. Values listed are means \pm S.E., the number of independent experiments are in brackets. For the statistical analysis a 2-tailed, unpaired *t*-test with Welch correction was used.

Peptide	Actin in supernatant ^a	P	Relative fluorescence ^b	p	Slope at t=0 min ^c	p	Slope at t=60 min ^d	p	Slope at t=60 min ^e	p
Actin			1.00 \pm 0.02 (N=5, S.E.)		0.049 \pm 0.004 (N=5, S.E.)		0.0006 \pm 0.0003 (N=3, S.E.)		0.0003 \pm 0.000 3 (N=3, S.E.)	0.003 ⁱ
AQP2-WT	0.37 \pm 0.08 (N=6, S.E.)	0.04 ^f	0.67 \pm 0.03 (N=9, S.E.)	0.04 ^f	0.040 \pm 0.002 (N=9, S.E.)	0.08 ^h	0.0008 \pm 0.0002 (N=3, S.E.)	0.66 ^h	0.0027 \pm 0.000 3 (N=3, S.E.)	0.022 ⁱ
AQP2-S256A	0.29 \pm 0.08 (N=5, S.E.)	0.27 ^g	0.75 \pm 0.04 (N=7, S.E.)	0.13 ^g	0.053 \pm 0.006 (N=7, S.E.)	0.66 ^h	0.0011 \pm 0.0002 (N=3, S.E.)	0.23 ^h	0.0054 \pm 0.000 9 (N=3, S.E.)	0.876 ⁱ
AQP2-S256D	0.40 \pm 0.07 (N=5, S.E.)	0.40 ^g	0.67 \pm 0.02 (N=12, S.E.)	0.98 ^g	0.46 \pm 0.005 (N=12, S.E.)	0.57 ^h	0.0009 \pm 0.0002 (N=3, S.E.)	0.50 ^h	-0.0022 \pm 0.000 4 (N=3, S.E.)	0.0003 ⁱ
TM β 4	0.16 \pm 0.02 (N=5, S.E.)	0.11 ^g	0.65 \pm 0.01 (N=3, S.E.)	0.34 ^g	0.025 \pm 0.001 (N=3, S.E.)	0.01 ^h	0.0003 \pm 0.0002 (N=3, S.E.)	0.51 ^h	0.0038 \pm 0.000 8 (N=3, S.E.)	0.242 ⁱ
Sermorelin	0.16 \pm 0.07 (N=5, S.E.)		0.88 \pm 0.08 (N=6, S.E.)		0.032 \pm 0.005 (N=6, S.E.)	0.02 ^h	0.0007 \pm 0.0002 (N=3, S.E.)	0.89 ^h	0.0072 \pm 0.001 9 (N=3, S.E.)	0.409 ⁱ

^a Actin was polymerized and sedimented after 1 h. The normalized G-actin concentration values at molar ratio 2 (peptide:actin) are listed (Figure 1A). TM β 4 shows the normalized G-actin concentration value at molar ratio 0.5 (peptide:actin).

^b Actin polymerization was monitored by the fluorescence of pyrene-labelled actin. For each experiment actin alone and actin in the presence of peptide were measured and compared. Normalized fluorescence values after 60 min are listed (Figure 4). All values are determined in a molar ratio of 2 (peptide:actin) except for TM β 4 (molar ratio of 0.5; peptide:actin).

^c Initial polymerization rates were determined by linear regression of averaged normalized fluorescence signal between t=0 min and t=5 min (Figure 4).

^d Polymerization rates were determined by linear regression of averaged normalized fluorescence signal after addition of peptides (or buffer) to polymerized actin (molar ratio of 2; peptide:actin) between t=60 min and t=120 min (Figure 5).

^e Polymerization rates were determined by linear regression of averaged normalized fluorescence signal after addition of peptides (or buffer) to actin (molar ratio of 2; peptide:actin) polymerized in the presence of tropomyosin-5b between t=60 min and t=90 min (Figure 6), linear regression of actin in the presence of Tm5b was 0.0052 \pm 0.0005 (N=3, S.E.).

^f Compared to sermorelin

^g Compared to AQP2-WT

^h Compared to actin alone

ⁱ Compared to actin+Tm5b

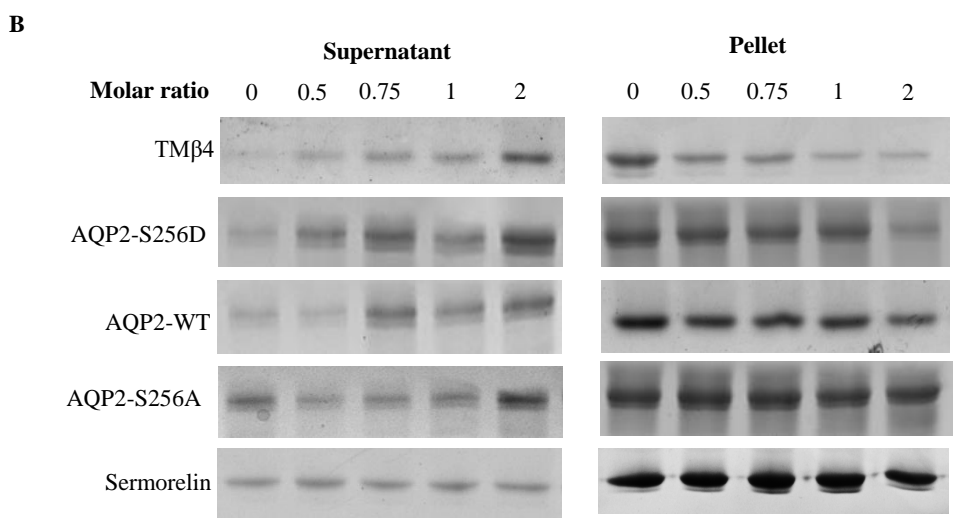
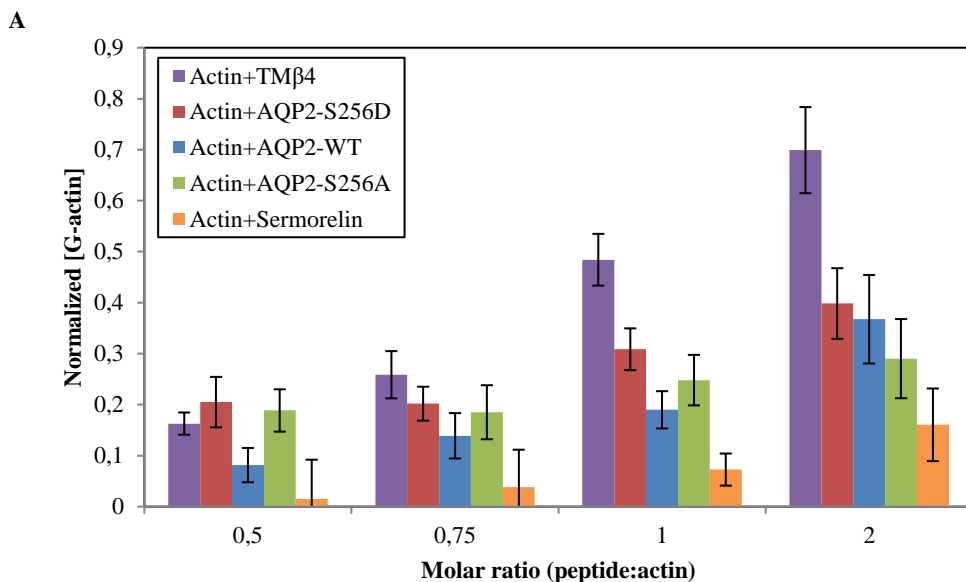


Figure 3.1: Actin polymerization experiments. (A) Normalized fraction of protein in the supernatant with increasing molar ratios of peptide. Actin concentration is normalized against the total concentration at the start. Standard errors are obtained from multiple independent experiments (N=5). (B) SDS gels of actin in the supernatant (left; unpolymerized actin) and in the pellet (right; polymerized actin) after ultracentrifugation incubated with different peptides in different molar ratios (peptide:actin).

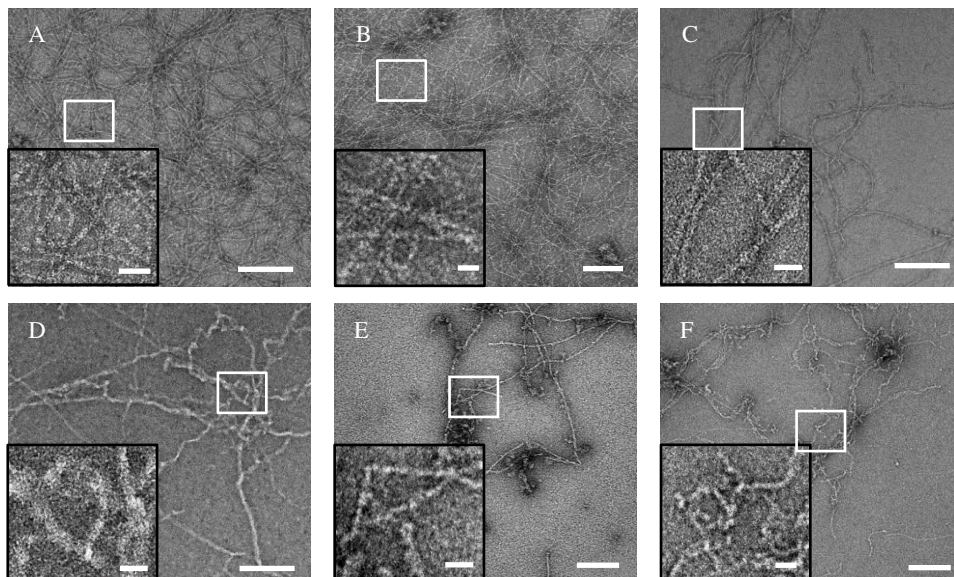


Figure 3.2: Negative stain transmission Electron Microscopy of actin filaments produced in the absence of peptide (A), or in the presence of Sermorelin (B), AQP2-S256A (C), AQP2-WT (D), AQP2-S256D (E) or TM β 4 (F) in a molar ratio of 2 (peptide:actin). Actin filaments were derived from the pellet after ultracentrifugation. Pellets were dissolved in a total volume of 200 μ l GAB prior to loading on EM copper grids. Scale bar is 200 nm. Magnification is 41,000x. Insert shows a 4x magnification of the region indicated by a white box. Scale bar of the insert is 25 nm.

gels were run for all sedimentation experiments and they showed the same trend (Figure S3.1).

3.3.2: C-terminal AQP2 interferes with f-actin filament assembly

Although AQP2 is able to inhibit actin polymerization, actin is still able to form some filaments. Even when actin polymerization is highly inhibited by TM β 4, we still observe some f-actin in the pellet. We therefore used TEM to visualize the negatively stained actin filaments formed in the presence of assembly-perturbing peptides. Without peptides, actin forms long 9 nm wide filaments (Figure 3.2A, Figure S3.2). As displayed in Figure 3.2B sermorelin has no effect on the filament morphology (width of 8.9 nm, Figure S3.2), while after addition of AQP2-S256A shorter filaments coexist with long filaments (Figure 3.2C) but still with an average width of 8.9 nm (Figure S3.2). In contrast, addition of AQP2-WT, AQP2-S256D and TM β 4 lead to the formation of short, crippled actin filaments of various widths (Figure 3.2D-F, Figure S3.2).

3.3.3: AQP2 C-terminal peptides inhibit formation of small actin oligomers

Actin polymerization can be divided into three phases: (i) a slow initial nucleation phase, (ii) a faster elongation phase and (iii) the equilibrium between polymerization and

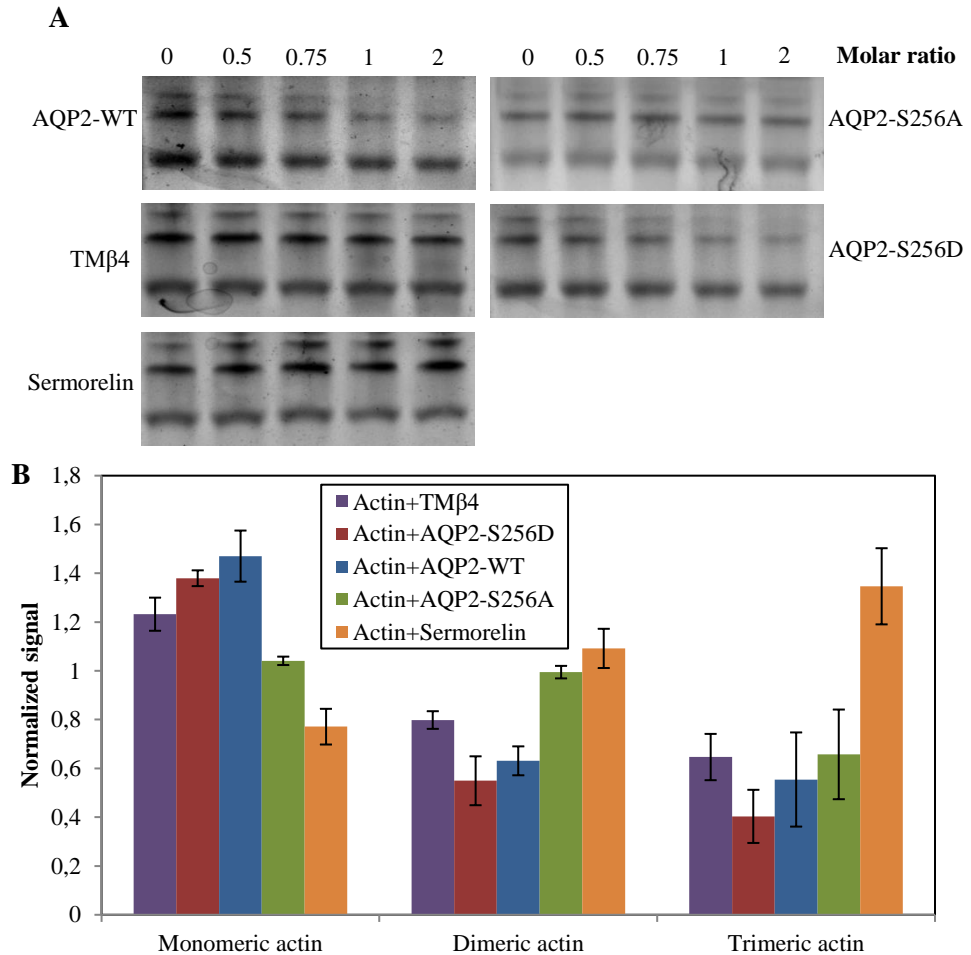


Figure 3.3: The effect of peptides on the formation of actin trimers. (A) Native gels of g-actin incubated with increasing molar ratios of different peptides (peptide:actin). (B) Quantified results of the signals measured at an peptide:actin molar ratio of 2 for mono-, di- and trimeric actin. Values are normalized to the signals measured for actin alone. Quantification is executed by using ImageJ. Normalized signal is mean \pm S.E. (TM β 4 N=4, AQP2-S256D N=3, AQP2-WT N=5, AQP2-S256A N=3, Sermorelin N=5).

depolymerization. The elongation phase begins after f-actin nuclei are formed. In 1982, Barden *et al.* postulated that an actin trimer is most likely the nucleus of the polymerization process (41), which was confirmed by a theoretical analysis (42). Native PAGE allows the presence of actin monomers and small oligomers to be demonstrated, even without initiating polymerization (Figure S3.3A) (43).

Table 3.3: Mean relative intensity measured for monomeric, dimeric and trimeric actin in the presence of peptides in a ratio of 2 (peptide:actin) on native PAGE. Intensity for each band was measured by using ImageJ and normalized against the corresponding signal for actin alone for each band. The relative intensity listed is the mean \pm S.E., the number of independent experiments are in brackets. A statistical analysis was performed by comparing the relative intensity for each peptide with the relative intensity measured for actin in the presence of AQP2-WT. The relative intensity of actin in the presence of AQP2-WT is compared to the relative intensity of actin alone. For statistical analysis a 2-tailed, unpaired *t*-test with Welch correction was used.

Peptide		Relative intensity	p
AQP2-WT	Monomeric actin	1.47 \pm 0.10	0.05 ^a
	Dimeric actin	0.63 \pm 0.06	0.02 ^b
	Trimeric actin	0.55 \pm 0.19 (N=5, S.E.)	0.05 ^c
AQP2-S256A	Monomeric actin	1.04 \pm 0.02	0.06 ^d
	Dimeric actin	0.99 \pm 0.03	0.01 ^e
	Trimeric actin	0.66 \pm 0.18 (N=3, S.E.)	0.72 ^f
AQP2-S256D	Monomeric actin	1.38 \pm 0.03	0.50 ^d
	Dimeric actin	0.55 \pm 0.10	0.53 ^e
	Trimeric actin	0.40 \pm 0.11 (N=3, S.E.)	0.54 ^f
TM β 4	Monomeric actin	1.23 \pm 0.07	0.13 ^d
	Dimeric actin	0.80 \pm 0.04	0.10 ^e
	Trimeric actin	0.65 \pm 0.09 (N=4, S.E.)	0.70 ^f
Sermorelin	Monomeric actin	0.77 \pm 0.07	0.01 ^d
	Dimeric actin	1.09 \pm 0.08	0.01 ^e
	Trimeric actin	1.34 \pm 0.16 (N=5, S.E.)	0.03 ^f

^a Compared to the relative intensity of monomeric actin in the absence of peptides

^b Compared to the relative intensity of dimeric actin in the absence of peptides

^c Compared to the relative intensity of trimeric actin in the absence of peptides

^d Compared to the relative intensity of monomeric actin in the presence of AQP2-WT

^e Compared to the relative intensity of dimeric actin in the presence of AQP2-WT

^f Compared to the relative intensity of trimeric actin in the presence of AQP2-WT

We studied the effect of peptides on these small actin oligomers that are thought to nucleate the f-actin assembly. On native PAGE, actin mono-, di- and trimers are distinct, while higher oligomers are sometimes visible as well (Figure 3.3A, Figure S3.3A). Addition of AQP2-WT lead to a significant decrease in trimeric and dimeric actin (Table 3.3) with increasing amounts of peptide (Figure 3.3A) and a relative increase of the monomeric actin signal (Figure 3.3B blue). A similar effect was observed after adding AQP2-S256D and TM β 4 (Figure 3.3A, -B red and purple respectively, Table 3.3). Addition of AQP2-S256A did not lead to major differences in actin monomers and dimers, while a significant decrease of actin trimers was evident (Figure 3.3A, -B green, Table 3.3). Addition of sermorelin did not lead to major differences visible on Native PAGE (Figure 3.3A), but quantification of the gel bands showed an increase in relative trimeric actin after addition of sermorelin and a decrease in relative monomeric actin (Figure 3.3B, orange). Quantification of Native PAGE (Figure 3.3B) indicates that AQP2 C-terminal peptides interfere with formation of small actin oligomers and could therefore inhibit f-actin assembly from the start. The same trend was visible for lower peptide:actin ratios (Figure S3.3C), however, addition of peptide to actin at a ratio of 0.5 did not lead to significant changes (Figure S3.3B).

3.3.4: Actin polymerization reaches equilibrium earlier in the presence of AQP2

Although Figures 3.1 and 3.2 demonstrate the inhibiting effect of AQP2 peptides on actin polymerization, an assessment of its kinetics in the presence of peptides could shed more light on AQP2-actin interactions. We therefore monitored actin polymerization by using pyrene labelled actin (pyrene-actin) (44,45). The fluorescence of pyrene-actin increases with increasing concentration of f-actin, allowing actin polymerization to be monitored (Figure 3.4A, grey line).

Addition of C-terminal AQP2 in a molar ratio (peptide:actin) of 2 did not affect the polymerization rate during the first 10 minutes after addition of polymerization buffer. The relative initial polymerization rate after addition of AQP2-WT, -S256D and -S256A was comparable to pyrene-actin alone (slopes in the first 10 minutes were $0.040\pm 0.002/\text{min.}$, $0.046\pm 0.005/\text{min.}$, $0.053\pm 0.006/\text{min.}$ and $0.049\pm 0.004/\text{min.}$, respectively) (Table 3.2). However, equilibrium was reached earlier in the presence of AQP2 peptides as compared to actin alone, typically after 30 minutes (Figure 3.4A-D). In the presence of AQP2-S256A a maximum relative fluorescence of 0.75 ± 0.04 was reached (Figure 3.4B), while in the presence of AQP2-WT and AQP2-S256D a maximum signal of 0.67 (± 0.03 and ± 0.02) was measured (Figure 3.4C and -D). The effect of the different AQP2 peptides on actin polymerization did not significantly differ (Table 3.2), suggesting that the AQP2 C-terminus inhibits f-actin formation independent of its phosphorylated state.

The measured maximum relative fluorescence for AQP2 peptides is comparable to the maximum relative fluorescence measured for actin incubated with TM β 4 at a molar ratio of 0.5 (peptide:actin), which reached an equilibrium at a relative fluorescence signal of 0.65 ± 0.01 after 50 minutes (Figure 3.4E open triangles, Table 3.2). However, the relative initial polymerization rate of actin in the presence of TM β 4 was significantly slower than

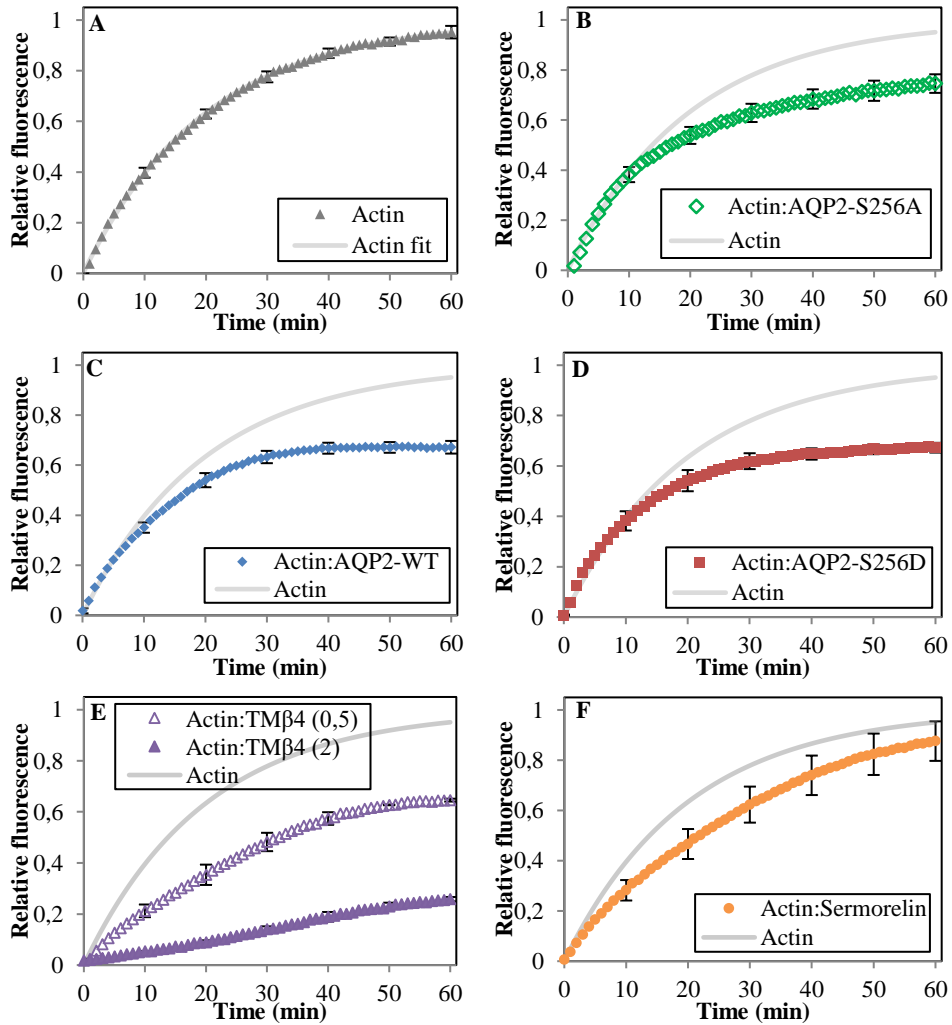


Figure 3.4: Pyrene actin polymerization inhibition assay. Pyrene actin polymerization was initiated in the absence of peptide (A; N=5) or in the presence of AQP2-S256A (B; N=7), AQP2-WT (C; N=9), AQP2-S256D (D; N=12), TM β 4 (E; N=3) or Sermorelin (F; N=6) in a molar ratio of 2 (peptide:actin). For TM β 4 polymerization assays of both a molar ratio of 0.5 and 2 (peptide:actin) are visualized. Fluorescent signals were normalized against the fluorescent signals obtained from actin alone. Relative fluorescence signals are means \pm S.E. (A) Curve is fit to $P(t) = (P_0 - P_\infty) * e^{-N(k_+)t} + P_\infty(45)$. Where $P(t)$ is the measured relative fluorescence at time point t , P_0 is the relative fluorescence measured at $t=0$, P_∞ is the relative fluorescence measured at $t=\infty$, N is the number of nuclei, k_+ is the elongation rate and t is the time in minutes. Fitted curve is visualized in grey (A-F).

actin in the presence of AQP2 peptides (Figure 3.4B, -C and -D) with a measured slope of $0.024\pm 0.001/\text{min}$. in the first 10 minutes (Table 3.2).

When actin was polymerized in the presence of sermorelin (molar ratio of 2; sermorelin:actin) the fluorescent signal increased more slowly than actin alone (a slope of $0.030\pm 0.004/\text{min}$, Table 3.2) and after 60 minutes the f-actin signal did not reach a plateau comparable to the other traces (Figure 3.4F). The maximum relative fluorescence measured was 0.88 ± 0.08 . This shows that the presence of sermorelin seems to slow down f-actin formation, but sermorelin does not prevent actin polymerization.

3.3.5: AQP2 C-terminal peptides do not sever f-actin

During transfer of AQP2 to the apical membrane, AQP2-bearing vesicles need to pass through the actin cortex before they can fuse with the apical membrane. It is therefore important that the cortex is remodelled to facilitate this passage. The results above show that less f-actin is formed in the presence of AQP2, however this effect would only be useful after the cortex barrier is already broken. One possibility could be that AQP2 is able to depolymerize f-actin. In order to test this, AQP2-peptides were added to pyrene labelled f-actin filaments and fluorescence was measured for 60 minutes (Figure 3.5). Addition of AQP2(-WT, -S256A, -S256D) peptides did not lead to any significant changes in measured fluorescence over the period of the experiment (Figure 3.5; blue, red and green, respectively). After addition of AQP2-WT ($t=60$ min) a slope of $0.0008\pm 0.0002/\text{min}$ was measured, as compared to a slope of $0.006\pm 0.0003/\text{min}$ for actin alone (Table 3.2). Addition of AQP2-S256A and AQP2-S256D showed similar results, with a measured slope of $0.0011\pm 0.0002/\text{min}$ and $0.0009\pm 0.0002/\text{min}$ respectively (Table 3.2). Similarly, addition of neither Tm β 4 nor sermorelin affected the pyrene fluorescence (Figure 5; purple and orange, respectively) (measured slopes were $0.0002\pm 0.0002/\text{min}$. and $0.0007\pm 0.0003/\text{min}$. respectively). This shows that neither C-terminal AQP2 peptides nor control peptides promote f-actin depolymerization.

3.3.6: Do AQP2 C-terminal peptides destabilize actin thin filaments?

The C-terminus of AQP2 is not able to depolymerise actin filaments, however AQP2 could play an indirect role in remodelling the actin cortex. Many different proteins stabilize actin filaments (46). Tropomyosin-5b (Tm5b), a coiled-coil protein binding along f-actin, stiffens these filaments and protects them against severing and depolymerization by gelsolin, cofilin, and DNase I, thus stabilizing f-actin in the form of thin filaments (47). It was previously reported that AQP2 binds to Tm5b (32) and that phosphorylated AQP2 can increase actin depolymerization in vesicle-free fractions of rat kidney papillae extracts by interacting with Tm5b (30). Although unphosphorylated AQP2 was shown to destabilize actin thin filaments to some extent, the effect was not as strong as with phosphorylated AQP2 (30). This suggests that the destabilizing effect of AQP2 on actin thin filaments depends on the phosphorylation state of the AQP2 C-terminus. Therefore, we explored the interaction of C-terminal AQP2 peptides with Tm5b stabilized f-actin in general actin buffer (GAB; 5 mM Tris-HCl pH 8.0,

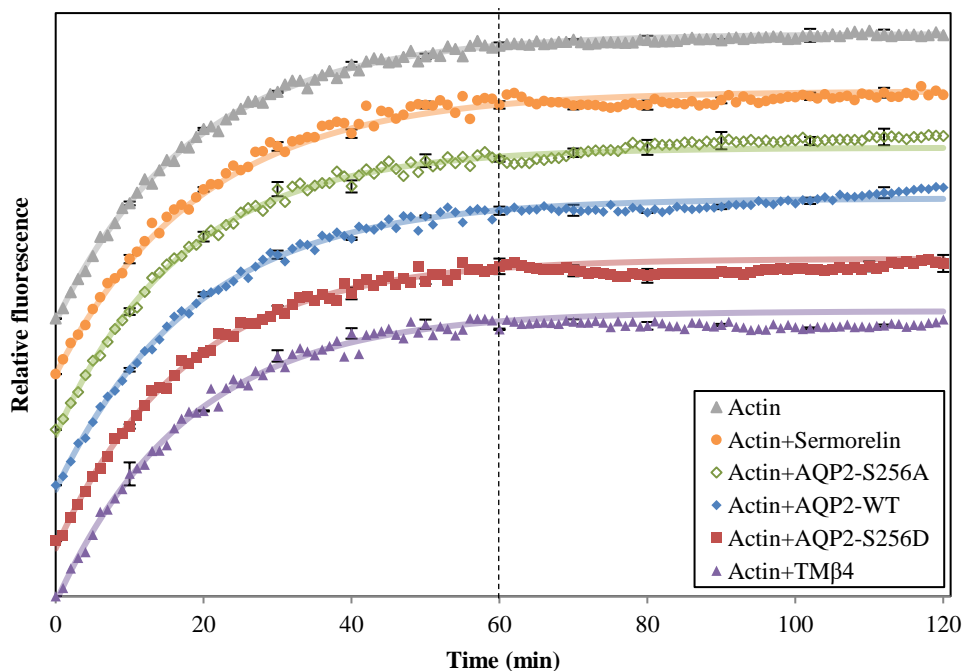


Figure 3.5: Pyrene actin depolymerization assay. Pyrene actin polymerization was initiated in the absence of peptide. At $t=60$ min actin polymerization reached equilibrium and peptides were added (dashed line) in a molar ratio of 2 (peptide:actin). For the first 60 min each experiment was fitted against equation 5 and normalized against the determined P_{∞} . The fits were extrapolated until $t=120$ min and visualized as a solid line. Relative fluorescence is the mean \pm S.E. ($N=3$ for each experiment).

0.2 mM CaCl_2 , 0.2 mM ATP). We initiated polymerization of pyrene-actin in the presence or absence of Tm5b (molar ratio 7:1; Actin:Tm5b (48)). As previously observed (49), addition of Tm5b to actin lead to a lower dissociation rate at the pointed end, resulting in a significantly higher fluorescence signal ($p=0.0006$) at $t=60$ min (1.15 ± 0.06) as compared to actin alone (1.00 ± 0.05).

After 60 min sermorelin, TM β 4, or AQP2(-WT, -S256A, -S256D) peptides dissolved in GAB were added to the filaments in a molar ratio of 2 (peptide:actin) (Figure 3.6, dashed vertical line), equal volumes of peptide-less GAB were added to the actin alone and actin with Tm5b samples. The polymerization curves, up to 60 min., were fitted against equation 5 (Experimental procedures), normalized, and extrapolated to assess the effect of added peptides. Figure 3.6 displays the characteristic filament behaviour of Tm5b stabilized actin filaments after addition of GAB (black open triangles), demonstrating that the pyrene signal continues to increase linearly as before GAB addition. Apparently, addition of buffer does not have an effect on Tm5b stabilized f-actin, in spite of g-actin dilution. The measured relative fluorescence follows the extrapolated trend, with a slope of $0.0052 \pm 0.0005/\text{min}$. In the absence of Tm5b, however, addition of GAB reduces the relative actin polymerization

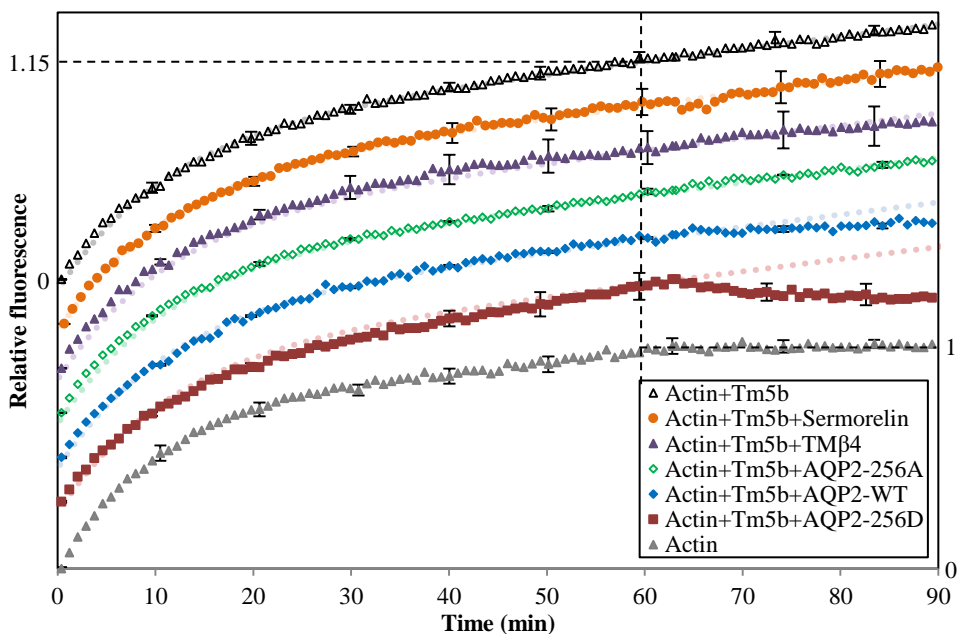


Figure 3.6: Pyrene actin polymerization and Tm5b interaction. Pyrene actin was incubated with Tm5b for 10 min in a molar ratio of 7 (actin:Tm5b) prior to polymerization was initiated ($t=0$ min). At $t=60$ min. peptides were added in a molar ratio of 2 (peptide:actin) (dashed line). For the first 60 min each experiment was fitted against equation 5 and normalized against the determined P_{∞} . The fits were extrapolated until $t=90$ min and visualized as a dotted line. Relative fluorescence is the mean \pm S.E. ($N=3$ for each experiment).

rate (Figure 3.6, grey triangles) causing a change in the slope to 0.0003 ± 0.0003 /min. (Table 3.2), because g-actin is diluted (50).

In the presence of Tm5b, addition of AQP2-S256A, TM β 4 or sermorelin, has no measurable influence on the actin polymerization rate (Figure 3.6; green open diamonds, purple triangles and orange circles, respectively) (Table 3.2). All three fluorescence signals compare well to that measured for Tm5b stabilized f-actin after GAB addition (Figure 3.6, black open triangles). Thus AQP2-S256A, TM β 4 or sermorelin peptides do not interact with Tm5b, keeping actin thin filaments intact. In contrast, addition of AQP2-S256D to Tm5b stabilized f-actin leads to a strong deviation from the extrapolated actin polymerization fit (Figure 3.6, red squares), the normalized fluorescence signal even shows a decrease with a measured slope of -0.0022 ± 0.0004 /min. (Table 3.2). As documented in Figure 3.5 (red squares) AQP2-S256D peptides do not destabilize f-actin filaments directly, suggesting that the effect of AQP2-S256D peptides on Tm5b stabilized actin thin filaments is caused by the interaction of AQP2-S256D with Tm5b. This confirms the previously observed strong interaction of S256 phosphorylated AQP2 with Tm5b (30,32).

AQP2-WT peptides had a weaker effect on the actin thin filaments than AQP2-S256D peptides. The normalized fluorescence signal increased less than the extrapolated signal after

peptide addition (Figure 3.6, blue diamonds) with a slope of $0.0027 \pm 0.0003/\text{min}$. (Table 3.2). This compares to the fluorescence of the actin alone sample (Figure 3.6, grey triangles) rather than to the results from Tm5b stabilized actin thin filaments (Figure 3.6, black open triangles). Therefore, AQP2-WT appears to interact with Tm5b as well, but to a lesser extent than AQP2-S256D, demonstrating the importance of the phosphorylation of residue S256.

3.3.7: Where do AQP2 C-terminal peptides bind to g-actin?

Detailed structural information on the interaction between actin and its regulator proteins has been obtained from X-ray crystallography (34). Many of these regulators bind to actin with a ~ 30 Å long α -helical segment that fits into the groove between actin subdomains one and three, i.e., at the barbed actin filament end. X-ray crystallography revealed that the C-terminus of AQP2 is a 38 Å long α -helix as well (PDB entry 4OJ2). To explore whether this C-terminal helix could interact specifically with actin, sequence alignments of the AQP2 C-terminus with actin binding helices were performed. Homology between the AQP2 C-terminus and different RPEL domains whose structures are available became evident (Figure 3.7A). The AQP2 C-terminus exhibits the non-canonical RPEL motive (RRxxxEL) that is found in some RPEL1 domains (51), but the top matches are with the RPEL2 domains of serum response factor cofactor MAL (PDB entry 2V52), and the phosphatase and actin regulator 1, Phactr1 (PDB entry 4B1X). Except for 4B1X all tested alignments with individual actin binding helices introduced either a much shorter sequence overlap than in the top scorers or a gap at the N-terminus of the ledge-binding helix, imposing constraints in model building. For 4B1X, sequence identity is observed for four out of six residues critical for the primary actin binding helix (Figure 3.7A, actin-1, 'o') (52). One of the three residues involved in ledge-binding helix/actin interactions is conserved (E258), while residue R252 shares strong similar properties with residue Q468 from 4B1X (Figure 3.7A, actin-2, 'o'). Figure 3.8 displays the predicted structure of the AQP2 C-terminus interacting with actin at the barbed end. Accordingly, the highly conserved arginine residue (R253) is inserted in the cleft between actin domains one and three, forming hydrogen bonds with the C-terminus of actin at residue F375 (Figure 3.8; right panel).

The other actin binding regulator family, the WASP proteins, exhibit the α -helical WH2 domain that binds at the same location as the RPEL domain but in an antiparallel orientation (35). Therefore, the C-terminal AQP2 sequence was aligned to a set of C \rightarrow N arranged WH2 domain sequences. Again, some sequence homology was found, and the best score obtained with PDB entry 2D1K exhibited 64% sequence identity or similarity in the actin cleft region (Figure 3.7B), but the ledge-binding helix is missing. Altogether this suggests that the AQP2 C-terminus is likely to interact with the barbed end of actin.

3.3.8: The influence of AQP2 R253 and R254 on f-actin formation and stability

Figures 7A and 8 indicate that one important actin interacting arginine residue is either R253 or R254. To explore the influence of these arginine residues on actin polymerization inhibition, two peptides were synthesized (AQP2-R253A and AQP2-R253A-R254A) (Table

A) Alignment of RPEL actin binding helices & AQP2

```

AQP2          --PDTWEEREVRRRQSV-ELHSPQSLPRGT
2V51_F        -SERKNVLQLKLQQRRTREELVVSQGIM---- RPEL1
2V52_M        -ARTEDYLKRKIRSRPERAELVVMHIL---- RPEL2
4B1U_M        -KHTSAALERKISMRQSREELIKRGVL---- RPELN
4B1X_M        -QQIGTKLTRRLSQRPPTAEELERQFNIL---- RPEL2
4B1Y_M        -REIKRRLTRKLSQRPTVEELRERKIL---- RPEL3
4B1Z_M        KVCRCDSLAIKLSNRPSKRELEEKNIL---- RPEL1
                . : * ** :

```

```

AQP2          --PDTWEEREVRRRQS-VELHSPQSLPR
2V52_M        -ARTEDYLKRKIRSRPERAELVVMHIL-- RPEL2
                *: :*: * * . **. : *

```

```

AQP2          --PDTWEEREVRRRQSVELHSPQSLPR
4B1X_M        QQIGTKLTRRLSQRPPTAEELERQFNIL-- RPEL2
                .* . * : * : ** . : *
actin-1       o o o o o
actin-2       o o o

```

B) Alignment of WH2 actin binding helices (C→N) & AQP2

```

AQP2          WEEREVRRRQSVELHSPQ
2D1K_C        --KLKVGRRIANLMDEGQ
2A41_C        --KLKKGKSIDSLLANRG
3M1F_V        ASKLKVGQRIQEMLKSH-
2A3Z_C        -KNLQIGQRIQDLLAGR-
2VCP_D        -SKLQIGQRIQDLLADR-
3M3N_W        -KKLQIGQRIQDLLADR-
2A40_C        --RLQFGQRIASLLDSRA
                . : : :

```

```

AQP2          WEEREVRRRQSVELHSPQ
2D1K_C        --KLKVGRRIANLMDEGQ
                : :* ** : :.. *

```

Figure 3.7. (A) Sequence alignments of six actin binding RPEL domains with known structures against the C-terminus of AQP2. The only gap-free match found was for PDB entry 4B1X. Actin cleft and ledge helices are indicated by horizontal lines. (B) Alignments against WH2 domains produced good overlap and small gaps only for the short segment corresponding to the actin cleft binding domain. A good match was obtained for PDB entry 2D1K_C. The actin cleft helix is indicated by a horizontal line. Asterisks (*) indicate a conserved residue, colons (:) indicate conservation between groups of strongly similar properties and periods (.) mark conservation between groups of weakly similar properties. Sequence alignments were executed by using Clustal Omega (www.ebi.ac.uk/Tools/msa/clustalo/) (53).

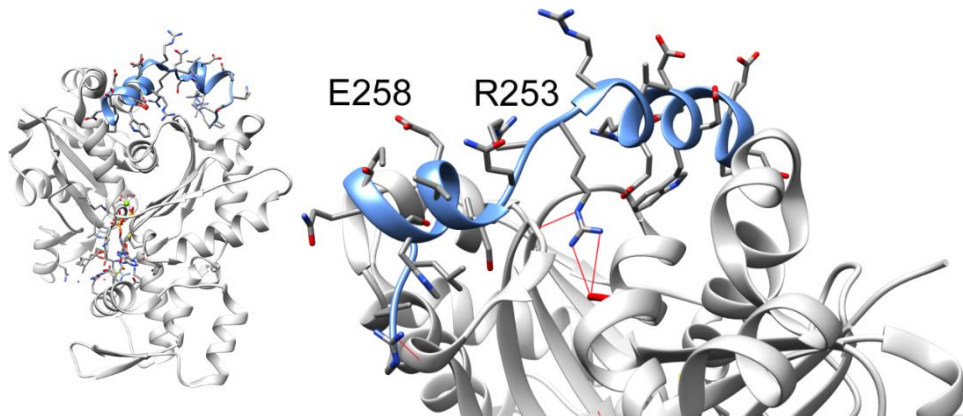


Figure 3.8. Predicted structure of the C-terminus of AQP2 (bright blue) interacting with g-actin (light grey). The C-terminal AQP2 structure was built using COOT (54) based on sequence homology with PDB entry 4B1X. As the left panel illustrates, the AQP2 C-terminal helix fits into the barbed end actin groove. The conserved arginine residue (right panel; R253) reaches into the actin cleft to engage in hydrogen bonds with actin's C-terminal F375 (red). The conserved glutamate (right panel; E258) may be involved in secondary actin contacts.

3.1), and their effect on actin polymerization dynamics was measured. Pyrene actin was polymerized in the presence of either peptide in a molar ratio of 2 (peptide:actin) and the increase in fluorescence over time was monitored (Figure 3.9A and -B). Initial relative actin polymerization rates in the presence of either AQP2-R253A ($0.041 \pm 0.005/\text{min.}$) or AQP2-R253A-R254A ($0.042 \pm 0.004/\text{min.}$) were similar to AQP2-WT ($0.040 \pm 0.002/\text{min.}$), (Table 3.4). However, actin in the presence of AQP2-WT reaches equilibrium after 30 min. with a maximum relative fluorescence of 0.67 ± 0.03 (Figure 3.4C), while actin in the presence of either AQP2-R253A or AQP2-R253A-R254A did not reach equilibrium within 50 min. (Figure 3.9A and -B). The maximum relative fluorescence measured for actin in the presence of AQP2-R253A was 0.82 ± 0.03 , which was significantly higher compared to actin in the presence of AQP2-WT ($p=0.002$) (Figure 3.9A, Table 3.4). Actin in the presence of AQP2-R253A-R254A also showed a significantly higher relative maximum fluorescence as compared to AQP2-WT, reaching a value of 0.91 ± 0.02 at $t=60$ min. ($p<0.001$) (Figure 3.9B, Table 3.4). These results suggest that residues R253 and R254 indeed play a major role in the interaction of AQP2 with actin.

Destabilization of actin thin filaments by AQP2-S256p fosters f-actin depolymerization, and thus promotes opening of the cortex. We therefore tested the effect of Arg253 and Arg254 mutations on the interactions of the AQP2-terminus with Tm5b. To this end, two peptides were synthesized, AQP2-R253A-S256D and AQP2-R254A-S256D (Table 3.1), representing the phosphorylated state of Ser256 and a mutation in one of the important arginine residues. Pyrene-actin was polymerized in the presence of Tm5b and in the absence of AQP2 C-

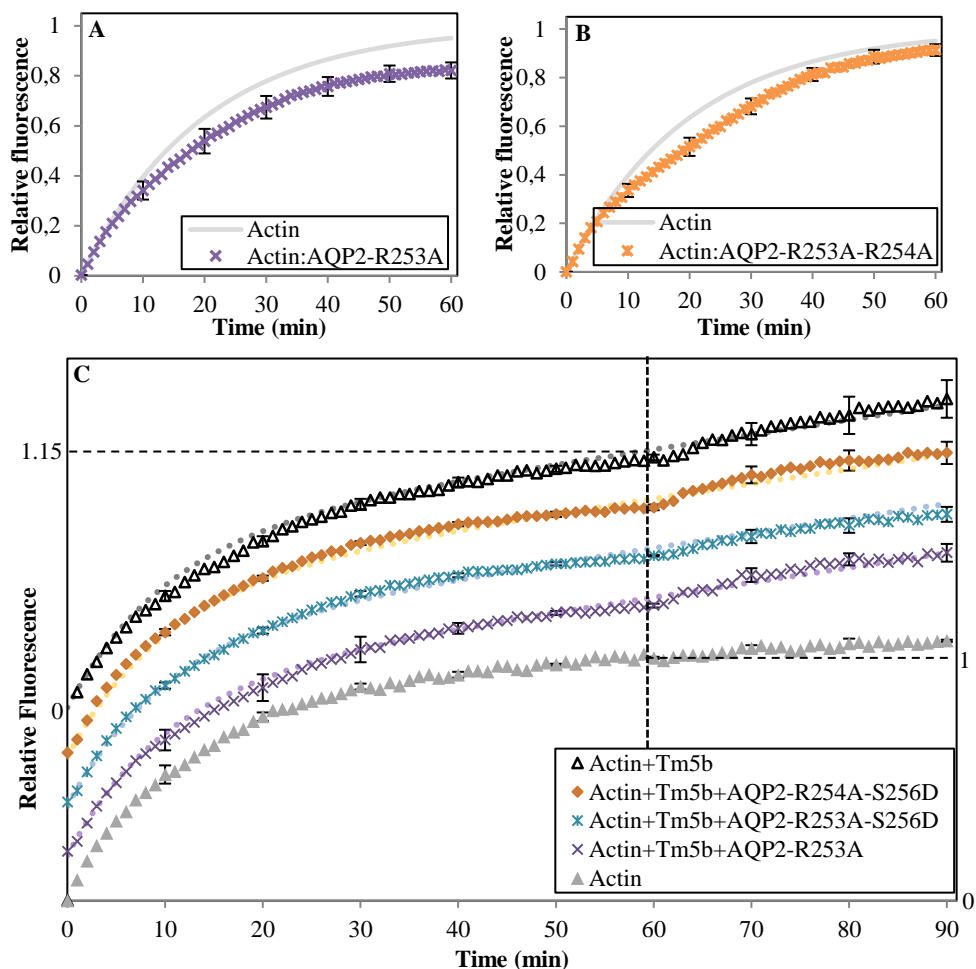


Figure 3.9. (A,B) Pyrene actin polymerization inhibition assay. Pyrene actin polymerization was initiated in the absence of peptide (grey line) or in the presence of AQP2-R253A (A; N=9) or in the presence of AQP2-R253A-R254A (B; N=8) in a molar ratio of 2 (peptide:actin). The fluorescent signal of actin alone was fit to equation 1, $P(t)=(P_0-P_\infty)*e^{-N(k^+)t}+P_\infty$ (45). Fluorescent signals were normalized against P_∞ determined for actin alone. Relative fluorescent signals are means \pm S.E. (C) Pyrene actin polymerization and Tm5b interaction assay. Pyrene actin was incubated with Tm5b for 10 min. in a molar ratio of 7 (actin:Tm5b) prior to polymerization was initiated ($t=0$ min.). At $t=60$ min. peptides were added in a molar ratio of 2 (peptide:actin) (dashed line). The average relative fluorescent signal measured during polymerization of actin in the presence of Tm5b was fitted against equation 5 and normalized against the determined P_∞ . The fit was extrapolated until $t=90$ min. and visualized as a dotted line. The same was done for the average relative fluorescence measured for actin alone. Relative fluorescence is the mean \pm S.E. (N=3 for each experiment).

Table 3.4. Statistical analysis of pyrene actin polymerization assays in the presence of AQP2-WT, AQP2-R253A and AQP2-R253A-R254A. Values listed are means \pm S.E., the number of independent experiments are in brackets. For the statistical analysis a 2-tailed, unpaired *t*-test with Welch correction was used.

Peptide	Relative fluorescence (t=60 min.) ^a	p	Slope at t=0 min ^b	p	Peptide	Slope at t=60 min ^f	p
Actin	1.00 \pm 0.02 (N=5, S.E.)		0.049 \pm 0.004 (N=5, S.E.)		Actin	0.0003 \pm 0.0003 (N=3, S.E.)	0.0002 ^g
AQP2-WT	0.67 \pm 0.03 (N=9, S.E.)	0.04 ^c	0.040 \pm 0.002 (N=9, S.E.)	0.08 ^e	AQP2-S256D	-0.0022 \pm 0.0004 (N=3, S.E.)	0.0006 ^g
AQP2-R253A	0.82 \pm 0.03 (N=8, S.E.)	0.002 ^d 0.54 ^c	0.041 \pm 0.006 (N=8, S.E.)	0.91 ^d 0.23 ^c	AQP2-R253A	0.0055 \pm 0.0010 (N=3, S.E.)	0.95 ^g
AQP2-R253A-R254A	0.91 \pm 0.02 (N=9, S.E.)	<0.0001 ^d 0.67 ^c	0.042 \pm 0.005 (N=9, S.E.)	0.71 ^d 0.15 ^c	AQP2-R253A-R256D	0.0051 \pm 0.0006 (N=3, S.E.)	0.51 ^g
Sermorelin	0.88 \pm 0.08 (N=6, S.E.)		0.032 \pm 0.005 (N=6, S.E.)	0.17 ^d 0.02 ^e	AQP2-R254A-R256D	0.0058 \pm 0.0007 (N=3, S.E.)	0.71 ^g

^a Actin polymerization was monitored by the fluorescence of pyrene-labelled actin. For each experiment actin alone and actin in the presence of peptide were measured and compared. Normalized fluorescence values after 60 min are listed (Figure 9A, -B)(Figure 4C, -E). All values are determined in a molar ratio of 2 (peptide:actin).

^b Initial polymerization rates were determined by linear regression of averaged normalized fluorescence signal between t=0 min and t=5 min (Figure 9A, -B)(Figure 4C, -E).

^c Compared to sermorelin

^d Compared to AQP2-WT

^e Compared to actin alone

^f Polymerization rates were determined by linear regression of averaged normalized fluorescence signal after addition of peptides (or buffer) to actin (molar ratio of 2; peptide:actin) polymerized in the presence of tropomyosin-5b between t=60 min and t=90 min (Figure 9C), linear regression of actin in the presence of Tm5b was 0.0055 \pm 0.0003 (N=3, S.E.).

^g Compared to Actin+Tm5b

terminal peptides. After $t=60$ min. either GAB or one of the AQP2 C-terminal peptides dissolved in GAB was added, and the pyrene-actin fluorescence was monitored (Figure 3.9C). As observed before, actin in the presence of Tm5b does not reach complete equilibrium within 60 min. and the fluorescence increases after the addition of GAB at $t=60$ min. following the extrapolated trend indicated by the dotted line (Figure 3.9C, black open triangles). Actin alone and actin in the presence of Tm5b exhibited similar pyrene fluorescence as before (Figure 3.6; Figure 3.9C, grey triangles and black open triangles, respectively). Addition of AQP2-R253A did not lead to a statistically significant deviation from the proposed trend (Figure 3.9C, purple crosses, Table 3.4), similar to that previously observed AQP2-S256D (Figure 3.6, red squares); indicating that mutation R253A diminishes the propensity of AQP2 to interact with Tm5b. These interactions could not be saved by S256 phosphorylation, since both AQP2-R253A-S256D and AQP2-R254A-S256D showed the same trend as for actin thin filaments in the absence of AQP2 C-terminal peptides (Figure 3.9C, blue crosses and orange diamonds, respectively, Table 3.4).

3.3.9: Arginine mutants inhibit AQP2 exocytosis in vivo

Mutations in AQP2 Arg253 and Arg254 may diminish the propensity of AQP2 to open up the actin cortex by destabilizing actin thin filaments. Opening the actin cortex is an important step in AQP2 apical membrane fusion and a loss in this function should lead to retention of AQP2 in internal vesicles. We tested the effect of Arg253 and Arg254 mutations on AQP2 exocytosis *in vivo*. AQP2 fusion to the apical membrane was measured in polarized MDCK cells transfected with either an *aqp2-wt* gene or an *aqp2-R253A-R254A* gene. AQP2 exocytosis was initiated by addition of forskolin to the basolateral membrane, a selective activator of adenylate cyclases. AQP2 apical membrane expression was measured by biotinylation of accumulated AQP2 and compared to the total AQP2 in the cell. Forskolin stimulation of the MDCK cells lead to a significant increase in biotinylated AQP2 (relative to total AQP2) in AQP2-WT cells. However, forskolin had no significant effect on biotinylated AQP2 levels in AQP2-R253A-R254A expressing cells (Figure 3.10A, -B). These observations were confirmed using immunofluorescence, with forskolin stimulation resulting in accumulation of AQP2 in the apical membrane in cells expressing AQP2-WT, whereas a more subapical, diffuse staining is visible in the cells expressing AQP2-R253A-R254A (Figure 3.10C). These results confirm an important role of these arginine residues in AQP2 apical membrane accumulation.

3.3.10: Arginine mutants can be phosphorylated by PKA

PKA can phosphorylate AQP2 at residue Ser256, inducing transport of AQP2 to the apical membrane (17,18). However, the potential PKA consensus sequence (XRRXSX or XKKXSX) may be disrupted by mutations at residue 253 and 254, suggesting that AQP2-R253A-R254A subapical retention after forskolin stimulation is caused by a lack of Ser256 phosphorylation instead of the reduced effect on actin cortex remodelling. To assess whether AQP2 arginine mutants can be phosphorylated by PKA, different AQP2 peptides were

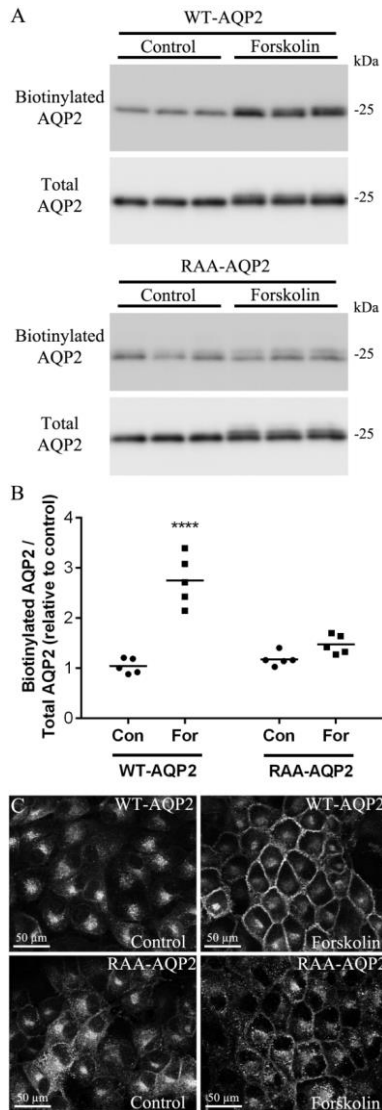


Figure 3.10. Effect of arginine mutations on membrane accumulation of AQP2. AQP2-WT and AQP2-R253A-R254A are both stably expressed in MDCK cells. (A, B) Biotinylation assay of AQP2 accumulated in the apical membrane. (A) Western blot analysis of biotinylated AQP2 compared to total AQP2 in the cell without (control) and with forskolin stimulation. Forskolin stimulation lead to a strong increase in biotinylated AQP2-WT as compared to the control cells, while total levels of AQP2 stayed relatively constant. Forskolin stimulation did not induce a strong increase in biotinylated AQP2-R253A-R254A as compared to control cells. (B) Quantification of the biotinylation assays. (C) Immunofluorescence assay of MDCK cells stably expressing AQP2-WT or AQP2-R253A-R254A, with or without forskolin stimulation. Forskolin stimulation led to an accumulation of AQP2-WT in the plasma membrane, while AQP2-R253A-R254A locates predominantly intracellular.

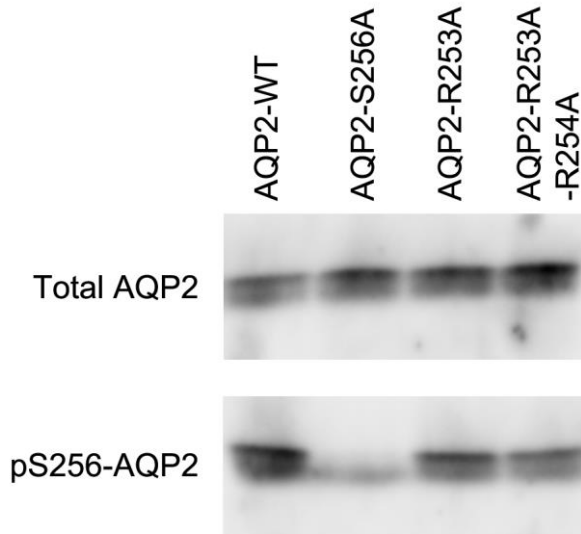


Figure 3.11: PKA can phosphorylate AQP2 at Ser 256 *in vitro* despite mutation of Arg253 and Arg 254. *In vitro* phosphorylation assays were performed on various AQP2 peptides (see methods) and the degree of AQP2 phosphorylation at Ser256 assessed using a phospho-specific antibody. Apart from a peptide mutated at Ser256, all peptides could be phosphorylated to various degrees *in vitro* by PKA.

phosphorylated by PKA *in vitro*. Ser256 phosphorylation was addressed by using a phospho-specific antibody, while AQP2-S256A was used as a negative control. PKA enhanced Ser256 phosphorylation in all AQP2 arginine mutants, although the extent was less than AQP2-WT (Figure 3.11). These results show that AQP2-R253A-R254A subapical retention was, at least in part, due to decreased interaction of AQP2 with Tm5b and actin.

3.4: Discussion

Actin filaments form a dynamic network near the apical membrane, the actin cortex, providing stability to the cell but also preventing vesicles from reaching the membrane. This dense meshwork of thin filaments has openings smaller than the dimensions of AQP2-bearing vesicles, ranging between 41 nm and 230 nm depending on the cell-type (55-57). Therefore, this barrier needs to be broken before AQP2 vesicles can fuse with the apical membrane.

Although AQP2 trafficking and actin cortex remodelling has been extensively studied, the direct link between AQP2 and actin dynamics still needed to be resolved. Here we show for the first time that the C-terminal helix of AQP2 is able to inhibit actin polymerization (Figures 3.1, 3.2C-E and 3.4B-D). Addition of AQP2-WT and AQP2-S256D C-terminal peptides in a molar ratio of 2 (peptide:actin) reduced actin polymerization to a degree similar to TM β 4 at a molar ratio of 0.5 (peptide:actin). Unexpectedly, the actin polymerization dynamics were quite different (Figure 3.4B-E).

Actin polymerization has been modelled before (58) and is described in equation 1 (Material & Methods). The polymerization rate depends on the amount of actin nuclei (N), the product

of association rate (k_5) and concentration of assembly competent g-actin (A_1), and the dissociation rate (k_6). Blue native gel electrophoresis revealed a decrease of actin trimers, the putative nuclei of actin polymerization (41), after addition of TM β 4 or AQP2 peptides to actin (Figure 3.3). According to equation 1, a decrease in the actin nuclei concentration should induce a decrease in the actin polymerization rate, which is indeed observed after addition of TM β 4 (Figure 3.4E). In stark contrast, polymerization rates were equal to, or even higher in the presence of AQP2 peptides than polymerization rates of g-actin alone immediately after initiating polymerization, although these peptides reduced actin trimer formation even more than TM β 4 (Figure 3.3 and Figure S3.3).

Actin polymerization kinetics in the presence of C-terminal AQP2 are comparable to those observed in the presence of gelsolin (59,60). Gelsolin is a multifunctional actin regulator involved in cell motility, in signal transduction into cytoskeletal dynamics, and in apoptosis (61). Micromolar calcium promotes gelsolin to sever actin filaments, and cap their fast-growing barbed ends. Under depolymerizing conditions gelsolin-capped f-actin filaments disassemble by subunit loss from the pointed ends, whereas under polymerizing conditions, gelsolin exhibits calcium-dependent actin nucleating activity, stimulating actin filament assembly at the pointed ends. Actin nucleation by gelsolin is a two step process. The first, relatively slow step is the binding of gelsolin to one monomeric actin resulting in the GA-complex. The second step produces the GA₂-complex and is 1,000 times faster (62). The GA₂-complex is the actin nucleus, from which actin can rapidly polymerize (63).

Addition of C-terminal AQP2 peptides to g-actin in GAB resulted in a decrease in actin trimers and an increase in actin monomers (Figure 3.3B). The rapid initial f-actin assembly upon addition of 10x polymerization buffer to g-actin incubated with AQP2 peptides at close to equimolar ratios may suggest that the peptide:actin complex acts as a seed for actin polymerization. If AQP2 peptides bind at the barbed filament ends as suggested by sequence comparisons (Figure 3.7), the low association rate at the pointed end would explain the lower f-actin concentration at equilibrium with AQP2 peptides than without (Figure 3.4A-D). Actin filaments formed in the presence of gelsolin are short and crippled (64), comparable to filaments formed in the presence of C-terminal AQP2 (Figure 3.2C-E). Nevertheless, gelsolin is an 82 kDa protein, carrying multiple domains that can interact with actin monomers, while C-terminal AQP2 peptides have a molecular weight of approximately 3 kDa (Table 3.1).

The structural model of a g-actin:AQP2-WT complex (Figure 3.8) supports the conclusion from sequence alignments (Figure 3.7) that the AQP2 C-terminal helix is likely to bind in the hydrophobic cleft of the barbed actin end. While both RPEL and WH2 domains exhibit an actin cleft-binding helix with a conserved C- (or N-) terminal arginine that interacts with the actin C-terminal carboxyl (F375), only RPEL domains have in addition a ledge-binding helix. The latter has been found to provide a secondary actin binding interface thereby promoting the formation of actin oligomers (52). Four AQP2 residues are identical to residues involved in the primary actin binding interface of the RPEL domain (Figure 3.7A): The arginine (Arg253) interacting with actin's C-terminal carboxyl, and residues Arg249, Leu259, and Leu265. They position the AQP2 C-terminal peptide in the barbed end cleft such that Glu258

is at the same location as Glu474 of the RPEL domain in 4B1X (Figure 3.8). Glu474 has been identified as one of the two ledge helix residues that form secondary actin contacts (52). The third residue of the secondary actin interface is Gln468 located in the linker region between the cleft and the ledge helix, which corresponds to Arg252 in AQP2 (Figure 3.7A). Taken together, we hypothesize that this interface formed by bound AQP2 C-terminal peptide promotes f-actin seed formation upon addition of polymerization buffer.

Noda et al (30) suggested that the destabilizing effect of AQP2 on actin thin filaments is regulated by the phosphorylation state of the AQP2 C-terminus. We observed that AQP2 is able to inhibit actin polymerization, but that addition of C-terminal AQP2 to f-actin does not lead to actin depolymerization (Figure 3.5), documenting that AQP2 is not able to remodel the actin cortex in a direct manner. As previously demonstrated, AQP2-S256p is able to interact with Tm5b, destabilising actin filaments (30,32). Addition of the C-terminal peptide AQP2-S256D to Tm5b stabilized pyrene-actin filaments did lead to a decrease in relative fluorescence (Figure 3.6), confirming that the C-terminus of AQP2 is able to destabilize actin thin filaments once residue 256 is phosphorylated.

AQP2 residue Arg254 has been linked to the dominant form of nephrogenic diabetes insipidus (NDI) (65-67), a disease resulting in production of excessive volumes of dilute urine. Mutations R254L, R254Q, and R254W have all been found in patients suffering from this disease, and in vitro expression of these mutants resulted in AQP2 remaining in intracellular vesicles even after forskolin stimulation (65-67). These mutations disrupt the PKA consensus sequence (XRRXSX or XKKXSX) in the AQP2 C-terminal tail, leading to decreased Ser256 phosphorylation, thus originally providing a straightforward interpretation of these phenotypes. Early oocyte experiments showed that AQP2-S256D alone induced an osmotic water permeability (Pf) of 60 $\mu\text{m/s}$ compared to AQP2-S256A alone (7 $\mu\text{m/s}$), because AQP2-S256A mainly remained in internal membranes. At least a 3:1 ratio of AQP2-S256D/AQP2-S256A was necessary for a prominent localization of AQP2 in the plasma membrane (21). The dominant nature of mutations that inhibit phosphorylation of Ser256 is therefore explained by hetero-oligomerization of AQP2-WT with AQP2 mutants, and the stringent requirement of four phosphorylated Ser256 for transportation to the plasma membrane. Results from similar experiments with AQP2-R254L showed AQP2-WT to reach Pf=130 $\mu\text{m/s}$ compared to AQP2-R254L with Pf=60 $\mu\text{m/s}$ under identical conditions (65), whereas AQP2-R254Q unexpectedly induced only a low Pf comparable to AQP2-256A (66). A base signal of phosphorylated Ser256 was measured for all three mutants expressed in MDCK cells, but this signal did not increase after forskolin stimulation (65-67). Accordingly, trafficking of AQP2 was impaired: R254L and R254Q were mainly found in early endosomes (65,66), while Dollerup *et al* (67) showed that AQP2-R254W is not in late endosomes. Trafficking could be induced by introducing S256D: both the AQP2-R254L-256D and AQP2-R254Q-256D were found in apical membranes of MDCK cells (65,66). This strongly suggests that the interaction with the subapical actin cortex is not impaired and supports our model in which R253 binds to the actin carboxy-terminus buried in the cleft between the actin domains one and three (Figure 3.8).

Although autosomal dominant mutations of Arg-254 appear to be primarily related to disruption of the PKA consensus sequence (65-67), phosphorylation of S256 by PKA is observed *in vitro* even when the PKA site is disrupted (Figure 3.11). We have measured the interaction of AQP2 C-terminal peptides mutated at locations R253 and R254, to explore whether a mutation of either R253 or R254 leads to a decreased inhibition of actin polymerization and decreased AQP2-Tm5b interaction. Neither the peptide AQP2-R253A (Figure 3.9A) nor AQP2-R253A-R254A (Figure 3.9B) hindered actin polymerisation to the same extent as AQP-WT (Figure 3.4C) and AQP-S256D (Figure 3.4D). Furthermore, mimicking the S256 phosphorylation was insufficient to induce a significant interaction of peptides AQP2-R253A-S256D and R254A-S256D with actin thin filaments, as documented in Figure 3.9C and Table 3.4. Our data show that AQP2-R253A-R254A predominantly resides in the subapical region of MDCK cells, even after forskolin stimulation (Figure 3.10). The wide variety in AQP2-R254L-S256D localization (65) may implicate that this mutation hinders actin cortex remodelling leading to AQP2 trafficking to other membranes, complementary to our findings for AQP2-R254A-S256D (Figure 3.9C). Further research is necessary to visualize the importance of AQP2-Tm5b interactions in AQP2 exocytosis *in vivo*.

Cells harbour a wide variety of actin binding proteins that control actin remodelling (34). Rho GTPases are molecular switches that activate actin nucleators WASP/WAVE and formins. Located at the plasma membrane as a result of post-translational prenylation or palmitoylation RhoGTPases are key to actin cortex assembly (68). Therefore, AVP induced cAMP-signalling leads not only to phosphorylation of the AQP2 C-terminus, but also to RhoA inhibition through Rho phosphorylation, an essential event in AQP2 translocation (28). An array of actin binders promotes actin disassembly, gelsolin being an abundant and well-studied example (61). Because tropomyosin stabilizes actin thin filaments, and is remarkably effective in transforming gelsolin-actin complexes into long filaments (69), actin cortex disassembly is inhibited unless tropomyosin is sequestered. Thus, we propose that AQP2 exocytosis initiated by phosphorylation of the master switch S256, and the inactivation of RhoA, evolves in four steps: (i) translocation of AQP2 bearing vesicles to the sub-apical space, (ii) binding of the phosphorylated AQP2 C-termini S256-p to tropomyosin, (iii) local disassembly of the destabilized cortex by the cell's f-actin severing proteins, and (iv) vesicle fusion with the apical membrane. The fact that RhoA inactivation is essential for AQP2 translocation underlines the necessity to maintain openings in the cortex until exocytosis is completed. The actin polymerization inhibiting property of the AQP2 terminus reported here ensures that vesicles have an open path to the apical membrane. The unexpected gelsolin-like property of AQP2 C-terminal peptides may be of functional importance once the fusion process is completed and new cortex needs to be formed.

3.5: Materials and Methods

Peptides-Synthesized C-terminal AQP2 peptides were ordered from Peptide 2.0. (Peptide 2.0 inc., Chantilly, VA). The peptide sequence started at residue D245 and ended at residue G268 (AQP2-WT; DWEEREVRRR QSVELHSPQS LPRG) resulting in a peptide with molecular weight of 2946 Da. A longer peptide starting at residue F224 (AQP2-WT long; FPPAKLSLSEK LAVLKGLEPD TDWEEREVRR RQSVELHSPQ SLPRG) was synthesized at 99% purity by Genscript. An S256 phosphorylation mimicking mutant was synthesized by changing residue S256 into an aspartic acid (AQP2-S256D; DWEEREVRRR QDVELHSPQS LPRG) and an S256 dephosphorylated mutant was synthesized by changing residue S256 into an alanine (AQP2-S256A; DWEEREVRRR QAVELHSPQS LPRG). Important arginine residues were mutated into alanines to inhibit the proposed AQP2-actin interactions (AQP2-R253A; DWEEREVRAR QSVELHSPQS LPRG) (AQP2-R253A-R254A; DWEEREVRAA QSVELHSPQS LPRG). A Ser256 phosphorylation mimic for both Arg253 mutated AQP2 (AQP2-R253A-S256D; DWEEREVRAR QDVELHSPQS LPRG) and Arg254 mutated AQP2 (AQP2-R254A-S256D; DWEEREVRAA QDVELHSPQS LPRG) were synthesized. Thymosin- β -4 (TM β 4) and sermorelin were both purchased from DRS labs (DRS labs online UK).

Actin polymerization sedimentation assay-Lyophilized rabbit skeletal muscle g-actin (Tebu-bio, Cytoskeleton inc. Davis, Ca) was resuspended in general actin buffer (GAB; 5 mM Tris-HCl pH 8.0, 0.2 mM CaCl₂, 0.2 mM ATP) to a final concentration of 200 μ g/mL and incubated for 1 hr at 4°C. g-actin was incubated for 10 min at room temperature (RT) with AQP2-WT, -S256A, -S256D, TM β 4 or sermorelin in a molar ratio (peptide:actin) of 0.5, 0.75, 1 and 2. Polymerization was initiated by adding 10x polymerization buffer (500 mM KCl, 20 mM MgCl₂, 10 mM ATP). Samples were incubated for 1 hr at RT followed by pelleting of the f-actin by centrifugation at 100,000 g for 1 hr at 4°C (Beckman Coulter Optima L-90K ultracentrifuge). Supernatant was harvested and protein concentration was measured via BCA following the manufacturer's protocol (Pierce™ BCA Protein Assay Kit). Protein concentrations were normalized against the total protein concentration at the start (actin+peptide) and corrected for residual g-actin in the actin alone samples (the polymerization incompetent fraction). Both supernatant and pellet were loaded on 15% SDS-gels, stained with staining buffer (0.1% Coomassie R250, 10% HAc, 40% EtOH) for 30 min. and destained with destaining solution (7.5% HAc, 15% EtOH). Signal intensity of each lane was measured by using ImageJ (70) and normalized against the control signal (polymerized actin without added peptide).

Negative Stain Transmission Electron Microscopy (TEM)-Pelleted f-actin was dissolved in 200 μ L GAB and adsorbed to carbon-coated copper TEM-grids rendered hydrophilic by glow discharge in air at low pressure, washed 3 times in distilled water and negatively stained with 2% Uranyl acetate. 400 mesh TEM-copper grids were purchased

from Electron Microscopy Sciences and coated with an 8 nm thick carbon film produced in a Cressington 208 carbon coater where the thickness was measured by using a Jeol FC-TM10 thickness monitor. Grids were examined with a Philips CM200 transmission electron microscope at 200 kV accelerating voltage and images were recorded with a Tietz f416 CCD camera.

Native PAGE-Lyophilized rabbit skeletal muscle actin (Tebu-bio, Cytoskeleton inc. Davis, Ca) was resuspended in GAB and incubated as described above. 2 μ g of g-actin was incubated with peptides (TM β 4, sermorelin, AQP2-WT, -S256A, -S256D) in a molar ratio (peptide:actin) of 0.5, 0.75, 1 and 2. Samples were for 10 min at RT. 5 μ L of sample buffer (50% glycerol, bromo-phenol blue) was added to load the sample on a 12% Native PAGE (Tris pH 8.8 lower gel, Tris pH 6.8 upper gel, no SDS) and electrophoresed for 60 min at 180 V (71). Gels were then stained with staining buffer (0.1% Coomassie R250, 10% HAc, 40% EtOH) for 30 min and incubated for 30 min with destaining solution (7.5% HAc, 15% EtOH) followed by destaining with water over night (O/N). Signal intensity of each lane was measured using ImageJ (70) and normalized against the control signal (monomeric, dimeric, trimeric actin; no peptides).

Pyrene actin polymerization assay-Lyophilized pyrene labelled rabbit skeletal muscle actin (Tebu-bio, Cytoskeleton inc. Davis, Ca) was resuspended in GAB (described above) to a final concentration of 0.4 mg/mL and incubated for 1 hr at 4°C. Pyrene actin was mixed with peptides (TM β 4, AQP2-WT, -S256A, -S256D, -R253A, -R253A-R254A and sermorelin) in a molar ratio (peptide:actin) of 0.5, 1 and 2. The baseline of the mixture was measured in a Cary Eclipse fluorescence spectrophotometer (Agilent Technologies) with an excitation wavelength of 365 nm and an emission wavelength of 407 nm for 10 min at RT. After baseline measurements, 10x polymerization buffer (described above) was added and polymerization was tracked using the fluorescence spectrophotometer with the same settings as described above. Measurements were stopped after a total of 70 minutes. All measurements were fitted and normalized as described below.

Curve Fitting-The f-actin elongation rate dP/dt is written as described in equation 1 (58).

$$dP/dt = N (k_5 A_1 - k_6) \quad \text{Equation 1}$$

Here, N is the number of filament ends per volume, A_1 the concentration of assembly competent g-actin molecules, k_5 the association rate constant, and k_6 the dissociation rate constant. Numerical simulations of actin polymerization have shown that during polymerization the concentration of actin dimers and actin trimers declined slowly compared to the actin in elongating f-actin (42), and represent a small fraction of the total actin. Therefore, A_1 is to a first approximation given as equation 2.

$$A_1(t) \approx A_{\text{tot}} - A_0 - P(t) \quad \text{Equation 2}$$

Here, A_{tot} is the total actin concentration and A_0 the concentration of unproductive g-actin, leading to equation 3.

$$dP/dt \approx N (k_5 (A_{\text{tot}} - A_0 - P(t)) - k_6) \quad \text{Equation 3}$$

Equation 3 has a solution in the form of equation 4.

$$P(t) \approx (P_0 - P_{\infty}) \exp(-N k_5 t) + P_{\infty} \quad \text{Equation 4}$$

Here P_0 is the relative fluorescence measured at $t=0$, and P_{∞} is the relative fluorescence at equilibrium, i.e. at $t=\infty$. We used this function to fit the experimental actin polymerization curves in order to calculate the normalization constants. The actin polymerization in the presence of sermorelin exhibited a distinct linear region; to obtain a better fit an empirical linear term was added to Eq. (4) resulting in equation 5.

$$P(t) \approx (P_0 - P_{\infty}) \exp(-N k_5 t) + P_{\infty} + Ct \quad \text{Equation 5}$$

Fitting was achieved using the IGOR Pro software.

Tropomyosin interaction assay/F-actin depolymerization assay-Pyrene actin (Tebu-bio, Cytoskeleton inc. Davis, Ca) was resuspended in GAB (described above) and mixed with Tm5b (Tebu-bio) in a 7:1 molar ratio (actin:Tm5b). Baseline of the mixture was measured for 10 min and polymerization was initiated by addition of 10x polymerization buffer (described above). Polymerization was monitored for 60 min, i. e., to the point where polymerization of actin alone reached equilibrium. Peptides in GAB were then added in a molar ratio (peptide:actin) of 2 and fluorescence was measured for another 60 minutes. Results for each experiment were normalized, fitted and extrapolated using equation 5 as described above.

Western blot-Native PAGEs were blotted on Immun-Blot[®] Polyvinylidene Difluoride (PVDF) Membranes (Bio-RAD) using a semidry transfer cell (Novex Semi-Dry Blotter, Invitrogen) and transfer buffer (25 mM Tris base, 192 mM Glycine, 20% MetOH, 0.05% SDS). Blotting membrane was blocked for 1 hr at RT in TBS-T (10 mM Tris pH 7.5, 150 mM NaCl, 0.1% Tween-20) containing 5% milk powder, followed by a 1hr incubation at RT with the polyclonal primary antibody rabbit anti human actin (Tebu-Bio, catalog number AAN01-A, Cytoskeleton, 1:1,000). After incubation, membranes were washed 3 x 15 min with TBS-T followed by 1 hr incubation at RT with the secondary antibody horseradish peroxidase (HRP) conjugated goat anti rabbit IgG (Thermo Scientific, 1:40,000) and 3 x 15 min wash with TBS-T. Chemiluminescence was activated by using the

Supersignal™ West Pico Rabbit IgG detection kit (Thermo Scientific) and signal was detected with a Gel Doc™ XR+ Gel Documentation system (Bio-RAD).

Sequence alignment and model building-Sequences of actin-binding helices belonging to different actin regulator families were aligned with the wild-type AQP2 C-terminal sequence using ClustalOmega available at www.ebi.ac.uk/Tools/msa/clustalo/ (53) to identify the best matching family. Sequences were selected from structures of actin:regulator complexes in the PDB. Sequences of WH2 domains were inverted to take the helix orientation in the actin binding cleft into account. Swiss model (72) was used to obtain initial models of the AQP2 C-terminus/actin interactions. The final model was built in COOT (54) by replacing the residues of PDB entry 4B1X with AQP2 residues according to sequence alignments.

Transfection and cell culture. Mutant forms of N-terminal FLAG-tagged AQP2 were generated by site-directed mutagenesis using standard protocols. Generation of stable MDCK cell lines and cell culture conditions were as previously described (73). Multiple individual cell lines were characterized by examination of cell morphology, and AQP2 expression by western blotting, immunocytochemistry and RT-PCR. For all experiments, cells were cultured on semi-permeable supports (0.4 µM pore size, Corning) until a confluent monolayer formed, and cell surface biotinylation assays performed as previously described (74). Immunocytochemistry and confocal microscopy was performed as described (75).

In vitro phosphorylation assays. 1 µg peptides were incubated for 1 h at 30°C in a 20 µL reaction buffer containing 200 ng PKACα (PRKACA, 01-127 Carna), 100 µM ATP, 32.5 mM HEPES pH 7.5, 0.005% BRIJ-35, 5 mM MgCl₂, 500 µM EGTA, 2 mM CaCl₂, and 0.01% NaN₃. Reactions were stopped by addition of Laemmli sample buffer and heating to 65°C for 15 mins. Peptides were detected using standard immunoblotting techniques with antibodies targeting total AQP2 (C17, Santa Cruz) or pS256-AQP2 as previously described (75).

3.6: References

1. Agre, P., King, L. S., Yasui, M., Guggino, W. B., Ottersen, O. P., Fujiyoshi, Y., Engel, A., and Nielsen, S. (2002) Aquaporin water channels - from atomic structure to clinical medicine. *The Journal of Physiology* **542**, 3-16
2. Agre, P., and Kozono, D. (2003) Aquaporin water channels: molecular mechanisms for human diseases1. *FEBS Letters* **555**, 72-78
3. Deen, P. M. T., and van Os, C. H. (1998) Epithelial aquaporins. *Current Opinion in Cell Biology* **10**, 435-442
4. Engel, A., Fujiyoshi, Y., and Agre, P. (2000) The importance of aquaporin water channel protein structures. *The EMBO Journal* **19**, 800-806
5. King, L. S., Yasui, M., and Agre, P. (2000) Aquaporins in health and disease. *Molecular Medicine Today* **6**, 60-65
6. Kortenoeven, M. L. A., and Fenton, R. A. (2014) Renal aquaporins and water balance disorders. *Biochimica et Biophysica Acta (BBA) - General Subjects* **1840**, 1533-1549
7. Verkman, A. S. (2012) Aquaporins in clinical medicine. *Annu Rev Med* **63**, 303-316
8. Nielsen, S., Frøkiær, J., Marples, D., Kwon, T.-H., Agre, P., and Knepper, M. A. (2002) Aquaporins in the Kidney: From Molecules to Medicine. *Physiological Reviews* **82**, 205-244
9. Rojek, A., Fuchtbauer, E. M., Kwon, T. H., Frokiaer, J., and Nielsen, S. (2006) Severe urinary concentrating defect in renal collecting duct-selective AQP2 conditional-knockout mice. *Proceedings of the National Academy of Sciences* **103**, 6037-6042
10. Stanton, B. A., and Knoepfen, B. M. (1998) Solute and Water Transport along the Nephron: Tubular Function. in *Berne & Levy Physiology*, Mosby, Inc., St. Louis. pp 699-714
11. Knepper, M. A., Valtin, H., and Sands, J. M. (2011) Renal Actions of Vasopressin. in *Comprehensive Physiology*, John Wiley & Sons, Inc. pp
12. Fushimi, K., Uchida, S., Harat, Y., Hirata, Y., Marumo, F., and Sasaki, S. (1993) Cloning and expression of apical membrane water channel of rat kidney collecting tubule. *Nature* **361**, 549-552
13. Ecelbarger, C. A., Terris, J., Frindt, G., Echevarria, M., Marples, D., Nielsen, S., and Knepper, M. A. (1995) Aquaporin-3 Water Channel Localization and Regulation in Rat Kidney. *Am. J. Physiol.* **269**, F663-672
14. Terris, J., Ecelbarger, C. A., Marples, D., Knepper, M. A., and Nielsen, S. (1995) Distribution of Aquaporin-4 Water Channel Expression within Rat Kidney. *Am. J. Physiol.* **1995**
15. Murata, K., Mitsuoka, K., Hirai, T., Walz, T., Agre, P., Heymann, J. B., Engel, A., and Fujiyoshi, Y. (2000) Structural Determinants of Water Permeation through Aquaporin-1. *Nature* **407**, 599-605
16. Vahedi-Faridi, A., and Engel, A. (2016) Aquaporin Structure and Selectivity. in *Aquaporins in Health and Disease*, CRC Press
17. Nielsen, S., Chou, C. L., Marples, D., Christensen, E. I., Kishore, B. K., and Knepper, M. A. (1995) Vasopressin increases water permeability of kidney collecting duct by inducing translocation of aquaporin-CD water channels to

- plasma membrane. *Proceedings of the National Academy of Sciences* **92**, 1013-1017
18. Hoffert, J. D., Fenton, R. A., Moeller, H. B., Simons, B., Tchapyjnikov, D., McDill, B. W., Yu, M. J., Pisitkun, T., Chen, F., and Knepper, M. A. (2008) Vasopressin-stimulated Increase in Phosphorylation at Ser269 Potentiates Plasma Membrane Retention of Aquaporin-2. *Journal of Biological Chemistry* **283**, 24617-24627
 19. van Balkom, B. W. M., Savelkoul, P. J. M., Markovich, D., Hofman, E., Nielsen, S., van der Sluijs, P., and Deen, P. M. T. (2002) The Role of Putative Phosphorylation Sites in the Targeting and Shuttling of the Aquaporin-2 Water Channel. *Journal of Biological Chemistry* **277**, 41473-41479
 20. Moeller, H. B., Olesen, E. T. B., and Fenton, R. A. (2011) Regulation of the water channel aquaporin-2 by posttranslational modification. *AJP: Renal Physiology* **300**, F1062-F1073
 21. Kamsteeg, E. J., Heijnen, I., van Os, C. H., and Deen, P. M. T. (2000) The Subcellular Localization of an Aquaporin-2 Tetramer Depends on the Stoichiometry of Phosphorylated and Nonphosphorylated Monomers. *The Journal of cell biology* **151**, 919-930
 22. Wade, J. B., and Kachadorian, W. A. (1988) Cytochalasin B Inhibition of Toad Bladder Apical Membrane Responses to ADH. *Am. J. Physiol.* **255**, C526-530
 23. Muallem, S. (1995) Actin filament disassembly is a sufficient final trigger for exocytosis in nonexcitable cells. *The Journal of Cell Biology* **128**, 589-598
 24. Ding, G. H., Franki, N., Condeelis, J., and Hays, R. M. (1991) Vasopressin depolymerizes F-actin in toad bladder epithelial cells. *American Physiological Society* **260**, C9-16
 25. Simon, H., Gao, Y., Franki, N., and Hays, R. M. (1993) Vasopressin Depolymerizes Apical F-actin in Rat Inner Medullary Collecting Duct. *Am. J. Physiol.* **265**, C757-762
 26. Loo, C. S., Chen, C. W., Wang, P. J., Chen, P. Y., Lin, S. Y., Khoo, K. H., Fenton, R. A., Knepper, M. A., and Yu, M. J. (2013) Quantitative apical membrane proteomics reveals vasopressin-induced actin dynamics in collecting duct cells. *Proceedings of the National Academy of Sciences* **110**, 17119-17124
 27. Jang, K.-J., Cho, H. S., Kang, D. H., Bae, W. G., Kwon, T.-H., and Suh, K.-Y. (2011) Fluid-shear-stress-induced translocation of aquaporin-2 and reorganization of actin cytoskeleton in renal tubular epithelial cells. *Integr. Biol.* **3**, 134-141
 28. Tamma, G. (2003) cAMP-induced AQP2 translocation is associated with RhoA inhibition through RhoA phosphorylation and interaction with RhoGDI. *Journal of Cell Science* **116**, 1519-1525
 29. Noda, Y., Horikawa, S., Katayama, Y., and Sasaki, S. (2004) Water channel aquaporin-2 directly binds to actin. *Biochemical and Biophysical Research Communications* **322**, 740-745
 30. Noda, Y., Horikawa, S., Kanda, E., Yamashita, M., Meng, H., Eto, K., Li, Y., Kuwahara, M., Hirai, K., Pack, C., Kinjo, M., Okabe, S., and Sasaki, S. (2008) Reciprocal interaction with G-actin and tropomyosin is essential for aquaporin-2 trafficking. *The Journal of Cell Biology* **182**, 587-601

31. Yui, N., Lu, H. J., Bouley, R., and Brown, D. (2011) AQP2 is necessary for vasopressin- and forskolin-mediated filamentous actin depolymerization in renal epithelial cells. *Biology Open* **1**, 101-108
32. Noda, Y., Horikawa, S., Katayama, Y., and Sasaki, S. (2005) Identification of a multiprotein “motor” complex binding to water channel aquaporin-2. *Biochemical and Biophysical Research Communications* **330**, 1041-1047
33. Sasaki, S., Yui, N., and Noda, Y. (2014) Actin directly interacts with different membrane channel proteins and influences channel activities: AQP2 as a model. *Biochimica et Biophysica Acta (BBA) - Biomembranes* **1838**, 514-520
34. Carlier, M.-F., Pernier, J., Montaville, P., Shekhar, S., and Kühn, S. (2015) Control of polarized assembly of actin filaments in cell motility. *Cellular and Molecular Life Sciences* **72**, 3051-3067
35. Mouilleron, S., Guettler, S., Langer, C. A., Treisman, R., and McDonald, N. Q. (2008) Molecular basis for G-actin binding to RPEL motifs from the serum response factor coactivator MAL. *The EMBO Journal* **27**, 3198-3208
36. Fushimi, K. (1997) Phosphorylation of Serine 256 Is Required for cAMP-dependent Regulatory Exocytosis of the Aquaporin-2 Water Channel. *Journal of Biological Chemistry* **272**, 14800-14804
37. Fushimi, K., Kuwahara, M., Terada, Y., Bai, L., Marumo, F., and Sasaki, S. (1995) cAMP-dependent Phosphorylation Stimulates Water Permeability of Aquaporin-collecting Duct Water Channel Protein Expressed in *Xenopus* Oocytes. *Journal of Biological Chemistry* **270**, 10384-10387
38. Lu, H. J., Matsuzaki, T., Bouley, R., Hasler, U., Qin, Q. H., and Brown, D. (2008) The phosphorylation state of serine 256 is dominant over that of serine 261 in the regulation of AQP2 trafficking in renal epithelial cells. *AJP: Renal Physiology* **295**, F290-F294
39. Dos Remedios, C. G., Chhabra, D., Kekic, M., Dedova, I. V., Tsubakihara, M., Berry, D. A., and Nosworthy, N. J. (2003) Actin Binding Proteins: Regulation of Cytoskeletal Microfilaments. *Physiological Reviews* **83**, 433-473
40. Srivastava, J., and Barber, D. (2008) Actin Co-Sedimentation Assay; for the Analysis of Protein Binding to F-Actin. *J Vis Exp*
41. Barden, J. A., Grant, N. J., and dos Remedios, C. G. (1982) Identification of the nucleus of actin polymerization. *Biochemical International* **5**, 685-692
42. Sept, D., and McCammon, J. A. (2001) Thermodynamics and kinetics of actin filament nucleation. *Biophys J* **81**, 667-674
43. Kekic, M., Nosworthy, N. J., Dedova, I., Collyer, C. A., and dos Remedios, C. G. (2001) Regulation of the Cytoskeleton Assembly: a Role for a Ternary Complex of Actin with Two Actin-Binding Proteins. in *Results and Problems in Cell Differentiation*, Springer Berlin Heidelberg
44. Kouyama, T., and Mihashi, K. (2005) Fluorimetry Study of N-(1-Pyrenyl)iodoacetamide-Labelled F-Actin. *European Journal of Biochemistry* **114**, 33-38
45. Cooper, J. A., Walker, S. B., and Pollard, T. D. (1983) Pyrene actin: documentation of the validity of a sensitive assay for actin polymerization. *Journal of Muscle Research and Cell Motility* **4**, 253-262

46. Blanchoin, L., Boujemaa-Paterski, R., Sykes, C., and Plastino, J. (2014) Actin Dynamics, Architecture, and Mechanics in Cell Motility. *Physiological Reviews* **94**, 235-263
47. Kostyukova, A. S., and Hitchcock-DeGregori, S. E. (2003) Effect of the Structure of the N Terminus of Tropomyosin on Tropomodulin Function. *Journal of Biological Chemistry* **279**, 5066-5071
48. Mannherz, H. G., and Goody, R. S. (1976) Proteins of Contractile Systems. *Annual Review of Biochemistry* **45**, 427-466
49. Hitchcock-DeGregori, S. E. (1988) Tropomyosin inhibits the rate of actin polymerization by stabilizing actin filaments. *American Chemical Society* **27**, 9182-9185
50. Gordon, D. J., Boyer, J. L., and Korn, E. D. (1977) Comparative biochemistry of non-muscle actins. *J Biol Chem* **252**, 8300-8309
51. Mizuguchi, M., Fujii, T., Obita, T., Ishikawa, M., Tsuda, M., and Tabuchi, A. (2014) Transient alpha-helices in the disordered RPEL motifs of the serum response factor coactivator MKL1. *Sci Rep* **4**, 5224
52. Mouilleron, S., Wiezlak, M., O'Reilly, N., Treisman, R., and McDonald, N. Q. (2012) Structures of the Phactr1 RPEL domain and RPEL motif complexes with G-actin reveal the molecular basis for actin binding cooperativity. *Structure* **20**, 1960-1970
53. Sievers, F., Wilm, A., Dineen, D., Gibson, T. J., Karplus, K., Li, W., Lopez, R., McWilliam, H., Remmert, M., Soding, J., Thompson, J. D., and Higgins, D. G. (2014) Fast, scalable generation of high-quality protein multiple sequence alignments using Clustal Omega. *Molecular Systems Biology* **7**, 539-539
54. Emsley, P., Lohkamp, B., Scott, W. G., and Cowtan, K. (2010) Features and development of Coot. *Acta Crystallogr D Biol Crystallogr* **66**, 486-501
55. Morone, N., Fujiwara, T., Murase, K., Kasai, R. S., Ike, H., Yuasa, S., Usukura, J., and Kusumi, A. (2006) Three-dimensional reconstruction of the membrane skeleton at the plasma membrane interface by electron tomography. *The Journal of Cell Biology* **174**, 851-862
56. Murase, K., Fujiwara, T., Umemura, Y., Suzuki, K., Iino, R., Yamashita, H., Saito, M., Murakoshi, H., Ritchie, K., and Kusumi, A. (2004) Ultrafine Membrane Compartments for Molecular Diffusion as Revealed by Single Molecule Techniques. *Biophysical Journal* **86**, 4075-4093
57. Hirokawa, N. (1989) The cytoskeletal architecture of the presynaptic terminal and molecular structure of synapsin 1. *The Journal of Cell Biology* **108**, 111-126
58. Cooper, J. A., Buhle, E. L., Walker, S. B., Tsong, T. Y., and Pollard, T. D. (1983) Kinetic evidence for a monomer activation step in actin polymerization. *Biochemistry* **22**, 2193-2202
59. Coue, M., and Korn, E. D. (1985) Interaction of plasma gelsolin with G-actin and F-actin in the presence and absence of calcium ions. *J Biol Chem* **260**, 15033-15041
60. Mannherz, H. G., Mazur, A. J., and Jockusch, B. (2010) Repolymerization of actin from actin:thymosin beta4 complex induced by diaphanous related formins and gelsolin. *Ann N Y Acad Sci* **1194**, 36-43

61. McGough, A. M., Staiger, C. J., Min, J.-K., and Simonetti, K. D. (2003) The gelsolin family of actin regulatory proteins: modular structures, versatile functions. *FEBS Letters* **552**, 75-81
62. Ditsch, A., and Wegner, A. (1994) Nucleation of Actin Polymerization by Gelsolin. *European Journal of Biochemistry* **224**, 223-227
63. Schoepper, B., and Wegner, A. (1991) Rate constants and equilibrium constants for binding of actin to the 1:1 gelsolin-actin complex. *European Journal of Biochemistry* **202**, 1127-1131
64. Harris, H. E., and Weeds, A. G. (1984) Plasma gelsolin caps and severs actin filaments. *FEBS Letters* **177**, 184-188
65. de Mattia, F., Savelkoul, P. J., Kamsteeg, E. J., Konings, I. B., van der Sluijs, P., Mallmann, R., Oksche, A., and Deen, P. M. (2005) Lack of arginine vasopressin-induced phosphorylation of aquaporin-2 mutant AQP2-R254L explains dominant nephrogenic diabetes insipidus. *J Am Soc Nephrol* **16**, 2872-2880
66. Savelkoul, P. J., De Mattia, F., Li, Y., Kamsteeg, E. J., Konings, I. B., van der Sluijs, P., and Deen, P. M. (2009) p.R254Q mutation in the aquaporin-2 water channel causing dominant nephrogenic diabetes insipidus is due to a lack of arginine vasopressin-induced phosphorylation. *Human mutation* **30**, E891-903
67. Dollerup, P., Thomsen, T. M., Nejsum, L. N., Faerch, M., Osterbrand, M., Gregersen, N., Rittig, S., Christensen, J. H., and Corydon, T. J. (2015) Partial nephrogenic diabetes insipidus caused by a novel AQP2 variation impairing trafficking of the aquaporin-2 water channel. *BMC nephrology* **16**, 217
68. Ridley, A. J. (2006) Rho GTPases and actin dynamics in membrane protrusions and vesicle trafficking. *Trends Cell Biol* **16**, 522-529
69. Nyakern-Meazza, M., Narayan, K., Schutt, C. E., and Lindberg, U. (2002) Tropomyosin and gelsolin cooperate in controlling the microfilament system. *J Biol Chem* **277**, 28774-28779
70. Abramoff, M. D. (2007) ImageJ as an Image Processing Tool and Library. *Microscopy and Microanalysis* **13**
71. Arndt, C., Koristka, S., Bartsch, H., and Bachmann, M. (2012) Native polyacrylamide gels. *Methods Mol Biol* **869**, 49-53
72. Biasini, M., Bienert, S., Waterhouse, A., Arnold, K., Studer, G., Schmidt, T., Kiefer, F., Cassarino, T. G., Bertoni, M., Bordoli, L., and Schwede, T. (2014) SWISS-MODEL: modelling protein tertiary and quaternary structure using evolutionary information. *Nucleic Acids Research* **42**, W252-W258
73. Hoffert, J. D., Fenton, R. A., Moeller, H. B., Simons, B., Tchapyjnikov, D., McDill, B. W., Yu, M. J., Pisitkun, T., Chen, F., and Knepper, M. A. (2008) Vasopressin-stimulated increase in phosphorylation at Ser269 potentiates plasma membrane retention of aquaporin-2. *J Biol Chem* **283**, 24617-24627
74. Moeller, H. B., Praetorius, J., Rutzler, M. R., and Fenton, R. A. (2010) Phosphorylation of aquaporin-2 regulates its endocytosis and protein-protein interactions. *Proc Natl Acad Sci U S A* **107**, 424-429
75. Moeller, H. B., Aroankins, T. S., Slengerik-Hansen, J., Pisitkun, T., and Fenton, R. A. (2014) Phosphorylation and ubiquitylation are opposing processes that regulate endocytosis of the water channel aquaporin-2. *J Cell Sci* **127**, 3174-3183

3.7: Supplemental figures

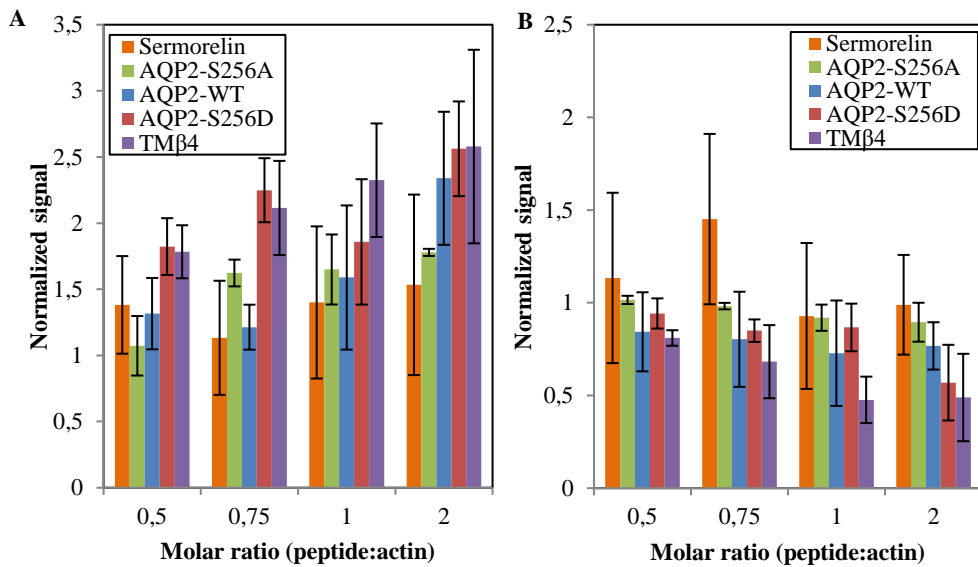
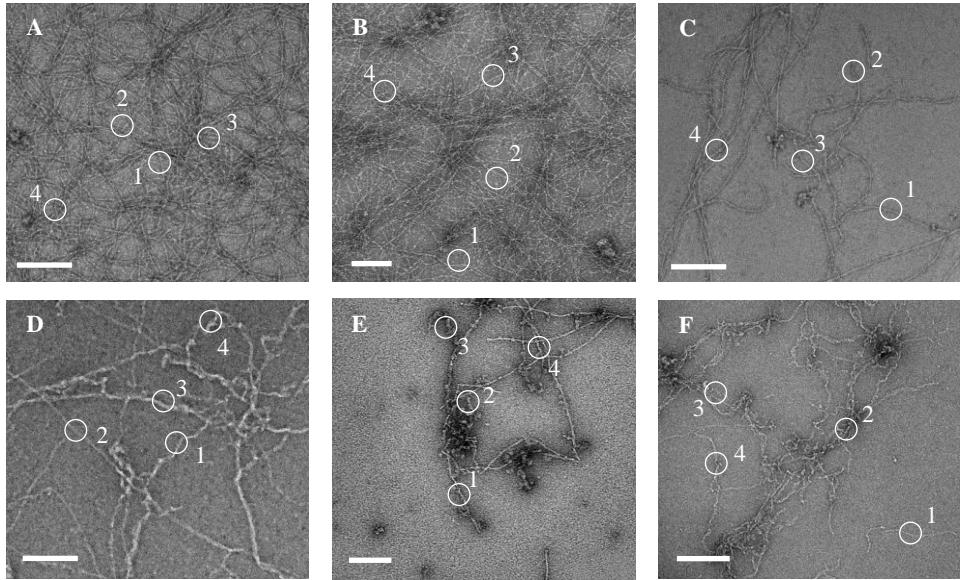


Figure S3.1: Quantified results of the SDS gels after polymerization experiments. Supernatant (A) and pellet (B). Quantification was executed by using ImageJ. Actin signal was normalized against the actin signal from the sample without peptide. Standard deviations are obtained from multiple independent experiments (N=6).



	Peptide	#	Width (nm)		Peptide	#	Width (nm)
A	No peptide	1	8.8	D	AQP2-WT	1	9.7
		2	8.9			2	10
		3	9.4			3	17.3
		4	8.7			4	15.7
B	Sermorelin	1	8.9	E	AQP2-S256D	1	9.5
		2	8.7			2	12.5
		3	8.9			3	18.6
		4	9.2			4	7.8
C	AQP2-S256A	1	9.6	F	TMβ4	1	9.8
		2	9.7			2	10.9
		3	7.6			3	15.4
		4	8.6			4	10.8

Figure S3.2: Negative stain transmission Electron Microscopy of actin filaments produced in the absence of peptide (A), or in the presence of Sermorelin (B), AQP2-S256A (C), AQP2-WT (D), AQP2-S256D (E) or TMβ4 (F) in a 1:1 (peptide:actin) molar ratio. Actin filaments were derived from the pellet after ultracentrifugation. Pellets were dissolved in 200μl GAB prior to loading on EM copper grids. Scale bar is 200 nm. Magnification is 41,000x. Width of actin filaments was measured at four different positions (circles) for every condition (A-F).

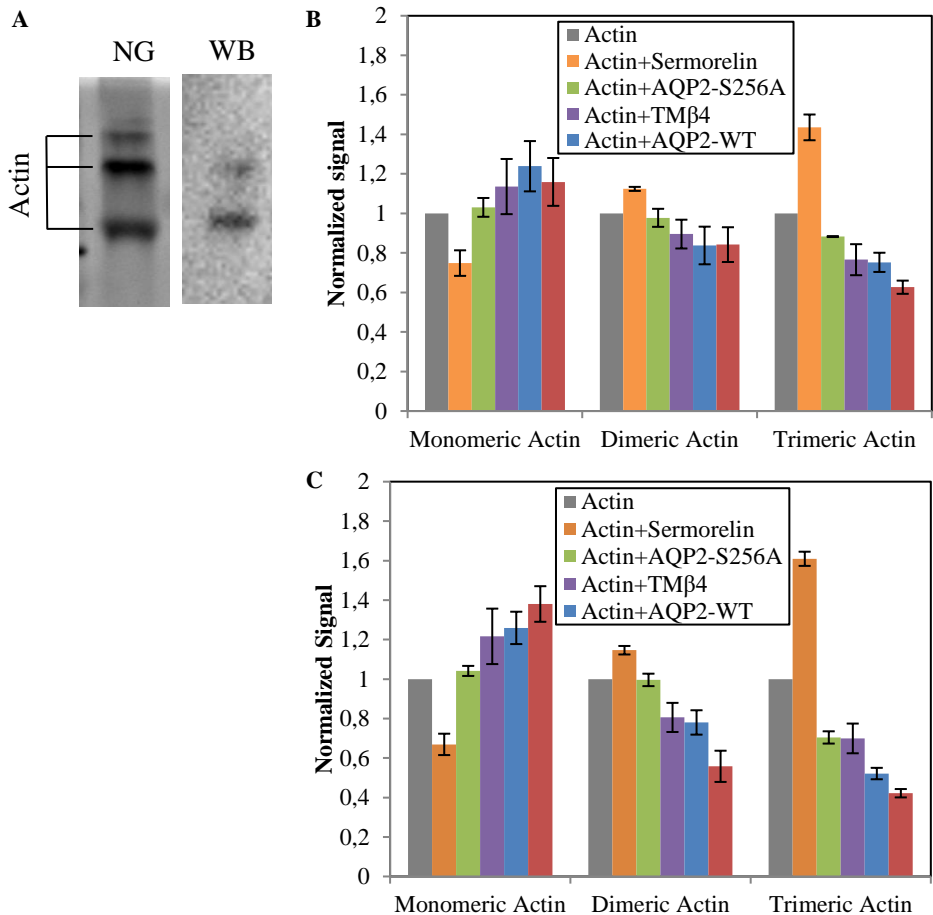


Figure S3.3: G-actin loaded on native gel. (A) G-actin loaded on native PAGE gel (NP) without peptide, compared to westernblot (WB). Actin signal was visualized by using a specific antibody against actin. Multiple bands show mono-, di- and trimeric actin. (B/C) Quantified results from native gels after addition of sermorelin (Orange), AQP2-S256A (green), TMβ4 (purple), AQP2-WT (blue), and AQP2-S256D (red), normalized against the signal measured for actin alone (grey). Quantification was executed by using ImageJ. (B) Peptide:actin ratio was 0.5. (C) Peptide:actin ratio was 1.

Chapter 4

Aquaporin-2: Production, purification and reconstitution

Parts of this chapter are under revision at Current Protocols (Carvalho, V; Pronk, J.W.; Engel, A.H. (2017) Characterization of membrane proteins using cryo-electronmicroscopy)

4.1: Introduction

To understand the underlying mechanism regulating AQP2 trafficking, AQP2 needs to be purified. Purified AQP2 can then be used for *in vitro* studies, as discussed in the previous chapters, or can be labelled and injected into cells to use for *in vivo* studies, as shortly discussed in chapter 1. The *in vivo* studies discussed in chapter 2 are now limited to the fact that AQP2 needs to be labelled by either fusing it to a fluorescent protein, which can lead to hindrance in AQP2 folding or function, or by fixing the cells and labelling AQP2 by using immuno fluorescence assays (IFA). Fixation, however, can only be used to visualize the cell at predetermined fixed time points, losing information induced by the mobility of the cell. AQP2 reconstituted in fluorescently labelled liposomes can be used to circumvent these limitations, by injecting these proteoliposomes into cells (as discussed in chapter 1). The fluorescent lipids can be used to visualize and localize AQP2 inside the cell in real life, while the fluorescent label does not comprehend the function of AQP2.

This chapter will discuss the production, purification and reconstitution of AQP2 in proteoliposomes. In **section 4.2** different methods to produce AQP2 are discussed, using different cell types. Purification of AQP2 can be executed by either using detergents or by the formation of nanodiscs, both methods are discussed in **section 4.3**. **Section 4.4** will focus on the reconstitution of purified AQP2 in fluorescently labelled liposomes. In the end the water permeability of these liposomes is tested, showing that AQP2 is still functional after purification and reconstitution.

Table 4.1: Aquaporin-2 phosphorylation mutants expressed in *Sf9* cells. Each AQP2 protein contains a 10 histidine tag and a prescission protease cleavage site at the N-terminus. Wildtype residues are coloured green. Mutant residues mimicking the dephosphorylated state (alanine) are coloured red. Mutant residues mimicking the phosphorylated state (aspartic acid for serine, glutamic acid for threonine) are coloured blue.

AQP2	Residue #				Purpose
	256	261	264	269	
Wildtype	S	S	S	T	Monitor AQP2 trafficking
Mutant-1	A	A	S	T	Does S261A drive exocytosis?
Mutant-2	A	D	S	T	Strong inhibition of exocytosis
Mutant-3	D	A	S	T	Strong activation of exocytosis
Mutant-4	D	D	S	T	Does S256D overrule S261D?
Mutant-5	D	A	D	A	What is the T269 kinase?
Mutant-6	D	A	D	E	Strongest activation of exocytosis
Mutant-7	A	D	A	A	Strongest inhibition of exocytosis
Mutant-8	A	A	A	A	State ready for endocytosis

4.2: Aquaporin-2 production

To obtain high yields of purified AQP2, large quantities of this protein needs to be produced. In native tissues, AQP2 is only present at low concentrations and recombinant systems are required to reach high expression levels. Although prokaryotic expression systems have been used to produce mammalian proteins, such as AQP2 (1), prokaryotes lack post-translational modification machineries critical for eukaryotic membrane protein expression. The use of eukaryotic expressions systems, such as yeast, insect cells (*Sf9*) infected with baculovirus and mammalian cells infected with Semliki Forest Virus (SFV), have been more successful methods to over-express functional eukaryotic proteins. In our research we focussed on AQP2 expression in both insect cells (*Sf9*) and yeast cells (*P. pastoris*). Both methods have their own advantages and limitations.

4.2.1: Aquaporin-2 expression in *Sf9* cells by baculovirus expression systems

Sf9 cells are clonal isolates derived from the *Spodoptera frugiperda* pupal ovarian tissue (2). Baculoviruses carrying an *aqp2* gene are used to infect *Sf9* cells, leading to the production of AQP2. Baculovirus expression systems in *Sf9* cells have been used successfully to produce recombinant glycoproteins or membrane proteins (3-5), and functional AQP2 was purified from baculovirus infected *Sf9* cells (6).

In chapter 2 the importance of the AQP2 phosphorylation sites in AQP2 trafficking regulation was discussed. Therefore, we focussed on the production of different AQP2 phospho-mutants, summarized in table 4.1. By mutating a serine (S) into an aspartic acid (D), the phosphorylation state of this residue can be mimicked by charge. While a serine (S) to alanine (A) mutation prevents the phosphorylation of this residue, thus leading to a dephosphorylation mimic. In humans, residue 269 is a threonine (T) while in rodents this is a serine; the phosphorylated state of a threonine can be mimicked with glutamic acid (E).

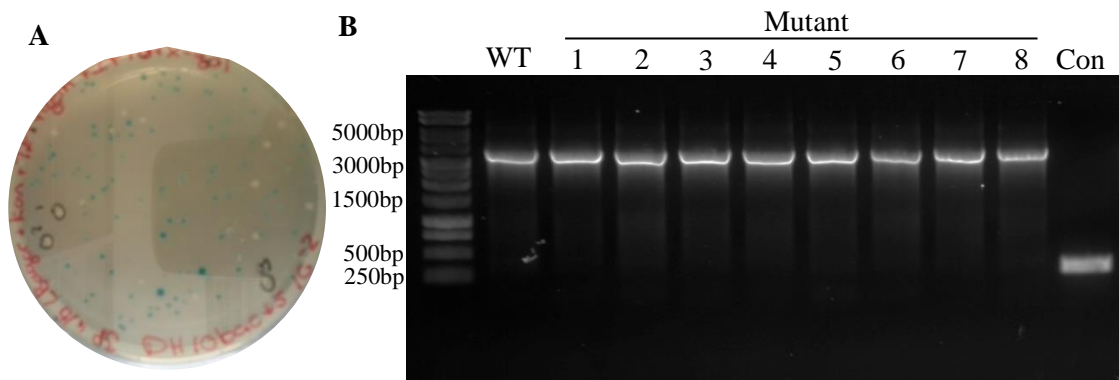


Figure 4.1: (A) Transformed DH10bac colonies growing on an LB agar plate containing kanamycin, tetracycline, gentamycin, IPTG and X-gal. The blue pigment is caused by the degradation of X-gal by active β -galactosidase. White colonies lack the active form of β -galactosidase due to a disruption of the *lacZ- α* gene caused by the incorporation of the *aqp2*-gene in the baculovirus DNA. (B) PCR results of *aqp2* insertion in the baculovirus DNA. Primers flanking the mini-attTn7 site were used. This site is disrupted by the incorporation of *aqp2* in the baculovirus DNA. Incorrect incorporation yields a band of ~300bp after PCR (Blue colony; Con). Correct transposition yields a band of ~3500bp (the *aqp2* gene + ~300bp of the disrupted site) after PCR (WT and mutant 1-8).

These mutations could give us more insight in the phosphorylation dependent AQP2 trafficking regulation. Furthermore, a ten-histidine tag (His10) and a prescission protease cleavage site were added to the N-terminus of AQP2. The His10 tag is used to purify AQP2 with affinity chromatography as will be discussed in chapter 4.3, while the prescission protease cleavage site was added to cleave the His10 tag from AQP2 after purification, leaving an additional glycine and proline at the N-terminus (7).

For AQP2 production in *Sf9* cells, the *aqp2* gene needs to be incorporated into the baculoviral DNA. For this DH10bac cells were transfected with a pUC19 plasmid carrying the *aqp2* gene, either the wildtype or one of the mutants discussed in table 4.1. DH10bac cells are *E. coli* cells carrying the baculovirus DNA and a helper plasmid. The helper plasmid encodes genes that help with the transposition of the *aqp2* gene from the pUC19 plasmid into the baculovirus DNA. The baculovirus DNA carries a *lacZ- α* gene, this gene is disrupted by the incorporation of the *aqp2* gene into the baculovirus DNA.

LacZ- α is part of the β -galactosidase complex and without LacZ- α , this complex is inactive. β -galactosidase is a glycoside hydrolase enzyme, that catalyzes the hydrolysis of β -galactosides into monosaccharides. When *E. coli* cells, carrying an active β -galactosidase complex, are cultured on plates loaded with halogenated indolyl- β -galactoside (Bluo-gal), the β -galactosidase will hydrolyze the Bluo-gal, producing a blue precipitate leading to the formation of blue *E. coli* colonies. Incorporation of the *aqp2* gene in the baculovirus DNA disrupts the *lacZ- α* gene, leading to an inactive β -galactosidase complex. Therefore, Bluo-gal is not hydrolyzed and the *E. coli* colonies are “white” in color. Figure 4.1A displays a

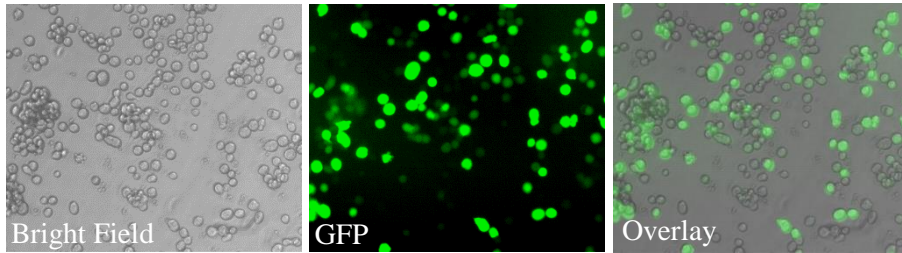


Figure 4.2: Transfection of baculovirus DNA carrying a *gfp* gene into *Sf9* cells. Left, a bright field image overview of the *Sf9* cells. Middle, production of GFP is monitored by fluorescence microscopy. Right, an overlay of the GFP signal with the bright field microscopy image, showing the transfected *Sf9* cells. Magnification was 40x.

typical culture plate after transformation of DH10bac cells, where both blue and white colonies are visible. The white colonies are then picked to purify the baculovirus DNA carrying the *aqp2* gene. *Aqp2* incorporation into the Bacmid DNA can be checked via PCR (Figure 4.1B) by using primers flanking the incorporation sites. No *aqp2* incorporation leads to a band of ~300bp (Figure 4.1B, blue colony lane) while *aqp2* incorporation yields a band of ~3500bp (Figure 4.1B, wildtype and mutants).

After the baculovirus DNA is purified from the DH10bac cells and correct incorporation of *aqp2* is confirmed by PCR, the baculovirus can be transfected into the *Sf9* cells. Transfection of baculovirus DNA into *Sf9* cells leads to the expression of baculovirus proteins, the expression of AQP2 and the production of new baculoviruses. The optimal transfection conditions were found by transfecting baculovirus DNA carrying a *gfp* gene into *Sf9* cells. GFP production could be monitored by using fluorescence microscopy, while brightfield microscopy visualized all the cells available in the field of view (Figure 4.2). Optimal transfection mixtures contained 5 μ L of baculovirus DNA (3 mg/ml) and 8 μ L of cellfectin[®]. The produced baculoviruses can be used to infect new *Sf9* cells and to produce AQP2. Multiple infection rounds are necessary to produce large quantities of the virus and a high viral titer. High viral titers are determined by an increased infection rate and increased AQP2 production, which can be visualized via westernblot analysis.

After a high viral titer was reached, the optimal multiplicity of infection and infection time was determined. To this end, 50 mL cultures of *Sf9* cells (2×10^6 cells/mL) were infected with different amounts of virus. Samples were obtained at different time points past infection and AQP2 production was analysed by dot-blot (Figure 4.3). Detectable AQP2 production started ~40 hours past infection (hpi), depending on the amount of virus added. Optimal AQP2 production was reached between 64 and 72 hpi. Longer incubation times (>72 hrs.) lead to a decrease in detectable AQP2, mostly noticeable after addition of 500 μ L or 1,000 μ L of virus (Figure 4.3). During infection, cell viability was measured by determining the cell life and death count (Table 4.2). Long infection times lead to increased cell death, which explains the AQP2 degradation after 72 hpi. Even when low amounts of virus are added,

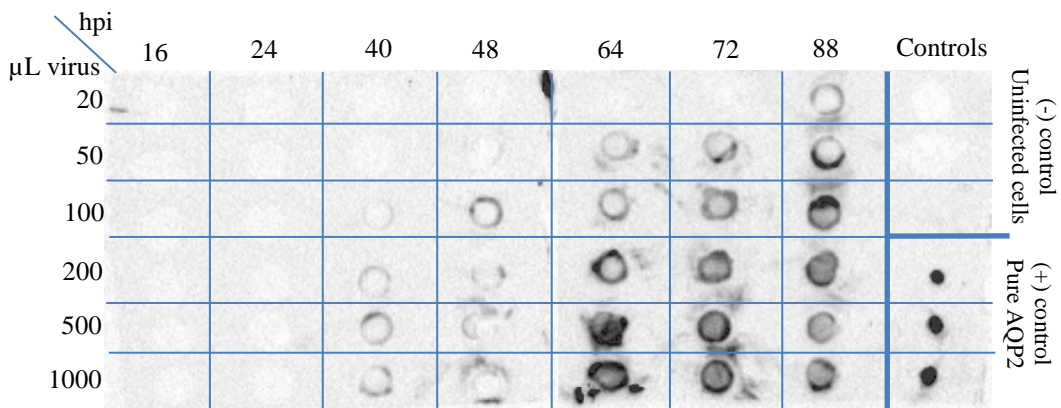


Figure 4.3: Dot-blot of AQP2 production in baculovirus-AQP2 infected *Sf9* cells. 50 ml *Sf9* cell cultures containing $\sim 2 \times 10^6$ life cells/mL were infected with different volumes of virus. Samples were taken at different time points after infection (hours past infection; hpi), lysed and loaded on PVDF membranes. AQP2 was detected by using a rabbit-anti-AQP2 antibody targeting the C-terminus of AQP2. Secondary antibody used was a goat-anti-rabbit antibody carrying a horse-radish peroxidase. As negative control, uninfected cells were lysed and loaded on the PVDF membrane. As a positive control, pure AQP2 was loaded on the PVDF membrane. Depending on the amount of virus added, detectable AQP2 production starts ~ 40 hours past infection (hpi), optimum is reached between 64 and 72 hpi.

roughly half of the cells are dead at 96 hpi (20 μL virus added), whereas addition of 1,000 μL virus to a 50 mL culture of *Sf9* cells lead to 90% dead cells at 96 hpi (Table 4.2). AQP2 production in *Sf9* cells can be visualized by using immuno fluorescence assays (Figure 4.4). Spreading of the virus is visualized by the increase in cells producing AQP2, while the effect of a viral infection on *Sf9* cells is evident due to the increased cell and nucleus size. The optimal amount of virus to use for AQP2 production was 4 mL virus/1,000 mL *Sf9* cells (2×10^6 cells/mL) when an infection time of 72 hrs was used.

4.2.2: Aquaporin-2 expression in *P. Pastoris*

Although AQP2 can be successfully expressed in *Sf9* cells, the expression system is not robust. AQP2 expression depends on the viability of the cells at the time of infection, the quality of the virus used and the success of viral infections. Therefore, a different expression method was tested as well, which should lead to a more robust expression of AQP2.

Pichia pastoris (*P. pastoris*) is a methanotrophic yeast strain, meaning it can utilize methanol as a carbon-source in the absence of glucose, and has been used to over-express a broad range of different eukaryotic proteins (reviewed in (8-11)). *P. pastoris* is an easy to handle micro-organism and grows on inexpensive, easy to prepare culture media. Furthermore, being an eukaryote, *P. pastoris* is able to perform many of the post-translational modifications found in higher eukaryotic cells (12).

Table 4.2: Life and dead cell count during baculovirus-AQP2 infection of *Sf9* cells. 50 ml *Sf9* cell cultures containing $\sim 2 \times 10^6$ life cells/mL were infected with different volumes of virus. Total cell concentration was determined by using a counting chamber. Dead cell count was determined by staining the cells with trypan blue. Cells were counted every 24 hours past infection (hpi). The percentage of life cells decreased over time due to infection. Viral infections limit *Sf9* cell division.

hpi	μl virus added											
	20 μl		50 μl		100 μl		200 μl		500 μl		1,000 μl	
	cells/ mL ($\times 10^6$)	Life (%)	cells/ mL ($\times 10^6$)	Life (%)	cells/ mL ($\times 10^6$)	Life (%)	cells/ mL ($\times 10^6$)	Life (%)	cells/ mL ($\times 10^6$)	Life (%)	cells/ mL ($\times 10^6$)	Life (%)
0	2.1	96.2	2.1	96.2	2.1	96.2	2.1	96.2	2.1	96.2	2.1	96.2
24	2.7	96.3	2.7	97.7	3.0	98.7	3.4	99.4	2.9	97.9	4.1	96.6
48	4.4	98.2	4.1	97.1	3.6	94.4	3.7	92.9	3.0	94.0	3.8	87.3
72	5.9	76.0	4.6	78.6	4.0	65.8	3.8	72.9	3.5	45.5	4.2	47.2
96	5.6	43.2	4.8	40.6	4.0	32.8	3.3	30.3	3.9	20.0	3.2	9.9

AQP2 producing *P. pastoris* strains were kindly provided by Prof. Robert Fenton from Aarhus University (Denmark). AQP2 production in *P. pastoris* and cell division was monitored by measuring the OD_{600nm} of the *P. pastoris* culture and by using dot blot analysis with samples taken at different time points (Figure 4.5). Expression of AQP2 increased over time and cells were harvested after 72 hrs. once the culture reached an OD_{600nm} of ~ 12 (Figure 4.5, bottom) and AQP2 production was clearly detected (Figure 4.5, top).

4.3: Aquaporin-2 purification

After AQP2 is produced in either *Sf9* cells or *P. pastoris*, the cells are lysed and AQP2 needs to be purified. However, purifying membrane proteins is not a trivial endeavour. Membrane proteins contain both hydrophilic as well as hydrophobic domains, making them unstable in an aqueous solution. To maintain the structure and functionality of the membrane protein during purification, the hydrophobic domains need to be protected from the aqueous environment. Therefore, detergents are a viable option to solubilise membrane proteins, where the hydrophobic tail of the detergent interacts with the hydrophobic domains of the membrane protein, protecting these domains from the aqueous surroundings. The polar headgroup of the detergent interacts with the aqueous solution, making it possible to solubilise the protein.

The detergent used for membrane protein solubilisation needs to be determined experimentally, for the stability and functionality of the solubilised membrane protein depends on the detergent used. Furthermore, the detergent used should be compatible with the desired purification method and further downstream experiments. The optimal detergent for AQP2 purification was found to be *n*-Octyl- β -D-glucopyranoside (OG)(6).

Although detergents are a viable option to successfully solubilise membrane proteins, membrane proteins themselves need specific lipids to maintain their structure and function over time (13-16), making a prolonged incubation in the absence of lipids and the presence

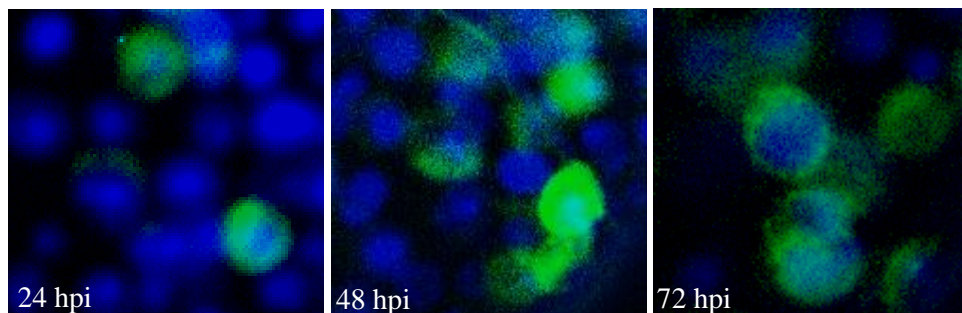


Figure 4.4: Immunofluorescence images of *Sf9* cells, infected with baculoviruses carrying an *aqp2* gene, producing AQP2 at various hours past infection (hpi). Cells were fixed by using 4% PFA. AQP2 was labelled by using a Rabbit-anti-AQP2 primary antibody and an alexa fluor conjugated Goat-anti-Rabbit secondary antibody (green). Nuclei were stained by using Hoechst (blue). Baculovirus infection leads to enlarged nuclei and the production of AQP2. Over time more cells are infected and able to produce AQP2. Magnification was 60x.

of detergents undesirable. A different method to solubilise membrane proteins is by producing nanodiscs (17,18). Nanodiscs are membrane patches held together by an amphipathic co-polymer, containing both a hydrophobic and a hydrophilic part. The hydrophobic part interacts with the hydrophobic tails of the lipids, while the hydrophilic surface interacts with the aqueous environment. Addition of these co-polymers to cellular membranes, carrying membrane proteins, leads to the formation of nanodiscs and the entrapment of the membrane proteins in the nanodiscs. With this method, the membrane protein is kept in its native lipid environment and is therefore more stable. The membrane protein carrying nanodiscs can then be purified in the same manner as detergent solubilised proteins. Possible co-polymers to use are either membrane scaffold proteins (MSPs) or Styrene Maleic Acid (SMA)(17,19-25).

In this thesis, AQP2 is purified from both *Sf9* cells and *P. Pastoris*, purifying both detergent (OG) solubilised AQP2 and AQP2 carrying SMA nanodiscs.

4.3.1: Aquaporin-2 purification from *Sf9* and *P. Pastoris*

After overexpression of AQP2, the protein is purified. This is executed by lysing the cells, separating the membranes from the soluble proteins, solubilisation of the cell membranes and protein purification by Nickel affinity chromatography. Depending on the cell type, different cell lysis methods are necessary.

Sf9 cells have a cell membrane to protect its cellular components, which can easily be disrupted by sonication that leads to cell lysis. However, *P. pastoris* carries both a cell membrane and a cell wall, making cell lysis challenging. Different methods, such as French press, sonication, enzymatic cell wall degradation or cryomilling, can be utilized to lyse *P. pastoris* cells. During our research we both tested the French press and enzymatic cell wall degradation, both in combination with sonication. *P. pastoris* lysis with the French press did not lead to adequate cell breaking and no pure AQP2 could be obtained from cells lysed with

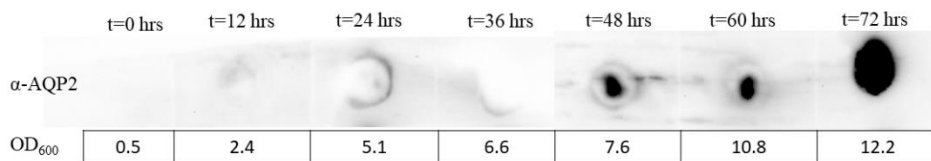


Figure 4.5: Production of AQP2 in *P. pastoris*. 0.5% methanol was added every 24 hrs to compensate for methanol metabolism. Samples were taken every 12 hrs and analysed via dot-blot (top) for AQP2 production or used for OD₆₀₀ measurements to track *P. pastoris* growth. Clear AQP2 production was detected ~48 hrs after incubation. A strong AQP2 signal was measured 72 hrs after incubation, while the OD₆₀₀ reached 12.2. Cells were harvested after 72 hrs.

this method. However, enzymatic cell wall degradation allowed adequate cell lysis to be achieved and AQP2 could be purified in high quantities, as will be discussed below. Besides cell lysis, the AQP2 purification protocol is identical for both *Sf9* produced AQP2 and *P. pastoris* produced AQP2.

The different purification steps are summarized in Figure 4.6. After cell lysis, the cellular membranes are separated from the cytosol by ultracentrifugation and are stripped from loosely bound membrane proteins by incubation in Urea (Figure 4.6, lanes 4 and 5) and NaOH (Figure 4.6, lanes 6 and 7). The cellular membranes are then solubilised in OG. For this the mass of the membrane fraction was determined and 1 gram of OG was used for every 2 grams of membranes. After solubilisation the insolubilized fraction was separated from the solubilised fraction by using ultracentrifugation (Figure 4.6, lanes 8 and 9). The mass of the insolubilized fraction was measured and was roughly half of the total membrane weight before solubilisation. Solubilisation efficiency could not be enhanced by increasing the amount of OG used or by longer incubation times.

The solubilised fraction was incubated overnight in the presence of nickel agarose beads at 4°C. Histidine has an affinity for nickel; therefore, the His10 tag at the N-terminus of AQP2 strongly interacts with the nickel on the agarose beads. The agarose beads, with bound AQP2, can then be collected from the solution and separated from the unbound proteins (Figure 4.6, lane 10).

Besides AQP2, other proteins carrying one or more accessible histidine residues can bind to the nickel agarose beads as well. However, these proteins have a weaker interaction with the nickel beads as compared to AQP2 and can be easily removed by washing the beads with a low concentration of imidazole. Imidazole is structurally comparable to histidine and has an equal affinity to nickel. Addition of imidazole to the nickel beads leads to an affinity competition between histidine carrying proteins and imidazole. Weakly bound proteins can easily be released from the nickel beads, while strongly bound proteins need higher imidazole concentrations to be eluted. After the weakly bound, impurities are washed from the nickel beads (Figure 4.6, lane 11-13), AQP2 can be eluted by incubating the beads in a high imidazole concentration (250 mM). For this, 1 mL of elution buffer was added to the nickel agarose beads and incubated for 10 min. After incubation, the elution buffer is collected from

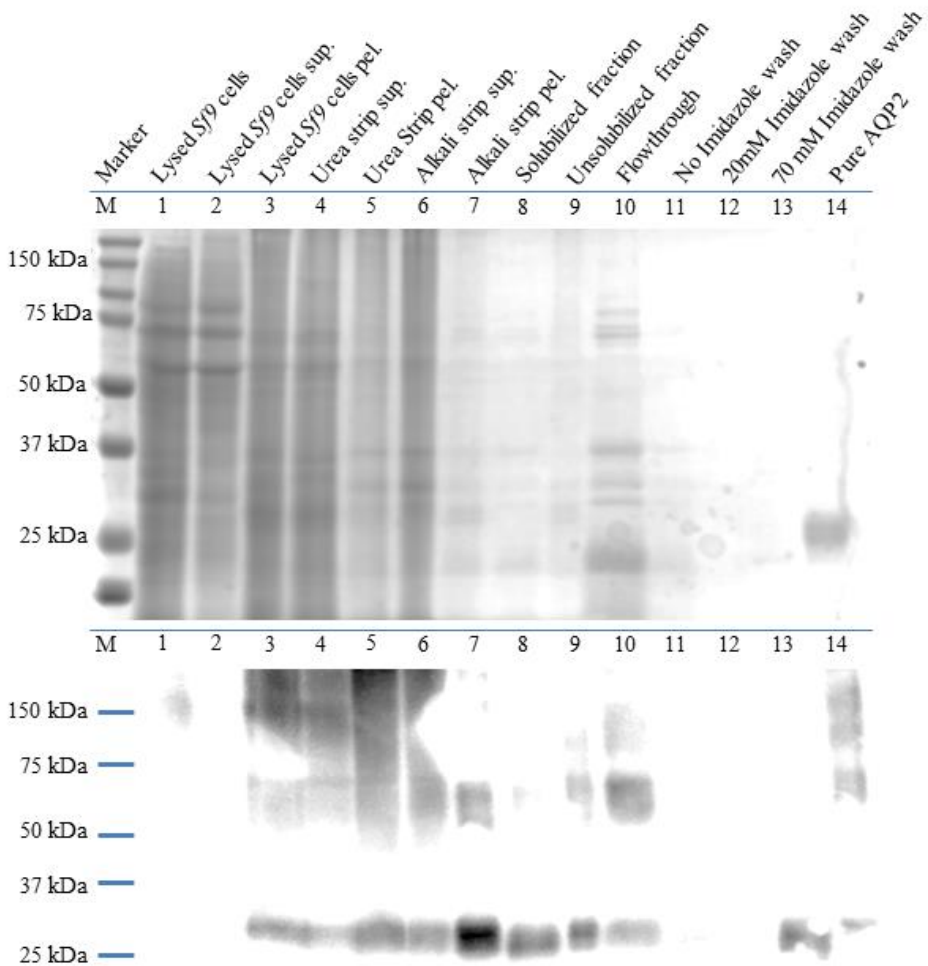


Figure 4.6: SDS-gel and western blot visualizing the purification of AQP2. Lysed *Sf9* cells (1) were separated in the soluble (2) and membrane fraction (3). Loosely bound membrane proteins are stripped from the membrane by using a urea (4,5) and alkali (6,7) strip. The stripped membranes are solubilized in OG and the solubilized (8) and insolubilized fraction (9) were separated by ultracentrifugation. The solubilized fraction was incubated with nickel beads to bind AQP2. Unbound AQP2 was collected in the flowthrough (10). Washing the nickel beads with increasing concentrations of imidazole leads to loss of small quantities of AQP2 (11,12,13). However, pure AQP2 could be eluted from the nickel beads. The top shows the SDS-gel summarizing the purification step, bottom shows the corresponding western blot. The relative low AQP2 signal in lanes 1 and 14 can be caused due to insufficient protein transfer to the PVDF membrane around the edges of the SDS-gel

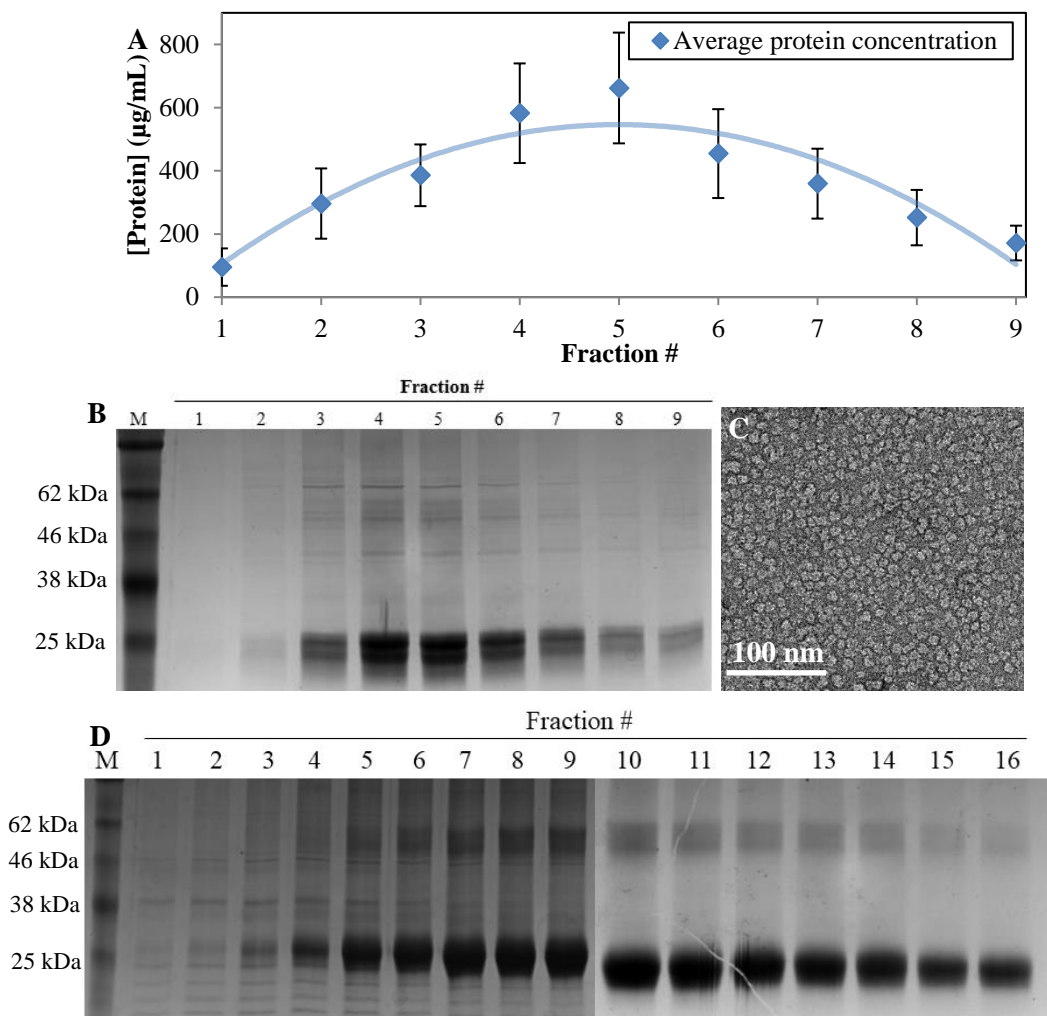


Figure 4.7: (A) Typical elution profile of AQP2 purified from *Sf9* cells. Points visualized are the average protein concentration of eluted AQP2 (N=6, S.E.). Optimal elution is reached with fractions 3-7. (B) NiNTA elution fractions loaded on an SDS-gel. AQP2 is a 28 kDa protein. AQP2 forms two bands around 25 kDa, which is thought to be the glycosylated and unglycosylated form of AQP2. The eluted fractions follow the elution profile visualized in (A) with optimal elution reached between fractions 3 and 7. (C) Negative stain TEM image of pure AQP2. 3 µl of AQP2 (500 µg/ml) was loaded on a glow discharged EM-grid and stained by using 2% Uranyl Acetate. The hydrodynamic radius of AQP2 was ~5 nm. Magnification was 57,000x (D) Elution profile of AQP2 produced in *P. pastoris*. A total of 16 fractions were collected and loaded on two SDS-gels. SDS-gels were aligned. More AQP2 was purified from *P. pastoris* as compared to *Sf9* cells.

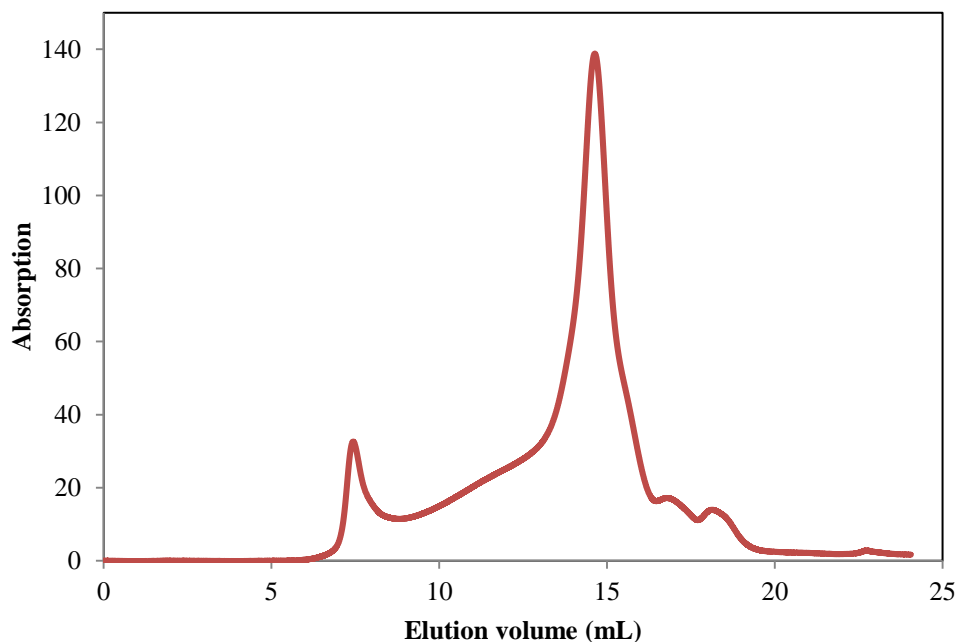


Figure 4.8: Size exclusion chromatography elution profile of AQP2 after nickel elution. AQP2 eluted around 15 ml, corresponding to a protein with a molecular mass of 300 kDa and a hydrodynamic radius of 5.7 nm. The first peak in the elution profile contains protein aggregates.

the nickel beads and again 1 mL of elution buffer was added and incubated for 10 min. During incubation the protein concentration of the eluted sample was measured by using nanodrop. With this method the protein elution can be monitored. A typical elution profile is displayed in Figure 4.7A, where maximum elution was reached between fractions 3-7 for *Sf9* cells. The purity of the eluted fractions was determined by using SDS PAGE-gels (Figure 4.7B) and negative stain TEM (Figure 4.7C). Purification of AQP2 from *P. pastoris* yielded higher quantities of AQP2 and the elution profile was extended as compared to *Sf9* cells (Figure 4.7D). Size exclusion chromatography (SEC) resulted in elution of AQP2 after ~15 ml, corresponding to a molecular weight of 300 kDa and a hydrodynamic radius (R_s) of 5.7 nm (Figure 4.8). Although SEC can be used for molecular weight determination of the purified protein, the determined molecular weight can differ from the actual molecular weight due to residual lipids, detergent binding and protein folding (26). The determined R_s corresponds to the radius determined from negative stain TEM (Figure 4.7D). Pure fractions were pooled together, concentrated and stored for further experiments. Typically, 0.5-1 mg of AQP2 was purified from ~15 grams of *Sf9* cellular membranes obtained from 4 L of cell culture, while 10-15 mg of AQP2 was purified from equal amounts of *P. pastoris* cellular membranes.

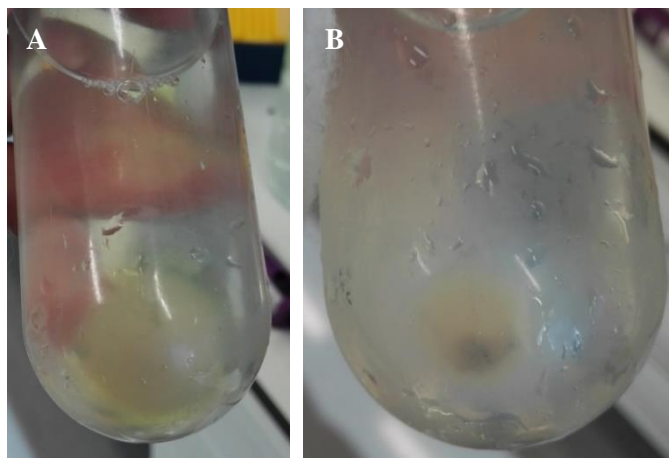


Figure 4.9: Insolubilised membrane fractions after (A) solubilisation in the presence of OG or (B) solubilisation in the presence of SMA. (A) The insolubilised membrane fraction forms a large yellow pellet with a small transparent halo. (B) The insolubilised membrane fraction forms a relative small yellow pellet with a relatively large white/transparent halo. Both unsolubilised membrane fractions were equal in weight.

4.3.2: Aquaporin-2 purification with Styrene Maleic Acid from *Sf9* cells

Although AQP2 purification with OG yields structurally and functionally stable pure AQP2 (6), AQP2 is not stable for long periods of time in detergents. AQP2 requires its native lipid environment to yield long lasting stable proteins. For that, AQP2 was purified while incorporated in SMA prepared nanodiscs. Besides the use of SMA, to solubilise the membranes and prepare AQP2 bearing nanodiscs, the purification method did not differ from the above described method.

AQP2 bearing membranes were solubilised in 2.5% SMA, leading to the formation of nanodiscs. With this method, half of the total membrane weight was not solubilised, independent of the incubation time or SMA concentration used. This yield is comparable to OG solubilisation. However, the insolubilized fraction, resulting after SMA solubilisation, differed in texture as compared to the insolubilized fraction obtained after OG solubilisation (Figure 4.9).

AQP2 purification was monitored via dot blot analysis (Figure 4.10A). Figure 4.10B shows the affinity of AQP2 bearing nanodiscs to nickel agarose beads as compared to OG solubilised AQP2. A relatively strong AQP2 signal can be measured in the flow-through, unbound fraction, after nickel incubation for AQP2 bearing nanodiscs, although some AQP2 was lost in the flow-through of OG solubilised AQP2 as well. The washing steps did not show any loss of OG solubilised AQP2, while AQP2 bearing nanodiscs were lost during the first two washing steps (no imidazole and 20 mM imidazole). Small quantities of AQP2 bearing nanodiscs could be eluted from the nickel beads (Figure 4.10B right, eluted AQP2). However, higher yields were obtained with OG solubilised AQP2 (Figure 4.10B left, eluted

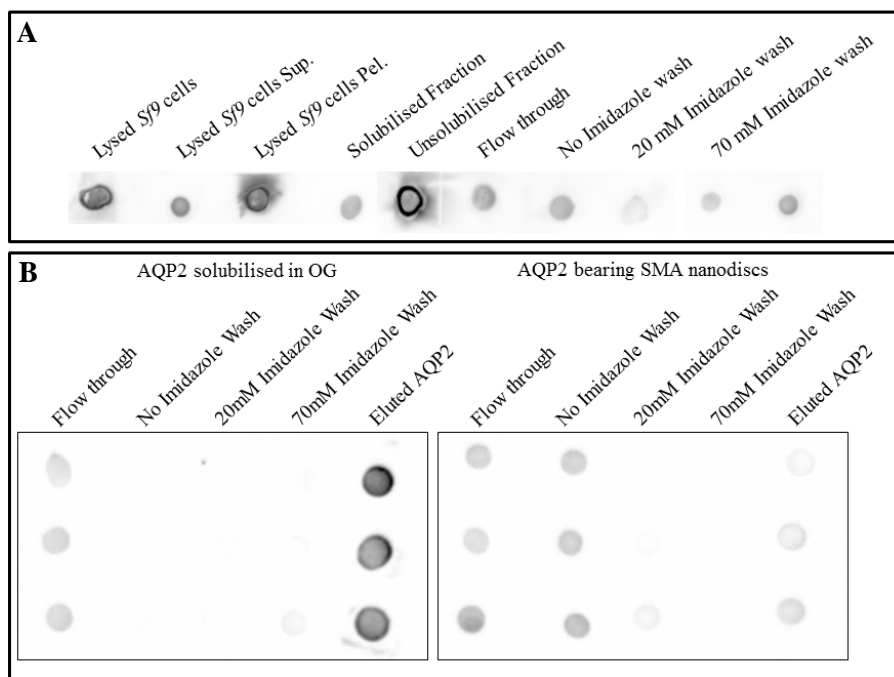


Figure 4.10: (A) Dot blot visualizing AQP2 during different purification steps. *Sf9* cells were lysed by using sonication. The soluble proteins (Lysed *Sf9* cells sup.) were separated from the membrane fractions (Lysed *Sf9* cells pel.) by ultracentrifugation, although some AQP2 could be measured in the soluble fraction. Membranes were solubilized in 2.5% SMA for 4 hrs. at RT and the solubilized membranes were separated from the insolubilized membranes by ultracentrifugation. The solubilized fraction was incubated with NiNTA agarose beads O/N at 4°C and beads were collected. The flow through shows the unbound AQP2. Next the beads were washed with increasing concentrations of imidazole. AQP2 was eluted by 1 hr. incubation in elution buffer (250 mM imidazole). (B) AQP2 affinity to NiNTA. Equal amounts of membranes were solubilized, the membranes originated from the same infected *Sf9* batch. Left: AQP2 was solubilized in OG. Right: AQP2 bearing membranes were solubilized with SMA leading to the formation of nanodiscs. Both dotblots show a strong signal for AQP2 in the flowthrough, showing that some AQP2 was lost due to insufficient binding to NiNTA. Left: AQP2 did not elute during washing of the NiNTA beads, only a weak AQP2 signal was measured during the 70 mM imidazole wash. A strong signal of AQP2 was measured in the eluted fraction. Right: AQP2 was lost during the washing steps, some AQP2 eluted after 1 hr. incubation in elution buffer (250 mM), but the signal is weaker as compared to OG purification.

AQP2). The nickel affinity of AQP2 was increased by using NaPO_4 (pH 8) in the nickel affinity buffer instead of Tris-HCl (pH 8), but did not lead to comparable purification yields as compared to OG solubilised AQP2. Increasing salt concentrations (500 mM NaCl) did not enhance the nickel affinity of AQP2.

Purified AQP2 bearing nanodiscs were analysed by negative stain TEM (Figure 4.11A) and the size distribution was analysed with DLS, yielding nanodiscs with an average diameter of 16.47 ± 6.021 nm (Figure 4.11B). AQP2 incorporation was monitored by immunofluorescence (Figure 4.11C) and immuno-gold labelling (Figure 4.11D). Gold nanoparticles co-localized with SMA nanodiscs, although unlabelled nanodiscs were found as well. The presence of unlabelled nanodiscs is either caused by insufficient labelling of AQP2 or the presence of empty nanodiscs in the sample. This presence suggests that SMA can interact with the nickel beads and is eluted from this resin after addition of imidazole. Indeed, it was found that SMA can bind to nickel resin due to its negative charge (27). The relative low nickel binding yield of AQP2 bearing nanodiscs, visualized in Figure 4.10B, could be explained, in part, by a-specific binding of empty SMA-nanodiscs to the nickel beads, leading to saturation of these beads.

The above discussed results show that AQP2 can successfully be incorporated into SMA-nanodiscs. By preserving the native lipid environment around AQP2, the stability of the protein can be enhanced. AQP2 bearing nanodiscs can further be used for AQP2-protein interaction studies or structural studies. However, AQP2 activity can not be determined once AQP2 is incorporated into nanodiscs, making it difficult to study the stability of AQP2 in nanodiscs. Furthermore, AQP2 bearing SMA-nanodiscs have a relatively low nickel binding yield leading to a relatively low purification yield. The use of higher salt concentrations in the affinity buffer (up to 1 M NaCl (27)) could limit a-specific SMA-nickel interactions, which could increase the AQP2-nickel binding yield. However, the effect of high salt concentrations on AQP2 stability should be tested. Moreover, the accessibility of the N-terminal his-tag of AQP2 needs to be tested as well. The presence of the native lipid environment surrounding AQP2 or the presence of SMA could hinder interactions between the his-tag and the nickel resin, hindering AQP2-nickel affinity. In chapter 2, the two conformations of the AQP2 N-terminus were discussed (28,29), it could be that, due to the presence of the native lipid environment, the N-terminus is positioned in a less accessible conformation as compared to the OG solubilised AQP2. Further research is necessary to improve AQP2 bearing SMA-nanodisc purification yields.

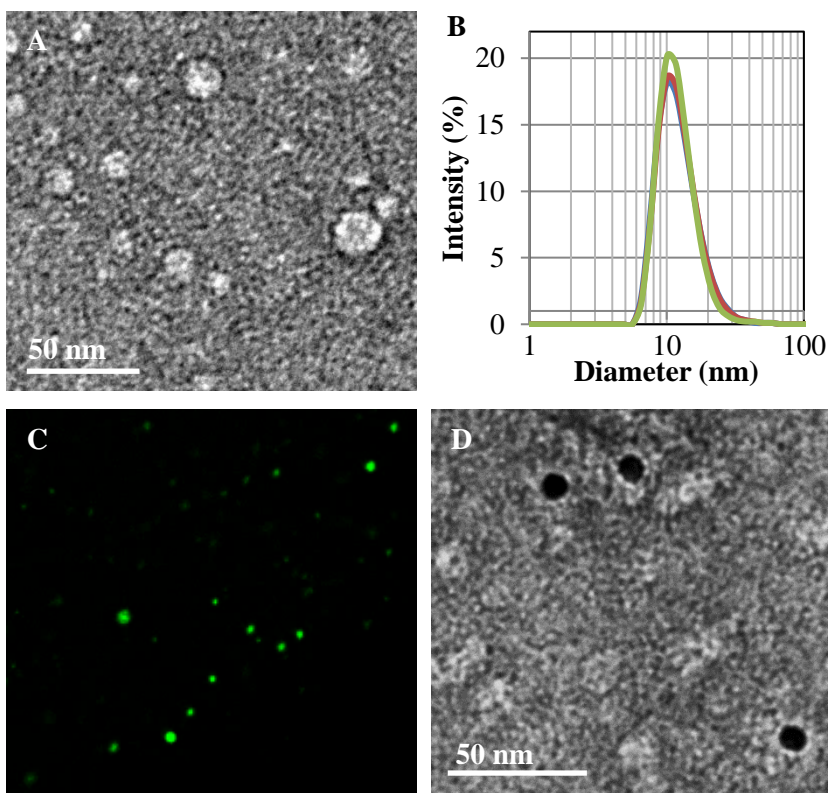


Figure 4.11: (A) Negative stain TEM image of AQP2 bearing SMA nanodiscs. Cell membranes are solubilized by using SMA, leading to the formation of nanodiscs. AQP2 bearing nanodiscs are purified by using NiNTA. Nanodiscs are loaded on a carbon-coated copper EM-grid and stained with 2% Uranyl acetate. The magnification was 25,000x. (B) Intensity based particle diameter distribution, obtained from DLS eluted from the nickel agarose beads. Size distribution was determined from three independent measurements (blue, red and green curve). Average nanodisc size was 16.47 ± 6.02 nm. (C) Immuno fluorescence image of fluorescently labelled AQP2 in SMA-nanodiscs. AQP2 was labelled with a R α AQP2 primary antibody and an Alexa-Fluor conjugated G α R secondary antibody. (D) Negative stain TEM image of immuno-gold labelled AQP2 incorporated in SMA-nanodiscs. AQP2 was labelled with a R α AQP2 primary antibody and a gold ($\varnothing=10$ nm) conjugated G α R secondary antibody. Colocalization of gold particles with SMA-nanodiscs shows correct incorporation of AQP2 in the nanodiscs.

Table 4.3: Lipid composition used during AQP2 reconstitution. Detergent solubilised AQP2 was mixed with the detergent solubilised lipid mixture. Detergent was removed via dialysis, leading to the reconstitution of AQP2 in the lipid bilayer.

Lipid	Concentration
POPC	25%
POPE	30%
POPS	10%
SM	5%
Cholesterol	30%
Fluorescent lipid	1%

4.4: Aquaporin-2 reconstitution

As discussed in chapter 4.3, AQP2 solubilised in OG is not stable over long periods of time. Stability could be enhanced by AQP2 incorporation in nanodiscs, as discussed in chapter 4.3.2. However, our research is focussed on the injection of AQP2 in mpkCCD cells to monitor AQP2 trafficking regulation. For this AQP2 needs to be in an as native state as possible, i.e. AQP2 bearing proteoliposomes. Furthermore, the functionality of the purified AQP2 needs to be tested, which is only possible when AQP2 is incorporated in a closed vesicle. By using AQP2 bearing proteoliposomes, water transport from the proteoliposomes to the environment can be monitored, which is not possible with AQP2 bearing nanodiscs. Therefore, detergent solubilised purified AQP2 was reconstituted in proteoliposomes.

For protein reconstitution, the detergent solubilised protein is mixed with detergent solubilised lipids, after which the detergent is removed, leading to the incorporation of the protein in the lipid bilayer. The protein reconstitution method depends on the detergent used during solubilisation. Detergents with a high critical micelle concentration (CMC) can easily be removed from solution via dialysis or dilution, while detergents with lower CMCs need alternative methods for removal, like biobeads (reviewed in (30) and (31)). OG has a relative high CMC (23-25 mmol/L (32)) and can therefore be removed via dialysis.

As described above, our research is focussed on AQP2 injection in mpkCCD cells and, therefore, an as native reconstituted AQP2 as possible is required. Literature does not provide the exact lipid composition of AQP2 bearing vesicles. Therefore, an estimation was made based on the limited literature available describing AQP2 bearing membranes (33-35) and the lipid composition from well-studied vesicle transport mechanisms (36-38). From this, a lipid composition was determined as shown in Table 4.3, with the addition of a fluorescent lipid (DHPE-TRITC) to monitor the proteoliposome trafficking after injection in mpkCCD cells.

Here AQP2 reconstitution in proteoliposomes will be discussed. AQP2 incorporation was measured via fluorescence microscopy, while the proteoliposome size distribution was determined by DLS and negative stain TEM. Furthermore, AQP2 activity was measured with a home-made rapid mixing device.

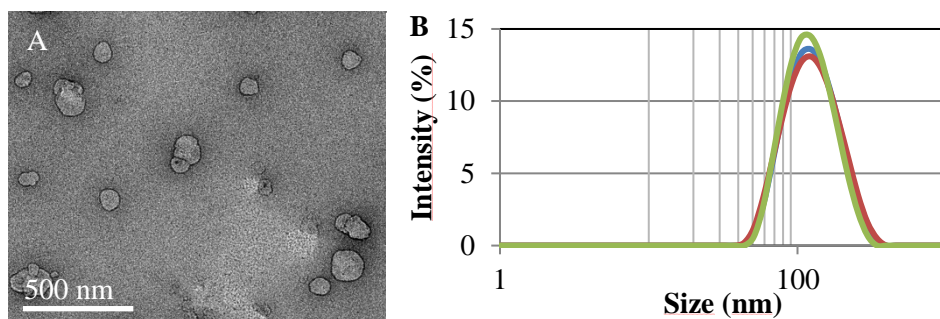


Figure 4.12: (A) Negative stain TEM image of AQP2 bearing proteoliposomes. OG-purified AQP2 was mixed with an OG solubilized lipid mixture with an LPR of 50. The OG was removed via dialysis. Dialysis buffer was refreshed every 48 hrs. Proteoliposomes were extruded through a 100 nm filter, loaded on a carbon-coated copper EM-grid and stained with 2% Uranyl acetate. Magnification was 13,000x. (B) Size distribution of AQP2 bearing proteoliposomes. Size distribution was determined via DLS from three different measurements (blue, red and green). All measurements show comparable results. Proteoliposomes had a mean diameter of 105 ± 49 nm.

4.4.1: Aquaporin-2 bearing proteoliposomes

After purification AQP2 was reconstituted in proteoliposomes, containing the lipid composition given in Table 4.3, via dialysis. For this, OG solubilised AQP2 was mixed with the OG solubilised lipid mixture and the solution was dialysed for 1 week at room temperature. Sufficient detergent removal was determined by eye by pipetting a $50\mu\text{L}$ sample on a hydrophobic surface, leading to a compact droplet on this surface. Proteoliposomes were then extruded through a 100 nm filter to obtain unilamellar vesicles and a relatively homogeneous size distribution. The average liposome diameter, determined by DLS, was $\sim 105\pm 49$ nm after extrusion, where the vesicle diameter ranged between 50 and 300 nm (Figure 4.12A). AQP2 bearing proteoliposomes were visualized by using negative stain TEM, showing that spherical proteoliposomes were formed (Figure 4.12B).

Although both TEM and DLS show the formation of liposomes after dialysis and extrusion, correct incorporation of AQP2 in the proteoliposomes is not visualized with these methods. For this, immuno fluorescence assays were used, where AQP2 was fluorescently labelled by using a Rabbit-anti-AQP2 antibody as primary antibody and an Alexa Fluor conjugated Goat-anti-Rabbit antibody as secondary antibody. The liposomes were visualized by using the fluorescently labelled lipid during AQP2 reconstitution. Fluorescence microscopy showed correct incorporation of AQP2 in the liposomes (Figure 4.13 top), although some liposomes did not show any AQP2 signal. This could either mean that AQP2 was not reconstituted in all liposomes, or that the fluorescent signal was too weak to measure. Empty liposomes did not show any AQP2 signal after immuno fluorescence labelling (Figure 4.13 bottom), showing that the measured green fluorescence found in proteoliposomes is indeed reconstituted AQP2.

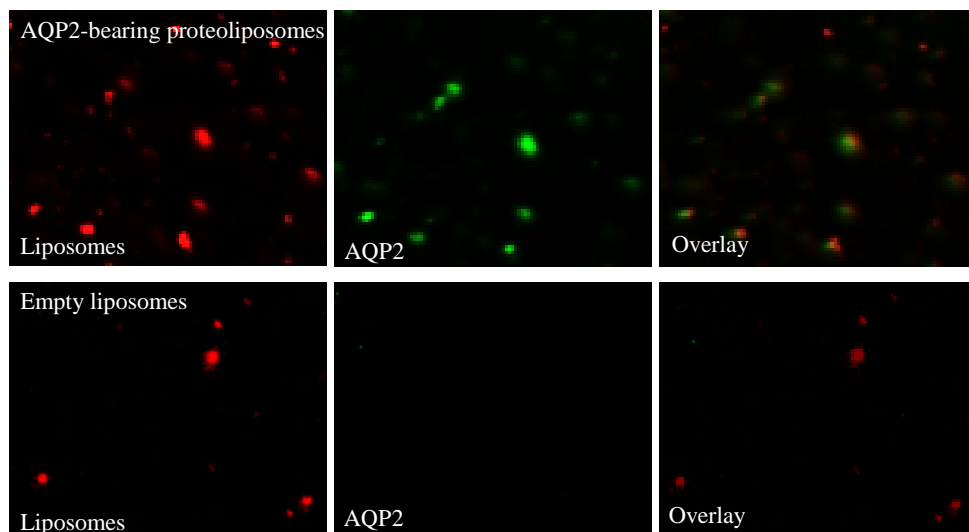


Figure 4.13: AQP2 reconstituted in proteoliposomes. Reconstitution of AQP2 in proteoliposomes was monitored by using fluorescence microscopy. Top: AQP2 bearing proteoliposomes, bottom: empty liposomes. Left, (proteo)liposomes were fluorescently labelled by incorporating 1% Tritc-DHPE in the lipid bilayer (red). Middle, AQP2 was fluorescently labelled by using a rabbit-anti-AQP2 antibody, recognizing the C-terminus of AQP2, and a goat-anti-rabbit antibody Alexa Fluor conjugated (green). Right, overlay of the AQP2 signal and the (proteo)liposome signal. For AQP2 bearing proteoliposomes (top) green and red fluorescence overlap, showing correct incorporation of AQP2 in the lipid bilayer. Liposomes (bottom) do not show any green fluorescence signal, showing the absence of AQP2 in these bilayers.

4.4.2: Aquaporin-2 activity measurements

Although Figure 4.13 shows that AQP2 is correctly incorporated in the proteoliposomes, the activity of AQP2 after purification is not shown. Werten et al. used a stopped-flow apparatus to measure water transport of AQP2 reconstituted in proteoliposomes (6). Water transport was activated by rapidly mixing AQP2 bearing liposomes with a high concentration of sucrose, leading to a large osmotic difference between the interior of the liposomes and the outside environment. This osmotic difference induces water to permeate through AQP2 from the liposomes towards the high sucrose environment, leading to shrinkage of the proteoliposomes. This shrinkage can then be measured by monitoring the scattering of the incoming laser beam at an angle of 90° . When using AQP2 bearing proteoliposomes with an LPR of 60, equilibrium is reached within 0.1 sec. This shows the necessity of a rapid mixing machinery. Even when AQP2 is absent, equilibrium is reached within 0.6 sec. caused by water transport over the lipid bilayer.

Stopped-flow machines have been used extensively to study AQP water transportation. However, these machines are relatively expensive and were not available at our department. Therefore, we developed our own machinery capable of both mixing proteoliposomes with high concentration sucrose buffer in a rapid manner and measuring the light scattering at a 90° angle (Figure 4.14). Our machine carries two vials, one containing proteoliposomes, the other containing sucrose buffer, which are kept under pressure (2 bar). The pressure pushes both liquids towards a mixing cuvette where they are mixed. This cuvette holds ~4μL of volume. The cuvette is kept closed by using a computer-controlled pressure valve connected to the outlet (~45μL volume between the mixing cuvette and the pressure valve). A laser is directed through the bottom of the cuvette, while a detector measures the light scattering at a 90° angle. For experiments, the pressure valve is opened for 30 msec., leading to the injection of proteoliposomes and sucrose buffer into the mixing cuvette and the release of the old mixture into the outlet. After the valve is closed, the light scattering is measured by the detector. Light scattering was measured for 3 sec. after that a new measurement can be started by opening the pressure valve.

Proteoliposomes (LPR 60 and LPR120) and control liposomes were mixed with sucrose buffer (420 mM) to induce an inwardly directed osmotic gradient. The shrinkage of the liposomes was measured over time by monitoring the change in intensity of the scattered light. AQP2 activity was inhibited by incubating AQP2 bearing proteoliposomes for 15 min in the presence of 1 mM HgCl₂. Liposomes reached saturation ~1400 msec after mixing with sucrose, comparable results were obtained with proteoliposomes (LPR60 and LPR120) incubated in 1 mM HgCl₂ (Figure 4.15; green, purple (A) and orange (B) curve respectively). Proteoliposomes with LPR60 reached saturation ~400 msec after mixing was initiated (Figure 4.15A, red curve), while proteoliposomes with LPR120 reached saturation ~700 msec after mixing (Figure 4.15B, blue curve). The light scattering traces were averaged, normalized and fitted to a single exponential function to obtain rate constant K (chapter 4.6 eq. 1). K was used to calculate the osmotic permeability coefficient (P_f) as discussed in chapter 4.6 eq. 2. The determined P_f for liposomes was 7.8 μm/s, while proteoliposomes incubated in 1 mM HgCl₂ had a P_f of 8.8 μm/s (LPR60) and 7.2 μm/s (LPR120)(Table 4.4). The determined P_f of AQP2 bearing proteoliposomes was corrected for the corresponding P_f of proteoliposomes incubated in 1 mM HgCl₂ and resulted in a corrected P_f of 17.4 μm/s for proteoliposomes with LPR60 and a corrected P_f of 6.2 μm/s for proteoliposomes with LPR120 (Table 4.4). The water permeability of a single AQP2 monomer can be determined by dividing the P_f of proteoliposomes by the single channel density (SuD), which can be calculated by using Eq. 5 from chapter 4.6. The amount of AQP2 monomers per proteoliposome can be estimated by using Eq. 3 and 4 from chapter 4.6. On average one proteoliposome with LPR60 carries 23 monomers, while a proteoliposome with LPR120 carries 7 monomers of AQP2 on average. These estimates result in a single water permeability (p_f) of 1.4x10⁻² μm³/s for LPR60 and a p_f of 1.0x10⁻² μm³/s for LPR120 (Table 4.4). Although the determined p_f from LPR60 and LPR120 are comparable, these values differ from the p_f determined by Werten *et al.* (6).

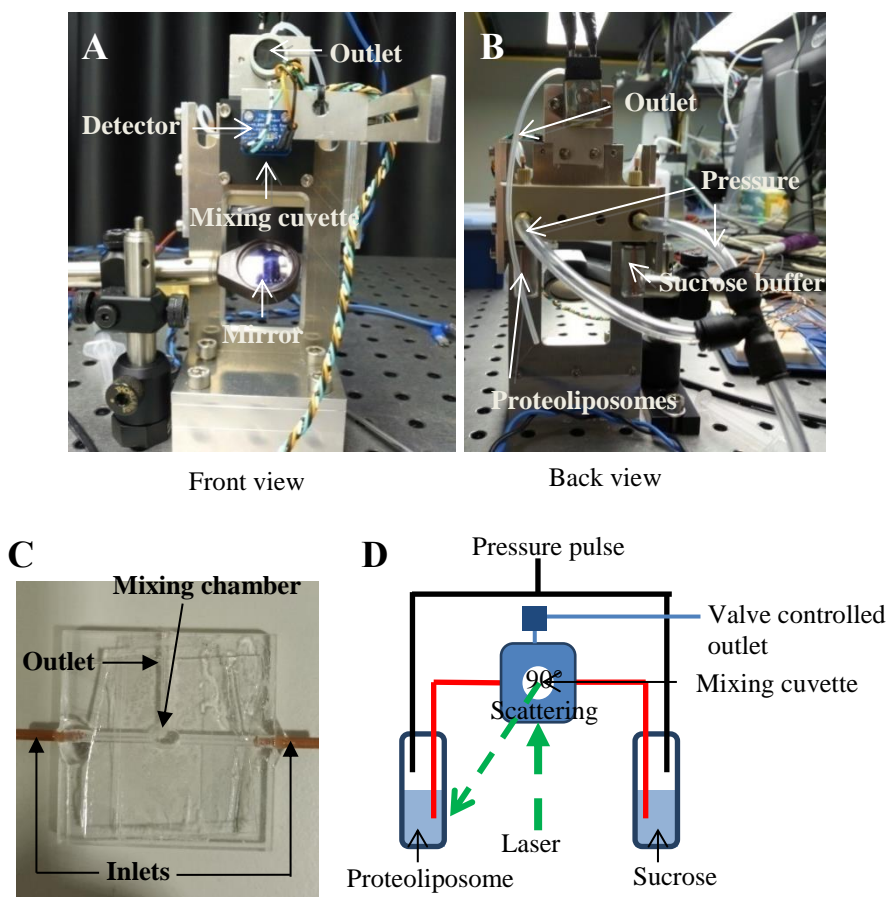


Figure 4.14: Rapid mixing device. AQP2 water transport over the lipid bilayer in proteoliposomes is measured by rapidly mixing AQP2 bearing proteoliposomes with a sucrose buffer. The increased environmental osmolarity induces excretion of water from the proteoliposomes to the sucrose containing environment until equilibrium is reached. Water excretion leads to shrinkage of the proteoliposomes. Liposome shrinkage is detected by measuring the change in laser scattering at an angle of 90° . (A) Front view of the rapid mixing device. A laser beam is focussed into the mixing chamber via the mirror. The detector measures the scattered light at an angle of 90° . The outlet of the mixing cuvette is controlled by a pressure valve. Rapid mixing of two fresh solution volumes ($50\ \mu\text{L}$) and ejection of used mixture occurs during opening of the valve during 50 ms. (B) Back view of the rapid mixing device. Two tubes are kept under pressure (2 bar). The left tube contains (proteo) liposomes, the right tube contains a sucrose buffer. The pressure pushes both liquids into the mixing cuvette (front) inducing water excretion from the (proteo)liposomes. (C) The mixing cuvette. Two inlets come together at the mixing chamber with a height of 1 mm, a width of 2 mm and a thickness of 1 mm. The outlet has a diameter of 1.5 mm. The mixing chamber is closed by two glass plates. (D) A schematic overview of the mixing device.

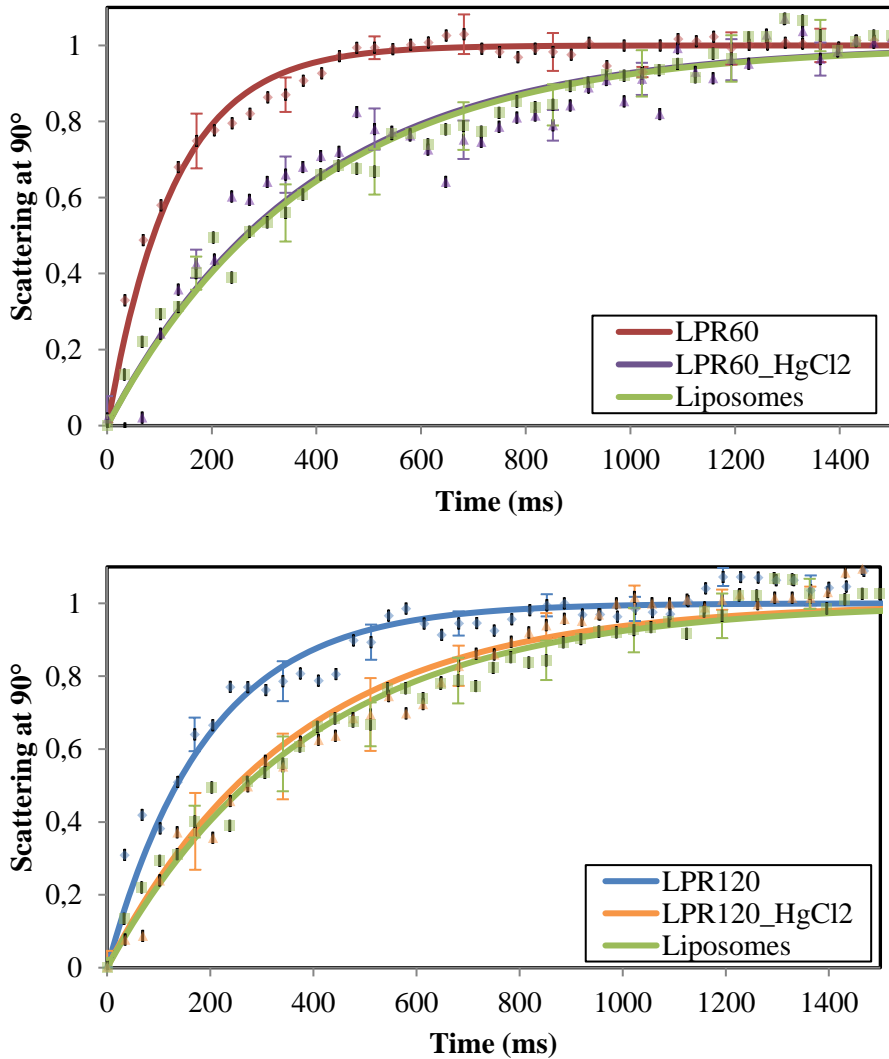


Figure 4.15: Activity measurements of AQP2 by the rapid mixing device. Reconstituted AQP2, with LPR 60 (A) and LPR120 (B) was mixed with equal volumes of 420 mM sucrose buffer and the change in light scattering at a 90° angle was measured. Upon mixing an increase in light scattering was measured. (A) AQP2 bearing proteoliposomes (LPR60) reached equilibrium ~400 msec after mixing (red curve; N=12), while liposomes reached equilibrium ~1400 msec after mixing (green curve; N=12). AQP2 activity could be inhibited by incubation in 1mM HgCl₂(purple curve; N=9). (B) AQP2 bearing proteoliposomes (LPR120) reached equilibrium ~700 msec after mixing (blue curve, N=17). AQP2 activity could be inhibited by incubation in 1 mM HgCl₂ (orange curve; N=8), leading to comparable results as obtained with liposomes (green curve; N=12). Error bars are ±S.E.

Table 4.4: Quantification of AQP2 activity based on the curves of Figure 4.15. Empty liposomes do not carry AQP2 tetramers, while proteoliposomes incubated with HgCl₂ carry inactive AQP2. Therefore, the SuD and p_f cannot be determined for these samples.

	AQP2-proteoliposomes				Liposomes
	-HgCl ₂		+HgCl ₂		
	LPR60	LPR120	LPR60	LPR120	
Liposome diameter (nm)	76	58.8	76	58.8	69
K (s ⁻¹)	7.83	5.15	2.63	2.77	2.58
P _f (μm/s)	17.4*	6.2*	8.8	7.2	7.8
SuD (μm ²)	1263.37	612.46			
p _f (μm ³ /s)	0.014	0.010			

*P_f of AQP2 bearing proteoliposomes was determined by subtracting the P_f of HgCl₂ incubated proteoliposomes from the P_f value derived from Eq 2.

4.5: Conclusion

Production and purification of membrane proteins requires overexpression of the protein of interest, for protein concentrations are too low to obtain high yields of pure protein from native tissue. To reach this, dedicated expression systems are necessary. AQP2 is a mammalian, human, protein and undergoes posttranslational modifications. Although functional AQP2 was successfully purified from *E. coli* cells previously (1), our research is focussed on producing an as native AQP2 as possible. Therefore, AQP2 was expressed in, and purified from eukaryotic expression systems, i.e. *P. pastoris* and baculovirus infected *Sf9* cells. Both *Sf9* cells and *P. pastoris* are relatively easy to handle, they grow relatively fast and do not need elaborate requirements in their growing medium.

Although AQP2 can be produced in *Sf9* cells, the method is not robust and over-expression depends on a range of different variables, like cell viability at the start of infection, the passage number of the *Sf9* cells, baculovirus stability in solution and the infection rate of *Sf9* cells. Furthermore, optimal AQP2 over-expression depends on the duration of the viral infection and the viral titer, which both must be determined experimentally. Too low viral titers or too short viral infections lead to sup-optimal expression of AQP2 (Figure 4.3), while too much baculovirus or too long viral infections lead to AQP2 degradation caused by cell death (Figure 4.3, Table 4.2). AQP2 over-expression in *P. pastoris* is a more reproducible method. However, the optimal expressing yeast strain needs to be determined experimentally and different *P. pastoris* strains need to be explored and optimized for each mutant of AQP2. With *Sf9* cells, the same cell strain can be used to produce a wide variety of different AQP2 mutants, depending on the virus stocks available (Table 4.1).

Higher yields of purified AQP2 could be obtained from *P. pastoris* cells as compared to *Sf9* cells. From *Sf9* cells ~0.5-1 mg of pure AQP2 was obtained from ~15 gr of membranes (4 L of *Sf9* cell culture), while ~10-15 mg of pure AQP2 was obtained from an equal amount of *P. pastoris* membranes. However, lysis of *P. pastoris* is challenging due to the cell wall of

this yeast strain. *Sf9* cells can easily be lysed by using a douncer homogenizer, a sonicator or a combination of these methods, while lysis of *P. pastoris* needs more dedicated methods and often a combination of different methods is used. In our hands, the optimal method to lyse *P. pastoris* was by using a combination of enzymatic cell wall degradation and sonication, while others achieved good cell lysis by either using a French press, a bead beater or Cryo-milling. All methods have their advantages and limitations and each method needs to be optimized to obtain sufficient cell lysis. After the cells are lysed, AQP2 is purified in the same manner from both *Sf9* cells as well as *P. pastoris*.

The best eukaryotic expression system to use depends on the desired yield, the resources available and the variety of desired protein mutants. In our research, a broad range of different AQP2 mutants needs to be produced and purified (Table 4.1). Although a broad range of different *P. pastoris* strains can be prepared and optimized to produce different AQP2 mutants, the use of *Sf9* cells is slightly more flexible and production of different AQP2 mutants is therefore easier to achieve. Furthermore, yeast cell lysis needs dedicated techniques or expensive materials while *Sf9* cells are relatively easy to lyse, making it easier to purify eukaryotic proteins from *Sf9* cells. However, if a high yield is the main goal, it is best to use *P. pastoris* as the expression system.

Membrane protein purification is not trivial. During purification, the hydrophobic domains of the protein need to be protected. This protection can be achieved by either solubilising the protein in detergent or by the formation of nanodiscs, capturing the membrane protein in a small, native, lipid domain. Although detergents protect the hydrophobic domains of the protein, the stability of the protein is affected by the removal of the native lipid environment. The stability of the membrane protein depends on the detergent used and needs to be determined experimentally. Furthermore, the detergent used should be compatible with the downstream processes after purification, like the desired method for reconstitution. Even if the optimal detergent is found, the membrane protein is not stable in detergent for a long period of time and to enhance the stability of the protein, the protein needs to be reconstituted in a lipid bilayer. Membrane proteins recruit dedicated lipids to enhance their stability in the membrane (13-16), therefore protein reconstitution does not always ensure proper protein stability. To retain AQP2 in its native lipid environment, AQP2 could be purified by forming nanodiscs. For this the co-polymer styrene-maleic acid (SMA) was used. Although AQP2 incorporation in nanodiscs did decrease the nickel binding affinity of AQP2 (Figure 4.10), AQP2 bearing nanodiscs could be purified from *Sf9* cells (Figure 4.10 and -11). However, the activity of AQP2 can only be measured in an environment containing different compartments, separated by a lipid bilayer. Nanodiscs do not provide such a separation and therefore the activity of AQP2 cannot be measured once incorporated into a nanodisc. Furthermore, for our purpose, AQP2 needs to be reconstituted in a proteoliposomes, for proteoliposomes mimic the native AQP2 bearing vesicles of the cell, and these proteoliposomes need to be fluorescently labelled so that they can be tracked after injection in the cell. To achieve maximum AQP2 stability and to mimic the native AQP2 bearing vesicles as much as possible, the native lipid composition was estimated from literature and

used for AQP2 reconstitution (Table 4.3). AQP2 was successfully reconstituted into proteoliposomes (Figure 4.12 and -13) and had an average diameter of 105 nm after extrusion.

Although Figure 4.13 shows AQP2 incorporation in the lipid bilayer, the number of reconstituted AQP2 tetramers per liposomes cannot be determined from these experiments. Furthermore, although some proteoliposomes do not show any signal for AQP2, it does not mean that they do not carry any AQP2 tetramers. The antibody used binds to the C-terminus of AQP2. During reconstitution, the incorporation of AQP2 in the lipid bilayer cannot be controlled, meaning that the C-terminus can be positioned towards the aqueous environment, as it is *in vivo*, or positioned in the interior of the proteoliposome. Once this is the case, the antibody cannot bind to AQP2 and no fluorescent signal can be measured for this AQP2. Furthermore, AQP2 tetramers are not evenly divided amongst all proteoliposomes, meaning that some proteoliposomes carry many AQP2 tetramers, while others carry only one tetramer or none. The fluorescent signal for just one tetramer in a proteoliposome could be too low to measure.

By using Eq. 3 and Eq. 4, it was estimated that a proteoliposome reconstituted with an LPR of 60 and an average diameter of 76 nm, carried on average 23 AQP2 monomers. However, this estimation does not take into account possible aggregation of the protein or incomplete reconstitution, leading to a possible higher estimation as compared to reality. A better estimation could be obtained from Freeze fracture EM (39-42), where the proteoliposomes are frozen, fractured, etched and platinum shadowed, making it possible to count the AQP2 tetramers. Reconstitution of SoPiP2;1, an aquaporin expressed in spinach leaf plasma membranes, at an LPR of 100 leads to an average of 5 tetramers per proteoliposome and 13 AQP2 tetramers per liposome at LPR 50 (43). The results obtained from freeze fracture EM suggest that the initial estimation of 23 AQP2 monomers per proteoliposome (LPR60) is reasonable. However, the calculated p_f for AQP2 was lower as compared to previous measurements (6), suggesting that reconstitution was suboptimal and possibly the estimate of 23 AQP2 monomers per proteoliposome (LPR60) was too high. Although incorrect liposome size determination or insufficient mixing with sucrose could not be excluded either. The p_f value found for AQP2 bearing proteoliposomes with LPR120 was in good agreement with the p_f value found for LPR60 proteoliposomes (Table 4.3). Furthermore, AQP2 activity was successfully inhibited by incubation in $HgCl_2$, showing now difference with empty liposomes (Figure 4.15, Table 4.3). These results show that this set-up provides a reliable method to determine AQP2 activity after reconstitution.

The produced AQP2 bearing proteoliposomes can be monitored by fluorescence microscopy, while they carry active AQP2. The next step will be to inject these proteoliposomes into mpkCCD cells to monitor AQP2 trafficking depending on its phosphorylative state. To perform this task, the hollow cantilever set-up needs to be tested and optimized. The set-up will be discussed into more detail in chapter 5 and chapter 6.

4.6: Material and Methods

AQP2 incorporation in DH10Bac cells – The *aqp2* gene was incorporated in the pFastBac™ HT vector according to the Bac-to-Bac® Baculovirus Expression system manual provided by Invitrogen. The pFastBac™ HT vector was then transformed in DH10Bac Compotent *E. coli* cells (Invitrogen), incubated for 4 hrs at 37°C, while shaking at 225 rpm, and plated on LB-agar plates containing 50 µg/mL kanamycin, 7 µg/mL gentamycin, 10 µg/mL tetracycline, 100 µg/mL Bluo-gal and 40 µg/mL IPTG. The plates were incubated for 48 hrs at 37°C until clear blue and white colonies were formed. White colonies were picked and cultured overnight (O/N) in 2 mL LB medium containing 50 µg/mL kanamycin, 7 µg/mL gentamycin and 10 µg/mL tetracycline at 37°C (250 rpm). After O/N incubation, DNA was purified from the *E. coli* cells following the miniprep (Qiagen) guidelines. Purified DNA was checked for correct incorporation of the *aqp2* gene via PCR, following the instructions of the manual and DNA concentration was measured via Nanodrop.

Sf9 cell culture – *Sf9* cells were grown in ESF921-protein free insect cell medium (Expression systems) at 27°C while shaking at 130 rpm. 50 mL of insect cell culture medium was grown in 125 mL PC Erlenmeyer flasks (Fisher Scientific), while 100 mL culture was grown in 250 mL flasks and 200 mL culture was grown in 500 mL flasks. For AQP2 production, *Sf9* cells were grown in 3,000 mL Baffled Fernbach flasks (BioExpress) able to hold 1,000 mL of cell culture. The baffles in the flask ensure proper oxygen uptake by the cells. During cell transfer a minimum cell concentration of 0.5×10^6 cells/mL was cultured.

Baculoviral DNA transfection and virus amplification -- 8×10^5 Log phase *Sf9* cells were cultured in a well of a 6 well plate, while 8 µL Cellfectin® was mixed with 15 µg DNA for each transfection and 200 µL ESF921-protein free insect cell medium (Expression systems). Cells were left to attach and the transfection mixture was incubated for 15-30 min at room temperature (RT). 200 µL of transfection mixture was dropwise added to each well. The cells with transfection mixture was incubated for 3-5 hrs at 27°C, after which the transfection mixture was removed. Production of *aqp2*-carrying baculoviruses was achieved by incubating the cells for 72 hrs at 27°C. After incubation, viruses were harvested from the wells and amplified to produce high viral titers. Optimal virus volume for high yield AQP2 production was determined via dot-blot analysis (see in material and methods section) and cell life/death count. For cell life/death count, cells were stained with equal volumes of trypan blue.

AQP2 expression in Sf9 cells – 2×10^6 *Sf9* cells were cultured in 1,000 mL ESF921-protein free insect cell medium (Expression systems) and 5 mL of virus was added. *Sf9* cells were incubated for 72 hrs at 27°C while shaking at 130 rpm. After incubation a 200 µL sample was taken to monitor AQP2 expression via western blot analysis and cells were harvested by centrifuging at 500 g at 4°C for 20 min. Cells were flash-frozen in liquid nitrogen and stored at -80°C until purification.

Sf9 cell lysis — *Sf9* cells are thawed and mixed via a douncer homogenizer (Thomas scientific) with breaking buffer (5 mM Trish-HCl pH8, 100 mM NaCl, 1 mM EDTA) in a ratio of 1:3 (cells:breaking buffer; v/v). One tablet of cOmpete protease inhibitor (SigmaAldrich) was added per 50 mL of volume. Cells were broken by sonicating for 10 min

at 50% intensity, in cycles of ON/OFF of 30 sec. Unbroken cells were pelleted by centrifuging for 15 min at 500 rpm and 4°C.

P. pastoris culture – AQP2-WT producing *P. pastoris* strains were kindly provided by Prof. Robert Fenton from the Biomedicine department of Aarhus University, Denmark. On day 1, *P. pastoris* was streaked on a YPD plate and incubated at 30°C for 24 hrs.

The next day, a single colony was picked and inoculated in 50 mL BMGY medium (1% Yeast Extract, 2% Peptone, 100 mM Potassium Phosphate buffer pH6.0, 1% Glycerol, 1.34% YNB stock, 4×10^{-5} % Biotin) containing 200 μ L Zeocin (Sigma-Aldrich). The culture was incubated for 24-48 hrs at 29°C at 120 rpm until OD₆₀₀ = 2-6, after which the cells are harvested by centrifugation for 15 min at 5,000 g. After harvesting, the supernatant was discarded and the pellet was washed with BMMY medium (1% Yeast Extract, 2% Peptone, 100 mM Potassium Phosphate buffer pH6.0, 0.5% Methanol, 1.34% YNB Stock, 4×10^{-5} % Biotin) to remove residual traces of glycerol. The cells are collected by centrifuging for 15 min at 5,000 g. After harvesting, the *P. pastoris* cells are resuspended in BMMY medium to an OD₆₀₀ of 1 and are incubated in baffled flasks at 29°C and 200 rpm until OD₆₀₀ = 12 (~72 hrs). Every 24 hrs 0.5% Methanol is added to compensate for Methanol uptake and a sample was taken for AQP2 production analysis. Once OD₆₀₀ = 12, the cultures are harvested by centrifuging for 15 min at 4°C and 6,000 g. Harvested cells are snap frozen and stored at -80°C until purification.

Zymolyase P.pastoris lysis — Thaw the *P. pastoris* cells and resuspend in breaking buffer (5 mM Tris-HCl pH8, 100 mM NaCl, 1 mM EDTA) by using a douncer homogenizer (Thomas Scientific) at an Abs₈₀₀ of 1. Add 200 μ g of Zymolyase (10mg/ml; Zymo Research) per mL suspension. Incubate for ~1 hr at 37°C, while shaking. The Abs₈₀₀ can be measured to track cell lysis, a decrease in Abs₈₀₀ indicates cell lysis. During incubation the solution will look pinkish and cell will be sticky once they become spheroplasts. After successful cell lysis, AQP2 purification can start as discussed below.

AQP2 purification –Membranes of either *Sf9* cells or *P. pastoris* were separated from soluble proteins by using a Beckman Coulter Optima L-90K Ultracentrifuge carrying the 45Ti rotor. Membranes were pelleted by centrifuging for 1 hr at 4°C and 100,000 g. Membranes are stripped from loosely bound proteins by Urea/Alkaline wash. Membranes were homogenized in Urea buffer (5 mM Tris-HCl pH8, 5 mM EDTA, 4 M Urea), pelleted via ultracentrifugation as described above, followed by homogenization in Alkali buffer (20 mM NaOH) and pelleting via ultracentrifugation as described above. The pH was restored by homogenizing the pellet in pH restore buffer (5 mM Tris pH8, 100 mM NaCl) and membranes were collected via ultracentrifugation. The stripped membranes were then solubilized in solubilization buffer (20 mM NaPO₄ pH7.8, 200 mM NaCl, 2 mM β -mercaptoethanol, 5% Glycerol, 0.01% NaN₃, 20 mM Imidazole) and *N*-octyl- β -D-glucopyranoside (OG). Detergent was added in a ratio of 2:1 (membranes:detergent; w/w), while the maximum detergent concentration was set to 5%. Membranes were incubated in solubilization buffer for 2 hrs at 4°C followed by incubation for 1 hr at RT. The insolubilized fraction was harvested by ultracentrifugation as described above. The solubilized fraction was diluted with solubilization buffer to obtain a detergent concentration of 2%, NiNTA beads were added and incubated O/N at 4°C while stirring slowly. The NiNTA beads were collected in a 20 mL Econo-Pac Chromatography column (Bio-Rad) and were washed with

20 column volumes (CV) of wash buffer 1 (20 mM NaPO₄ pH7.8, 200 mM NaCl, 1.5% OG), 10 CV of wash buffer 2 (20 mM NaPO₄ pH7.8, 200 mM NaCl, 20 mM Imidazole, 1.5% OG) and 10 CV of wash buffer 3 (20 mM Tris-HCl pH7.5, 200 mM NaCl, 70 mM Imidazole, 1.5% OG). AQP2 was eluted by adding 1 mL of elution buffer (20 mM Tris-HCl pH7.5, 200 mM NaCl, 250 mM Imidazole, 1.5% OG) and incubation for 10 min. This step was repeated multiple times, while the protein concentration was measured via nanodrop. Once the protein concentration of eluted fractions drops, the elution was completed. Eluted fractions were analysed on a 12% SDS-gel and via westernblot. Pure fractions were pooled together and concentrated with an Amicon Ultra-15 centrifugal filter, cut-off 50 kDa (Millipore). The concentrated protein was loaded on an equilibrated (20 mM Tris-HCl pH7.5, 200 mM NaCl, 1.5% OG) Superose 6 10/300GL column and collected fractions were analysed with negative stain TEM.

AQP2-incorporated nanodisc purification – *Sf9* cells were lysed and stripped as described above. Membranes were solubilized in solubilization buffer (20 mM NaPO₄ pH7.8, 500 mM NaCl, 5% glycerol, 2.5% SMA) and incubated for 3 hrs at RT while gently shaking. The insoluble fraction was collected with a Beckman Coulter Optima L-90K Ultracentrifuge carrying the 45Ti rotor, centrifuging for 1 hr at 4°C and 100,000 g. NiNTA beads were added to the solubilized membranes and the mixture was incubated O/N at 4°C while gently stirring. Beads were collected in a 20 mL Econo-Pac Chromatography column (Bio-Rad), washed with 20 CV of washing buffer 1 (20 mM NaPO₄ pH7.8, 200 mM NaCl), followed by 10 CV of washing buffer 2 (20 mM NaPO₄ pH7.8, 200 mM NaCl, 20 mM Imidazole) and 10 CV of washing buffer 3 (20 mM Tris-HCl pH7.5, 200 mM NaCl, 70 mM Imidazole). AQP2 was eluted by incubating the NiNTA beads in 1 mL elution buffer (20 mM Tris-HCl pH7.5, 200 mM NaCl, 250 mM Imidazole) for 1 hr. AQP2 elution was detected via dotblot analysis. Size distribution was determined via dynamic light scattering (Zetasizer ZS (Malvern); DLS) and the presence of nanodiscs in the sample was monitored via negative stain TEM.

Westernblot or dotblot analysis – Samples were loaded on a 12% SDS-gel and run for ~1 hr. at 180 V, until sample buffer reached the bottom of the gel. SDS-gels were blotted on Immun-Blot® Polyvinylidene Difluoride (PVDF) membranes (Bio-RAD) using a semidry transfer cell (Novex, Semi-Dry Blotter, Invitrogen) and transfer buffer (25 mM Tris base, 192 mM Glycine, 20% MetOH, 0.05% SDS). For dot blot, samples were loaded on PVDF membranes and left to incubate in air for 2 hrs. After blotting or sample loading, the membrane was blocked for 1 hr at RT in TBS-T (10 mM Tris pH7.5, 150 mM NaCl, 0.1% Tween-20) containing 5% milk powder, followed by 1 hr incubation at RT with a polyclonal primary antibody goat anti rabbit AQP2 (a kind gift from Prof. Robert Fenton from Aarhus University; 1:5,000). After incubation, the membrane was washed for 3 x 15 min with TBS-T followed by 1 hr incubation at RT with the secondary antibody horseradish peroxidase (HRP) conjugated goat anti rabbit IgG (Thermo Scientific; 1:40,000) and 3 x 15 min wash with TBS-T. Chemiluminescence was activated by using the Supersignal™ West Pico Rabbit IgG detection kit (Thermo Scientific) and signal was detected with a Gel Doc™ XR+Gel documentation system (Bio-RAD).

AQP2 reconstitution – Lipids (Avanti Polar Lipids, overview in **Table 4.3**) were dissolved in 5% OG (Anatrace) in a total lipid concentration of 25 mg/mL. The lipid solution was sonicated in a Branson 2510 Ultrasonic Cleaner to induce proper solubilisation of the

lipids. AQP2 was mixed with the lipid mixture to a final lipid concentration of 10 mg/mL and an LPR of 60 or 120 (w/w). AQP2 concentration was determined via nanodrop and BCA measurements (Pierce; ThermoFisher Scientific). Detergent was removed by dialysis for 1 week against 20 mM Tris-HCl pH7.5, 200 mM NaCl. After incubation, liposome size was homogenized by extruding the proteoliposomes through a 100 nm pore-size filter (Avanti mini extruder). After 30 passages, liposomes size distribution was analysed by DLS (Zetasizer ZS, Malvern) and negative stain TEM. AQP2 incorporation was detected by fluorescently labelling of AQP2. An R α AQP2 antibody (kind gift from Prof. Robert Fenton, Aarhus University) was added (1:5,000) to 100 μ L of proteoliposomes and left to incubate for 1 hr. at RT. Liposomes were harvested by centrifugation (10,000 g, 15 min.) and washed three times with washing buffer (20 mM Tris-HCl pH7.5, 200 mM NaCl). An Alexa-488 conjugated G α R antibody (Abcam; 1:1,000) was added as a secondary antibody and left to incubate for 1 hr followed by three washing steps with washing buffer. Fluorescent signal was visualized with a Motic AE31 inverted light microscope with a fluorescent attachment, images were taken with an Andor iXon ultra 897 camera.

Negative Stain Transmission Electron Microscopy – 3 μ L samples were pipetted on carbon-coated copper TEM-grids rendered hydrophilic by glow discharge in air at low pressure. Samples were incubated for 1 min at RT, followed by 3 times washing in distilled water. Sample were stained by pipetting 3 μ L of 2% Uranyl Acetate and 1 min incubation at RT. 400 mesh TEM-copper grids were purchased from Electron Microscopy Sciences and coated with an 8 nm thick carbon film produced in a Cressington 208 carbon coater where the thickness was measured by using a JEOL FC-TM10 thickness monitor. Grids were examined with a JEOL JEM-1400plus transmission electron microscope and images were recorded with a Gatan Orius.

AQP2 bearing SMA-nanodisc labelling—SMA-nanodiscs were concentrated with an Amicon Ultra-15 centrifugal filter, cut-off 50 kDa (Millipore). 1 mL containing the primary antibody (R α AQP2; 1:5,000) was mixed with the concentrated nanodiscs and incubated for 1 hr at RT while shaking. After incubation, the unbound antibody was removed from the nanodiscs by centrifuging the nanodiscs in the concentrator (3,000 g, 15 min. 4°C). Nanodiscs were washed 2x by adding washing buffer (20 mM Tris-HCl pH7.5, 200 mM NaCl) and removing the washing buffer by centrifugation as described above. For fluorescent labelling of AQP2, 1 mL of a secondary antibody solution was added (Alexa-fluor conjugated G α R (Abcam; 1:1,000)) and solution was left to incubate for 1 hr at RT while shaking followed by removal of unbound antibody and 2 washing steps as described above. Fluorescently labelled AQP2 was then visualized with a Motic AE31 inverted light microscope with a fluorescent attachment, images were taken with an Andor iXon ultra 897 camera. For immuno-gold labelling of AQP2, 3 μ L of primary antibody labelled AQP2 was pipetted on a carbon-coated copper TEM grid rendered hydrophilic by glow discharge as discussed above (Negative stain TEM) and incubated for 1 min at RT. The excess of fluid was removed by blotting and TEM grids carrying AQP2 bearing SMA-nanodiscs were placed on 20 μ L droplets containing the secondary antibody (10 nm gold conjugated G α R antibody (Sigma Aldrich; 1:15), with the sample side touching the droplet. The TEM grid was left to incubate for 1 hr at RT. TEM grids were washed by placing the TEM grids on 20 μ L MiliQ droplets, sample side facing the MiliQ, and incubating for 15 min. at RT and repeating the washing step 3 times. Nanodiscs were stained by pipetting 3 μ L of 2% Uranyl Acetate on the

TEM grid and 1 min incubation at RT. Excess of stain was removed via blotting. Samples were examined with a JEOL JEM-1400plus transmission electron microscope and images were recorded with a Gatan Orius

AQP2 activity measurements – Equal volumes of 1 mg/mL AQP2 bearing proteoliposomes and Sucrose buffer (42 mM Sucrose, 20 mM Tris-HCl pH7.5, 200 mM NaCl) were mixed by using the rapid mixing device discussed in **chapter 4.4.2**, by opening the outlet valve for 50 msec, while the system was kept under a pressure of 2 bar. Changes in 90° scattering were measured for 2 sec, after which a new mixing experiment was initiated. Obtained results were normalized and fitted to an exponential curve (eq. 1).

$$N(t)=(N_0-N_\infty)*e^{kt} +N_\infty \quad \text{Equation 1}$$

Where N(t) is the normalized scattering signal at timepoint t, in msec, N₀ is the normalized scattering signal at timepoint 0, N_∞ is the normalized scattering signal at t=∞, k is the exponential and t is the time in msec. The exponential is used to calculate the permeability coefficient (P_f) via eq. 2.

$$P_f = \frac{k}{\frac{S}{V_0} * V_w * (C_{out} - C_{in}) * \sigma} \quad \text{Equation 2}$$

Where P_f is the permeability coefficient in cm/s, k is the exponential determined in eq. 1 (in sec), S/V₀ is the mean vesicle surface area to initial volume ratio, V_w is the partial molar volume of water (18 cm³), (C_{out}-C_{in}) is the difference in external and internal osmolarity (0.210 M) and σ is the reflection index of sucrose (1.33). The P_f of AQP2 was corrected for liposomal water transport by subtracting the P_f of empty liposomes from the calculated P_f of AQP2 bearing proteoliposomes. The single channel water permeability can be determined by estimating the amount of AQP2 molecules per proteoliposome, based on the AQP2:lipid molar ratio and the amount of lipids per proteoliposome. The amount of lipids per proteoliposome was calculated by using Eq. 3.

$$N_{tot} = \frac{\left[4\pi * \left(\frac{d}{2}\right)^2 + 4\pi * \left(\frac{d}{2} - h\right)^2 \right]}{a} \quad \text{Equation 3}$$

Where d is the diameter of the liposome (nm), h is the bilayer thickness (4.05 nm for POPC (44)) and a is the surface area of the lipids (0.64 nm² for POPC (44)). The AQP2:lipid molar ratio can be determined by using Eq. 4.

$$\text{Lipid:AQP2 molar ratio} = \frac{M_{W, lipids}}{M_{W, AQP2} * LPR} \quad \text{Equation 4}$$

Where M_{w, lipids} is the average molecular weight of the lipids (634.39 g/mol), M_{w, AQP2} is the molecular weight of AQP2 (28,000 g/mol) and LPR is the lipid-to-protein ratio used (60). The amount of AQP2 monomers per proteoliposome can then be determined by multiplying the outcome of Eq. 4 with the outcome of Eq. 3, giving an estimation of ~40 AQP2 monomers per proteoliposome. The single water channel water permeability (p_f) was then calculated by using Eq. 5

$$p_f = \frac{P_f}{SuD}$$

Equation 5

Where SuD is the single channel density per unit of surface area (cm^{-2}), based on the number of AQP2 monomers and the surface area of a proteoliposome.

4.7: References

1. Eto, K., Noda, Y., Horikawa, S., Uchida, S., and Sasaki, S. (2010) Phosphorylation of aquaporin-2 regulates its water permeability. *The Journal of biological chemistry* **285**, 40777-40784
2. Vaughn, J. L., Goodwin, R. H., Tompkins, G. J., and McCawley, P. (1977) The establishment of two cell lines from the insect *Spodoptera frugiperda* (Lepidoptera; Noctuidae). *In vitro* **13**, 213-217
3. Altmann, F., Staudacher, E., Wilson, I. B., and Marz, L. (1999) Insect cells as hosts for the expression of recombinant glycoproteins. *Glycoconjugate journal* **16**, 109-123
4. Kost, T. A., and Condreay, J. P. (1999) Recombinant baculoviruses as expression vectors for insect and mammalian cells. *Current opinion in biotechnology* **10**, 428-433
5. Madeo, M., Carrisi, C., Iacopetta, D., Capobianco, L., Cappello, A. R., Bucci, C., Palmieri, F., Mazzeo, G., Montalto, A., and Dolce, V. (2009) Abundant expression and purification of biologically active mitochondrial citrate carrier in baculovirus-infected insect cells. *Journal of bioenergetics and biomembranes* **41**, 289-297
6. Werten, P. J., Hasler, L., Koenderink, J. B., Klaassen, C. H., de Grip, W. J., Engel, A., and Deen, P. M. (2001) Large-scale purification of functional recombinant human aquaporin-2. *FEBS letters* **504**, 200-205
7. Cordingley, M. G., Callahan, P. L., Sardana, V. V., Garsky, V. M., and Colonno, R. J. (1990) Substrate requirements of human rhinovirus 3C protease for peptide cleavage in vitro. *The Journal of biological chemistry* **265**, 9062-9065
8. Cereghino, J. L., and Cregg, J. M. (2000) Heterologous protein expression in the methylotrophic yeast *Pichia pastoris*. *FEMS microbiology reviews* **24**, 45-66
9. Daly, R., and Hearn, M. T. (2005) Expression of heterologous proteins in *Pichia pastoris*: a useful experimental tool in protein engineering and production. *Journal of molecular recognition : JMR* **18**, 119-138
10. Gasser, B., Prielhofer, R., Marx, H., Maurer, M., Nocon, J., Steiger, M., Puxbaum, V., Sauer, M., and Mattanovich, D. (2013) *Pichia pastoris*: protein production host and model organism for biomedical research. *Future microbiology* **8**, 191-208
11. Macauley-Patrick, S., Fazenda, M. L., McNeil, B., and Harvey, L. M. (2005) Heterologous protein production using the *Pichia pastoris* expression system. *Yeast (Chichester, England)* **22**, 249-270
12. Cereghino, G. P., and Cregg, J. M. (1999) Applications of yeast in biotechnology: protein production and genetic analysis. *Current opinion in biotechnology* **10**, 422-427
13. Lee, A. G. (2004) How lipids affect the activities of integral membrane proteins. *Biochimica et biophysica acta* **1666**, 62-87
14. Yeagle, P. L. (2014) Non-covalent binding of membrane lipids to membrane proteins. *Biochimica et biophysica acta* **1838**, 1548-1559
15. Whitelegge, J. P. (2013) Integral membrane proteins and bilayer proteomics. *Analytical chemistry* **85**, 2558-2568
16. Laganowsky, A., Reading, E., Allison, T. M., Ulmschneider, M. B., Degiacomi, M. T., Baldwin, A. J., and Robinson, C. V. (2014) Membrane proteins bind lipids selectively to modulate their structure and function. *Nature* **510**, 172-175

17. Bayburt, T. H., and Sligar, S. G. (2010) Membrane protein assembly into Nanodiscs. *FEBS letters* **584**, 1721-1727
18. Ritchie, T. K., Grinkova, Y. V., Bayburt, T. H., Denisov, I. G., Zolnerciks, J. K., Atkins, W. M., and Sligar, S. G. (2009) Chapter 11 - Reconstitution of membrane proteins in phospholipid bilayer nanodiscs. *Methods in enzymology* **464**, 211-231
19. Gulati, S., Jamshad, M., Knowles, T. J., Morrison, K. A., Downing, R., Cant, N., Collins, R., Koenderink, J. B., Ford, R. C., Overduin, M., Kerr, I. D., Dafforn, T. R., and Rothnie, A. J. (2014) Detergent-free purification of ABC (ATP-binding-cassette) transporters. *The Biochemical journal* **461**, 269-278
20. Jamshad, M., Lin, Y. P., Knowles, T. J., Parslow, R. A., Harris, C., Wheatley, M., Poyner, D. R., Bill, R. M., Thomas, O. R., Overduin, M., and Dafforn, T. R. (2011) Surfactant-free purification of membrane proteins with intact native membrane environment. *Biochemical Society transactions* **39**, 813-818
21. Knowles, T. J., Finka, R., Smith, C., Lin, Y. P., Dafforn, T., and Overduin, M. (2009) Membrane proteins solubilized intact in lipid containing nanoparticles bounded by styrene maleic acid copolymer. *Journal of the American Chemical Society* **131**, 7484-7485
22. Orwick-Rydmark, M., Lovett, J. E., Graziadei, A., Lindholm, L., Hicks, M. R., and Watts, A. (2012) Detergent-free incorporation of a seven-transmembrane receptor protein into nanosized bilayer Lipodisq particles for functional and biophysical studies. *Nano letters* **12**, 4687-4692
23. Orwick, M. C., Judge, P. J., Procek, J., Lindholm, L., Graziadei, A., Engel, A., Grobner, G., and Watts, A. (2012) Detergent-free formation and physicochemical characterization of nanosized lipid-polymer complexes: Lipodisq. *Angewandte Chemie (International ed. in English)* **51**, 4653-4657
24. Swainsbury, D. J., Scheidelaar, S., van Grondelle, R., Killian, J. A., and Jones, M. R. (2014) Bacterial reaction centers purified with styrene maleic acid copolymer retain native membrane functional properties and display enhanced stability. *Angewandte Chemie (International ed. in English)* **53**, 11803-11807
25. Dorr, J. M., Koorengevel, M. C., Schafer, M., Prokofyev, A. V., Scheidelaar, S., van der Crujnsen, E. A., Dafforn, T. R., Baldus, M., and Killian, J. A. (2014) Detergent-free isolation, characterization, and functional reconstitution of a tetrameric K⁺ channel: the power of native nanodiscs. *Proc Natl Acad Sci U S A* **111**, 18607-18612
26. Irvine, G. B. (2001) Determination of molecular size by size-exclusion chromatography (gel filtration). *Current protocols in cell biology* **Chapter 5**, Unit 5.5
27. Lee, S. C., Knowles, T. J., Postis, V. L., Jamshad, M., Parslow, R. A., Lin, Y. P., Goldman, A., Sridhar, P., Overduin, M., Muench, S. P., and Dafforn, T. R. (2016) A method for detergent-free isolation of membrane proteins in their local lipid environment. *Nat Protoc* **11**, 1149-1162
28. Frick, A., Eriksson, U. K., de Mattia, F., Oberg, F., Hedfalk, K., Neutze, R., de Grip, W. J., Deen, P. M., and Tornroth-Horsefield, S. (2014) X-ray structure of human aquaporin 2 and its implications for nephrogenic diabetes insipidus and trafficking. *Proc Natl Acad Sci U S A* **111**, 6305-6310
29. Vahedi-Faridi, A., Lodowski, D., Schenk, A., Kaptan, S., de Groot, B. L., Walz, T., and Engel, A. (2014) The structure of Aquaporin. *To be published*

30. Wang, L., and Tonggu, L. (2015) Membrane protein reconstitution for functional and structural studies. *Science China. Life sciences* **58**, 66-74
31. Seddon, A. M., Curnow, P., and Booth, P. J. (2004) Membrane proteins, lipids and detergents: not just a soap opera. *Biochimica et biophysica acta* **1666**, 105-117
32. Israelachvili, J. N. (2011) *Intermolecular and surface forces*, Academic Press, Burlington, MA
33. Wade, J. B. (2011) Statins affect AQP2 traffic. *American Journal of Physiology - Renal Physiology* **301**, F308-F308
34. Procino, G., Barbieri, C., Carosino, M., Rizzo, F., Valenti, G., and Svelto, M. (2010) Lovastatin-induced cholesterol depletion affects both apical sorting and endocytosis of aquaporin-2 in renal cells. *American journal of physiology. Renal physiology* **298**, F266-278
35. Russo, L. M., McKee, M., and Brown, D. (2006) Methyl-beta-cyclodextrin induces vasopressin-independent apical accumulation of aquaporin-2 in the isolated, perfused rat kidney. *American journal of physiology. Renal physiology* **291**, F246-253
36. Takamori, S., Holt, M., Stenius, K., Lemke, E. A., Gronborg, M., Riedel, D., Urlaub, H., Schenck, S., Brugger, B., Ringler, P., Muller, S. A., Rammner, B., Gräter, F., Hub, J. S., De Groot, B. L., Mieskes, G., Moriyama, Y., Klingauf, J., Grubmüller, H., Heuser, J., Wieland, F., and Jahn, R. (2006) Molecular anatomy of a trafficking organelle. *Cell* **127**, 831-846
37. Meer, G. v., and Sprong, H. (2004) Membrane lipids and vesicular traffic. *Current Opinion in Cell Biology* **16**, 373-378
38. Klemm, R. W., Ejsing, C. S., Surma, M. A., Kaiser, H.-J., Gerl, M. J., Sampaio, J. L., de Robillard, Q., Ferguson, C., Proszynski, T. J., Shevchenko, A., and Simons, K. (2009) Segregation of sphingolipids and sterols during formation of secretory vesicles at the trans-Golgi network. *The Journal of cell biology* **185**, 601-612
39. Severs, N. J. (2007) Freeze-fracture electron microscopy. *Nature Protocols* **2**, 547
40. Moor, H., and Muhlethaler, K. (1963) FINE STRUCTURE IN FROZEN-ETCHED YEAST CELLS. *The Journal of cell biology* **17**, 609-628
41. Rash, J. E., Davidson, K. G., Yasumura, T., and Furman, C. S. (2004) Freeze-fracture and immunogold analysis of aquaporin-4 (AQP4) square arrays, with models of AQP4 lattice assembly. *Neuroscience* **129**, 915-934
42. Sun, T. X., Van Hoek, A., Huang, Y., Bouley, R., McLaughlin, M., and Brown, D. (2002) Aquaporin-2 localization in clathrin-coated pits: inhibition of endocytosis by dominant-negative dynamin. *American journal of physiology. Renal physiology* **282**, F998-1011
43. Itel, F., and Kukulski, W. (2008) Water Permeability Measurements of Proteoliposomes Reconstituted with Aquaporin SoPIP2;1. *Not Published*
44. Dickey, A., and Faller, R. (2008) Examining the Contributions of Lipid Shape and Headgroup Charge on Bilayer Behavior. *Biophysical Journal* **95**, 2636-2646

Chapter 5

Hollow cantilevers for Cryo-EM sample preparation; the set-up

The work presented in this chapter was executed in collaboration with ir. Eleonoor Verlinden (PhD student), Daniel Torres Gonzalez, Jelle van der Does, Paul Laeven (Maastricht instruments) and Patrick Frederix (Nanosurf)

5.1: Introduction

As discussed in chapter 1, studies on AQP2 trafficking are mostly limited by the techniques available at the moment. A new technique needs to be developed that can study cellular mechanisms which are impossible to study now. Recent progress in dispensing and aspirating extremely small volumes of samples using a hollow microcantilever in a standard atomic force microscope (AFM) setup has made it possible to manipulate compounds from target cells in a controlled manner. Progresses in cryo-EM imaging, like direct electron detectors and improved image analysis software, made it possible to visualize cells and cell-components in great detail. However, sample preparation for cryo-EM is still challenging, mainly due to laborious and time-consuming preparation steps (discussed in chapter 1). Combining controlled sample fluid pipetting using hollow microcantilevers with cryo-EM sample preparation should make cryo-EM more efficient, faster, easy to use and hence reduce the cryo-EM costs making it accessible for more researchers than now.

In this chapter the design of the set-up, combining hollow microcantilever AFM and cryo-EM sample preparation, is presented. Current methods to prepare cryo-EM samples and the use of micro-injection are discussed in **section 5.2**. **Section 5.3** presents the proposed set-up and its corresponding work-flow and control software. **Section 5.4** discusses the need of humidity control to prevent sample evaporation, while the sample stage and gridholder are discussed in **section 5.5**. In the end (**section 5.6**) the use of this system for cryo-EM sample preparation is tested.

5.2: Micro-injections and cryo-EM sample preparation

As discussed in chapter 1, recent advances in cryo-EM imaging techniques led to a major breakthrough in the use of this technique for high resolution imaging. The development of the direct electron detectors (1,2) and improved image analysis software (3,4), made it possible to correct for the two main limitations of cryo-EM imaging, specimen movement during irradiation and sample heterogeneity. The importance of cryo-EM in structural biology was acknowledged by the Nobel Prize committee in 2017, for the Nobel Prize of chemistry was awarded to the pioneers of cryo-EM (Jacques Dubochet, Joachim Frank and Richard Henderson) in that year. Although cryo-EM is a great method to obtain high resolution images of small biological samples, the use of cryo-EM is now mostly limited by the available complex sample preparation techniques. The development of new and better techniques should enhance the use of cryo-EM even more, by exploiting the possibilities of high resolution imaging, which will lead to a broad range of new biological insights.

One of the possible new cryo-EM sample preparation techniques relies on extraction of sub-cellular components from targeted single cells. Recent developments in micro and nanofabrication techniques made it possible to produce hollow AFM cantilevers, which can be used as “femto-pipettes”, pipettes able to dispense femtoliters (10^{-15} L) of volume (5,6). The small size and spatial control of these cantilevers made it possible to target and manipulate specific cells, with a low risk of cell death (5,7). By using hollow AFM cantilevers, subcellular volumes can be aspirated from a target cell (7), dispensed on an EM-grid (see chapter 6) and plunge frozen into liquid ethane (chapter 5.6), eliminating laborious sample preparation steps. In this section, current cryo-EM sample techniques and current micro-injection techniques are discussed, showing the necessity and possibilities of the set-up designed during our research.

5.2.1: Current techniques for cryo-EM sample preparation

With the development of electron microscopes, different sample preparation techniques were developed as well. Applying electron microscopy on biological samples is not trivial, with the first barrier to overcome being the high vacuum required to collect electrons scattered by the sample rather than by residual air inside the electron optical column. While water plays a crucial role in life, the use of a high vacuum during TEM limits the possibility to retain the biological samples in its native, liquid, aqueous environment. Therefore, water substitution or dehydration of samples became widely used methods to image the samples at a high magnification (8-10). Water substitution and dehydration destroys the native biological environment, leading to denaturation or deformation of the biological sample. Furthermore, heavy metals are often used to stain these samples, where the sample is not visualized directly but the staining itself is imaged. Resulting in poor analysis of weakly stained areas (11). Moreover, staining often leads to artefacts, which are not always obvious, leading to false interpretations. Sample preservation in a (near) native environment became therefore crucial. In the early 1980's, Jacques Dubochet *et al.* imaged samples that were frozen in a thin layer of non-crystalline ice, called vitreous ice (12-15). This discovery made it possible to visualize

biological samples at a high magnification within its native environment, retaining the biological structure as much as possible. Furthermore, the possibility to reconstruct 3D structures from 2D TEM images, developed by DeRosier and Klug at the end of the 1960's (16), confirmed the great potential of cryo-EM for biological research.

Formation of vitreous ice can only be achieved once the temperature drops faster than $\sim 10^5$ K/s (13). The cooling rate depends on the temperature of the cryogen, the heat transfer rate, and the thickness of the sample. Plunge freezing a sample into liquid ethane ($T = \sim -160^\circ\text{C}$) suffices to vitrify samples with a thickness of $< 1 \mu\text{m}$ (17), meaning that proteins and small (prokaryotic) cells can be vitrified for cryo-EM by this method.

Plunge freezing is a relatively straightforward method for cryo-EM sample preparation: A 3-5 μL volume of sample is pipetted on an EM-grid, excess fluid is removed via blotting, leaving a film of aqueous solution thin enough to vitrify, and the sample is rapidly shot into a cryogen, leading to sample vitrification. However, although this method is relatively straightforward, there are some limitations. Blotting the sample to obtain useable thin vitrified ice requires optimisation and training. Different blotting times are required, depending on the filter paper used and the sample studied. Manual blotting requires a trained eye to determine optimal blotting times, making it an art which experts execute best. Automated blotting requires dedicated machinery but even then, the optimal blotting conditions need to be determined experimentally. Although less protein is necessary for cryo-EM imaging, as compared to X-ray crystallography and NMR, still a relatively large sample volume (3-5 μl) is necessary to prepare one EM-grid. Only with such an excess volume a thin aqueous layer can be produced by the blotting step, which removes a large portion of the sample (18). Especially finding the optimal blotting conditions, could require large sample quantities. Furthermore, studying eukaryotic cells is not possible with plunge freezing, because even the smallest known eukaryotic cells have a diameter of 1-2 μm (19,20), while a typical eukaryotic cell has a diameter of 20 μm . Therefore, plunge frozen cryo-EM samples are now mainly used to study purified proteins for 3D reconstruction. However, many protein-protein interactions and related cellular complexes can only exist within the cellular environment. To visualize the complexity of (eukaryotic) cells, other methods are necessary to prepare cryo-EM samples.

Because pure water can only be vitrified to a thickness of $\sim 1 \mu\text{m}$ (15) at ambient pressure, high pressure (2100 bar) is applied during rapid cooling to prevent ice formation. Thick samples, like eukaryotic cells, can thus be cryo-preserved by using high-pressure freezing (HPF)(21). HPF allows up to 300 μm thick samples to be vitrified (22), meaning that eukaryotic cells and small pieces of tissue can be vitrified by this method. Although eukaryotic cells contain a complex mixture of proteins, polysaccharides, macromolecules, membrane structures and RNA (11), they often require an additional extracellular cryoprotectant additive to retain cellular structure during HPV. The optimal cryoprotectant needs to be determined experimentally, for it can induce osmotic differences leading to artefacts and cellular deformation.

Cryo-EM imaging of eukaryotic cells is also limited due to the short mean free path of electrons, which is about 150 nm within a vitrified cell for an electron accelerated by 300 kV (23). For transmission electron microscopy, imaging relies on the electrons passing through the sample ideally without being scattered multiple times. For cryo-EM a sample thickness between 25-250 nm will give the best results, which is far thinner than the thickness of eukaryotic cells. Therefore, vitrified eukaryotic cells need to be cryo-sectioned into thin slices.

Cell sectioning can be achieved by either using a cryo-ultramicrotome or a focussed ion beam (FIB). A cryo-ultramicrotome uses diamond knives to section the cell into thin slices, which can be collected as a band of multiple slices (24). But cryo-ultramicrotomes damage the vitrified cells, which are incompressible and brittle, leading to mechanical distortions and deformations (24,25). The FIB relies on a Gallium (Ga^+) ion beam to ablate the surface of a specimen until the desired thickness is reached. This method does not induce compression artefacts, but most of the sample volume is lost and the outermost region of the remaining sample lamellae suffers from damage induced by the ion beam (26). Thus, the major downside of this method is that only one thin section of the cell remains, while the rest is ablated, meaning that the presence of the region of interest within this area needs to be confirmed before applying this method. In contrast, the cryo-ultramicrotomy delivers the cell as a band of multiple slices to allow the cell volume to be studied.

Both cell sectioning and HPF are time consuming, labour intensive, prone to artefacts and require a lot of experience and optimization for obtaining cryo-EM samples of sufficient quality. Therefore, sample preparation methods need to be optimized to maximize the potential provided by cryo-EM. Although eukaryotic cells are generally too thick for plunge freezing, some eukaryotic cells tend to spread once attached to a surface, leading to thin enough samples for vitrification via plunging (27-29). Near its edges such a cell is usually thin enough to image cellular contents via cryo-EM without sectioning. Obviously, this approach can only be applied to cells that spread on their substrate, and it allows imaging only of their sufficiently thin regions.

Another method eliminating HPF and cell sectioning is based on plasma membrane isolation (30), where cells grown on an EM-grid are “unroofed” by blotting. With this method, only cell patches remain on the EM-grid. These cell patches are thin enough for plunge freezing and no cell sectioning is necessary (30). Although the results are promising, cellular “unroofing” is a relatively crude and uncontrolled method, where it is possible that the region of interest is blotted away during sample preparation. Furthermore, the region of interest is limited to the vicinity of one cellular membrane. Hence, this approach cannot be applied for the study of regions that are further away from the membrane. Fully differentiated polarized cells with basolateral and apical membranes will introduce further challenges for the “unroofing” method, if the structure of both membranes is to be studied.

One method able to completely visualize cellular contents, without a restricted field of view, while eliminating HPF and cell sectioning relies on targeted cell lysis by using microcapillaries (31-33). Here eukaryotic cells were cultured on conducting glass slides, a

single cell was targeted, lysed by electroporation and aspirated by a microcapillary. The aspirated volume was then dispensed on an EM-grid and plunge frozen into liquid ethane. By using cell lysate, the complete cellular components can be studied, while the sample is thin enough to eliminate the necessity of HPF and cell sectioning. Furthermore, working with small volumes (in the nanolitre range) eliminates the blotting step necessary for traditional cryo-EM sample preparation, meaning that samples can be plunge frozen without optimization of blotting time, pressure and used blotting paper (31,33). However, the aspirated volume is two orders larger (200-400 nL) as compared to the total cell volume (in the picolitre range), leading to a significant dilution of the cell lysate. The region of interest needs to be localized among the total cell lysate, while the search area is enlarged due to dilution, making it difficult to find the desired region of interest. Furthermore, although the electroporation pulse is relatively short (50 μ s)(33), the pulse could lead to sample damage or stress induced artefacts.

The optimal cryo-EM sample preparation method should combine the relative simplicity of plunge freezing while having the capacity to visualize the complexity of the eukaryotic cell. The method described above combines these two prerequisites, but does not allow targeted aspiration of a specific region of interest. Specific targeting makes sample localization after plunge freezing easier, improving the efficiency in cryo-EM imaging. Targeted aspiration can be achieved with hollow cantilevers as discussed in the next section.

5.2.2: Micro-injections into single cells

Diseases are often caused by a mutation in specific proteins that may lead to a deregulation of a cellular process. For instance, as discussed in chapter 2, NDI is caused by a mutation in either the V2R or AQP2 leading to impaired AQP2 trafficking towards the apical membrane. To study cellular processes, specific proteins need to be mutated, to allow the influence of this mutation on the cellular behaviour to be visualized. Since the beginning of cell research, researchers have focused on manipulating cellular processes and inducing protein modifications to study their role in the cell. Therefore, a broad range of different cell-modification techniques have been developed, which can be separated into three classes: 1) biological, 2) chemical and 3) physical methods.

Biological methods often rely on viruses to express foreign genes in the desired cell. One of these methods was discussed in chapter 4. By using baculoviruses carrying an *aqp2* gene, AQP2 could be expressed in *Sf9* cells. Other viral expression methods rely on either retroviral gene delivery (34-37) or adenoviral gene delivery (38-41). However, although these methods are able to introduce foreign genes into cells in a relatively easy manner, using viruses is not always an optimal method. Baculoviral infections will inhibit *Sf9* cell division and will kill the *Sf9* cells over time, while retroviral gene delivery only works on dividing cells and it carries the risk of insertional mutagenesis once cells are infected (36,37). Adenoviral gene expression could stimulate immune responses in infected and neighbouring cells (39,40), while it is not suited for long-term expression (41).

Chemical methods rely on cationic mediators, such as liposomes or polymers. The technique is relatively simple, can be used on a broad range of cells and does not stimulate immune responses (42-44). Chemical gene delivery was previously discussed in chapter 4, where Cellfectin® was used to transfect *Sf9* cells with baculovirus DNA. However, transfection efficiency depends on the cell type and is relatively low, while the used compounds can be toxic for the cells (45).

Physical methods require a dedicated machinery to perform cell modifications. Some examples of physical methods are electroporation (46,47), nucleofection (48-50), molecular vibration mediated transduction (51) and micro-injection (52,53).

Apart from micro-injections, all above described methods rely on batch-modification of cells. Furthermore, these methods are relatively uncontrolled, leading to variations in the transfection efficiencies from cell to cell in one culture. Some cells are highly transfected, while other cells are not affected at all. The lack of controlled transfection and the batch-mode type of transfection can be a limiting factor in controlled cell modification. Therefore, a quantifiable, reproducible, cell specific type of transfection is necessary to induce modifications in a cell in a controlled manner as required for studying cellular mechanisms. Micro-injection methods are able to specifically address individual cells for transfection and their use was first reported more than 45 years ago (54,55). For micro-injections, a glass micro-pipette with a fine tip of about 1 μm diameter is used to specifically inject compounds in either the nucleus or the cytoplasm. Micro-pipettes have been used to dispense proteins (56-58), cDNA (56-58), RNA (59-62) and even organelles into a cell (63). Furthermore, this technique is used to modify a broad variety of cells, even cells which are normally difficult to transfect, while it can be used to inject specific molecules at well-defined stages of the cell cycle (64). Micro-pipettes are able to inject precisely controlled volumes into specific cells, leading to exact reproducibility of the transfection for multiple (100-200) cells (64,65). In time, different methods have been developed to precisely control the dispensed volume, either based on pressure driven flow, temperature based expansion of liquids (66) and electrochemistry (67).

Although micro-pipettes have been used to inject a broad variety of different compounds into different cells and they allow small volumes to be precisely dispensed into specific cells, the use of micro-pipettes is challenging. Using micro-pipettes in a reproducible manner requires a lot of experience and even then, micro-injection is technically demanding. Furthermore, the relatively large tip size of the micro-pipettes often leads to cell damage (66), cell leakage (66) or cell death (68). Micropipettes also miss a force-feedback control, making positioning of the micro-pipette and subsequent cellular penetration a tricky operation that depends on the user's skills and the resolution of the light microscope that visualizes the cell and the pipette (68). Especially the relatively large size of the pipette and lack in force-feedback prevents the full exploitation of micro-pipettes.

Atomic Force Microscope (AFM) cantilevers have a relatively sharp pyramidal tip (~5 nm diameter at the apex) and AFMs are known for their precise force-feedback control, which necessary for their imaging capabilities. The geometry of the cantilever makes it possible to

minimize the contact force on the cell and the AFM set-up prevents lateral vibrations of the tip, to avoid tearing of the cell membrane during micro-injection (68). The force-feedback control for cell penetration has long been acknowledged, because AFM cantilevers have been used to abstract mRNA from living cells since the beginning of this millennium (69). The AFM cantilever was used to penetrate a specific target cell, while the mRNA in the cell bound to the cantilever tip in an uncontrolled manner (69). Aspirated mRNA was amplified via PCR and differences in gene expression between different cells in the same population were found (69). This method demonstrated that cantilevers can penetrate a cell, bind cellular contents and retract from the cell, without severely damaging the cell. Comparable results were obtained when cantilevers were used to insert DNA into target cells, where DNA plasmids were attached to AFM cantilever tips via incubation in a plasmid solution and plasmid release was achieved by diffusion of the DNA from the tip after penetration (70). Although AFM cantilevers can be used to penetrate specific cells for aspiration or transfection, aspiration or transfection itself is relatively uncontrolled. Insertion of plasmid DNA into cells via cantilevers resulted in a transfection efficiency of only 30% (70), while controlled injection with micro-pipettes has a potential transfection efficiency of 100% when utilized properly (64,65). The lack in dispensing and aspiration control make standard AFM cantilevers unfavourable for controlled cellular manipulation.

Optimal cellular manipulation can be achieved by combining the precise localization and positioning, by force-feedback control, of the cantilever with the controlled dispensing capacity of micro-pipettes. The introduction of hollow AFM cantilevers made it possible to combine the advantages of both systems. Hollow AFM cantilevers consist of a fluidic reservoir, connected by a micro-sized channel to a small opening (ranging from 0.1 - 2 μm) at the cantilever tip (68). By connecting the hollow cantilever reservoir via a macro-sized channel to a pressure controller, it is possible to controllably dispense or aspirate solutions as small as 0.5 fL (6). Even though the cantilevers are modified to include a micro-channel, the function of the cantilevers is not compromised and can still be used for force-controlled measurements (6,68). Hollow cantilevers have been used to deliver bioactive agents *ex vivo* in a controlled way, where trypsin was dispensed in close proximity of targeted attached HeLa cells, leading to the dissociation of only the targeted cells from the substrate (71). Furthermore, hollow AFM cantilevers were used to measure cell adhesion forces (72,73) and to displace specific cells by applying an underpressure on the cantilever while touching the cells (71,74,75). The use of hollow cantilevers as micro-injectors was demonstrated by Guillaume-Gentil *et al.* in 2013, where femtolitre volumes of GFP were injected in the cytoplasm of specifically targeted cells (5). Besides injection in the cytoplasm, plasmids carrying a *gfp* gene mixed with dextran tetramethylrhodamine (DexTRITC) were specifically injected in the cell nucleus. The confinement of DexTRITC in the nucleus proves the restoration of the nuclear membrane after penetration, while GFP expression proves

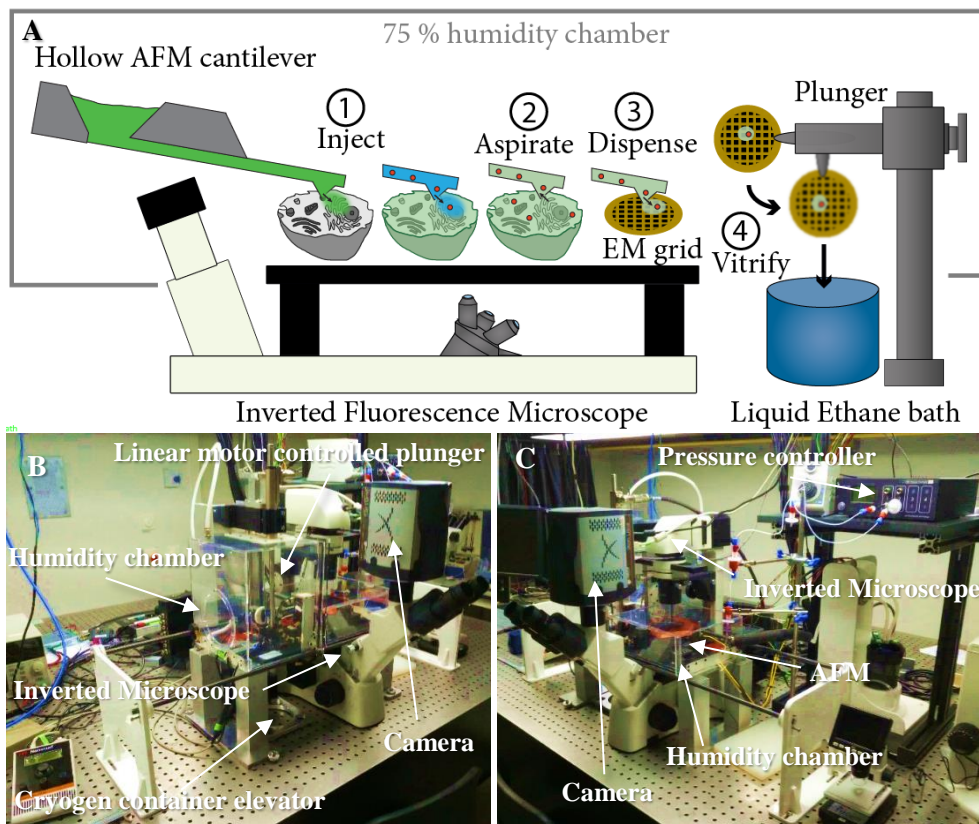


Figure 5.1: The NFP4Cryo-EM set-up. (A) Schematic overview of the developed set-up. 1) Fluorophores or fluorescently labelled biological compounds are injected into a targeted single cell by using a hollow AFM cantilever. 2) The region-of-interest is aspirated from the target cell by using a hollow AFM cantilever. 3) The aspirated subcellular volume is dispensed onto an EM-grid. 4) The dispensed volume, in the sub-picolitre range, is small and thin enough to be plunge frozen in liquid ethane. The EM-grid is picked up by a specially designed plunging system, able to plunge freeze the sample, preparing it for cryo-EM. The grid-handling part of the setup is put under humidity control to maintain the small volumes on the grid without/minimize evaporation before freezing. (B) Left side view of the set-up. The plunging system is located here. The plunger is controlled by a linear motor. The cryogen container can be lifted by a special designed elevator. (C) The right side view of the set-up. A pressure controller (ElveFlow) is connected to a hollow AFM cantilever to control the fluid pipetting. The hollow cantilevers are mounted on an AFM (Nanosurf). The AFM is placed on top of an inverted light microscope (Motic AE31), equipped for fluorescent and phase contrast microscopy. A camera (iXon Ultra) is able to monitor cantilever movement and hollow cantilever aspiration and dispensing. (B,C) The humidity and temperature of the set-up is controlled by a humidity chamber, while the gridholder can be separately cooled to control the local evaporation rate (Maastricht Instruments).

successful dispensing of DNA into the cell nucleus and cell survival (5). This shows that hollow cantilevers controlled by an AFM can be successfully used to specifically target and transfect designated cells, while the targeted cells can recover from this process. The force-feedback control of the AFM makes it possible to accurately position the cantilever and to ensure proper cell penetration. In 2016, the use of hollow cantilevers to specifically aspirate subcellular volumes from a cell was demonstrated (7).

The above-mentioned results show that hollow cantilevers can be used to specifically target subcellular volumes. Once dispensed on an EM-grid, the samples are thin enough for plunge freezing without the need for a blotting step. Combining AFM controlled hollow cantilevers with a plunge freezing machinery makes it possible to image specific complex (eukaryotic) cell contents without the need for elaborate cryo-EM sample preparation methods.

5.3: The set-up

To combine an AFM using hollow cantilevers with cryo-EM sample preparation, an elaborate set-up is necessary. The hollow cantilevers are controlled by an AFM, while they will be used to aspirate from cells. The aspirated volume will be dispensed on EM-grids, which should be kept near the cells. Furthermore, a light microscope is required to specifically position cells for aspiration. After dispensing the aspirated volume on an EM-grid, the sample will evaporate in an ambient environment. Therefore, humidity control is necessary. Finally, a plunging system plunge freezes the aspirated and dispensed sample in liquid ethane, thus vitrifying the sample for cryo-EM.

Although evaporation is prevented by humidity control, samples should be plunge frozen as fast as possible after dispensing, leading to the need of an automated process. Here the process flow and controlling software of the set-up will be discussed.

5.3.1: Process flow and set-up overview

A schematic representation of the designed work-flow is presented in Figure 5.1A. Specific cells are targeted with the hollow cantilever. The hollow cantilever can be used to inject specific (fluorescent) labels into a cell to label regions of interest, or to aspirate regions of interest from the cell. The aspirated volume is then dispensed on an EM-grid, which is immediately plunge-frozen in liquid ethane and ready for cryo-EM. The whole system is integrated into a humidity chamber, preventing sample evaporation. An overview of the set-up is displayed in Figure 5.1B and C. The set-up is divided into two main parts. 1) the plunging system (Figure 5.1B), where the grid is either placed in the specifically designed gridholder (chapter 5.5) or picked up from the gridholder and plunged into liquid ethane. 2) the AFM-system (Figure 5.1C). The AFM is placed on top of a light microscope, making it possible to visualize cells and the AFM cantilever at the same time. Aspiration and dispensing of samples is controlled in this part of the stage.

A range of different motors execute different steps in the work-flow, while different micro-switches are used as check points during the process. Three servo-motors are used to (i) lift the AFM (Figure 5.2A), (ii) to rotate the holder for loading/unloading the grid (Figure 5.2B),

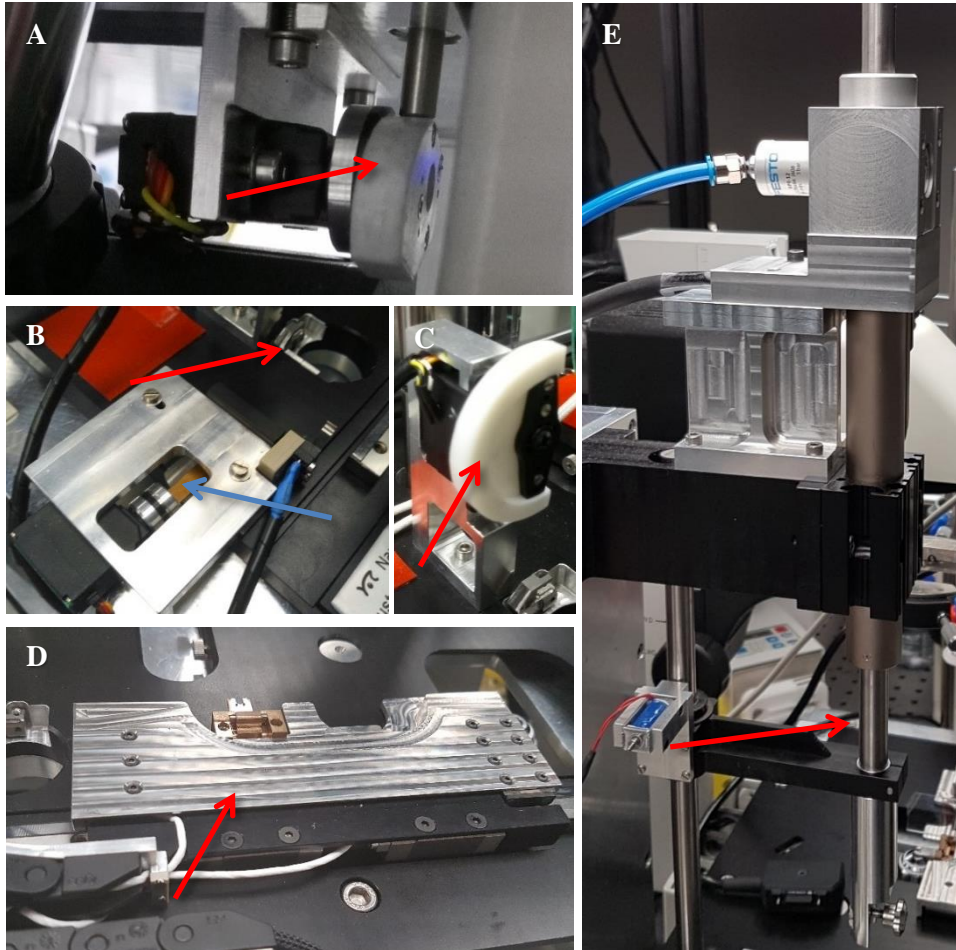


Figure 5.2: The various motors controlling the system. (A) The AFM lift (red arrow). This motor lifts the AFM for safe and rapid automated transfer of the XY -stage with EM-grid holder under the AFM. (B) The gridholder lift (red arrow). This motor (blue arrow) rotates the gridholder, changing its horizontal position to its vertical position, allowing the grid to be picked up for plunging. (C) The tweezers opener (red arrow). This motor opens or closes the tweezers, making it possible to pick-up or release the EM-grid. (D) The X,Y-stage (red arrow). The X,Y-stage is controlled by a piezo driven linear positioning system (SmarAct), leading to sub-micrometer positioning accuracy. (E) The plunger (red arrow). A linear motor activates the plunger by accelerating the tweezers to 1.5 m/sec just before entering the liquid ethane and stopping them within 8 mm. The linear motor positions the tweezers within 0.1 mm accuracy above the gridholder for automated pick up or release of the grid. A safety break (top) prevents the plunger rod from falling down in case of a power failure. The solenoid (lower left) operates a locking pin for lowering the ethane pot once vitrification is accomplished.

and (iii) to open/close the tweezers for releasing and picking up the grid (Figure 5.2C), while a piezo activated linear positioning system (SmarAct) drives the stage (Figure 5.2D). The plunger system is operated by a linear motor (LinMot) (Figure 5.2E).

A servo-motor is required to lift the AFM up during stage movement, because the z-movement of the AFM is too slow and too short to ensure a sufficient clearance for the cantilever during stage movement (Figure 5.2A). The lifting mechanism pushes the AFM up within 1 sec, to retract the cantilever to a sufficient height. The stage can then move towards the plunging system (Figure 5.1B), where the grid is picked up from the gridholder and plunged into liquid ethane. The gridholder is rotated to its vertical position by the second servomotor (Figure 5.2B), making the pick-up of the grid possible. To this end, the third servo-motor opens and closes the tweezers (Figure 5.2C). The linear motor positions the tweezers to a resolution of 0.1 mm (Figure 5.2E). Picking up the grid will be discussed in more detail in chapter 5.5.

The humidity within the chamber is controlled by a humidifier. Opening the humidity chamber during the process is not favourable, as it disturbs the controlled environment. Furthermore, EM-grids are fragile and need to be handled with care. Placing the EM-grid into the gridholder is therefore an automated process, as is the pick-up of the EM-grid from the gridholder and plunging into liquid ethane. The different steps, necessary to place the grid precisely into the gridholder and to pick-up the grid from the gridholder after dispensing are summarized in Figure 5.3A and B respectively. Although a shutter is added in the process-flow depicted in Figure 5.3, the shutter is not installed yet and will be added as soon as possible. The shutter closes the plunging-hole during operation, minimizing the contact with the outside environment and keeping the humidity constant.

5.3.2: Controlling software

After dispensing a sample on the EM-grid, it needs to be vitrified as soon as possible. Furthermore, the EM-grid is fragile, making it difficult to handle the grid by hand. The multitude of different steps to correctly place a grid into the gridholder or to pick up a grid from the gridholder (Figure 5.3) makes this process prone to mistakes when performed manually under time pressure. Last but not least, the humidity needs to be controlled during grid transfer. Therefore, an automated process is required. To achieve this, an operating system based on Labview was developed by Daniel Torres Gonzalez. With this software, an EM-grid can be placed in the gridholder or picked-up from the gridholder and plunged into liquid ethane with minor human interference, limiting the possibility for mistakes and possible damage to the EM-grid or sample.

When the software is activated, the different controllers (linear motor, the stage, the three servomotors and the micro-switches) need to be connected (Figure 5.4A). After connections are acknowledged, the system is turned on and all the components are moved to a secure home position. The AFM is pushed up, tweezers are closed, the gridholder is rotated to its horizontal position, tweezers are moved up and the stage position is calibrated by moving the



Figure 5.3: Flowcharts summarizing the different steps necessary to place an EM-grid in the gridholder for (A) liquid manipulation experiments with the hollow AFM cantilever or for (B) pick-up of the EM-grid after dispensing and plunge freezing in liquid ethane. The following steps are automated by the software designed by Daniel Torres-Gonzalez. (A) Steps 6-14 are automated. (B) Steps 3-12 are automated. The steps involving the shutter are coloured red, because the shutter is not installed yet and these steps are not as yet executed.

stage to the far left (this will be position 0 μm), followed by moving of the stage to a secure position (away from the plunging hole). After these steps the system is ready to use.

The software starts in the home screen (Figure 5.4B) where a schematic model of the set-up is displayed. On the right side the status of the three main components can be viewed, confirming correct connection, the ON/OFF state and, depending on the motor, the position. Above the screen there are seven tabs, which lead to different modules of the system. The first one, connection, is already executed and therefore not available anymore. When the system is not connected, however, the other modules are not available.

The most important module can be found under the “Start” menu. Here the loading, unloading and plunging of the EM-grid is controlled. This module is divided into two main stages. Stage 1: placing the grid in the gridholder (Figure 5.5), and stage 2: picking up the grid from the gridholder and plunging into liquid ethane (Figure 5.6). Depending on the experimental flow, either stage 1 can be started or stage 2 can be accessed by pressing the skip button. Pressing “Start” will initiate the process, leading the user through the different steps necessary to place the grid in the gridholder (Figure 5.5A). Although a shutter is not installed yet, the system waits till the shutter is opened (manually) (Figure 5.5B). When opened, the “OK” button can be pressed and a new button appears which, when pressed, leads to lowering of the tweezer to the bottom of the stage. Here the tweezer can be removed from the plunger and a freshly glow-discharged EM-grid can be installed while the system waits till the tweezer is mounted back to the plunger (Figure 5.5C). Next the tweezer is raised back in the humidity chamber and the system waits until the shutter is closed manually (Figure 5.5D). The steps are completely automated and lead to the release of the EM-grid into the gridholder when the button “Grid to AFM” is pressed. If everything was executed correctly according to the software, “Process accomplished” will appear and Stage 2 can be started by pressing the button “Next Stage” (Figure 5.5E). If it is necessary to control certain parts of the set-up manually, the “Pause” button can be pressed to enter the manual mode of the software.

Once the sample is dispensed on the EM-grid, Stage 2 is activated. Stage 2 starts with a message urging to open the shutter and to lift the cryogen under the plunging aperture (Figure 5.6A). Once this is accomplished, the button “Ethane introduction” appears (Figure 5.6B). By pressing this button, an automated process is launched leading to the transfer of the EM-grid from the AFM towards the plunging system, the pick-up of the EM-grid from the gridholder by the tweezers, moving of the stage away from the plunging aperture to a secure position, and plunging of the EM-grid into liquid ethane. The “Ethane introduction” process takes a total of 22 sec. After plunging, the ethane container and tweezers are lowered simultaneously, for this a solenoid driven pin (Figure 5.2E) is inserted in the ethane container lift, connecting the tweezers to the lift system. A lever at the back of the system must be pushed to release the cryogen container from the holder keeping it in place and before the “OK” button can be pressed (Figure 5.6C). Ethane container and tweezers are then lowered and the tweezers, holding the EM-grid, can be removed from the plunger (Figure 5.6D). Once this is accomplished, the plunger is moved back into the humidity chamber, the

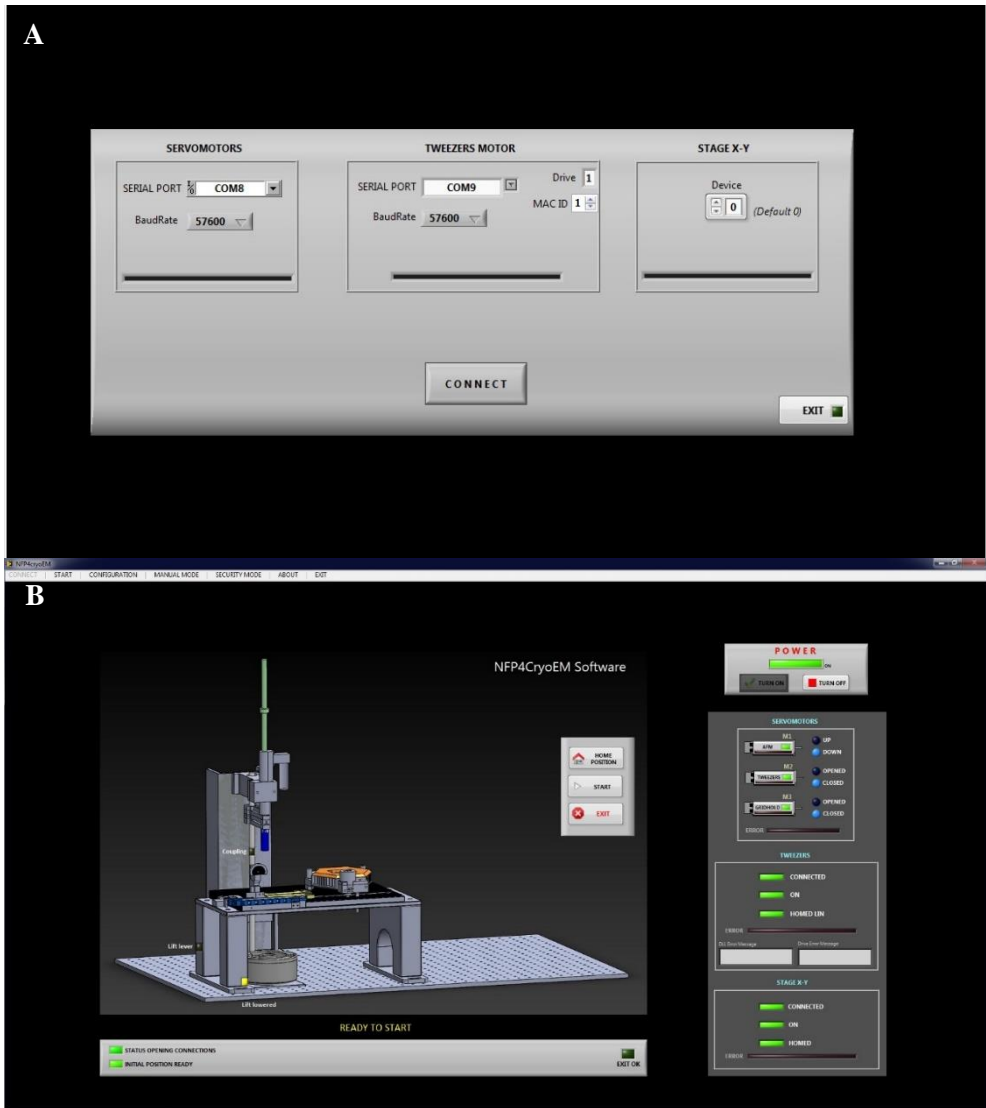


Figure 5.4: Images of the software user interface during the start-up procedure. (A) Connecting the motors. Once the software is started, the three controllers need to be connected. The three controllers are 1) the servomotors, controlling different steps in the placing and pick-up of the grid, 2) the tweezers motor, this is the linear motor used for plunging and handling the grid for pick-up and release in the gridholder, 3) the X, Y. stage. (B) The homescreen of the software. After connecting and homing all the components of the system, the home screen is visible. Here the different modules indicated at the top of the screen can be chosen and the status and position of all the components can be monitored.

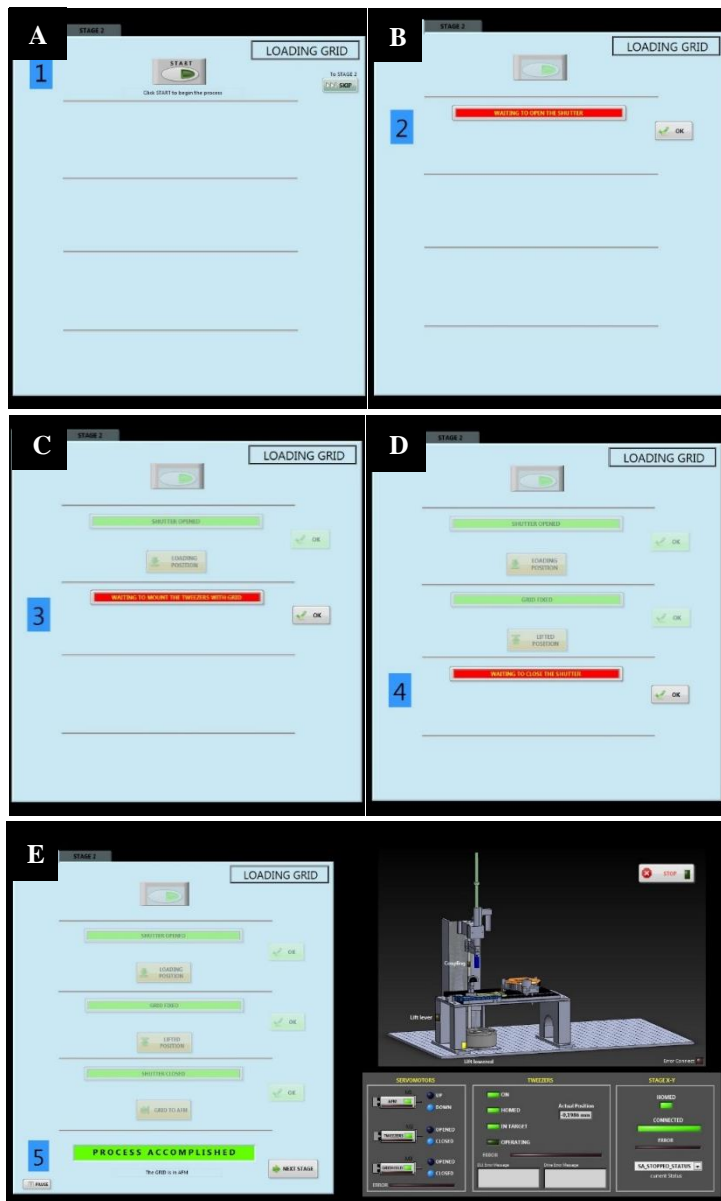


Figure 5.5: Stage 1 in the software is for loading an EM-grid in the gridholder. (A) Stage 1 can be started by pressing the “Start” button, or skipped by pressing “Skip”. (B) After pressing “Start”, the software waits till the shutter is opened. (C) The shutter is manually opened and tweezers are moved down below the stage to allow the EM-grid to be loaded manually. (D) Once an EM-grid is loaded in the tweezers, they are moved up back into the humidity chamber and the software waits until the shutter is closed. (E) The EM-grid is automatically placed into the grid holder and a message appears confirming successful grid transfer. Either the next stage can be launched, or the system can be switched to manual mode by pressing “Pause” (left corner).

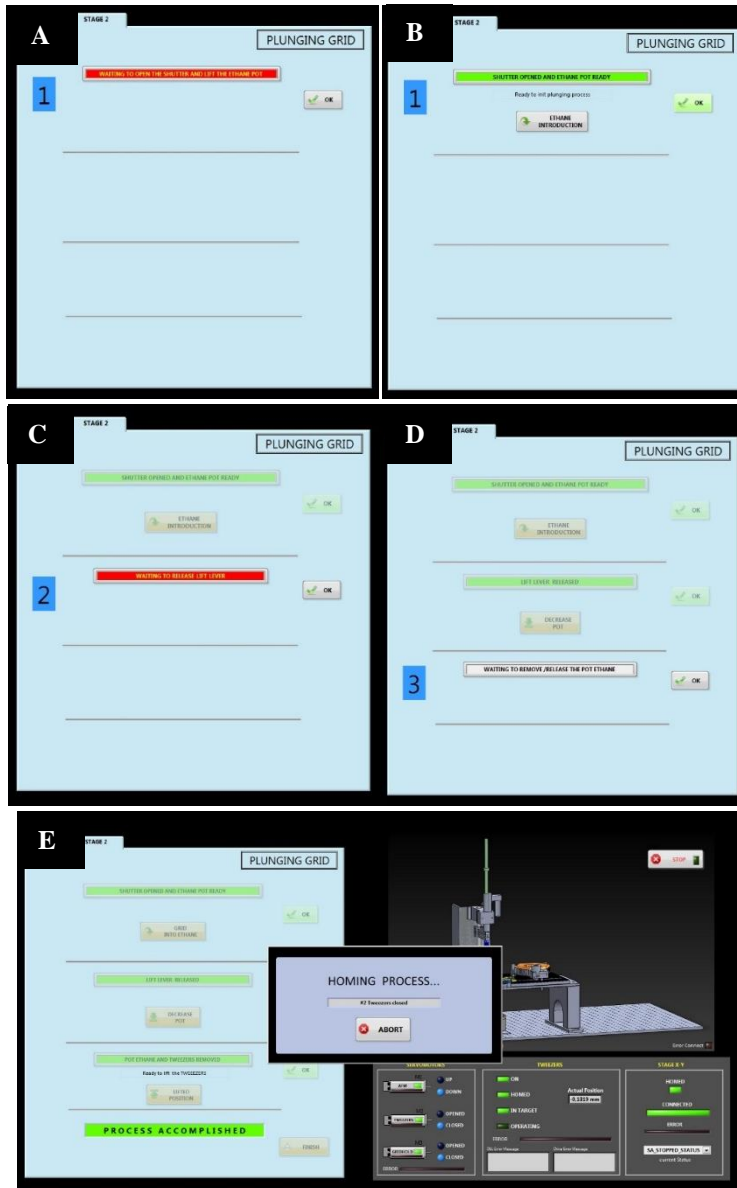


Figure 5.6: Stage 2 in the software is for EM-grid pick-up and plunge-freezing. (A) After stage 1, stage 2 is initiated. The first step displays a message to the user to load the cryogen container and to open the shutter, both manual steps (B) Once this is accomplished, the pick-up and plunge freezing of the EM-grid proceeds under computer control. The process is started by pressing the “Ethane introduction” button. (C) After plunging, the cryogen container is linked to the linear motor manually, making it possible to move the cryogen container and the tweezers together. The software pauses till the release of the cryogen container from the lifting system. (D) The cryogen container and tweezers are lowered and can be removed from the set-up and used for cryo-EM. (E) Stage 2 is finished and all components of the system are moved to their home positions so that a new sample can be prepared if necessary.

software urges the user to close the shutter, and the system is homed again by pressing the “Finish” button (Figure 5.6E).

The other modules of the software are “Configuration”, “Manual Mode” and “Security mode”. The configuration module can be used to change specific parameters of the system (Figure 5.7A). Positioning of the tweezer for pick-up and release of the EM-grid, positions of the stage during different process steps and the rotation angles of the different servo-motors.

“Manual Mode” can be used to manually control the different components of the system (Figure 5.7B-D). Although it is best to place the EM-grid into the holder, or to pick-up and plunge the EM-grid using the automated process, sometimes manual operation steps are necessary as well. This happens mainly during testing of the different components of the system, optimizing the parameters for the configuration module or during cell manipulation and dispensing on the EM-grid. During this last process, easy and quick transfer from the cells to the EM-grid can be accomplished by using the AFM servo-motor to quickly raise and lower the AFM while changing substrates (Figure 5.7B). Furthermore, sometimes precise positioning of the stage can be necessary during experiments, which can be achieved by entering the appropriate coordinates in the “Stage X-Y” module of the manual mode (Figure 5.7C).

The “Security mode” can be used to specifically home different components when necessary (Figure 5.7E). This mode is mainly added as a back-up system and should be handled with care, for incorrect handling of this mode could lead to crashing of certain components of the system. The homing method is designed in such a way that each component is homed when it is safe to change the position of this component, i.e. the stage not blocking the gridholder lift, while the manual security mode does not take the possibility of crashes into account. Normally, this module is not used, but may become important after an unknown failure of the system.

Although the software is able to load and unload a grid into and from the gridholder, the software is not able to control all the components of the system yet. Different software modules are necessary to control the camera, the AFM, the humidity chamber and the pressure controller. Integration of these software into one software could lead to better functionality of the system.

5.4: Humidity control

For cryo-EM, it is important that the sample is kept in its native aqueous environment, because the vitrified water is used as a fixation medium of the sample. Therefore, evaporation of the sample should be limited as much as possible. The evaporation rate mainly depends on relative humidity, the molecular weight of the solute, the local temperature and the area of the sample (76). Although additional factors play a role in the evaporation rate as well, e.g. the temperature of the substrate and the relative humidity surrounding the solution. When working with small volumes, evaporation of the sample is critical, because small volumes need a few seconds to evaporate completely (77). Therefore, sample evaporation should be

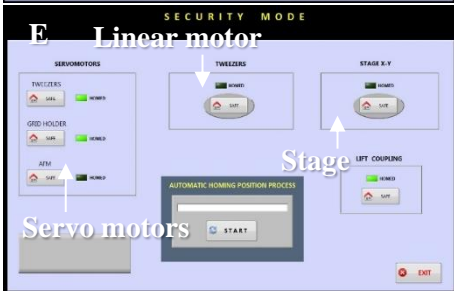
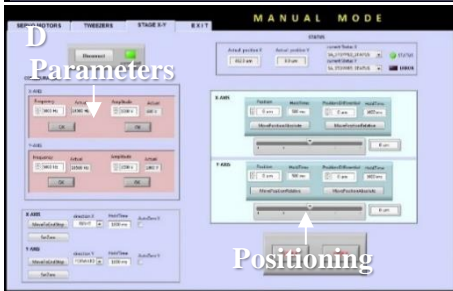
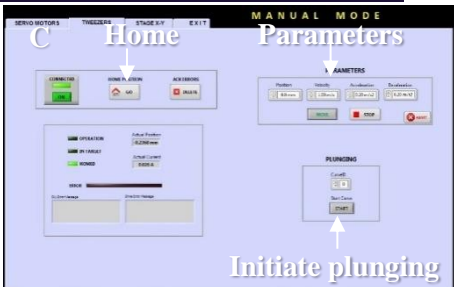
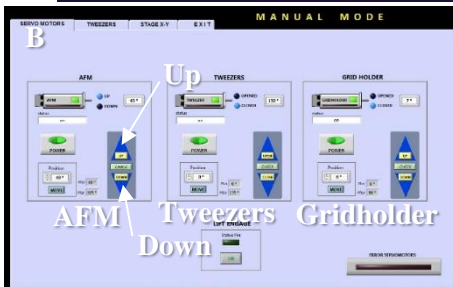
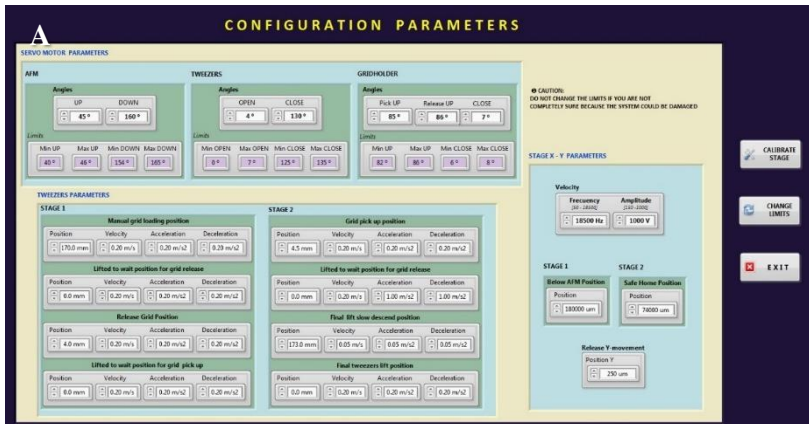


Figure 5.7: The different modules in the system. (A) The configuration module. This is the main module and contains all the parameters necessary to warrant correct operation. Small adjustments in this module can optimize or derail correct execution of all processes. (B-D) In the manual mode, each component of the system can be controlled individually when necessary. (B) The servomotor manual mode allows each servomotor to be controlled manually. Either standard up and down positions can be addressed, or specific X-Y coordinates can be reached. (C) The linear motor manual mode allows the linear motor to be moved to a specific position (top right), the plunging curve can be tested (bottom right), or the linear motor can be retracted to its home position (top left). (D) The X,Y stage manual mode allows the stage to be translated to specific, predetermined positions (left) or moved with less specific controls (right). (E) The security module of the system helps to reset the system after a crash. The security mode makes it possible to manually restore all the components in the system. This module needs to be handled with care, as the order of restoration is important. Restoring one sub-system could lead to crashes with other subsystems. In the automatic homing procedure these possible collisions are taken into account.

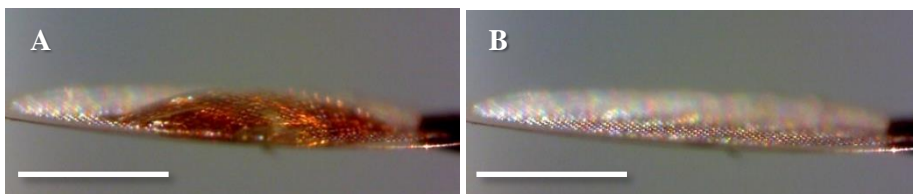


Figure 5.8: Evaporation in an ambient lab environment. (A) 0.5 μL of MiliQ water was dispensed with a conventional pipette on a glow discharged carbon-coated copper EM-grid placed in an ambient environment. Contact angle is $\sim 25^\circ$ (B) After 2.5 min, the liquid sample was evaporated. Evaporation rate is ~ 3.3 nL/sec. Scalebar is 1 mm.

avoided as much as possible and a humidity controller is necessary. The humidity control for the set-up was designed and implemented by Maastricht Instruments, and its use is discussed in this section.

5.4.1: Evaporation in an ambient environment

To test whether a humidity controlled environment during dispensing of femto- to picolitre volumes on an EM-grid is a necessity, 0.5 μL of MiliQ water was pipetted on a glow discharged EM-grid and left to incubate in an ambient environment (Figure 5.8A). The MiliQ water was completely evaporated 2.5 min after pipetting (Figure 5.8B), giving an estimated evaporation rate of 3.3 nL/sec. This means that a dispensed volume of 1 pL on a glow discharged EM-grid will evaporate within 0.3 msec after dispensing under ambient lab conditions. However, this test was performed with MiliQ water, while aspirated cellular samples are much more complex. This complexity will inhibit evaporation to some extent, due to its higher viscosity. Even with the added complexity, evaporation will be too fast to properly plunge freeze the sample after dispensing, making humidity control a necessity for performing these experiments.

5.4.2: The humidity chamber and dewpoint-controller

Ultimately, to inhibit sample evaporation, a humidity of 100% is required. However, the set-up comprises different components and electronics, which cannot survive in such a high humidity. Especially when the humidity control is switched off, condensation can lead to short-circuits in the system. Furthermore, maintaining a controlled humidity close to 100% is difficult due to the height differences in the set-up (Figure 5.1B and -C). Therefore, a maximum of 70% humidity was selected as target for the set-up.

Although the evaporation rate is lowered with increased humidity, dispensed volumes will still evaporate. To prevent evaporation, the temperature of the sample should be equal to the dewpoint. It is the temperature, at a given relative humidity and air temperature, where the evaporation rate and condensation rate are in equilibrium, inhibiting evaporation of the sample (78). At 70% humidity and 37°C air temperature, the dewpoint is $\sim 31^\circ\text{C}$. Therefore, the substrate on which the aspirated sample is dispensed, should have a lower temperature as compared to the air. To achieve this, the gridholder contains a temperature controller, which

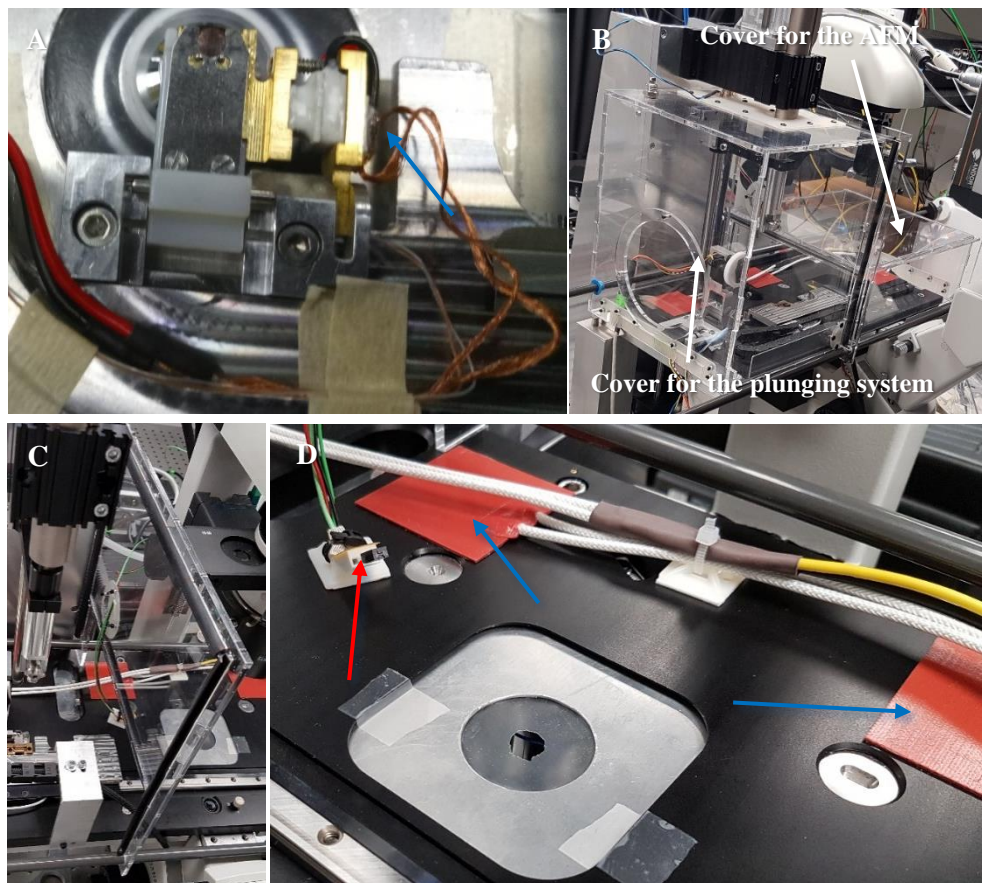


Figure 5.9: Humidity control and grid cooling of the set-up. (A) The dewpoint controller integrated in the gridholder. The gridholder is cooled by a miniature Peltier element (blue arrow). The local grid temperature is controlled by an integrated thermocouple. (B) Overview of the humidity chamber. The humidity chamber contains of two large boxes connected in the middle. The large box covers the plunging system, while the small box covers the AFM. (C) The dividing plate. This plate is used to close the cover, closing the plunging system, and to divide the humidity box into two connected, but separated compartments. (D). Heaters (blue arrows) attached to the stage plate regulate the set-up temperature. Temperature and relative humidity of the set-up are measured by the respective sensors (red arrow) mounted on the stage.

lowers the temperature of the EM-grid locally to the dewpoint, thereby inhibiting evaporation of the sample (Figure 5.9A).

The humidity chamber contains two separately movable boxes, which can be placed over the set-up (Figure 5.9B). The large box is placed around the plunging system, while the small box is small enough to fit under the microscope but provides enough space for the AFM. The two boxes meet in the middle, where the large box is closed by a dividing plate (Figure 5.9C).

Furthermore, heaters are placed on the stage table, to warrant the optimal temperature in the set-up for cellular experiments (Figure 5.9D).

The required air temperature depends on the cell-type used. Most cells used for research have an optimal growth temperature of 37°C, mammalian cells and *E. coli* for instance. However, some cell-types require different temperatures to survive. *Sf9* cells have a preferred temperature of 27°C, while the optimum temperature for *P. pastoris* is 30°C. It is therefore a requirement that the temperature in the set-up can be adjusted depending on the cell-type used for the experiments. The relative humidity and temperature of the chamber is measured by a sensor (Figure 5.9D).

The humidity chamber reaches a maximum humidity of 62%, according to the humidity sensor provided by Maastricht instruments. Even when a higher preferred humidity is set in the software (75%), humidity is constant and stays at 62%. An additional independent sensor was added to the set-up to monitor the stability of the humidity and temperature over time. Upon starting the humidity controller, the set-up requires ~80 min to reach a stable humidity and temperature (Figure 5.10A). However, the independent measured relative humidity is higher as compared to the humidity measured by the software. Where the software measures a maximum humidity of 62%, the independent sensor measures a relative constant humidity of ~70%. At t=175 min, there is a drop in the measured humidity (Figure 5.10A, dashed lines). This drop is caused by opening the humidity chamber for sample loading. Loading the sample took ~1 min. Humidity was restored 2 min after opening the humidity chamber. These results show that the humidity is relatively stable over time and is quickly restored after a sample is loaded into the system. During sample loading, the small box was removed from the set-up, opening up a large portion of the humidity controlled chamber. Based on the quick recovery to the set humidity we deduce that opening the shutter for grid-loading will not have a major effect on the humidity stability of the set-up. The chosen settings are visualized in Figure 5.10B.

Combining the humidity chamber with grid cooling by the temperature controller implemented in the gridholder should reduce possible evaporation to a negligible amount. To measure the evaporation rate, 0.5 µL MiliQ was pipetted on an EM-grid placed in the temperature controlled gridholder. The local temperature is adjusted automatically, corresponding to the dewpoint determined from the measured humidity and temperature of the system. As discussed in chapter 5.4.1, 0.5 µL MiliQ evaporates within 2.5 minutes when incubated in an ambient environment. With the humidity and dewpoint control, the lifetime of the 0.5 µL droplet was enhanced to 8.8 minutes, meaning an evaporation rate of 0.95 nL/s (Figure 5.11). Although the evaporation rate is lowered by this combination, the evaporation rate is still too high to work with picolitre or smaller volumes. While the system measures a relative humidity of ~60%, the independent sensor measures a relative humidity of ~70%. The dewpoint is set according to the humidity measured by the system, meaning that the temperature used by the dewpoint controller is probably too low as well, which should lead to condensation instead of evaporation. This suggests that heat-transfer from the dewpoint controlled gridholder towards the EM-grid is sub-optimal. The combination of humidity

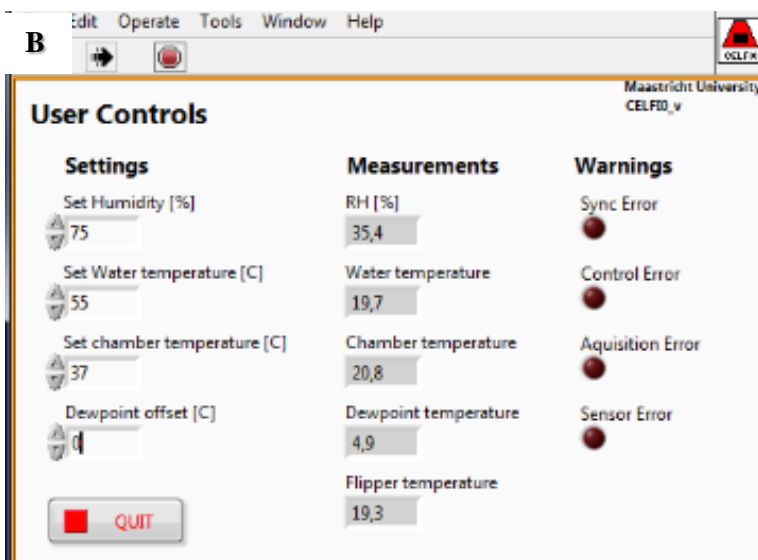
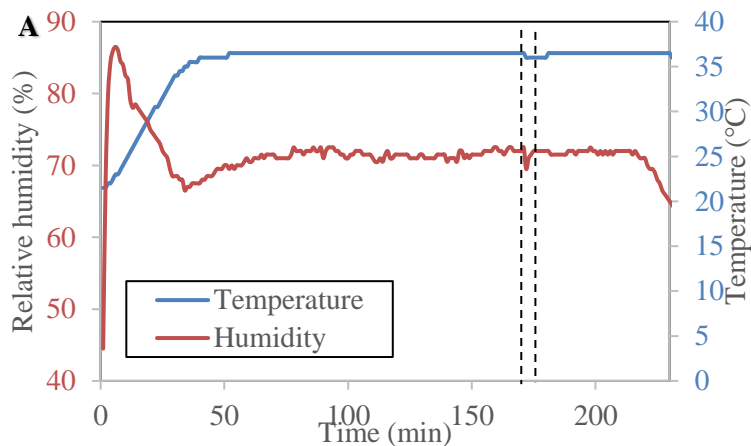


Figure 5.10: Humidity and temperature control of the set-up. (A) The measured temperature and humidity over time measured by the independent sensor. Temperature was set at 37°C, humidity was set at 75%. The temperature was stable after ~50 min. while the humidity reached a relatively stable plateau (~70%) after ~80 min. Opening the system leads to a drop in relative humidity, but it was restored after ~2 min (between dashed lines). After t=220 min, the chamber was opened and humidity control was stopped. (B) On the left, the settings used in the humidity software provided by Maastricht Instruments to control the temperature and humidity of the system. In the middle the measured values (humidity, water temperature and chamber temperature), the calculated dewpoint temperature and the measured gridholder (Flipper) temperature are visualized. On the right possible errors are visualized.

control and substrate dewpoint control needs to be optimized further to reduce sample evaporation as much as possible, the lowered evaporation rate measured at the moment shows promise for further improvements.

5.5: Grid handling, the sample stage and the AFM

Although the humidity control is key to keep the sample hydrated during grid transfer, the main parts of the set-up are the AFM controlling the hollow cantilevers and the plunging system. The plunging system will be discussed in chapter 5.6, while the use of hollow cantilevers for dispensing is mainly discussed in chapter 6.

Besides the possibility to aspirate and dispense picolitre or smaller volumes and plunge freezing a sample into liquid ethane, a dedicated gridholder is necessary to accommodate a smooth transition between the AFM and the plunger. The EM-grid should be in a horizontal position during cantilever approach and dispensing on the EM-grid. At the same time, the tweezers should be able to reproducibly pick-up the EM-grid from the stage, and to plunge it into liquid ethane as well. The steps necessary to perform these tasks are summarized in Figure 5.3 and discussed in chapter 5.3. In this section the gridholder, the AFM and the sample stage are described in more detail.

5.5.1: The AFM, hollow cantilevers and the sample stage

The hollow cantilevers used to aspirate and dispense subcellular volumes are controlled by a FlexAFM scanhead from Nanosurf. The FlexAFM is a versatile AFM able to scan both in liquid and air environments. This versatility is necessary for the set-up, because the cantilever is both used in liquid (during cell penetration) and air (during EM-grid dispensing). Furthermore, the relatively small size and the possibility to use this AFM in combination with a light microscope, makes this AFM scanhead very suitable for the designed set-up (Figure 5.12A).

The hollow cantilevers are provided by SmartTip BV, while the fluidic interface was designed and added to the hollow cantilevers by ir. Eleenoor Verlinden (Precision and Microsystems Engineering, Delft University of Technology in the Netherlands). Addition of the fluidic interface to the hollow cantilevers causes an elevation of the cantilever in the standard cantilever holders provided by Nanosurf (Figure 5.12B). Furthermore, the cantilever transition from liquid to air causes a misalignment of the laser, due to a change in the refractive index, impairing a proper approach on the EM-grid after cell aspiration. Therefore, the cantilever holder was modified by Nanosurf, to ensure proper placing of the cantilever with its fluidic interface and to ensure proper laser alignment after the liquid/air transition. To this end, a SureAlign™ cantilever holder was modified (Figure 5.12C).

The pressure controller (OB1-4 channels microfluidic flow controller from Elveflow) was tested and optimized by ir. Eleenoor Verlinden, a PhD student in the group of Dr. Murali Ghatkesar and Prof. Urs Staufer. The pressure controller contains two channels. The first one

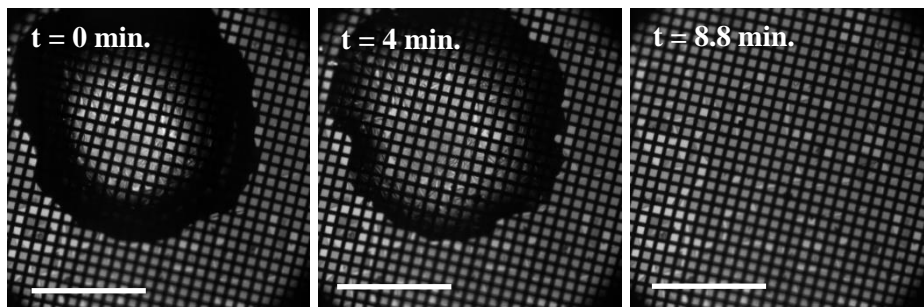


Figure 5.11: Evaporation of MiliQ in a humidity-controlled environment. A carbon coated EM-grid was loaded on the temperature controlled gridholder and 0.5 μL of MiliQ water was pipetted on the EM-grid. The humidity was measured to be $\sim 60\%$, while the local temperature was kept at the dewpoint ($\sim 31^\circ\text{C}$). At $t=4$ min. some evaporation is noticeable, and the sample was evaporated completely at $t=8.8$ min. At ambient temperature and humidity the same volume was evaporated after 2.5 min. Scale bar is 1 mm.

is able to produce an overpressure up to 8 bars, while the second channel is used to aspirate subcellular volumes from the cell by inducing an underpressure of ~ 1 bar (Figure 5.12D).

The stage is controlled by a piezo driven linear positioning system (SmarAct) able to achieve sub μm precision. The stage was designed and optimized for the proposed set-up by Nanosurf and can both move in the X-direction and the Y-direction, making it possible to precisely place a sample or substrate under the cantilever. The stage allows either cells to be positioned under the AFM tip, or the EM-grid for dispensing the aspirated sub-cellular volume (Figure 5.12E).

The “Manual mode” module of the software developed by Daniel Torres Gonzalez, allows the AFM to be rapidly lifted and the stage to be quickly displaced to a precise, predetermined position for sample dispensing. The combination of the designed stage and gridholder with the software ensures proper and fast aspiration from cells and dispensing of sub-cellular volumes on a specific location of the EM-grid.

5.5.2: Handling EM-grids in the system

As discussed above, the EM-grid holder is a crucial and complicated part in the set-up. The gridholder should keep the EM-grid horizontal during dispensing experiments, while the tweezers should be able to reproducibly pick-up the EM-grid from the gridholder to plunge freeze the sample. Furthermore, the temperature of the EM-grid, and therefore the gridholder, should be kept at dewpoint, limiting evaporation of the sample. The initial gridholder was designed and optimized by Jelle van der Does (TU Delft), while Maastricht Instruments refined this design by implementing the temperature controller. The gridholder contains a brass base containing a U-shaped opening at the tip, where the grid is placed (Figure 5.13A). The EM-grid is kept at its optimal position by two pins at the base of the opening and clamped to the base by a steel spring (Figure 5.13B). The gridholder can pivot around an axis, making

it possible to hold the EM-grid in a horizontal and vertical position. The gridholder can be opened by a pushbutton, which pushes the spring into its open position for pick-up of the grid (Figure 5.13A).

After the dispensing operation, the EM-grid is moved towards the plunging system of the set-up. While the EM-grid is kept horizontal during aspiration and dispensing experiments, the EM-grid is switched to its vertical position for grid pick-up by the tweezers. A specially designed lever, driven by a servo-motor (Figure 5.2B), rotates the gridholder to its vertical position, while a pin pushes the pushbutton to open up the gridholder (Figure 5.13C). By lowering the tweezers, the EM-grid can be picked up from its holder and is ready to be plunged (Figure 5.13D and E). The gridholder is then lowered to its horizontal position by the servo-motor driven lever and the stage moves away from the plunging hole (Figure 5.3B).

5.6: Cryo-EM sample preparation

As discussed in chapter 5.2.1, small volumes can be plunge frozen in liquid ethane for straightforward cryo-EM sample preparation. Commercial plungers require relatively large volumes (3-5 μl), but most of the fluid is blotted away to produce a thin aqueous film. Optimal blotting times, specific filter paper, and blotting force differ per sample and need to be determined experimentally. After blotting, the sample is rapidly plunged into liquid ethane.

The set-up discussed in this chapter is designed to operate with much smaller volumes for cryo-EM sample preparation (sub-picolitre range) and blotting is therefore not necessary. However, for sample placement and EM-grid transfer from the X,Y-stage to the plunging system an elaborate set-up is necessary. The gridholder design is therefore critical as discussed in chapter 5.5.2. Furthermore, the plunging system should be able to reproducibly pick-up the EM-grid from the gridholder, requiring precise positioning of tweezers at low velocity, whereas a high velocity is necessary during plunging to ensure proper vitrification. The cryogen should be close enough to the plunger to limit travel time and sample exposure to ambient environments. The cryogen should be displaced together with the vitrified grid to allow the tweezers to be released from the plunging system after plunge freezing. Here the plunger design, the handling of the cryogen before and after plunging and cryo-EM sample preparation with this system is presented.

5.6.1: Tweezers and the plunger

The plunger is operated by a linear motor (LinMot), while the tweezers are specifically designed for the set-up by Jelle van der Does. The linear motor is used, because it is precise, can reach a velocity of 1.5 m/sec, and can stop the immersed grid in the liquid ethane pot in a controlled manner. Low velocities are necessary for picking up the EM-grid from the gridholder or loading it in the gridholder, while a high velocity is necessary during plunging. During plunge freezing, vitreous ice is formed, preserving the sample. To form vitreous ice, the temperature has to drop faster than $\sim 10^5$ K/s (13). Therefore, the EM-grid must enter the cryogen at ~ 1.5 m/s (79). Based on the specifications of the linear motor chosen, the total

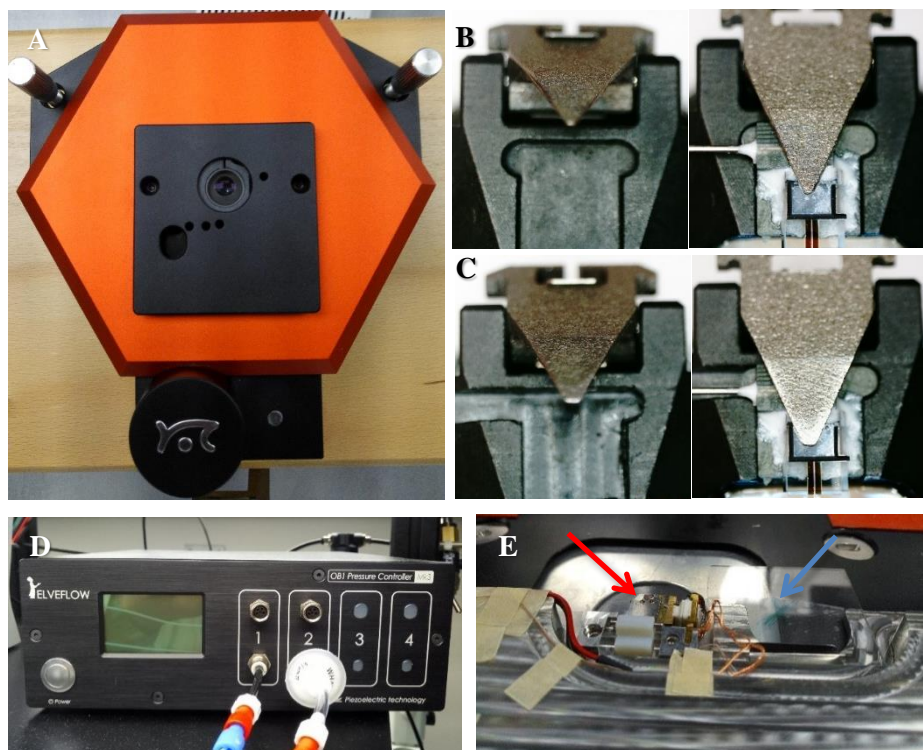


Figure 5.12: The Set-up to aspirate and dispense sub-cellular samples. (A) The FlexAFM scanhead from Nanosurf. The scanhead is used to control the positioning of the hollow cantilever. (B) The standard cantilever holder provided by Nanosurf. Left: Empty cantilever holder. Right: The cantilever holder clamping down a hollow cantilever with fluidic interface. The fluidic interface leads to an elevation of the cantilever in the cantilever holder. The tubing on the left is touching the cantilever holder, thus inducing a small tilt of the cantilever. (C) The adjusted cantilever holder. The cantilever holder was modified by Nanosurf to correctly accommodate the hollow cantilever with fluidic interface. Left: the empty cantilever holder, showing the modifications made. Right: the cantilever holder clamping down a hollow cantilever with fluidic interface. The insert is deepened to achieve a better fit of the fluidic interface in the holder, and an opening on the left provides space for the tubing. (D) The pressure controller (ElveFlow) used for dispensing and aspiration of sub-cellular volumes. Channel 1 is used for dispensing and generates an overpressure on the cantilever of up to 8 bars. Channel 2 is used for aspiration and reaches an underpressure on the cantilever of close to 1 bar. Channels 3 and 4 are not in use. (E) The stage. The stage holds the EM-grid (red arrow) and a glass substrate (blue arrow) in close proximity, making it possible to easily switch between aspiration from the cells (right) and dispensing on the EM-grid (left).

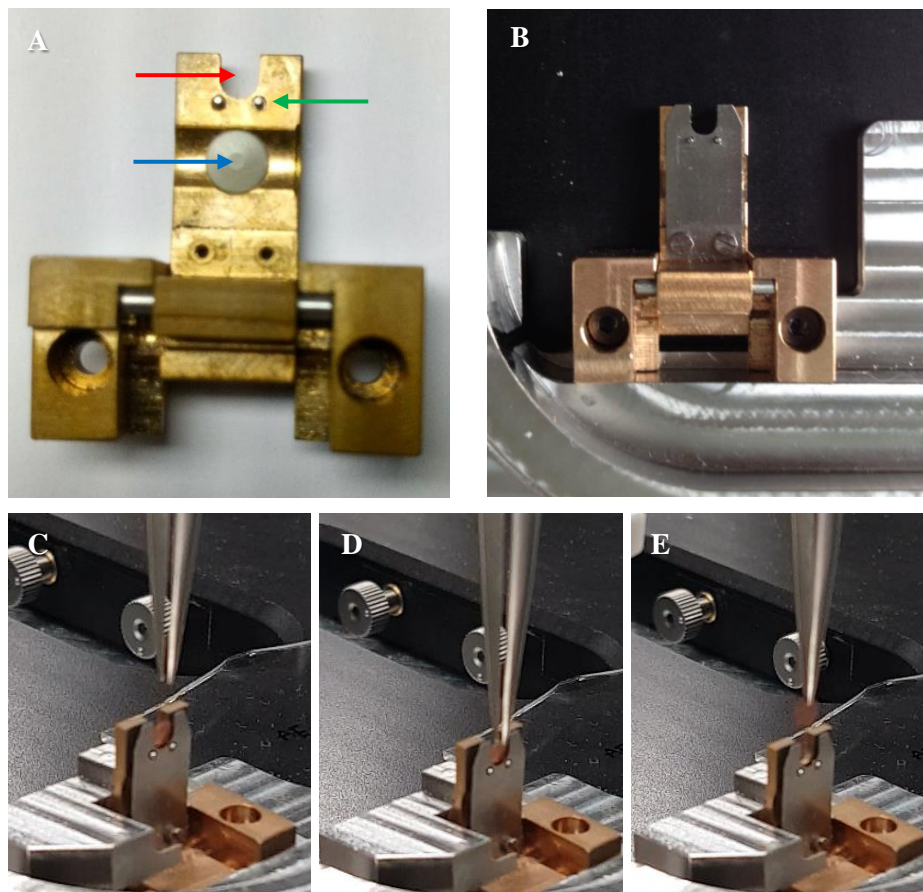


Figure 5.13: The gridholder. (A) Gridholder base (top view, no spring). The U-shaped opening at the top of the brass holder (red arrow) makes it possible to visualize the EM-grid. The EM-grid is placed on top of this opening and kept at its exact position by the two pins located near this opening (green arrow). The gridholder is opened by a lever pushing a pushbutton incorporated in the gridholder (blue arrow). (B) The gridholder (top view) with a steel spring. The spring is installed on the top of the gridholder, pushing the EM-grid to the gridholder base and holding it in place during manipulation. The spring is pushed open by the pushbutton displayed in (A). (C) The gridholder is rotated by 90° into its upright position by the gridholder servomotor. The rotation also operates a lever that pushes the pushbutton described in (A; blue arrow), leading to separation of the spring and the brass base. (D) The open tweezers are lowered and the arms embrace the copper EM-grid, making it possible to grab the grid by closing the tweezers. (E) Closing the tweezers and lifting them with the linear motor leads to the release of the EM-grid from the gridholder. The gridholder is then rotated back to its horizontal position by the servomotor and the stage is moved away from the plunging hole. The EM-grid can then be plunged into the liquid ethane.

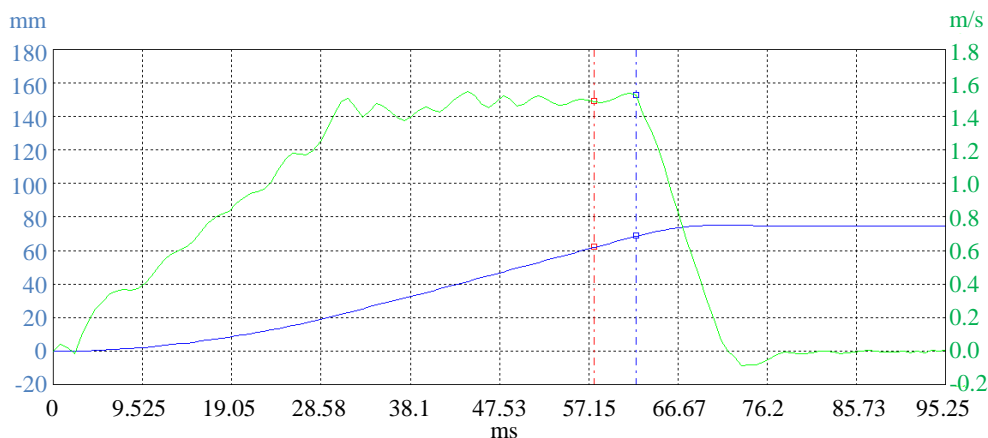


Figure 5.14: Plunging curve of the linear motor. For plunging the grid into the liquid ethane, the linear motor moves the plunger for 78 mm (blue curve) while accelerating it to 1.5 m/sec. This speed is reached ~30 msec after launching the plunger (green curve) or after a rod displacement of ~22 mm. Immersion to ethane occurred at ~57 msec or after a rod displacement of ~60 mm (red dotted line). After pushing the grid into the ethane for another ~10 mm (total 70 mm; ~62 msec) deceleration was initiated (blue dotted line). Deceleration takes ~14 msec, while the linear motor moves for another 8 mm. Total plunging takes ~76 msec.

travelled distance during plunging is 76 mm. Calibration of the plunging curve shows that maximum speed is reached after a displacement of ~22 mm (Figure 5.14). The plunger moves on at this speed for ~60 mm, when the grid reaches the liquid ethane, and then for another 10 mm, after which deceleration is initiated. The plunger stops when the grid is located ~2 mm from the bottom of the plunging pot. The total plunging time is ~76 msec.

To pick up the EM-grid from the gridholder and to load the EM-grid into the gridholder, push-button controlled reverse tweezers were designed (Figure 5.15A). The push button is pressed by a servo-motor controlled wheel (Figure 5.15B, Figure 5.2C). This wheel ensures that the tweezer can be opened while the tweezer moves a few mm necessary during the pick-up and release of the EM-grid. The tweezers can be easily mounted on and released from the plunger by a bolt holding the tweezer at its position.

5.6.2: Handling of the cryogenic liquid

A cryogen container is used, comparable to the ones used for the Vitrobot (FEI). The cryogen container is filled with liquid nitrogen to cool the interior to less than -160°C . Once cold, the brass cup is filled with ethane, which condenses at the low temperature of the cup, forming liquid ethane. The liquid ethane is used to plunge freeze the dispensed samples.

During plunging, the cryogen should be as close to the sample as possible, while the plunger has enough space to reach the speed of 1.5 m/s discussed chapter 5.6.1. After plunging or during grid-loading, enough space to handle the tweezers with the grid outside the humidity chamber should be available. Therefore, the cryogen container is pushed up towards the table before plunging, and lowered after vitrification is completed. To this end an elevator for the cryogen container was designed.

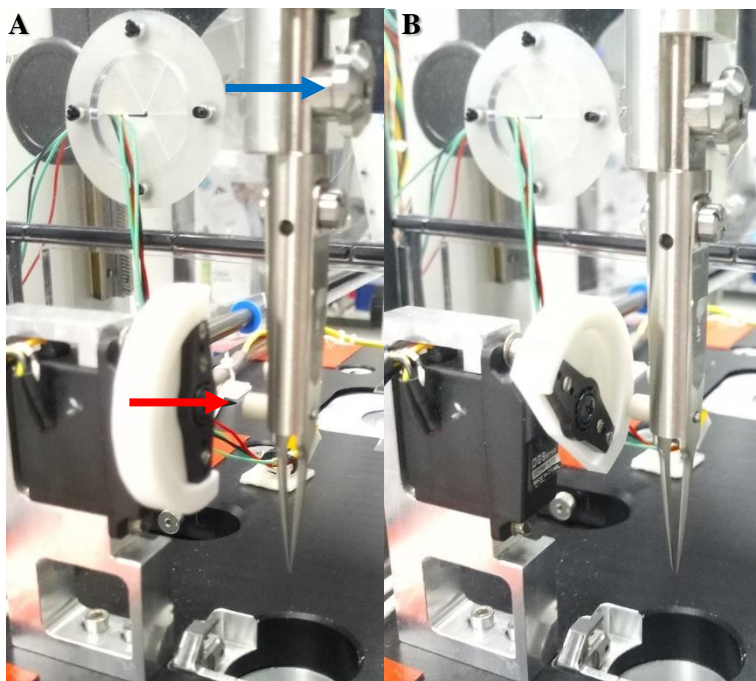


Figure 5.15: The tweezers used for plunge-freezing dispensed samples. (A) Closed tweezers. The tweezers were designed by Jelle van der Does. They can be opened by pushing the white pushbutton (red arrow). The tweezers are connected to the linear motor via a rotating bolt (blue arrow). (B) Open tweezers. A servomotor controlled rotating wheel is used to push the pushbutton and open the tweezers. The rotating wheel was designed to keep the tweezers open while displacing them by several millimetres to grab or release the grid.

Once the system is ready for plunge freezing, the cryogen container is placed on a plateau (Figure 5.16A). This plateau is raised by hand, placing the cryogen container close to the plunging aperture of the set-up (Figure 5.16B). The plateau is kept in place by a spring controlled lever. After plunging, a solenoid controlled pin locks the stabilising rod that also holds the cryogen container with the linear motor (Figure 5.16C). After correct pin insertion, the lever is released underneath the plateau and the elevator can lower the cryogen container together with the tweezers. Once the cryogen container reaches the table, the tweezers can be removed from the plunger by using a specifically designed container lid (Figure 5.16D). The plunger is retracted after tweezers are released.

5.6.3: Preparation of cryo-EM samples

Figure 5.14 shows that high plunging speeds can be achieved by. Furthermore, the placement of the cryogen container and the movement of this container have been optimized and thoroughly tested. To test the plunger for cryo-EM sample preparation, a glow discharged Quantifoil® copper EM-grid was loaded onto the plunging system and 3 μL of TMV (1 mg/mL) was pipetted on the grid. After pipetting, the grid was blotted, by hand, for ~ 3 sec

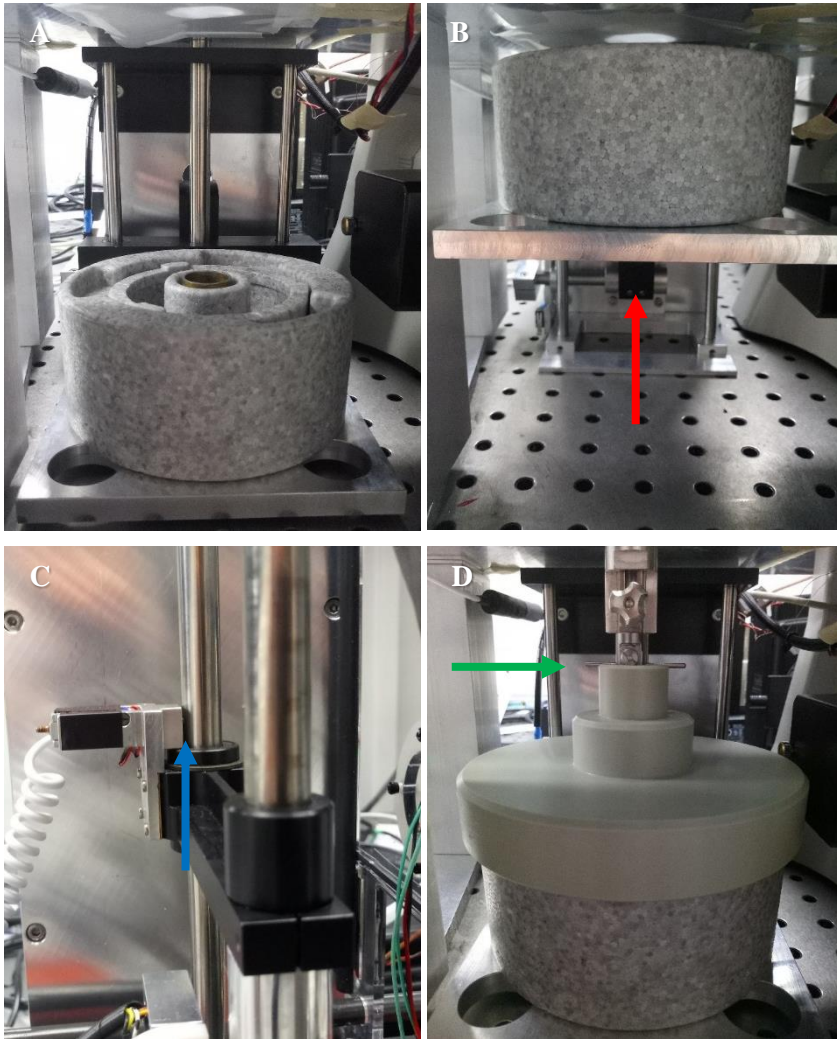


Figure 5.16: Handling the cryogenics and plunge freezing. (A) A cryogenic container is placed on the elevator, which makes it possible to manipulate the tweezers under the set-up during EM-grid loading and after plunge freezing. (B) Elevator and cryogenic container are lifted by hand and kept in place by a spring controlled lever (red arrow). The elevator holds the cryogenic container directly below the plunging hole. (C) After plunging, a solenoid controlled pin (blue arrow) is inserted in the stabilising rod connected to the elevator, locking it to the plunger rod holding the tweezers (front). This allows tweezers and cryogenic container to be lowered simultaneously after plunging. The lever (B; red arrow) must be removed to release the cryogenic elevator. (D) After lowering the cryogenic container, the container is closed with a lid used to stabilize the tweezers. To this end, a metal rod is inserted in the tweezers (green arrow), keeping the tweezers at their place after releasing them from the plunging rod. Cryogenic container and tweezers can be removed from the set-up.

and plunged into liquid ethane. After plunging, liquid ethane was found to freeze between the two arms of the tweezers preventing the grid to be released (Figure 5.17). Liquid nitrogen has a temperature of -195°C , while the freezing point of ethane is -183°C . Therefore, residual ethane between the tweezers arms will freeze once transferred into liquid nitrogen, a necessary step for placing the grid into a liquid nitrogen cooled grid-box.

In our presented system, the grid is fully immersed in liquid ethane before deceleration starts (Figure 5.14), and reaches a total depth in the liquid ethane of 18 mm. This is more than what is found in commercial plunging systems. Furthermore, at the tip, the tweezers are too wide, facilitating the formation of an ethane droplet between the tweezers arms. Therefore, the travel of the grid into the liquid ethane will be shortened, and a new tweezer design will limit the space between the two tweezer arms.

In spite of these challenges, relatively good cryo-EM images were obtained from this plunging device during the first test series. To preserve the sample after plunging, the EM-grid was handed over to a second, tighter, tweezer (commercially available for plunging systems) while kept in liquid ethane, eliminating the formation of an ethane droplet between the tweezer arms. With the second tweezers the EM-grid could be placed in the liquid nitrogen cooled grid-box and analysed via cryo-EM. Although the ice-thickness was relatively thick due to uncontrolled blotting, TMV could be recognized in the sample at both low magnification (Figure 5.18A) and high magnification (Figure 5.18B). This shows that the plunging mechanisms designed for this set-up can successfully plunge freeze samples for cryo-EM.

5.7: Conclusion

As discussed in chapter 5.2.1, plunge freezing is a relatively straightforward method to prepare cryo-EM samples. Especially once the blotting step can be omitted, when samples are thin enough, plunge freezing is the most optimal method for cryo-EM sample preparation. To achieve thin samples, while retaining the complexity of the cell, hollow cantilevers can be used to aspirate and dispense subcellular volumes (7). For this, a complex set-up and controlling software were designed and built. The software controls the most crucial and time-critical steps in the set-up to allow their automated execution. Although the software handles the EM-grid almost completely automatically, the software does not control all the components of the set-up. The AFM, the pressure controller, the camera and the humidity controller all use different software, which requires five different programs to run simultaneously for controlling all the components of the system. The main software was designed by Daniel Torres-Gonzalez and is coded in Labview. The humidity controller software is based on Labview as well, and the pressure controller can also be integrated into Labview. Complete integration of all components into one controlling software system will improve the functionality of the set-up, making it easier to use and to combine the different components this system offers.

The designed set-up now contains most of the necessary components for cryo-EM sample preparation. However, individual components still need to be optimized for routine

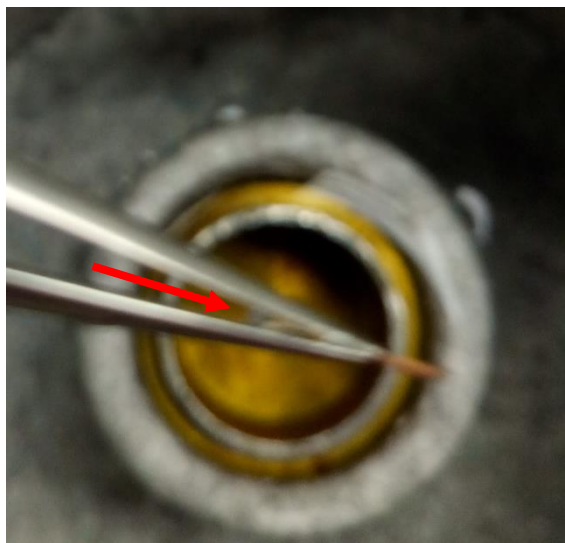


Figure 5.17: Liquid ethane droplet formation between the tweezers arms due to capillarity (red arrow). The grid is stored in liquid nitrogen after plunging. During the transfer to liquid nitrogen, the liquid ethane will freeze, causing the EM-grid to stick to the tweezers. A new tweezers design is under development to prevent liquid ethane from creeping into the tweezers.

preparation and plunge freezing of samples in the femto- to picolitre range. Although Figure 5.18 shows the possibility to use the plunging machinery to plunge freeze samples for cryo-EM, the tweezers currently used are not optimal for sample vitrification. After plunging a droplet of liquid ethane forms between the tweezer arms due to capillary forces (Figure 5.17), making it impossible to release the grid into its liquid nitrogen storage container after plunging. In commercial plungers the tweezer arms are kept very tight to each other at the tip, while the tweezers from our set-up have a relatively large opening between the tweezer arms (Figure 5.15A). Furthermore, after plunging, the EM-grid is kept relatively close to the ethane surface in commercial plungers. In our set-up the EM-grid is plunged deeply into liquid ethane, stopping at 2 mm from the bottom, which means that when the brass ethane-container is completely filled, the EM-grid is plunged 18 mm deep into liquid ethane. This is mainly because the EM-grid moves at full speed through liquid ethane for 10 mm (Figure 5.14), which does not seem to be necessary. Therefore, a new tweezer design, with closer tweezer arms, and a shorter liquid ethane travel path will be implemented to eliminate the formation of the capillary force induced ethane droplet, making it easier to use this plunging system routinely.

The plunge frozen cryo-EM sample (Figure 5.18) was prepared by pipetting 3 μL of TMV solution (1 mg/mL) on a glow discharged EM-grid, while the excess of fluid was removed via blotting. The system has not been used yet for cryo-EM sample preparation of picolitre or smaller dispensed volumes. Although the evaporation rate was lowered, as compared to

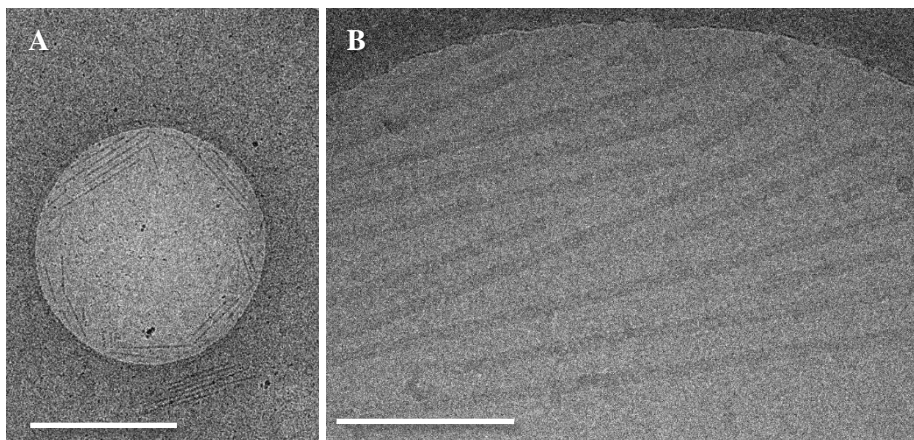


Figure 18: Cryo-EM images of Tabaco Mosaic Virus (TMV). 3 μL of TMV (1 mg/mL) was pipetted on a glow discharged Quantifoil coated copper EM-grid. The EM-grid was blotted for 3 sec prior to plunge freezing using the linear motor-driven plunging system described here. (A) TMV is visualized at low magnification (8,000x). Scalebar is 1 μm . (B) TMV is imaged at higher magnification. The ice is too thick, leading to low contrast TMV images that exhibit no high resolution features. Magnification was 50,000x, scalebar is 200 nm.

the evaporation in an ambient environment, the evaporation rate is still too high to work with sub-picolitre samples. As discussed in chapter 5.4, a sample of 1 pL volume evaporates within 0.3 msec at ambient humidity and temperature. Therefore, a humidity chamber and a temperature controlling gridholder, keeping the grid around dewpoint temperature, were designed and implemented into the system. Although the evaporation rate was lowered by using this combination (from 3.3 nL/s to 0.95 nL/s), the evaporation rate is still too high to properly plunge freeze picolitre samples. Constant humidity was reached after ~ 80 min (Figure 5.10A). However, when the humidity within the chamber was measured with an independent sensor ($\sim 70\%$) a discrepancy was observed between the measured humidity and that of the system implemented sensor (62%, Figure 5.9D red arrow). In contrast, the measured temperature was comparable between the two sensors and equals the set temperature in the software. The dewpoint of the gridholder is determined from both the temperature and the relative humidity measured by the set-up. The dewpoint at 37°C and a 70% humidity is $\sim 32^\circ\text{C}$, while at 60% the dewpoint is $\sim 28^\circ\text{C}$. Therefore, if the humidity was truly 70% instead of the measured 60%, the set dewpoint is too low and water should condense on the EM-grid. But as this is not the case the EM-grid was not properly cooled by the dewpoint controller. Further optimization is necessary to decrease the evaporation rate to a range where it is possible to work with picolitre or smaller volumes.

Besides appropriate evaporation inhibition and a working plunging system, the set-up should be able to dispense small volumes on an EM-grid and vitrify them. The design of the sample stage aids in combining aspiration from cells and dispensing on an EM-grid in a fast and

efficient manner (Figure 5.12). The manual mode in the controlling software allows the AFM to be quickly pushed up for moving the cells away and the EM-grid below the cantilever instead (Figure 5.7B). Furthermore, predetermined stage coordinates can be used to precisely move to specific locations on either the grid or to specific cells (Figure 5.7C). Novel hollow cantilevers and their fluidic interface are currently being designed, while experiments are performed routinely to find possible points for optimization. The adapted cantilever holder from Nanosurf improved the positioning and clamping of the cantilever with its fluidic interface (Figure 5.12C). In addition, this new holder provides a better optical system and facilitates the laser alignment and improved thermal tuning for spring constant determination of the cantilever enormously.

Although most components are now in its place, the controlling software works, the plunging mechanism vitrifies samples, and chapter 6 shows that dispensing small volumes on an EM-grid is possible with hollow cantilevers, the set-up has not been used yet for its proposed function. Evaporation control and plunging tweezers need to be improved for reproducible and routine cryo-EM sample preparation of picolitre or smaller volumes.

5.8: Materials and methods

AFM and hollow cantilevers—A FlexAFM scan head with a C3000 controller and a I100 interface box was purchased from Nanosurf. Initially cantilevers were clamped by using a flat cantilever holder suitable for both liquid and air (Nanosurf). Hollow cantilevers attached to a fluidic interface do not fit properly in the flat cantilever holder. Furthermore, transitioning from liquid to air (or reversed) leads to miss-alignment of the laser. Therefore, a modified SureAlign™ cantilever holder was purchased from Nanosurf (Figure 5.12C). The software used to control the AFM was the C3000 control software, version 3.8.2.4 provided by Nanosurf. The hollow cantilevers are provided by Smarttip and modified at the precision and microsystems engineering department of Delft University of Technology by ir. Eleonor Verlinden to include a fluidic interface and a connecting tube to connect the hollow cantilever to the pressure controller (Elveflow).

Motors—The set-up is controlled by three servo-motors, one linear motor (LinMot) and an X,Y-stage (SmarAct/Nanosurf). The servomotors are controlled by an Arduino and aid in lifting the AFM (motor 1), opening the tweezers (motor 2) and lifting the gridholder to its horizontal position (motor 3). The linear motor is used for precise positioning of the tweezers for pick-up and release of the EM-grid and high-speed plunging. The linear motor is electromagnetically driven, where the tube is made of neodymium magnets mounted in a stainless steel tube, while the stator contains motor windings, bearings for the slider, position capture sensors and a microprocessor circuit for monitoring the motor. The internal positioning sensor is able to monitor the position of the linear motor both during the motion and when it is stopped. The plunging motion of the EM-grid into liquid ethane is saved as a curve in the servo drive. The X,Y-stage is controlled by piezo driven linear positioners from SmarAct and carry nm precision. The stage surrounding the positioners, able to hold the EM-grid and the glass plate was designed by Nanosurf.

Evaporation control—The humidity controller and temperature controlled gridholder were designed by Maastricht Instruments. A maximum humidity of 70% is used at a temperature of 37°C. The maximum humidity was chosen based on the maximum humidity in which the AFM scanhead is still functional. The temperature was chosen, for it is the most commonly used temperature for cellular experiments. The set-temperature is achieved by heating the microscopy plate. Humidity and temperature of the set-up are measured by an integrated sensor. The temperature controlled gridholder keeps the EM-grid at dewpoint, leading to a local humidity of 100% and preventing evaporation of the dispensed sample. The dewpoint is calculated based on the measured humidity and temperature of the set-up. The temperature of the gridholder is controlled by an attached peltier and an integrated thermocouple.

Cryo-EM—3 μL of TMV (1 mg/mL) was pipetted on a glow discharged Quantifoil® copper EM-grid picked by the tweezers and attached to the linear motor. The excess of fluid

was removed by blotting for ~3 sec by hand followed by immediate plunging into liquid ethane. After plunging the tweezers were removed from the linear motor and the linear motor was retracted. The EM-grid was picked up from the tweezers by using a secondary pair of tweezers (Dumont HP 5, stainless steel, 0.10x0.06 mm tip) while the grid was kept in liquid ethane. The grid was then transferred towards a liquid nitrogen cooled storage container and analyzed by using a JEOL 3200 electron microscopy. Images were taken by using an Tietz f416 CCD camera.

5.9: References

1. Campbell, M. G., Cheng, A., Brilot, A. F., Moeller, A., Lyumkis, D., Veesler, D., Pan, J., Harrison, S. C., Potter, C. S., Carragher, B., and Grigorieff, N. (2012) Movies of ice-embedded particles enhance resolution in electron cryo-microscopy. *Structure (London, England : 1993)* **20**, 1823-1828
2. Li, X., Mooney, P., Zheng, S., Booth, C. R., Braumfeld, M. B., Gubbens, S., Agard, D. A., and Cheng, Y. (2013) Electron counting and beam-induced motion correction enable near-atomic-resolution single-particle cryo-EM. *Nature methods* **10**, 584-590
3. Scheres, S. H. W. (2012) RELION: Implementation of a Bayesian approach to cryo-EM structure determination. *Journal of Structural Biology* **180**, 519-530
4. Bai, X.-c., Fernandez, I. S., McMullan, G., and Scheres, S. H. W. (2013) Ribosome structures to near-atomic resolution from thirty thousand cryo-EM particles. *eLife* **2**, e00461
5. Guillaume-Gentil, O., Potthoff, E., Ossola, D., Dorig, P., Zambelli, T., and Vorholt, J. A. (2013) Force-controlled fluidic injection into single cell nuclei. *Small (Weinheim an der Bergstrasse, Germany)* **9**, 1904-1907
6. Guillaume-Gentil, O., Potthoff, E., Ossola, D., Franz, C. M., Zambelli, T., and Vorholt, J. A. (2014) Force-controlled manipulation of single cells: from AFM to FluidFM. *Trends in biotechnology* **32**, 381-388
7. Guillaume-Gentil, O., Grindberg, R. V., Kooger, R., Dorwling-Carter, L., Martinez, V., Ossola, D., Pilhofer, M., Zambelli, T., and Vorholt, J. A. (2016) Tunable Single-Cell Extraction for Molecular Analyses. *Cell* **166**, 506-516
8. Brenner, S., and Horne, R. W. (1959) A negative staining method for high resolution electron microscopy of viruses. *Biochimica et biophysica acta* **34**, 103-110
9. Booth, D. S., Avila-Sakar, A., and Cheng, Y. (2011) Visualizing proteins and macromolecular complexes by negative stain EM: from grid preparation to image acquisition. *Journal of visualized experiments : JoVE*
10. Bullock, G. R. (1984) The current status of fixation for electron microscopy: A review. *Journal of Microscopy* **133**, 1-15
11. Ellis, R. J. (2001) Macromolecular crowding: obvious but underappreciated. *Trends in biochemical sciences* **26**, 597-604
12. Dubochet, J., Booy, F. P., Freeman, R., Jones, A. V., and Walter, C. A. (1981) Low temperature electron microscopy. *Annual review of biophysics and bioengineering* **10**, 133-149
13. Dubochet, J., and McDowell, A. W. (1981) VITRIFICATION OF PURE WATER FOR ELECTRON MICROSCOPY. *Journal of Microscopy* **124**, 3-4
14. Adrian, M., Dubochet, J., Lepault, J., and McDowell, A. W. (1984) Cryo-electron microscopy of viruses. *Nature* **308**, 32-36
15. Dubochet, J., Adrian, M., Chang, J. J., Homo, J. C., Lepault, J., McDowell, A. W., and Schultz, P. (1988) Cryo-electron microscopy of vitrified specimens. *Quarterly reviews of biophysics* **21**, 129-228
16. Klug, A., and Crowther, R. A. (1972) Three-dimensional Image Reconstruction from the Viewpoint of information Theory. *Nature* **238**, 435

17. Leis, A., Rockel, B., Andrees, L., and Baumeister, W. (2009) Visualizing cells at the nanoscale. *Trends in biochemical sciences* **34**, 60-70
18. Kemmerling, S., Ziegler, J., Schweighauser, G., Arnold, S. A., Giss, D., Muller, S. A., Ringler, P., Goldie, K. N., Goedecke, N., Hierlemann, A., Stahlberg, H., Engel, A., and Braun, T. (2012) Connecting mu-fluidics to electron microscopy. *Journal of structural biology* **177**, 128-134
19. Courties, C., Vaquer, A., Troussellier, M., Lautier, J., Chrétiennot-Dinet, M. J., Neveux, J., Machado, C., and Claustre, H. (1994) Smallest eukaryotic organism. *Nature* **370**, 255
20. Matsuzaki, M., Misumi, O., Shin, I. T., Maruyama, S., Takahara, M., Miyagishima, S. Y., Mori, T., Nishida, K., Yagisawa, F., Nishida, K., Yoshida, Y., Nishimura, Y., Nakao, S., Kobayashi, T., Momoyama, Y., Higashiyama, T., Minoda, A., Sano, M., Nomoto, H., Oishi, K., Hayashi, H., Ohta, F., Nishizaka, S., Haga, S., Miura, S., Morishita, T., Kabeya, Y., Terasawa, K., Suzuki, Y., Ishii, Y., Asakawa, S., Takano, H., Ohta, N., Kuroiwa, H., Tanaka, K., Shimizu, N., Sugano, S., Sato, N., Nozaki, H., Ogasawara, N., Kohara, Y., and Kuroiwa, T. (2004) Genome sequence of the ultrasmall unicellular red alga *Cyanidioschyzon merolae* 10D. *Nature* **428**, 653-657
21. Moor, H. (1987) Theory and Practice of High Pressure Freezing. in *Cryotechniques in Biological Electron Microscopy* (Steinbrecht, R. A., and Zierold, K. eds.), Springer Berlin Heidelberg, Berlin, Heidelberg. pp 175-191
22. Studer, D., Graber, W., Al-Amoudi, A., and Eggli, P. (2001) A new approach for cryofixation by high-pressure freezing. *J Microsc* **203**, 285-294
23. Grimm, R., Typke, D., Barmann, M., and Baumeister, W. (1996) Determination of the inelastic mean free path in ice by examination of tilted vesicles and automated most probable loss imaging. *Ultramicroscopy* **63**, 169-179
24. Al-Amoudi, A., Dubochet, J., Gnaegi, H., Luthi, W., and Studer, D. (2003) An oscillating cryo-knife reduces cutting-induced deformation of vitreous ultrathin sections. *J Microsc* **212**, 26-33
25. Lučić, V., Leis, A., and Baumeister, W. (2008) Cryo-electron tomography of cells: connecting structure and function. *Histochemistry and cell biology* **130**, 185
26. Marko, M., Hsieh, C., Schalek, R., Frank, J., and Mannella, C. (2007) Focused-ion-beam thinning of frozen-hydrated biological specimens for cryo-electron microscopy. *Nature Methods* **4**, 215
27. Yi, H., Strauss, J. D., Ke, Z., Alonas, E., Dillard, R. S., Hampton, C. M., Lamb, K. M., Hammonds, J. E., Santangelo, P. J., Spearman, P. W., and Wright, E. R. (2015) Native immunogold labeling of cell surface proteins and viral glycoproteins for cryo-electron microscopy and cryo-electron tomography applications. *The journal of histochemistry and cytochemistry : official journal of the Histochemistry Society* **63**, 780-792
28. Nicastro, D., Schwartz, C., Pierson, J., Gaudette, R., Porter, M. E., and McIntosh, J. R. (2006) The molecular architecture of axonemes revealed by cryoelectron tomography. *Science (New York, N.Y.)* **313**, 944-948
29. Medalia, O., Weber, I., Frangakis, A. S., Nicastro, D., Gerisch, G., and Baumeister, W. (2002) Macromolecular architecture in eukaryotic cells visualized by cryoelectron tomography. *Science (New York, N.Y.)* **298**, 1209-1213

30. Peitsch, C. F., Beckmann, S., and Zuber, B. (2016) iMEM: Isolation of Plasma Membrane for Cryoelectron Microscopy. *Structure (London, England : 1993)* **24**, 2198-2206
31. Arnold, S. A., Albiez, S., Bieri, A., Syntychaki, A., Adaixo, R., McLeod, R. A., Goldie, K. N., Stahlberg, H., and Braun, T. (2017) Blotting-free and lossless cryo-electron microscopy grid preparation from nanoliter-sized protein samples and single-cell extracts. *Journal of structural biology* **197**, 220-226
32. Arnold, S. A., Albiez, S., Opara, N., Chami, M., Schmidli, C., Bieri, A., Padeste, C., Stahlberg, H., and Braun, T. (2016) Total Sample Conditioning and Preparation of Nanoliter Volumes for Electron Microscopy. *ACS nano* **10**, 4981-4988
33. Kemmerling, S., Arnold, S. A., Bircher, B. A., Sauter, N., Escobedo, C., Dernick, G., Hierlemann, A., Stahlberg, H., and Braun, T. (2013) Single-cell lysis for visual analysis by electron microscopy. *Journal of structural biology* **183**, 467-473
34. Hahn, W., Ho, S. H., Jeong, J. G., Hahn, E. Y., Kim, S., Yu, S. S., Kim, S., and Kim, J. M. (2004) Viral vector-mediated transduction of a modified thrombospondin-2 cDNA inhibits tumor growth and angiogenesis. *Gene therapy* **11**, 739-745
35. Selkirk, S. M., Greenberg, S. J., Plunkett, R. J., Barone, T. A., Lis, A., and Spence, P. O. (2002) Syngeneic central nervous system transplantation of genetically transduced mature, adult astrocytes. *Gene therapy* **9**, 432-443
36. Kang, Y., Stein, C. S., Heth, J. A., Sinn, P. L., Penisten, A. K., Staber, P. D., Ratliff, K. L., Shen, H., Barker, C. K., Martins, I., Sharkey, C. M., Sanders, D. A., McCray, P. B., Jr., and Davidson, B. L. (2002) In vivo gene transfer using a nonprimate lentiviral vector pseudotyped with Ross River Virus glycoproteins. *Journal of virology* **76**, 9378-9388
37. Modlich, U., Bohne, J., Schmidt, M., von Kalle, C., Knoss, S., Schambach, A., and Baum, C. (2006) Cell-culture assays reveal the importance of retroviral vector design for insertional genotoxicity. *Blood* **108**, 2545-2553
38. Mathis, J. M., Williams, B. J., Sibley, D. A., Carroll, J. L., Li, J., Odaka, Y., Barlow, S., Nathan, C. O., Li, B. D., and DeBenedetti, A. (2006) Cancer-specific targeting of an adenovirus-delivered herpes simplex virus thymidine kinase suicide gene using translational control. *The journal of gene medicine* **8**, 1105-1120
39. Bruder, J. T., and Kovsdi, I. (1997) Adenovirus infection stimulates the Raf/MAPK signaling pathway and induces interleukin-8 expression. *Journal of virology* **71**, 398-404
40. Shifrin, A. L., Chirmule, N., Gao, G. P., Wilson, J. M., and Raper, S. E. (2005) Innate immune responses to adenoviral vector-mediated acute pancreatitis. *Pancreas* **30**, 122-129
41. Wang, S., Baum, B. J., Yamano, S., Mankani, M. H., Sun, D., Jonsson, M., Davis, C., Graham, F. L., Gaudie, J., and Atkinson, J. C. (2000) Adenoviral-mediated gene transfer to mouse salivary glands. *Journal of dental research* **79**, 701-708
42. Jeschke, M. G., Barrow, R. E., Hawkins, H. K., Yang, K., Hayes, R. L., Lichtenbelt, B. J., Perez-Polo, J. R., and Herndon, D. N. (1999) IGF-I gene transfer in thermally injured rats. *Gene therapy* **6**, 1015-1020
43. Felgner, P. L., Gadek, T. R., Holm, M., Roman, R., Chan, H. W., Wenz, M., Northrop, J. P., Ringold, G. M., and Danielsen, M. (1987) Lipofection: a highly

- efficient, lipid-mediated DNA-transfection procedure. *Proc Natl Acad Sci U S A* **84**, 7413-7417
44. Zanda, M., Perrone, S., Usai, M., Lazzari, P., J Tucker, S., and Wallace, H. (2013) *Efficient Cell Transfection with Melamine-Based Gemini Surfactants*,
 45. Cortesi, R., Esposito, E., Menegatti, E., Gambari, R., and Nastruzzi, C. (1996) Effect of cationic liposome composition on in vitro cytotoxicity and protective effect on carried DNA. *International Journal of Pharmaceutics* **139**, 69-78
 46. Neumann, E., Schaefer-Ridder, M., Wang, Y., and Hofschneider, P. H. (1982) Gene transfer into mouse lyoma cells by electroporation in high electric fields. *The EMBO Journal* **1**, 841-845
 47. Orłowski, S., and Mir, L. M. (1993) Cell electropermeabilization: a new tool for biochemical and pharmacological studies. *Biochimica et biophysica acta* **1154**, 51-63
 48. Zernecke, A., Erl, W., Fraemohs, L., Lietz, M., and Weber, C. (2003) Suppression of endothelial adhesion molecule up-regulation with cyclopentenone prostaglandins is dissociated from IkappaB-alpha kinase inhibition and cell death induction. *FASEB journal : official publication of the Federation of American Societies for Experimental Biology* **17**, 1099-1101
 49. Lakshminpathy, U., Pelacho, B., Sudo, K., Linehan, J. L., Coucouvanis, E., Kaufman, D. S., and Verfaillie, C. M. (2004) Efficient transfection of embryonic and adult stem cells. *Stem cells (Dayton, Ohio)* **22**, 531-543
 50. Lorenz, P., Harnack, U., and Morgenstern, R. (2004) Efficient gene transfer into murine embryonic stem cells by nucleofection. *Biotechnology Letters* **26**, 1589-1592
 51. Song, L., Chau, L., Sakamoto, Y., Nakashima, J., Koide, M., and Tuan, R. S. (2004) Electric field-induced molecular vibration for noninvasive, high-efficiency DNA transfection. *Molecular therapy : the journal of the American Society of Gene Therapy* **9**, 607-616
 52. Brandner, G., Mueller, N., Graessmann, A., Graessmann, M., Niebel, J., and Hoffmann, H. (1974) Inhibition by interferon of SV40 tumor antigen formation in cells injected with SV40 cRNA transcribed in vitro. *FEBS letters* **39**, 249-251
 53. Celis, J. E. (1977) Injection of tRNAs into somatic cells: search for in vivo systems to assay potential nonsense mutations in somatic cells. *Brookhaven symposia in biology*, 178-196
 54. Diacumakos, E. G., Holland, S., and Pecora, P. (1970) A microsurgical methodology for human cells in vitro: evolution and applications. *Proc Natl Acad Sci U S A* **65**, 911-918
 55. Grassman, A. (1970) [Microsurgical cell nucleus transplantation in mammalian cells]. *Experimental cell research* **60**, 373-382
 56. Zhang, Y., Champagne, N., Beitel, L. K., Goodyer, C. G., Trifiro, M., and LeBlanc, A. (2004) Estrogen and androgen protection of human neurons against intracellular amyloid beta1-42 toxicity through heat shock protein 70. *The Journal of neuroscience : the official journal of the Society for Neuroscience* **24**, 5315-5321
 57. Zhang, Y., Goodyer, C., and LeBlanc, A. (2000) Selective and protracted apoptosis in human primary neurons microinjected with active caspase-3, -6, -7,

- and -8. *The Journal of neuroscience : the official journal of the Society for Neuroscience* **20**, 8384-8389
58. Zhang, Y., Hong, Y., Bounhar, Y., Blacker, M., Roucou, X., Tounekti, O., Vereker, E., Bowers, W. J., Federoff, H. J., Goodyer, C. G., and LeBlanc, A. (2003) p75 neurotrophin receptor protects primary cultures of human neurons against extracellular amyloid beta peptide cytotoxicity. *The Journal of neuroscience : the official journal of the Society for Neuroscience* **23**, 7385-7394
 59. Leonetti, J. P., Mechti, N., Degols, G., Gagnor, C., and Lebleu, B. (1991) Intracellular distribution of microinjected antisense oligonucleotides. *Proc Natl Acad Sci U S A* **88**, 2702-2706
 60. Khanam, T., Raabe, C. A., Kiefmann, M., Handel, S., Skryabin, B. V., and Brosius, J. (2007) Can ID Repetitive Elements Serve as Cis-acting Dendritic Targeting Elements? An In Vivo Study. *PLOS ONE* **2**, e961
 61. Dascal, N. (1987) The use of *Xenopus* oocytes for the study of ion channels. *CRC critical reviews in biochemistry* **22**, 317-387
 62. Preston, G. M., Carroll, T. P., Guggino, W. B., and Agre, P. (1992) Appearance of water channels in *Xenopus* oocytes expressing red cell CHIP28 protein. *Science (New York, N.Y.)* **256**, 385-387
 63. Celis, J. E. (1984) Microinjection of somatic cells with micropipettes: comparison with other transfer techniques. *Biochemical Journal* **223**, 281-291
 64. Stephens, D. J., and Pepperkok, R. (2001) The many ways to cross the plasma membrane. *Proceedings of the National Academy of Sciences* **98**, 4295-4298
 65. Zhang, Y., and Yu, L. C. (2008) Single-cell microinjection technology in cell biology. *BioEssays : news and reviews in molecular, cellular and developmental biology* **30**, 606-610
 66. Knoblauch, M., Hibberd, J. M., Gray, J. C., and van Bel, A. J. (1999) A galinstan expansion femtosyringe for microinjection of eukaryotic organelles and prokaryotes. *Nature biotechnology* **17**, 906-909
 67. Laforge, F. O., Carpino, J., Rotenberg, S. A., and Mirkin, M. V. (2007) Electrochemical attosyringe. *Proceedings of the National Academy of Sciences* **104**, 11895-11900
 68. Meister, A., Gabi, M., Behr, P., Studer, P., Vörös, J., Niedermann, P., Bitterli, J., Polesel-Maris, J., Liley, M., Heinzlmann, H., and Zambelli, T. (2009) FluidFM: Combining Atomic Force Microscopy and Nanofluidics in a Universal Liquid Delivery System for Single Cell Applications and Beyond. *Nano letters* **9**, 2501-2507
 69. Osada, T., Uehara, H., Kim, H., and Ikai, A. (2003) mRNA analysis of single living cells. *Journal of Nanobiotechnology* **1**, 2
 70. Cuerrier, C. M., Lebel, R., and Grandbois, M. (2007) Single cell transfection using plasmid decorated AFM probes. *Biochemical and biophysical research communications* **355**, 632-636
 71. Guillaume-Gentil, O., Zambelli, T., and Vorholt, J. A. (2014) Isolation of single mammalian cells from adherent cultures by fluidic force microscopy. *Lab on a chip* **14**, 402-414
 72. Potthoff, E., Guillaume-Gentil, O., Ossola, D., Polesel-Maris, J., LeibundGut-Landmann, S., Zambelli, T., and Vorholt, J. A. (2012) Rapid and Serial

- Quantification of Adhesion Forces of Yeast and Mammalian Cells. *PLOS ONE* **7**, e52712
73. Potthoff, E., Franco, D., D'Alessandro, V., Starck, C., Falk, V., Zambelli, T., Vorholt, J. A., Poulikakos, D., and Ferrari, A. (2014) Toward a Rational Design of Surface Textures Promoting Endothelialization. *Nano letters* **14**, 1069-1079
 74. Dörig, P., Stiefel, P., Behr, P., Sarajlic, E., Bijl, D., Gabi, M., Vörös, J., Vorholt, J. A., and Zambelli, T. (2010) Force-controlled spatial manipulation of viable mammalian cells and micro-organisms by means of FluidFM technology. *Appl. Phys. Lett* **97**, 023701-023701-023703
 75. Stiefel, P., Zambelli, T., and Vorholt, J. A. (2013) Isolation of optically targeted single bacteria by application of fluidic force microscopy to aerobic anoxygenic phototrophs from the phyllosphere. *Applied and environmental microbiology* **79**, 4895-4905
 76. Zemansky, M. W., and Dittman, R. H. (1997) *Heat And Thermodynamics (Sie)* 7E, McGraw-Hill Book company, Boston
 77. Bonaccorso, E., Golovko, D. S., Bonanno, P., Raiteri, R., Haschke, T., Wiechert, W., and Butt, H.-J. (2009) Atomic Force Microscope Cantilevers Used as Sensors for Monitoring Microdrop Evaporation. in *Applied Scanning Probe Methods XI: Scanning Probe Microscopy Techniques*, Springer Berlin Heidelberg, Berlin, Heidelberg. pp 17-38
 78. Wallace, J. M., and Hobbs, P. V. (2006) 3 - Atmospheric Thermodynamics. in *Atmospheric Science (Second Edition)*, Academic Press, San Diego. pp 63-111
 79. Kasas, S., Dumas, G., Dietler, G., Catsicas, S., and Adrian, M. (2003) Vitrification of cryoelectron microscopy specimens revealed by high-speed photographic imaging. *J Microsc* **211**, 48-53

Chapter 6

Hollow cantilever dispensing and transmission electron microscopy

The work in this chapter was obtained with equal contributions from ir. Eleonoor Verlinden from the department of precision and microsystems engineering at Delft University of Technology.

6.1: Introduction

In chapter 5 the possibilities and challenges in Cryo-EM and FluidFM were discussed. Furthermore, an overview of the set-up and its components was revealed.

The main challenges in Cryo-EM, at the moment, are mostly caused by the thickness of the samples being used to study. The thicker the sample is, the harder it is to freeze the samples without forming ice-crystals, which will disrupt the sample. Furthermore, electrons have a relatively short mean free path, making it hard to visualize thick samples. To circumvent this challenge, just small parts of a cell could be studied. With the use of a hollow cantilever AFM small fractions, in the femtolitre range, can be aspirated from cells and dispensed on EM-grids. These fractions are small enough, so that high pressure freezing (to prevent the formation of ice-crystals) and sectioning (to reduce the thickness of the sample) are not necessary.

However, factors which normally can be neglected, could play a major role once you work with small volumes. The main hurdles that need to be tested are how the hollow cantilever reacts on the viscosity of a sample, what role hydrophobicity plays in the hollow cantilever and on the substrate, and how fast the samples will evaporate.

In this chapter the use of a hollow cantilever AFM to prepare TEM samples is discussed. In **section 6.2** interactions between the AFM cantilever and EM-grid are discussed, followed by cell targeting and cell-cantilever interactions in **section 6.3**. At the end of this chapter (**section 6.4**) TEM samples are prepared by dispensing picolitre volumes on an EM-grid.

Table 6.1: Cantilevers used in this chapter. Two cantilevers were used during the AFM experiments, one with a proposed spring constant of $k=2$ N/m the other with a proposed spring constant of 7 N/m. Although both cantilevers carry hollow channels, only the 2 N/m cantilever was used for dispensing.

	Cantilever ($k=2$ N/m)	Cantilever ($k=7$ N/m)
Width (μm)	36 μm	43 μm
Length (μm)	201 μm	130 μm
Channel width (μm)	30 μm	9.5 μm
Channel height (μm)	1 μm	1 μm
Tip shape	Pyramidal	Pyramidal
Pyramid base (μm)	7x7 μm	9.91x9.91 μm
Aperture size (μm)	Triangular with 1 μm base	Rectangular: 0.35x1 μm
Proposed spring constant (N/m)	2 N/m	7 N/m
Frequency (kHz)	80-85 kHz	180-200 kHz
Q factor	91	140
Determined spring constant (N/m)	1.2-1.5 N/m	5.0-6.5 N/m

6.2: The cantilever and EM-grids

As previously reported dispensing pico- to femtolitre volumes on a substrate is possible by using the FluidFM set-up (1,2). Forces, which are negligible at larger volumes, could become important when dispensing femtolitre volumes. Both the hydrophobicity of the substrate surface as well as the hydrophilicity of the cantilever may inhibit dispensing such small volumes, while a viscous sample may clog the cantilever. FluidFM has been used to prepare negatively stained samples for TEM imaging (3), but the interactions between the cantilever, the EM-grid and the dispensed volume have not been described.

In electron microscopy (EM) grids are used as the sample holder. These grids are often made of a fine copper mesh, but gold or other metals are used as well. A thin (~10 nm) carbon film on top of the mesh carries the sample. The carbon film is hydrophobic by itself and needs to be glow-discharged before a sample can be adsorbed. The hydrophilicity of the EM-grid depends on the glow discharge efficiency and the time past after glow discharging. In general, an EM-grid is hydrophilic for 30-60 min. after plasma treatment.

Cantilevers made from Silicon Nitride are hydrophilic by nature. This property and the resulting differences in surface tension between cantilever and carbon film of the EM-grid, will have a strong influence on dispensing the aqueous sample from the cantilever to the grid. Also, capillary forces as well as forces during tip approach could lead to carbon rupture.

Here the interactions between the carbon film and the hollow cantilever during approach and dispensing are tested. The maximum force the carbon film can hold before rupture is measured through a force-distance curve. Furthermore, the effect of hydrophobicity and hydrophilicity of either substrate or cantilever on dispensing is tested.

6.2.1: Cantilever force and carbon rupture

To use this set-up for cryo-EM sample preparation, the cantilever tip needs to approach the carbon film of the EM-grid. Completion of the tip approach is indicated by bending of the cantilever upon touching the substrate. An optical system measures the cantilever bending, which is related to the force of the tip pushing on the carbon film. When the force reaches the set-point the tip displacement stops. The set-point is large enough to ensure proper approach of the tip, but small enough to prevent carbon film rupture or tip damage. A cantilever with a force constant $k=7$ N/m (Table 6.1) was used to measure force distance curves on EM-grids. For this, a set-up was prepared as described in Figure 6.1A. An EM-grid was fixed to a glass plate by carbon tape that also served as a spacer to warrant measuring the carbon film rather than the glass.

First force-distance curves obtained from the carbon film was compared to force-distance curves obtained from the copper grid-bar (Figure 6.1B blue and red arrow respectively). By applying a fixed-length force-distance curve, where the travelled distance is kept constant, the forces on the cantilever, induced by the carbon film or copper grid-bar, can be compared. To this end, the substrate was approached with a set-point of 20 nN, followed by a 1 μm withdrawal of the tip from the substrate. Subsequently, the tip moved forward for a total of 2 μm , while the change in force applied on the cantilever was measured. When the tip was approached to the carbon film, a maximum force of 1,500 nN was measured (Figure 6.1C, blue). Retraction of the cantilever leads to an initial relative constant force signal, but the force applied on the cantilever rapidly decreases when the cantilever is withdrawn more than 400 nm from the substrate (Figure 6.1C, red). This initial force plateau may indicate the carbon film elasticity, or other tip-carbon film interactions. Force-distance curves obtained under the same conditions on the grid-bar, exhibit a maximum force of 4,200 nN (Figure 6.1D). Such a higher force was as expected, because the copper grid bar is less flexible than the carbon film and should induce a higher force on the tip during similar measurements. These experiments demonstrate that force-distance curves can be measured on the copper grip as well as on the carbon film.

When dispensing on an EM-grid, the integrity of the carbon film should not be compromised. Therefore, the maximum force the carbon film can hold was determined. To this end, a fixed-length force-distance curve was measured on the carbon film over a distance of 10 μm . An initial steep increase in force was observed, reaching a maximum of 3,200 nN at 4.5 μm (Figure 6.1E, blue). Thereafter, the force drops back to 0 nN, indicating the rupture of the film at a force of 3,200 nN. A second force increase occurred upon further forward movement of the cantilever, reaching a maximum of 4,200 nN at 8 μm (Figure 6.1E, blue). For the last 2 μm the measured force stays constant, suggesting saturation of the optical system. Upon withdrawal the force curve was close to that of the approach, but without the first peak (Figure 6.1E, red). The second force increase may have been caused by the cantilever touching the copper gridbar for the measured force is comparable to the maximum force found in Figure 6.1D. To confirm carbon film rupture, the cantilever was approached at the

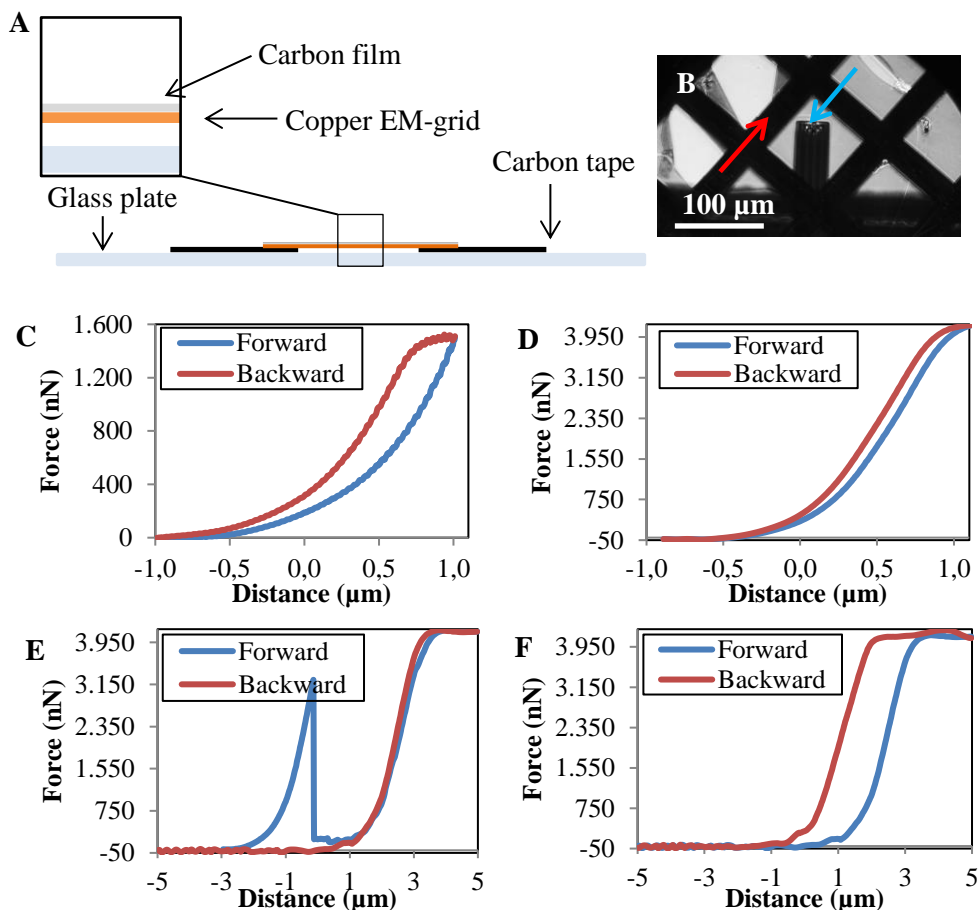


Figure 6.1: Force distance curves on carbon coated copper electron microscopy grids. (A) The substrate. A carbon coated ($\sim 8\text{nm}$) mesh copper EM-grid was fixed by double sided carbon tape onto a glass surface. (B) Bright-field image shows a hollow cantilever with a stiffness of 7 N/m , touching the carbon film. During the experiments either the carbon film (blue arrow) or the gridbar (red arrow) was approached. (C/D) Typical force-distance curve obtained from the carbon film (C) and from the grid bar (D). A fixed-length force distance curve was performed by approaching the carbon film or grid bar with a hollow cantilever ($k=7\text{ N/m}$). Forward and backward movement were $2\ \mu\text{m}$. (E) Force-distance curve obtained from the carbon film. A fixed-length force distance curve was performed by approaching the carbon film with a hollow cantilever ($k=7\text{ N/m}$). Forward and backward movement were $10\ \mu\text{m}$. Forward movement leads to an initial increase in measured force, followed by a steep decrease in force, due to rupture of the carbon film. The second increase in force measured is caused by the tip touching copper gridbar. (F) Force-distance curve obtained at the exact same position as from (E). The same settings were used. No initial increase in force is measured, while the second force peak is reproduced, showing that the initial force increase measured in (E) was indeed the carbon film rupturing.

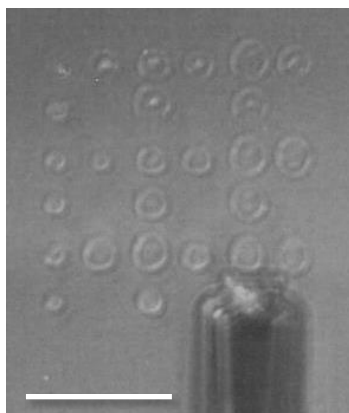


Figure 6.2: Dispensing picolitre volumes on a glass substrate with a hollow cantilever ($k=2$ N/m). The hollow cantilever was loaded with MilliQ water. Neither the hollow cantilever was coated, nor the glass substrate was pretreated. Different pressure and time pulses resulted in dispensing of different volumes on the glass substrate. Pressure pulses ranged between 0.5 and 1.5 bar, while the time ranged 0.5-1.5 sec. Scale bar is 50 μ m.

exact same position on the carbon film and a second force-distance curve was measured. Now the initial force increase was not observed, while the same maximum force was measured after the cantilever had travelled for 8 μ m (Figure 6.1F, blue). The backward curve shows a prolonged plateau of measured maximum force, which decreases only after the cantilever has withdrawn for more than 4 μ m (Figure 6.1F, red). This plateau could be related to damage of the tip, cantilever glass interactions, or the carbon film sticking to the tip. These results demonstrate that a relatively high force is necessary to puncture the carbon film. Therefore, small volumes can be dispensed on an EM-grid without breaking the film.

6.2.2: The effect of hydrophobicity on dispensing

Dispensing pico- to femtolitre volumes on an EM-grid depends on the hydrophobicity of cantilever and carbon film. Dispensing small volumes on a glass substrate is often possible without specific pre-treatments. Glass substrates are hydrophilic enough to allow femtolitre droplets to be dispensed on such surfaces (Figure 6.2). However, EM-grids are initially hydrophobic (Figure 6.3A) due to the thin carbon film added on top of the EM-grid. For TEM sample preparation, the EM-grids are made hydrophilic by glow discharge in air at low pressure, leading to deposition of negatively charged ions on the carbon film. Glow discharging an EM-grid warrants even spreading of the sample (Figure 6.3B). Glow-discharged carbon coated EM-grids become hydrophobic again after exposure to air (Figure 6.3C).

For the proposed set-up, thin samples aspirated from cells are deposited on glow-discharged EM-grids (carbon films, Quantifoils, or lacey films) and plunge frozen in liquid ethane. To measure the effect of EM-grid hydrophilicity on cryo-EM sample preparation, grids were glow discharged and kept in an ambient environment for 1 or 2 hrs. Deposition of femtolitre

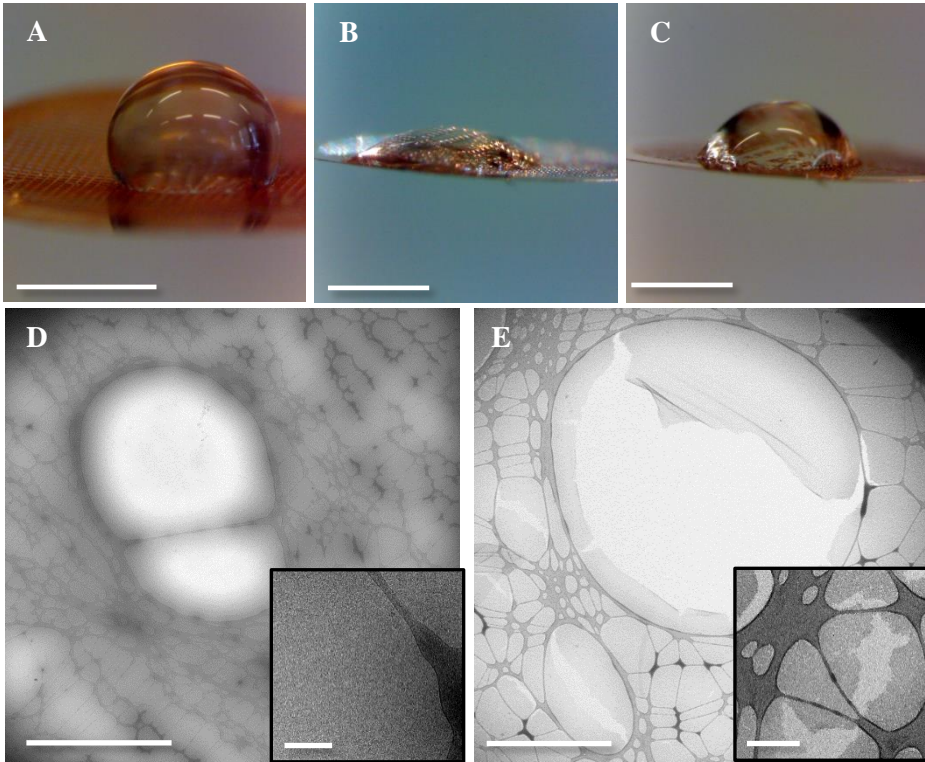


Figure 6.3: Hydrophobicity of a carbon coated EM-grid. (A) 0.5 μL water was pipetted on a non-glow discharged grid, (B) shortly after glow discharging or (C) 35 min. after glow discharging. The grid was glow discharged for 90 sec, which made the carbon film hydrophilic, leading to a spread-out flat water droplet with an estimated contact angle of 25° . 35 min. after glow discharge the grid is less hydrophilic and the contact angle of the water droplet is increased ($\sim 60^\circ$). Scale bar is 1 mm. (D, E) Cryo-EM images of plunge frozen human serum. 6 μL of human serum was added to an EM-grid (D) 1 hr after glow-discharge or (E) 2 hrs after glow discharge. Excess of sample was blotted, and the thin film was incubated for 30 sec before plunging. Scale bar is 5 μm . Inserts show the clear difference between stable ice (D) and non-stable ice (E). Scale bars are 400 nm (D) and 1 μm (E).

volumes on the EM-grids was mimicked by pipetting 6 μL of human serum, pre-mixed with gold colloids, and a 1 sec blot. Blotting resulted in a thin film of human serum on the EM-grid, comparable to dispensed femtolitre volumes. After blotting the samples were kept for 30 sec at 70% humidity before plunging. One hour after glow discharge the EM-grids were still hydrophilic enough to maintain a thin film of human serum for 30 sec (Figure 6.3D). However, after 2 hrs, grids were no longer able to maintain a stable film of human serum (Figure 6.3E). This demonstrates that samples should be dispensed within less than one hour after glow-discharge to produce proper cryo-EM samples.

When working with pico- to femtolitre volumes, the hydrophobicity of the substrate can lead to difficulties in dispensing. Furthermore, the hydrophilicity of the cantilever can lead to

sticking of the sample to the cantilever base, rather than deposition of the sample on the substrate. Therefore, dispensing on an EM-grid while varying the hydrophobicity of both the EM-grid and the cantilever was tested.

When a hollow, non-coated, cantilever (2 N/m, Table 6.1) approached a hydrophobic, non-glow discharged, surface, it was possible to produce a large droplet once the pressure on the cantilever was increased (Figure 6.4A, middle). The droplet reached a maximum diameter of 132 μm with an approximated volume of ~ 1.2 nL. However, once the pressure is released and the cantilever is retracted, only a small droplet (diameter 9 μm) remains on the carbon film (Figure 6.4A, right) with an approximated volume of 0.2 pL (assuming the dispensed droplet forms a half sphere on the EM-grid). The rest of the droplet retracted back into the cantilever or remained on the cantilever.

When a non-coated cantilever approached a glow-discharged EM-grid, a droplet with a comparable diameter formed (diameter 108 μm ; ~ 600 pL) as with the non-glow discharged grid (Figure 6.4B, middle). But after pressure release and while withdrawing the cantilever, the carbon film remained stuck to the cantilever and was ruptured (Figure 6.4B, right). Such cantilever-carbon film interactions are caused by capillary forces of the liquid trapped between the cantilever and EM-grid. Although it is possible to dispense small volumes on a glow discharged grid without coating the cantilever, carbon film rupture could not be prevented under these conditions.

It was possible to induce droplet formation by increasing the pressure on a non-coated cantilever. But the droplet formed was stuck to the cantilever base, rather than the substrate (Figure 6.4A and -B (both middle panels)). To prevent this, a hydrophobic coating, trichloro(octyl)silane (OS), was applied to cantilevers via evaporation in a closed container. With OS coated cantilevers, droplets could be produced by applying a pressure on the cantilever after approaching the carbon film (Figure 6.4C and -D; middle panel). The droplet produced did not interact with the cantilever base and stayed in contact with the carbon film. When the carbon film was not glow discharged, the dispensed droplet moved towards the gridbar (Figure 6.4C, right panel) after withdrawal of the cantilever. The best dispensing results were obtained when both the cantilever was coated with OS and the EM-grid was glow discharged (Figure 6.4D, right panel). The dispensed droplet visualized in Figure 6.4D has a diameter of ~ 112 μm and an approximated volume of 62 pL, based on a contact angle of 25° determined from the 0.5 μL droplet pipetted on a glow discharged EM-grid visualized in Figure 6.3C.

The combination of a glow discharged EM-grid and a hydrophobic coating allowed picolitre droplets to be dispensed reproducibly. However, aqueous solutions were sucked towards the hydrophilic EM-grid without applying pressure, making controlled dispensing of small droplets difficult. Furthermore, the hydrophilicity of the substrate changed over time, limiting the reproducibility of these experiments. Further tests are necessary to quantify the dispensed volume based on pressure, hydrophilicity and time pulse.

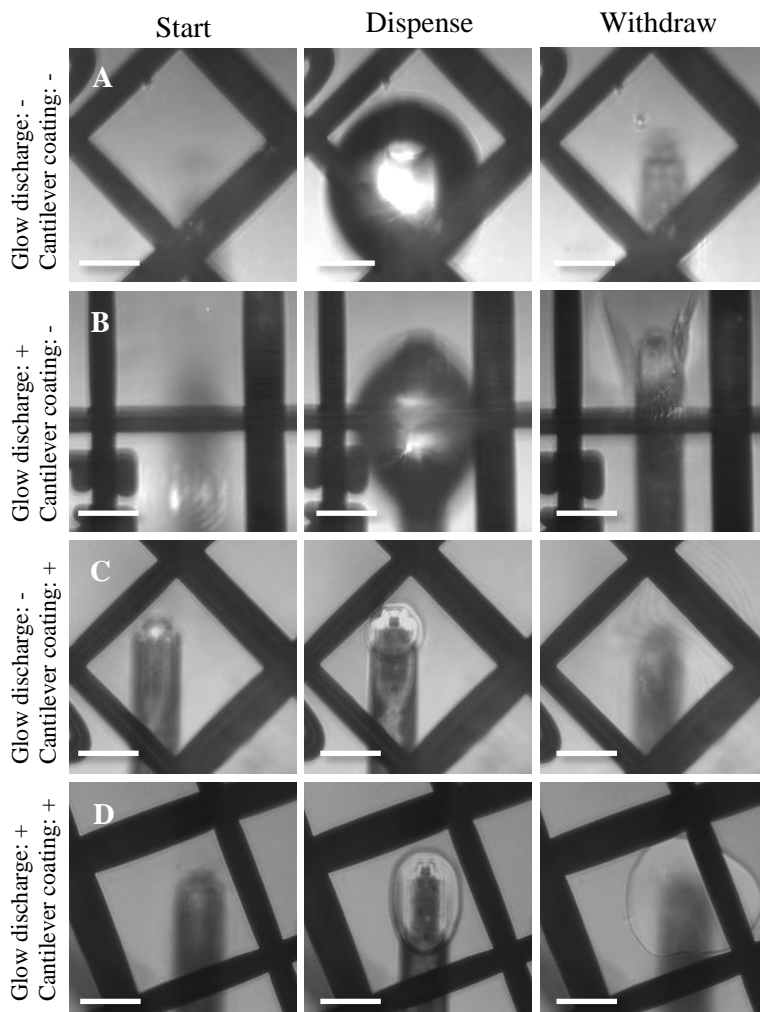


Figure 6.4: Dispensing liquids on grids. A hollow cantilever (2 N/m) is used to dispense aqueous solutions on a carbon coated copper EM-grid by varying the hydrophobicity of grid and cantilever. (A) A non-coated, hydrophilic, cantilever was used to approach a non-glow discharged, hydrophobic EM-grid (left). A pressure pulse of 2 bar was applied for 5 sec (middle). After dispensing the cantilever was withdrawn. A very small droplet remained (right). (B) A non-coated cantilever was used to approach a glow discharged, hydrophilic, EM- grid (left). A pressure pulse of 2 bar was applied for 5 sec (middle). After dispensing the cantilever was withdrawn. During withdrawal, the carbon film remained stuck to the cantilever, leading to disruption of the carbon film (right). (C) A coated, hydrophobic, cantilever was used to approach a non-glow discharged EM-grid (left). A pressure pulse of 3 bar was applied for 5 sec (middle). After dispensing the cantilever was withdrawn. After withdraw the dispensed droplet moves to the, slightly, hydrophilic copper grid-bar, visualized by the ripple structure (right). (D) A coated cantilever was used to approach a glow-discharged EM-grid (left). A pressure pulse of 4 bar was applied for 12 sec (middle). After dispensing the cantilever was withdrawn and the dispensed droplet remained (right). Scale bars are 50 μm . Magnification was 40x.

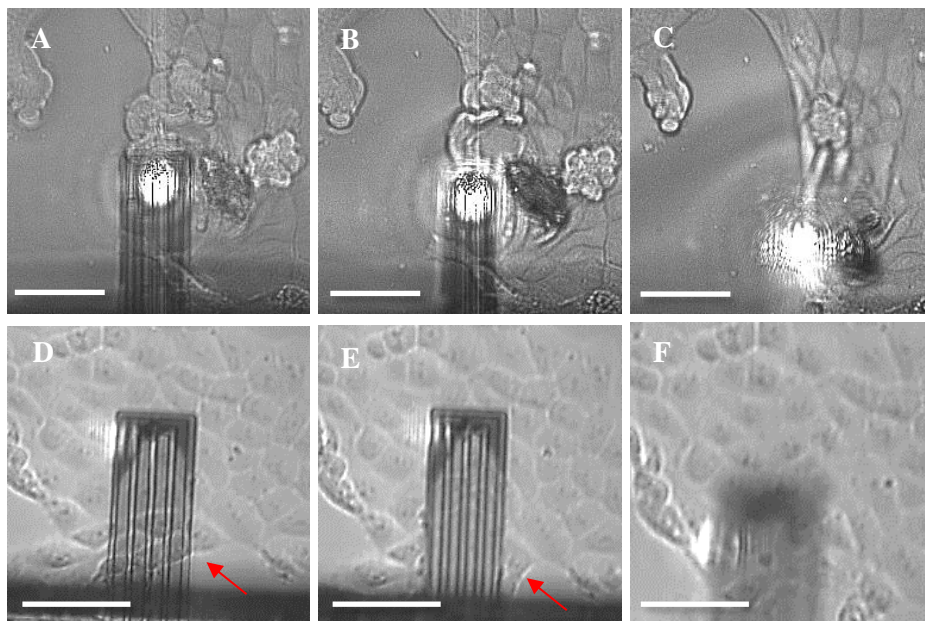


Figure 6.5: Cell-cantilever interactions. (A,B,C) An uncoated, hydrophilic, cantilever ($k=7$ N/m) was approached on mpkCCD cells grown on a glass coverslip kept in cell growth medium. (B) The cantilever was slightly withdrawn from the surface. Because the approached cell was attached to the cantilever it was pulled away from the substrate by the cantilever. (C) Upon complete withdrawal, cells were pulled off the glass substrate due to cantilever-cell and cell-cell interactions. (D,E,F) A coated, hydrophobic cantilever ($k=7$ N/m) was approached on mpkCCD cells grown on a glass coverslip kept in cell growth medium. (E) The cantilever was completely approached, denting cells and pushing cells aside (red arrow). (F) After the cantilever was withdrawn from the surface, cells stayed attached to the coverslip. No cell-cantilever interactions were detected. Scale bars are 50 μ m.

6.3: Cells and the cantilever

Besides dispensing of picolitre to femtolitre volumes on an EM-grid for Cryo-EM sample preparation, the system is also used for injection in and aspiration from cells. Therefore, the cantilever needs to be able to penetrate the cell and retract from it, while leaving the cell intact. For cellular injection and aspiration, the cell membrane needs to be penetrated. The cellular membrane is a complex organelle composed of phospholipids and membrane proteins. Phospholipids consist of a polar headgroup, and two hydrophobic tails, which are protected from the aqueous environment by the formation of a lipid bilayer (4). During cell penetration the polar headgroups of the phospholipids should not interact with the tip, because cantilever retraction could lead to cell membrane disruption. Ideally, the lipid hydrophobic tails should not interact with the tip as well. Previously, a poly(1-lysine-graft-poly(ethylene glycol)) (PLL-PEG) coated cantilever was used to inject GFP into a cell after penetration (2), without disturbing the cell. However, a PLL-PEG coated cantilever needs to be used in an aqueous environment to maintain its hydrophobic capacity. In our set-up the

cantilever is both used in an aqueous environment, cell growth medium, and in air, during sample dispensing on EM-grids, making the use of PLL-PEG unfavourable. The previously discussed OS coating can be used in air, as discussed in chapter 6.2.2, but has not been tested on cells so far. Therefore, the tip-cell interactions were tested for different cantilever coatings. Furthermore, local dispensing and specific cell targeting were explored to gain further insights on drop deposition, cellular reactions and specific targeting necessary for injection into single cells.

6.3.1: Cantilever coating for cellular interactions

In chapter 6.2.2 the use of OS as a hydrophobic cantilever coating was discussed. By using OS in combination with a glow discharged EM-grid, picolitre volumes could be dispensed on the carbon film. To test tip-cell interactions, mpkCCD cells were grown on a glass coverslip and approached by an AFM cantilever ($k=7$ N/m, Table 6.1) (Figure 6.5A and -F). Both OS coating as well as non-coated cantilevers were explored.

When non-coated cantilevers were used to approach cells, the cells got stuck to the cantilever. Withdrawal of the cantilever led to the release of the targeted cell from the glass substrate (Figure 6.5B). Multiple cells were released from the glass substrate upon further withdrawal of the cantilever as result of cell-cell interactions (Figure 6.5C).

Coating the cantilever with OS reduced cantilever-cell interactions. Even when the cantilever is in contact with multiple cells (Figure 6.5E), cells did not stick to the cantilever and were left on the glass substrate after withdrawal (Figure 6.5F).

Although cells do not interact with OS coated cantilevers, enhancing cell-substrate interactions are likely to improve further cell penetration experiments. The release of multiple cells during withdrawal of an uncoated cantilever suggests relatively weak cell-substrate interactions (Figure 6.5C). For cell penetration, cell-substrate interactions should be sufficiently strong to prevent cells to detach from the substrate during withdrawal of the penetrating cantilever. To this end, glass coverslips could be coated by poly-L-Lysine (PLL), which enhances cell-substrate interactions.

6.3.2: Cell targeted dispensing

Micro injection into cells is a challenging technique. Cell membrane penetration could disrupt cells, leading to cell stress or even cell death (5). Furthermore, the cytoplasm is completely packed with proteins, lipids, nucleic acids and sugars, leading to a dense, highly concentrated, viscous solution with an estimated macromolecular concentration of 400 mg/mL (6).

Picolitre dispensing in an aqueous solution has not yet been tested with the cantilevers used. Therefore, we dispensed a small compound in the vicinity of targeted cells with a hollow cantilever ($k=2$ N/m, Table 6.1). To this end, *Sf9* cells were grown on a glass substrate and kept in a thin layer of cell growth medium. The cantilever was loaded with 1 mM of 5(6)-carboxyfluorescein (CF) to observe dispensing by fluorescent microscopy, while the cells were imaged by bright field microscopy. CF is sufficiently small to prevent clogging of the

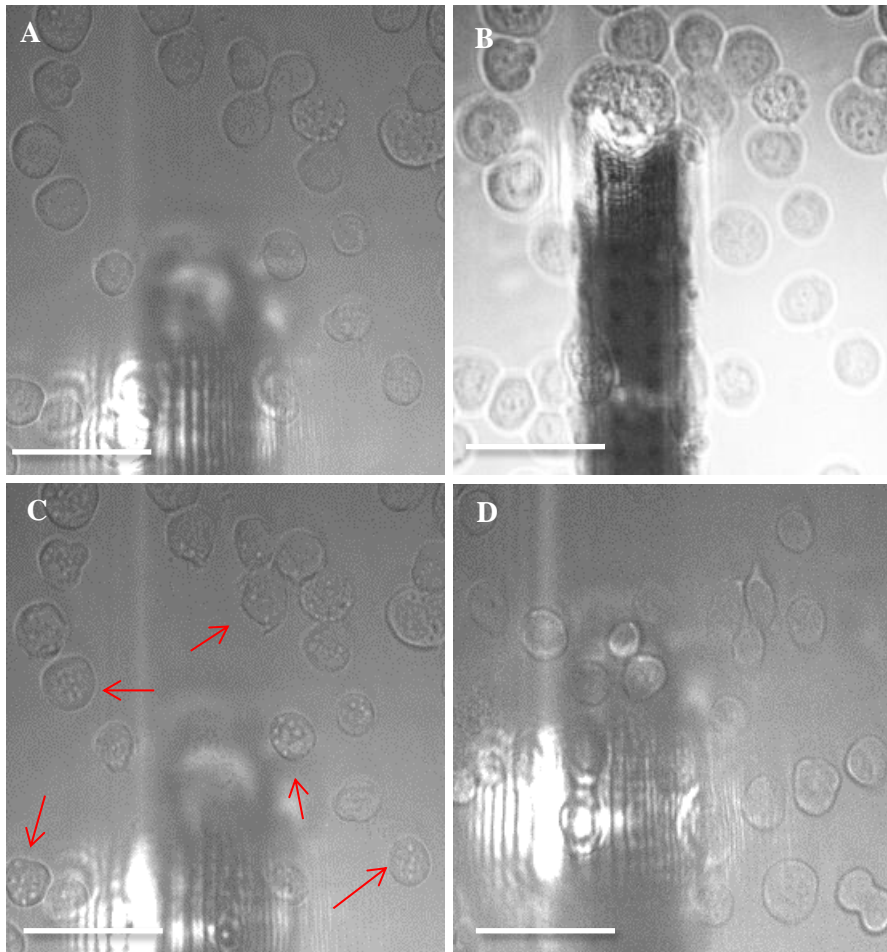


Figure 6.6: Targeted cellular stress induction. *Sf9* cells were grown on a glass substrate and kept in a thin layer of growth medium. A hollow cantilever was filled with 1 mM carboxyfluorescein and attached to a pressure controller. Bright field imaging was combined with fluorescent imaging, to observe dispensing of carboxyfluorescein in the cell medium. Light intensity was kept the same for all images. (A) Bright field image of the targeted cells. (B) Cantilever is approached towards the surface and a pressure pulse of 6.3 bar was applied for 2 sec. to release carboxyfluorescein into the cell medium as documented by the appearance of a light flash. (C) Cantilever was withdrawn after dispensing. Cells displayed signs of stress as indicated by red arrows. (D) In the bright field image of cells away from the area of fluorescein deposition, no signs of stress were discernible. Scale bars are 50 μm . Magnification was 60x.

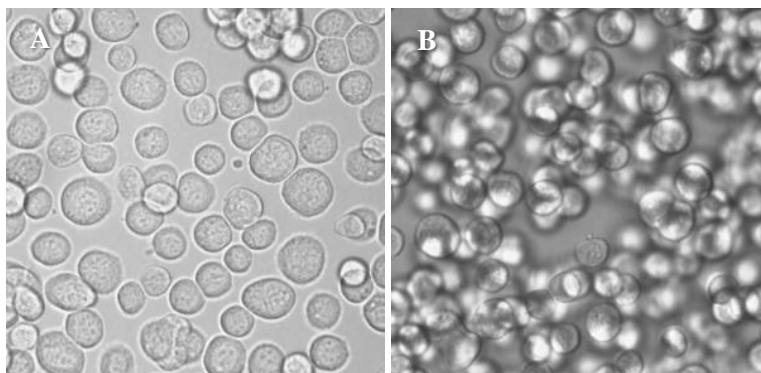


Figure 6.7: Effect of 1 mM 5(6)-Carboxyfluorescein (CF) on *Sf9* cells. (A) *Sf9* cells were grown on a petridish in *Sf9* cell growth medium. (B) CF was added to a total concentration of 1 mM. 10 min. later, the majority of the *Sf9* cells died, visualized by detached cells floating, out of focus in the growth medium. Magnification was 60x.

cantilever, is membrane-impermeant, has been used to study cell proliferation before (7) and is non-toxic in low concentrations (8).

The glass substrate was approached with a hollow cantilever ($k=2$ N/m, Table 6.1), loaded with 1 mM CF, in the vicinity of *Sf9* cells (Figure 6.6A). A pressure pulse of 6.3 bar was applied for 2 sec. and CF was dispensed in the medium, monitored via fluorescence microscopy (Figure 6.6B). Upon withdrawal of the cantilever, vesicular structures were formed in the *Sf9* cells (Figure 6.6C), suggesting that these cells reacted on the dispensed CF in the medium. When the stage was moved towards *Sf9* cells which were previously outside the field of view, these vesicular structures were absent (Figure 6.6D), showing that a local response was induced in the *Sf9* cells. This effect was reproduced at multiple positions on the substrate.

The formation of such vesicular structures could not be reproduced by incubating *Sf9* cells in 1 mM CF. Addition of CF to these cells did lead to cell death (Figure 6.7), suggesting that the local temporal high concentration of CF in the vicinity of the *Sf9* cells induces a stress response leading to vesicle formation as result of CF toxicity, but not to cell death. CF diffused fast enough in the total cell medium, preventing apoptosis and allowing cells to recover.

6.3.3: Cellular dissection

In the previous sections, cell-cantilever interactions and cellular targeting were discussed. Although the hollow cantilever was used to trigger cellular responses, the response was not triggered in one specific cell, but rather in multiple cells in a chosen field of view. Furthermore, although the cell-cantilever interactions were tested depending on the cantilever coating, the effect of cell penetration on cellular-cantilever interactions was not explored either. To test this, specific targeted cells were disrupted by using the tip as a nano-scalpel.

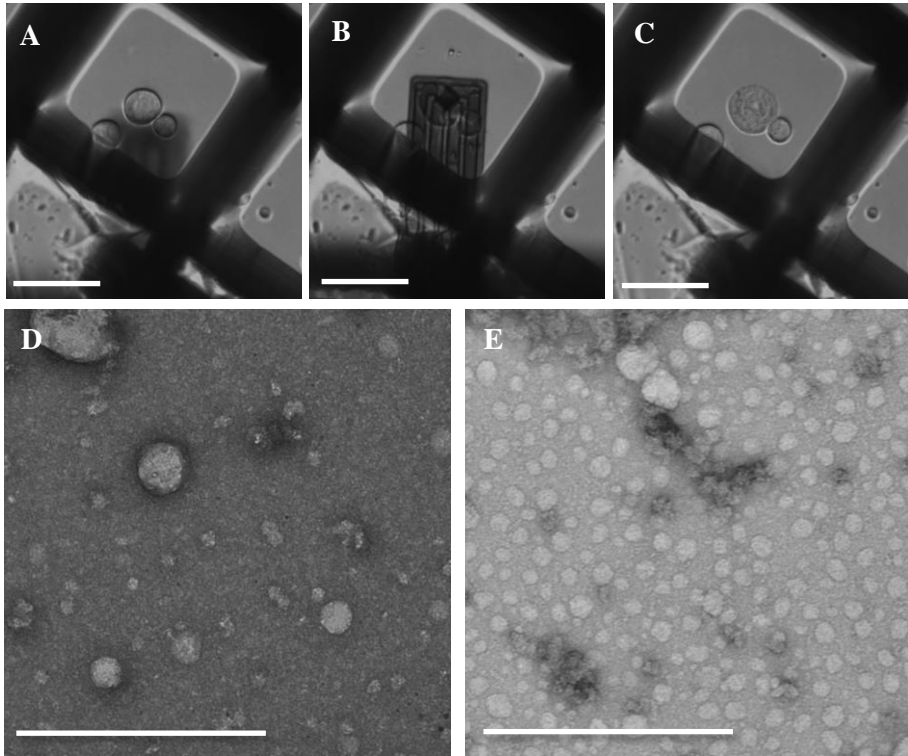


Figure 6.8: Cell targeted disruption by an AFM cantilever. (A) *Sf9* cells are pipetted on a carbon coated gold EM-grid were left to attach in an ambient environment. A thin layer of medium was maintained on top of the cells to keep them hydrated. (B) A cell is approached by an OS coated AFM cantilever ($k=7$ N/m) and scratched by using contact mode imaging at a force of 100 nN (0.18 s/line). (C) The cantilever was withdrawn after scratching. The targeted *Sf9* cell was lysed and left on the carbon film. The specificity of targeting is documented by the neighbouring cell being still intact after scratching. (A,B,C) Scale bar is 50 μm . (D) Negative stain TEM image of the lysed cell. Vesicles and cellular contents are visible. Magnification was 10,000x. (E) Negative stain TEM image of a random position on the grid, used as a negative control. No cellular contents are visible. Staining artefacts are visualized. Magnification was 10,000x. (D,E) Scale bars are 500 nm.

Sf9 cells were pipetted on a glow discharged carbon coated gold EM-grid and were incubated in an ambient environment to allow cells to attach to the EM-grid (Figure 6.8A). An OS coated AFM cantilever ($k=7$ N/m, Table 6.1) was used to approach a specific cell with a setpoint of 100 nN, which led to a deformation of the cell and sometimes to cell bursting (Figure 6.8B). Cell disruption was achieved by scratching over the cell in contact mode with a velocity of 55.5 $\mu\text{m/s}$ at 100 nN. After withdrawal, the targeted cell was broken and the cellular remains were left on the EM-grid (Figure 6.8C). This suggests that the used cantilever coating (OS) is suitable for cellular penetration, and nano-dissection.

After cell disruption, the cellular remains were negative stained by applying 2% Uranyl acetate to the EM-grid. Excess of staining was removed by blotting and the negatively stained cellular components were visualized by TEM. Figure 6.8D shows the cellular remains left on the EM-grid, which are distinctly different from the control position where no cell disruption was performed (Figure 6.8E). Cellular vesicles and proteins are visualized. However, due to the crude method to dissect the cell, clear cellular structures, such as mitochondria or the cytoskeleton, could not be found. This method shows that specific cell targeting for manipulation is possible, while the OS coating prevents cell-cantilever interactions preventing uncontrolled abstraction from cells.

6.4: Transmission electron-microscopy of dispensed picolitre volumes

Besides dispensing into and aspiration from cells, the set-up will be used to dispense small, preferably femtolitre, volume samples on EM-grids for analysis. As discussed in chapter 6.1 and 6.2, working with small volumes, involves parameters influencing sample preparation which are negligible when working with larger volumes. Here dispensing of small specific sample volumes on glow discharged EM-grids is described. Besides hydrophobicity of cantilever and EM-grid, rapid evaporation of the sample provides challenges in TEM sample preparation.

6.4.1: Dispensing Gold-nanoparticles

The possibility to dispense small volumes on a substrate depends on a broad variety of parameters. The viscosity of the solution, cantilever-sample interactions and sample-substrate interactions could hinder dispensing and deposition of small volumes. Solute concentration, particle size and solvent evaporation at the tip may dictate clogging of the cantilever. Gold-nanoparticles (au-NPs) were used to test TEM sample preparation via picolitre dispensing. Au-NPs exhibit a diameter of ~20 nm, reducing possible clogging of the tip. Au-NPs can be dissolved in water, yielding a viscosity of the solution close to that of water. The au-NPs purchased from BBI solutions should only contain residual salts. Because no staining is necessary to visualize the au-NPs in the TEM, EM-grids can be inspected directly after dispensing without further processing.

Dispensing au-NPs on a glow discharged grid led to the formation and release of a droplet on the EM-grid, as documented in chapter 6.2. After dispensing, the droplet rapidly evaporated in the ambient environment. The dispensed droplet can be located both by using bright field microscopy (Figure 6.9A) and low magnification transmission electron microscopy (Figure 6.9B). Three different particles could be distinguished. 1) Pure gold-nanoparticles (Figure 6.9C), 2) Salt crystals and 3) gold-salt hybrids (Figure 6.9D). Although au-NPs should only contain residual quantities of salts, salts were found to contaminate the grid after dispensing small au-NPs solution drops. To analyse the origin of these salts, 0.5 μ L of au-NPs was pipetted on a glow discharged EM-grid and left in air at RT to evaporate. Both au-NPs and salt crystals were visible in this sample (Figure 6.9E).

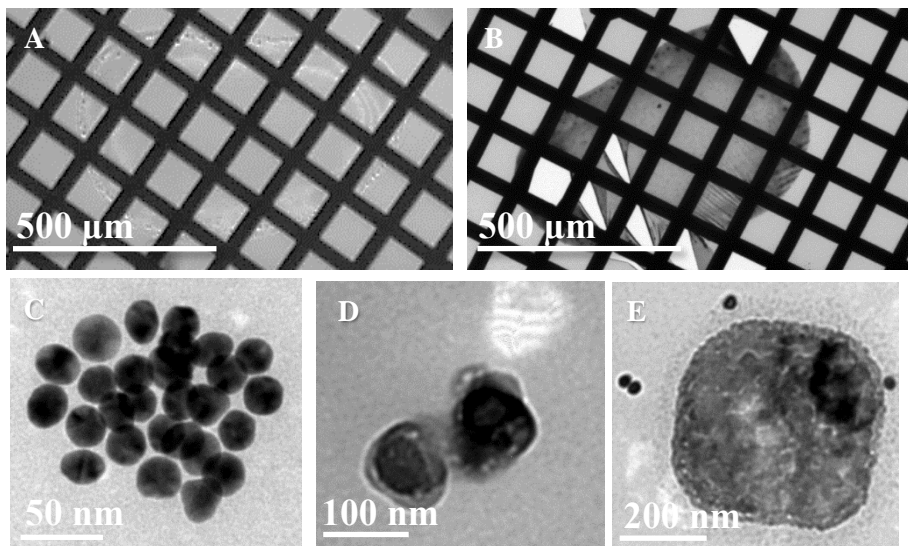


Figure 6.9: Dispersed gold nanoparticles. (A) Bright field light microscopy image of a dispensed droplet on a carbon coated copper EM-grid. Magnification was 40x. (B) Electron microscopy image of the same dispensed droplet as A. Magnification was 10x. (C) Dispersed gold nanoparticles on a non-glow discharged carbon coated copper EM-grid. Diameter is 20 nm. Magnification was 20,000x. (D) Dispersed gold nanoparticles on a glow discharged carbon coated copper EM-grid. Diameter is ~80 nm. A dark centre is surrounded by a grey halo. Magnification was 12,000x. (E) 0.5µL gold nanoparticles solution was pipetted on a non-glow discharged carbon coated copper EM-grid and dried in air prior to loading in the TEM. This sample revealed both gold nanoparticles and salt crystals. Magnification was 10,000x.

Particles were analysed by energy-dispersive X-ray spectroscopy (EDX), where the X-rays, released by the atoms in the sample due to electron irradiation, are measured to determine the chemical composition of the sample (9,10). In the sample produced by pipetting 0.5 µL onto the EM-grid, salt crystals and gold particles could be detected by EDX. Large peaks are visible for Potassium (K α) and Chloride (Cl α), suggesting that the residual salt in solution, as stated by the manufacturer, was potassium chloride (Figure S6.1, red arrows, page 213). Furthermore, carbon (carbon film, Figure S6.1, orange arrow, page 213) and copper (grid bars, Figure S6.1, green arrows, page 213) were present.

The pure gold nanoparticles found after dispensing show strong peaks for gold, but clear potassium chloride peaks are visible as well (Figure S6.2, blue and red arrows respectively, page 214). The gold-salt hybrids show gold peaks as well (Figure S6.3, blue arrows, page 215). However, strong peaks are found for potassium and chloride (Figure S6.3, red arrows, page 215). Although a specific region of interest was scanned by using EDX, atoms in the vicinity of the scanned region are monitored as well due to multiple scattering, leading to measured salt (red arrows), carbon (orange arrow) and copper (green arrows) peaks even when they are not visible in the field of view.

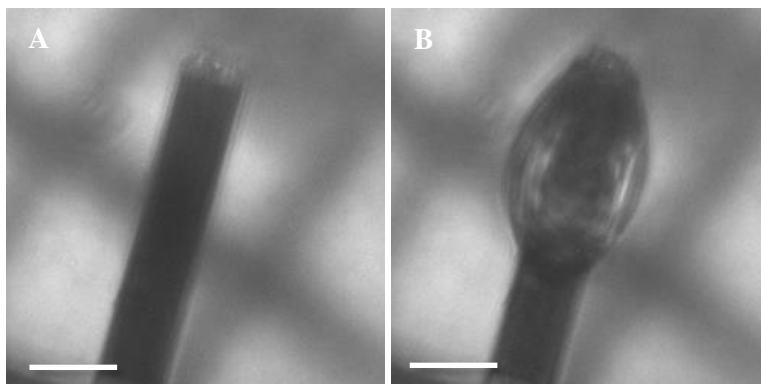


Figure 6.10: Dispensing apoferritin in air. (A) A hollow cantilever ($k=2$ N/m) was filled with apoferritin ($250 \mu\text{g/mL}$) and kept in air. There is no contact between the cantilever and the substrate (EM-grid). (B) Applying a pressure pulse of 1.7 bar (time 5 sec) led to the formation of a droplet on the cantilever tip in air. Scale bars are $50 \mu\text{m}$.

These results demonstrate the feasibility to dispense a predetermined solution on an EM-grid and its visualisation and analysis by TEM. Buffer salts and other contaminants may impair imaging of a test sample like au-NPs.

6.4.2: Dispensing Apoferritin

Although au-NPs could be dispensed on an EM-grid and visualised via TEM, the main goal of this set-up is to use the hollow cantilevers for biological sample deposition. Therefore, apoferritin was loaded into a hollow cantilever ($k=2$ N/m, Table 6.1) and dispensed on a glow discharged EM-grid.

Ferritin is an intracellular protein, capable of storing and releasing iron. Ferritin can be found in a broad variety of living organisms and acts as a buffer preventing iron deficiency or iron overload (11,12). When ferritin does not hold iron, it is called apoferritin.

(Apo)ferritin consists of 24 subunits forming a ring like protein structure of 450 kDa with an outer diameter of ~ 12 nm and an inner diameter of ~ 8 nm. Apoferritin was chosen as a biological sample, for it is a relatively small protein, limiting clogging of the cantilever, and soluble in water. For dispensing, a $250 \mu\text{g/mL}$ apoferritin concentration was used, which should contain, based on the molecular weight of apoferritin, ~ 500 apoferritins/pL. Apoferritin was dispensed by applying a pressure pulse of 1.7 bar (5 sec), leading to an oval droplet with a width of $86 \mu\text{m}$ and a length of $120 \mu\text{m}$ (~ 570 pL) (Figure 6.10).

The dispensed particles were analysed by negative stain TEM and the dispensed droplet could be located at low magnification in the TEM (Figure 6.11A). There is a clear difference in staining between the empty carbon film and the area of the dispensed volume (Figure 6.11B), where apoferritins are visible. Apoferritin aggregates and salts are found at the edge of the droplet as well. At higher magnification, particles were visualised with an outer diameter of ~ 11 nm (Figure 6.11C and D), and an inner diameter of ~ 5 nm (Figure 6.11D, insert). This

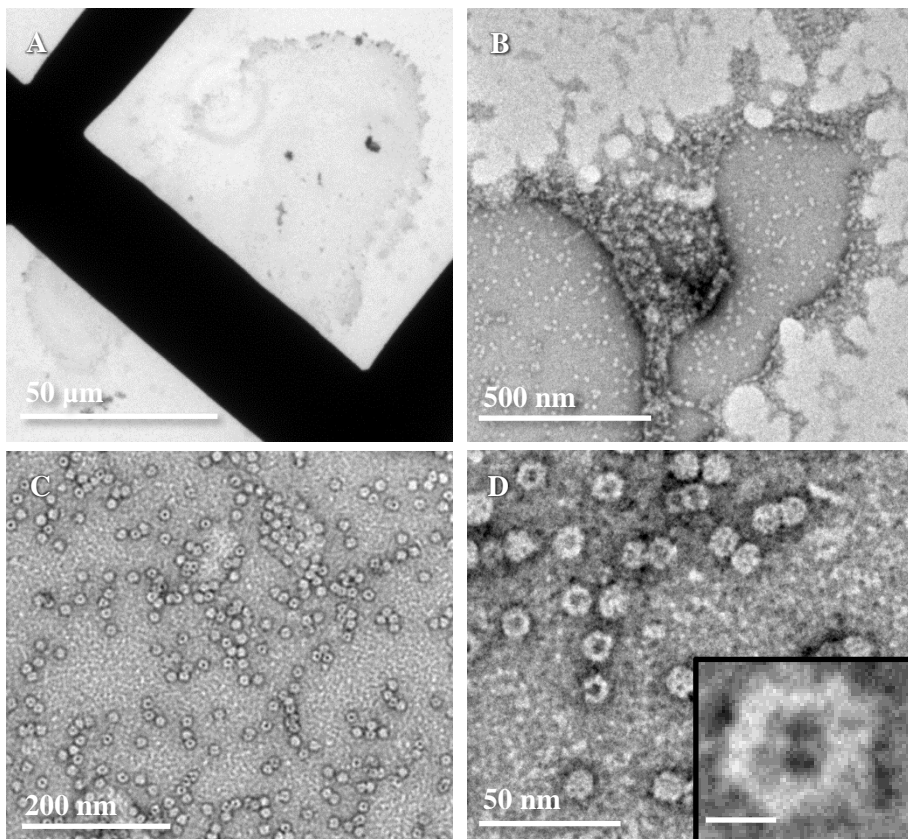


Figure 6.11: Dispensing and negatively staining apoferritin (0.25 mg/mL). Apoferritin was dispensed (1.7 bar, 5 sec) by a hollow cantilever (2 N/m) on a non-glow discharged formvar carbon coated copper EM-grid. The sample was stained by pipetting 0.5 μ l Uranyl acetate (0.2%) on the EM-grid and letting excess fluid evaporate. (A) TEM image of an apoferritin containing dispensed droplet. Magnification was 60x. (B) The edge of the dispensed droplet (dark grey). Free carbon film areas are lighter grey. Aggregates decorate the drop periphery, while white dots represent apoferritins. Magnification was 6,000x. (C) Overview of dispensed apoferritins. Magnification was 12,000x. (D) Close-up of dispensed apoferritins showing the \sim 8 nm hole in the middle. Magnification was 25,000x. Insert shows a 5x magnification of one apoferritin. Outer diameter is \sim 11 nm, inner diameter is \sim 5 nm. Scale bar is 5 nm.

demonstrates that apoferritin can be dispensed with the hollow cantilever and analysed by TEM.

6.4.3: Dispensing liposomes

Dispensing apoferritin on EM-grids shows that electron microscopy imaging of picolitre dispensed biological samples is possible. Whereas apoferritin is a relatively simple protein the cellular cytoplasm is much more complex. Besides large protein complexes, the cytosol contains multiple different membrane structures, all of which are densely packed in the cell.

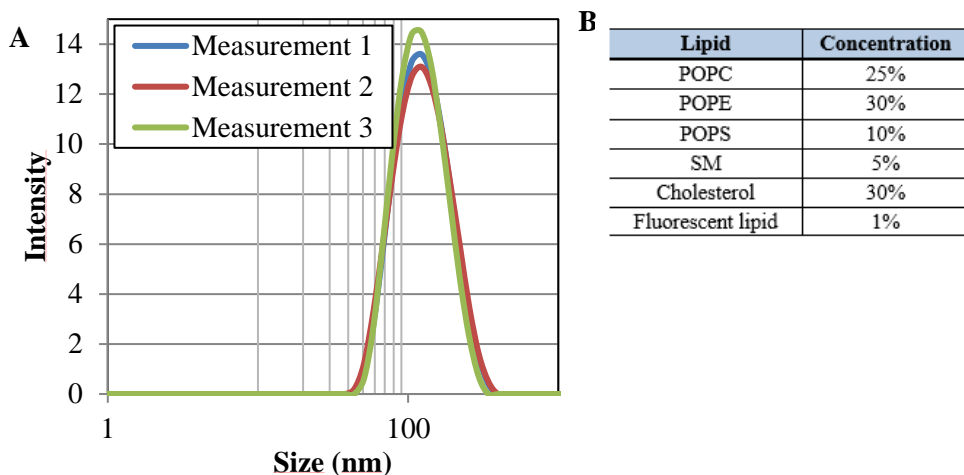


Figure 6.12: Lipid composition and size distribution of the dispensed liposomes. (A) Intensity based particle diameter distribution, obtained from DLS. Average liposomes size was 105 ± 35 nm. (B) Lipid composition of the liposomes. The fluorescent lipid used was TRITC-DHPE.

To gain experience in dispensing such more demanding solutions, hollow cantilevers were used to dispense fluorescently labelled liposomes on an EM-grid.

By incorporating a fluorescently labelled lipid during liposome production, dispensing of liposomes can be monitored. Liposomes mimic cellular membrane structures, making it possible to test the effect of shear stress, pressure pulses and cantilever coating on retaining membrane structures during and after dispensing.

Reconstituted liposomes had an average diameter of 105 nm, with sizes ranging between 50 nm and 300 nm (Figure 6.12A). The liposome concentration was adjusted to 0.1 mg/mL for dispensing with an untreated hollow cantilever, with a lipid composition displayed in Figure 6.12B. Applying a pressure pulse of 3.6 bar led to the formation of a droplet in air, where the presence of liposomes was demonstrated via fluorescent microscopy (Figure 6.13A and B). After approach, an oval droplet with diameters of $87 \mu\text{m}$ by $127 \mu\text{m}$ (~ 90 pL) was deposited on the EM-grid (Figure 6.13C). The presence of liposomes was confirmed via fluorescent microscopy (Figure 6.13D). However, the measured fluorescent signal was quickly quenched during sample dehydration.

When the cantilever was coated with OS, a build-up of structures appeared on the tip of the cantilever after dispensing (Figure 6.14). Such a build-up was not seen in previous experiments and is thought to be caused by an interaction between the lipids and the hydrophobic coating, leading to the formation of membrane aggregates or large vesicles near the tip of the cantilever. These aggregates could be washed away by dipping the cantilever in water. Dispensing liposomes with non-coated cantilevers was possible and led to a reduction of membrane aggregates.

After dispensing, the EM-grids were negatively stained and analysed by TEM. Dispensed samples show free liposomes with a diameter of ~ 120 nm (Figure 6.15A). However, stacked

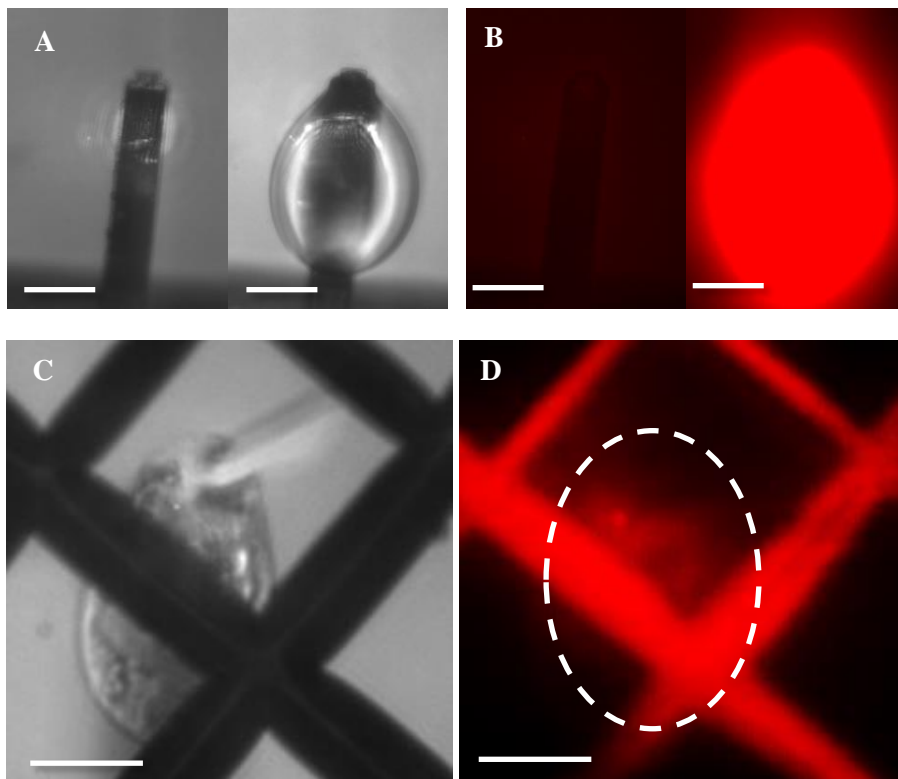


Figure 6.13: Dispensing liposomes with a non-coated hollow cantilever ($k=2$ N/m). (A) Bright field image of liposomes dispensed in air. Pressure pulse was 3.6 bar (time 6 sec). (B) Fluorescent image of liposomes dispensed in air. Pressure pulse was 3.6 bar (time 6 sec). (C) Bright field image of liposomes dispensed on a glow discharged EM-grid. Pressure pulse was 1.5 bar (time 3 sec). (D) Fluorescent image of dispensed liposomes on a glow discharged grid. The gridbars show auto-fluorescence, while the fluorescent signal of the liposomes is quenched due to dehydration. A faint fluorescent signal is found at the dispensed position (white dotted ellipse), suggesting that liposomes are deposited on the EM-grid. Scale bars represent 50 μ m in all panels.

membranes were visible as well (Figure 6.15B). The formation of stacked membranes could be caused by fusion of the liposomes due to the high pressure in the cantilever, liposome fusion induced by evaporation of the dispensed sample or release of the membrane aggregates or large vesicles from the cantilever tip.

The effect of dehydration on liposome fusion was tested by pipetting 0.5 μ L liposome solution (0.1 mg/mL) on a glow discharged EM-grid and letting it dry at RT for 5 min. After negative staining involving rehydration and drying again, fused membranes were visible on these EM-grids as well (Figure 6.15C), whereas independent liposomes were difficult to find (Figure 6.15D). This suggests that the fused membrane stacks were formed at the tip by the

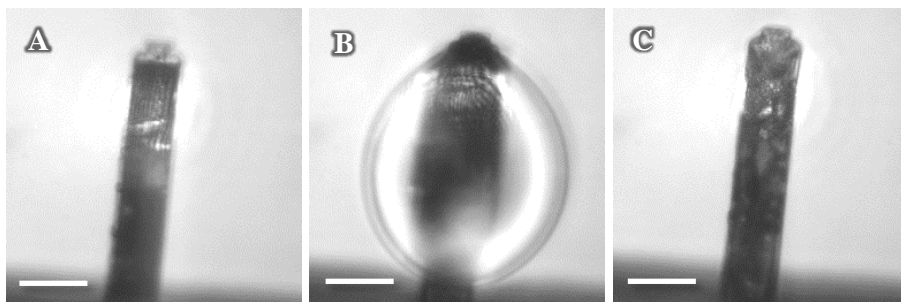


Figure 6.14: Membrane sheet formation on an OS coated cantilever after dispensing. (A) Hollow cantilever ($k=2$ N/m) filled with 0.1 mg/mL fluorescent liposomes. (B) Liposomes are dispensed in air after applying a pressure pulse of 3600 mbar. (C) Pressure is released, droplet retracts in the cantilever, on the cantilever a residual build-up of structures is formed, possibly lipids interacting with the hydrophobic coating of the cantilever. Scale bars are 50 μ m.

evaporation of the sample during dispensing, although other possibilities cannot be excluded yet.

6.5: Discussion

Although hollow cantilevers have been used to prepare negative stain TEM samples (3), experimental details necessary to reproducibly dispense femtolitre to picolitre volumes on an EM-grid, have not been presented yet. In this chapter, cantilever-sample solution-EM-grid interactions were studied and dispensing of samples such as aqueous solutions of nano-gold particles, apoferritin and liposomes on EM-grids was demonstrated. Dispensing of samples in an ambient environment is challenging. Besides the type of sample to dispense, the force of the cantilever on the EM-grid, the hydrophobicity of the cantilever, the hydrophobicity of the carbon film, sample-cantilever interactions and sample evaporation during dispensing all determine the success rate of EM-sample preparation. Although samples were successfully dispensed on non-glow discharged EM-grids and liposomes seemed to react with the hydrophobic coating during dispensing, the optimal and most reproducible results were obtained when samples were dispensed with a hydrophobic coated cantilever on a glow-discharged EM-grid.

Difficulties in dispensing particles on an EM-grid for TEM imaging that relate to cantilever-particle interactions depend on the sample used. Apoferritin and au-NPs could be dispensed with minimal interactions with OS coated cantilevers, while liposomes interacted with such coated cantilevers, leading to the formation of membrane aggregates and large vesicles at the tip. Membrane aggregate formation was reduced when uncoated cantilevers were used, but uncoated cantilevers lead to strong cell-cantilever interactions during cell penetration (Figure 6.5). The optimal cantilever coating needs to be determined experimentally and differ depending on the type of cells studied and sample to be aspirated and dispensed. Previously used PLL-PEG coatings (2) for dispensing fluids into a cell and aspirating

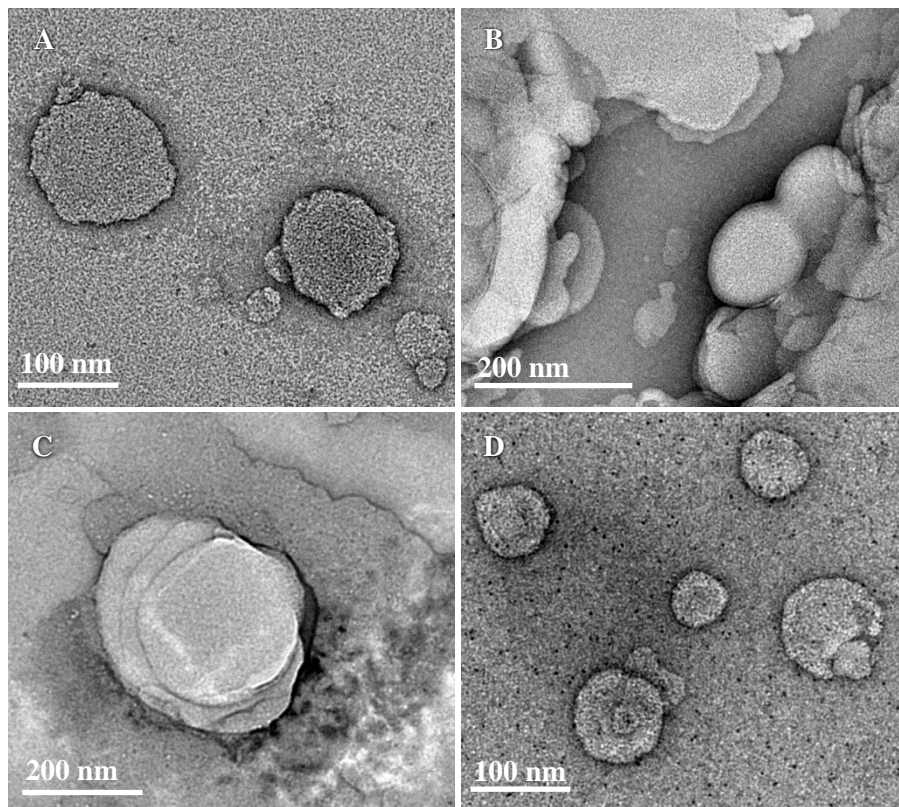


Figure 6.15: Dispensed liposomes. (A,B) A 100 μ g/mL liposome solution was dispensed at different positions on a formvar carbon coated copper EM finder grid by using hollow cantilever (2 N/m) AFM (1.5 bar, 3 sec). Samples were negative stained by pipetting 0.5 μ l of 0.2% Uranyl acetate on the EM-grid and letting it dry in air. Magnification was 15,000x. (C,D) 0.5 μ l of liposomes (100 μ g/ml) were pipetted on a formvar carbon coated copper EM finder grid and left to dry in air. Subsequently, 0.5 μ l of 0.2% Uranyl acetate were pipetted on the grid and left to dry in air. This harsh method resulted mainly in membrane aggregates on the EM-grid (C), but independent liposomes could be visualized as well (D). (C) Magnification was 10,000x. (D) Magnification was 15,000x.

subcellular volumes from a cell require an aqueous environment throughout. This is not possible when aspirated cytosolic cell fractions are to be deposited on an EM-grid for subsequent vitrification. In this case, evaporation of the dispensed volume must be suppressed. Due to evaporation, liposomes fuse, forming stacked membranes (Figure 6.15B and C), salt crystals form and may cluster around the dispensed particles (Figure 6.9D and E) and proteins may aggregate (Figure 6.11B). All such aggregates also will clog the tip. Especially for cryo-EM, evaporation of the water needs to be prevented as much as possible, for this technique completely relies on the aqueous environment of the particles for cryo-

fixation. Evaporation can be prevented by humidity and dewpoint control of the sample as discussed in chapter 5.4.

Although picolitre to sub-nanolitre samples were dispensed and analysed via TEM, the volumes were not dispensed in a controlled manner leading to relatively large samples. Volume dispensing can be controlled by the used pressure and time pulse. However, the necessary pressure and pulse time differ per substrate and per sample used. Higher particle concentrations appear to need higher pressures for both aspiration and dispensing. While aspiration with an OS-coated hollow cantilever is driven mainly by the negative pressure applied, a glow discharged hydrophilic EM-grid will enhance dispensing by capillary forces. How far this uncontrolled release of sample volume disturbs the formation of aqueous sample layers suitable for vitrification needs yet to be explored.

Calibration tests with samples exhibiting different viscosities and varying the time between glow discharging of and dispensing on the EM-grid need to be accomplished. Nevertheless, the dispensed volume will still differ per sample. Especially once samples are to be aspirated from cells and the viscosity of the sample is unknown, the necessary pressure and time pulse to dispense on the EM-grid may differ from the calibration. Aspired subvolumes from cells can be diluted in the cantilever, while evaporation at the cantilever tip could lead to possible clogging of the cantilever. To limit dilution of the aspired volume in the cantilever and cantilever tip evaporation and to enhance quantified sample dispensing, pL oil volumes might be used as plugs sealing the tip aperture and used as separators between aspirated volumes, leading to packages of cellular content in the cantilever. These packages could then be dispensed by writing them as a line on an EM-grid. High viscosity oils might also be used to control accurate release of aspirated volumes onto a hydrophilic EM-grid. The effect of oil on cryo-EM sample preparation and the possibility to use oil as a separator solution or clogging solution needs to be explored.

To aspirate from cells, cantilever-cell interactions and cell targeting need yet to be fully tested for the set-up described in chapter 5. Preliminary cellular dissection experiments show that specific cells can be targeted and nano surgery applied with this system (Figure 6.8). However, this is crude and induces cell lysis, whereas the goal is to aspirate subvolumes from cells while keeping them alive. Next experiments will focus on the controlled cantilever approach, to use the tip as a nanosyringe. OS coating allowed cantilevers to approach target cells and to withdraw from them without cellular release from the glass substrate (Figure 6.5). Cells grown on a pure glass substrate bind relatively weakly to the surface, as demonstrated by the release of multiple cells from the substrate by an uncoated cantilever (Figure 6.5C). For accurate cell penetration by the tip, and subsequent cellular aspiration and dispensing, the cells need to attach strongly to their substrate, to at least prevent their detachment from the substrate during cantilever retraction. A poly-lysine coating, as used in culture flasks, will increase cellular attachment to the glass surface as well. Applying a PLL coating to the substrate is expected to induce cell-substrate interactions that are strong enough to keep cells in place during cellular penetration and tip withdrawal.

Dispensing fluids in an aqueous solution differs from dispensing solutions in air. Therefore, dispensing in an aqueous solution needed to be tested as well. As compared to dispensing in air, higher pressure pulses were used to dispense into the aqueous environment. Whereas in air a maximum pressure of typically 3.5 bar was used, a pressure pulse of 6.3 bar was used to dispense CF into water. Because CF is a small molecule it is not expected to clog the cantilever, but to diffuse rapidly in water. Thus, a large dispensed volume was required to obtain a distinct signal, explaining the high pressure used. Dispensing CF in the vicinity of cells induced the formation of internal vesicle-like structures. Prolonged incubation of cells in the presence of mM concentrations of CF, lead to cell death (Figure 6.7) demonstrating the toxicity of CF for cells. While dispensing CF, a local high concentration of CF is introduced near the cells, which strongly perturbed the cells. However, as the dispensed volume is very small compared to the total surrounding cell medium, and because CF diffused quickly, the local CF concentration was above toxic levels for a short time only. The cellular vesicles formed resemble autophagosomes (13-15), which, in the light of CF toxicity, could be a reasonable hypothesis. During short exposure to mM concentration CF, the addressed cells were damaged but could be repaired after CF concentration dropped below a critical level. The formation of autophagosomes would explain the cellular survival after dispensing (15).

The set-up presented in Chapter 5 can now be used to target specific cells without inducing cell-cantilever interactions; solutions can be dispensed in an aqueous environment; biological samples can be dispensed on EM-grids and analysed via TEM. Next, dosing of dispensed femtolitre to picolitre volumes needs to be established. Furthermore, penetration of cell membranes with the tip, dispensing compounds into cells, aspiration from cells and finally cryo-EM sample preparation of femtolitre dispensed volumes need to be demonstrated. While the experiments described in this chapter provide a solid foundation, only future experiments will show the real functionality of the proposed set-up for cryo-EM sample preparation.

6.6: Materials and Methods

Hollow cantilevers—2 types of hollow cantilevers were used during these experiments. The properties of these hollow cantilevers are summarized in table 6.1. The hollow cantilevers were obtained from Smarttip and the 2 N/m cantilever was modified by ir. Eleonor Verlinden at the precision and microsystems engineering department of Delft University of Technology to include a fluidic interface and a tube to connect the cantilever to the pressure controller (Elveflow). The 7 N/m hollow cantilevers were not used for dispensing experiments.

Coating cantilevers – Cantilevers (Table 6.1) were placed in a petridish on a piece of double-sided carbon-tape. A small cotton ball was placed in the vicinity of the cantilevers and 20 μL trichloro(octyl)silane (OS; Sigma-Aldrich) was pipetted on the cotton ball. The petri-dish was closed and the cantilevers were incubated for 10 min at RT. Coating proceeded due to evaporation of OS and the formation of a thin coating layer on the cantilevers. Hydrophobicity was tested by pipetting 0.5 μL of MiliQ water on the cantilever, formation of a bubble with a high contact angle shows proper coating of the cantilever.

(Negative stain) Electron Microscopy –Carbon coated copper finder electron microscopy grids were glowdischarged for 90 sec to render them hydrophilic. After glow discharge the EM-grids were immediately loaded on the set-up for dispensing experiments. A cantilever filled with the desired solution was approached upon the carbon film and solute was dispensed on the EM-grid by applying a pressure pulse. Dispensing of solute was monitored via light microscopy. After evaporation of the sample, 0.5 μL of 0.2% Uranyl acetate was pipetted on the EM-grid and left to evaporate followed by immediate electron microscopy analysis in an JEOL 1400 microscopy. Images were obtained by using a Gatan Orius CCD camera.

Cryo-EM—Cryo-EM experiments were executed by dr. Tom Sharp from the Medical Microbiology-Electron Microscopy department of the Leiden University Medical Centre. Holey carbon electron microscopy grids were glow discharged and left in an ambient environment for 1 to 2 hrs. After incubation, 8 μl human serum was pipetted on the glow discharged EM-grids while incubated at 70% humidity and 4°C. The excess of fluid was immediately blotted to form a thin layer of human serum, mimicking sub-picolitre dispensing of cellular contents at the desired humidity. After 30 sec incubation, the samples were plunge frozen into liquid ethane and analysed via cryo-electron microscopy.

Sf9 cells— *Sf 9* cells were purchased from Expression systems and cultured in ESF921-cell culture medium at 27°C while shaking at 130 rpm until a cell density of 2×10^6 cells/mL was reached. Shortly before measurements a sample was taken from the suspension culture and placed on either a glow discharged EM-grid (chapter 6.3.3) or on a glass coverslip (chapter 6.3.2). The cells were left to attach for ~15 min until measurements started.

mpkCCD cells – *mpkCCD* cells were a kind gift from prof. Robert Fenton from Aarhus University (Denmark) and were cultured in DMEM medium (GIBCO) supplemented with 1X ITS-G (GIBCO), 20 $\mu\text{g/L}$ dexamethasone (Sigma-Aldrich), 1 nmol Triiodotyryne (Sigma-Aldrich), 10 ng/ μl EGF (Sigma-Aldrich), 100 mM HEPES (GIBCO), 10 mL FCS

(GIBCO) and 5 mL pen/strep (GIBCO). *mpkCCD* cells were cultured on glass coverslips placed in 6-well plates. The glass coverslips were used to test cantilever-cell interaction studies.

Dispensing—Hollow cantilevers were provided by SmartTip and attached to a fluidic interface by ir. Eleonor Verlinden (PhD student of prof. Urs Staufer and Dr. Murali Ghatkesar (assistant professor) at the department of precision and microsystems engineering at Delft University of Technology). The fluidic interface was connected to a fluidic reservoir by a tubing ($\varnothing = 0.5\text{mm}$). 50 μL samples were loaded into the fluidic reservoir and the reservoir was connected to the pressure controller (Elveflow). Cantilever channels were filled by applying an increasing overpressure on the fluidic reservoir, while the cantilever is kept in air. Dispensing was monitored by using an iXon ultra CCD camera attached to a Motic AE32 inverted microscope. Once a droplet forms at the tip of the cantilever, pressure was released and the cantilever was used for dispensing experiments.

Dispensed volume approximation – The dispensed volume was approximated accordingly depending on the position of the cantilever and the hydrophobicity of the substrate.

When volumes were dispensed in air, the dispensed volume was approximated by calculating the volume of a sphere based on the radius of the dispensed droplet.

When liquids were dispensed on a non-glow discharged grid, the assumption was made that the dispensed liquid forms a half sphere on the hydrophobic surface, meaning that the volume was approximated by taking half of the sphere volume based on the diameter of the dispensed liquid.

When droplets were dispensed on a glow discharged grid, a contact angle of 25° was used. This contact angle was determined from the 0.5 μL pipetted water droplet on a freshly glow discharged grid as is visualized in Figure 6.3B. With the diameter of the dispensed liquid and this surface angle, the radius of a virtual sphere can be determined by using equation 1.

$$r = \frac{r_{dispensed}}{\cos(90 - \text{contact angle})} \quad \text{Equation 1}$$

Where r is the radius of a virtual sphere and $r_{dispensed}$ is the radius of the dispensed liquid. The height of the dispensed liquid was determined by using equation 2.

$$h_{dispensed} = r - (\tan(90 - \text{contact angle}) * r_{dispensed}) \quad \text{Equation 2}$$

Where $h_{dispensed}$ is the height of the dispensed liquid. The volume of the dispensed liquid can be approximated by using equation 3.

$$V_{dispensed} = \frac{1}{6}\pi h_{dispensed} * (3r_{dispensed}^2 * h_{dispensed}^2) \quad \text{Equation 3}$$

6.7: References

1. Guillaume-Gentil, O., Potthoff, E., Ossola, D., Franz, C. M., Zambelli, T., and Vorholt, J. A. (2014) Force-controlled manipulation of single cells: from AFM to FluidFM. *Trends in biotechnology* **32**, 381-388
2. Guillaume-Gentil, O., Potthoff, E., Ossola, D., Dorig, P., Zambelli, T., and Vorholt, J. A. (2013) Force-controlled fluidic injection into single cell nuclei. *Small (Weinheim an der Bergstrasse, Germany)* **9**, 1904-1907
3. Guillaume-Gentil, O., Grindberg, R. V., Kooger, R., Dorwling-Carter, L., Martinez, V., Ossola, D., Pilhofer, M., Zambelli, T., and Vorholt, J. A. (2016) Tunable Single-Cell Extraction for Molecular Analyses. *Cell* **166**, 506-516
4. Alberts, B., Johnson, A., Lewis, J., Walter, P., Raff, M., and Roberts, K. (2002) *Molecular Biology of the Cell 4th Edition: International Student Edition*, Routledge
5. Kuncova, J., and Kallio, P. (2004) Challenges in capillary pressure microinjection. *Conference proceedings : ... Annual International Conference of the IEEE Engineering in Medicine and Biology Society. IEEE Engineering in Medicine and Biology Society. Annual Conference* **7**, 4998-5001
6. Guigas, G., Kalla, C., and Weiss, M. (2007) Probing the nanoscale viscoelasticity of intracellular fluids in living cells. *Biophys J* **93**, 316-323
7. Lyons, A. B. (1999) Divided we stand: tracking cell proliferation with carboxyfluorescein diacetate succinimidyl ester. *Immunology and cell biology* **77**, 509-515
8. Nakagawa, S., Usui, T., Yokoo, S., Omichi, S., Kimakura, M., Mori, Y., Miyata, K., Aihara, M., Amano, S., and Araie, M. (2012) Toxicity evaluation of antiglaucoma drugs using stratified human cultivated corneal epithelial sheets. *Investigative ophthalmology & visual science* **53**, 5154-5160
9. Wyroba, E., Suski, S., Miller, K., and Bartosiewicz, R. (2015) Biomedical and agricultural applications of energy dispersive X-ray spectroscopy in electron microscopy. *Cellular & molecular biology letters* **20**, 488-509
10. Goldstein, J. I., Newbury, D. E., Echlin, P., Joy, D. C., Lyman, C. E., Lifshin, E., Sawyer, L., and Michael, J. R. (2003) X-Ray Spectral Measurement: EDS and WDS. in *Scanning Electron Microscopy and X-ray Microanalysis: Third Edition*, Springer US, Boston, MA. pp 297-353
11. Wang, W., Knovich, M. A., Coffman, L. G., Torti, F. M., and Torti, S. V. (2010) Serum Ferritin: Past, Present and Future. *Biochimica et biophysica acta* **1800**, 760-769
12. Theil, E. C. (2012) Ferritin protein nanocages-the story. *Nanotechnology perceptions* **8**, 7-16
13. Tsai, S. C., Yang, J. S., Peng, S. F., Lu, C. C., Chiang, J. H., Chung, J. G., Lin, M. W., Lin, J. K., Amagaya, S., Wai-Shan Chung, C., Tung, T. T., Huang, W. W., and Tseng, M. T. (2012) Bufalin increases sensitivity to AKT/mTOR-induced autophagic cell death in SK-HEP-1 human hepatocellular carcinoma cells. *International journal of oncology* **41**, 1431-1442
14. Shen, C., Yan, J., Jiang, L. S., and Dai, L. Y. (2011) Autophagy in rat annulus fibrosus cells: evidence and possible implications. *Arthritis research & therapy* **13**, R132

15. Zhi, X., Feng, W., Rong, Y., and Liu, R. (2017) Anatomy of autophagy: from the beginning to the end. *Cellular and molecular life sciences : CMLS*

6.8: Supplemental figures

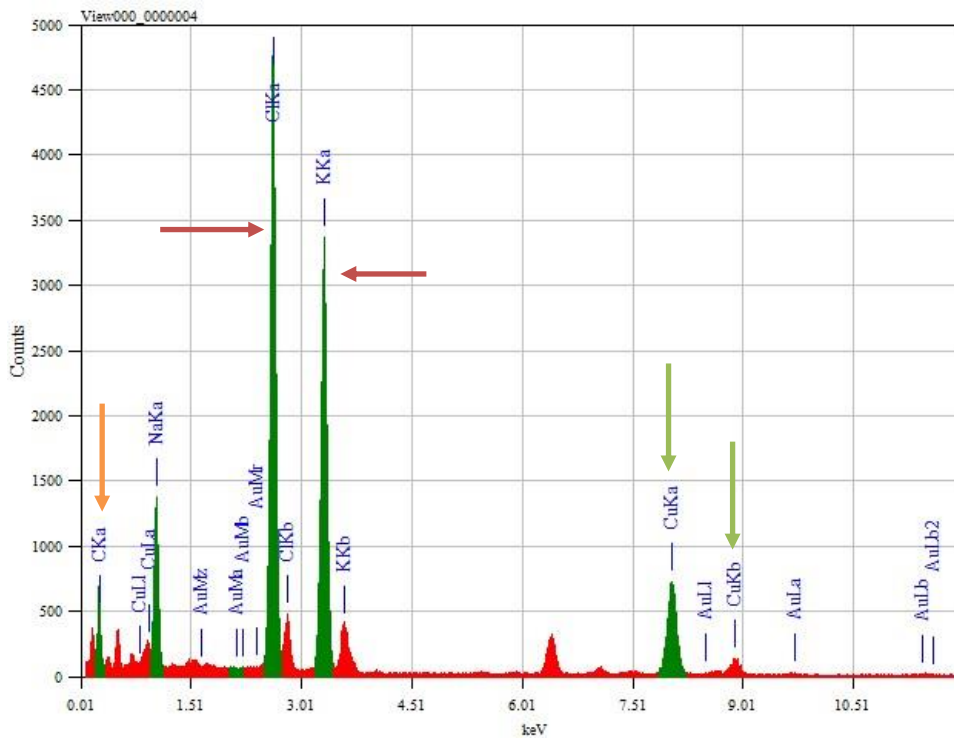


Figure S6.1: EDX spectrum corresponding to Figure 6.9E. Salt peaks (potassium and chloride) are indicated by red arrows, copper peaks are indicated by green arrows and the carbon peak is indicated by an orange arrow. Clear gold peaks are not visible in this image.

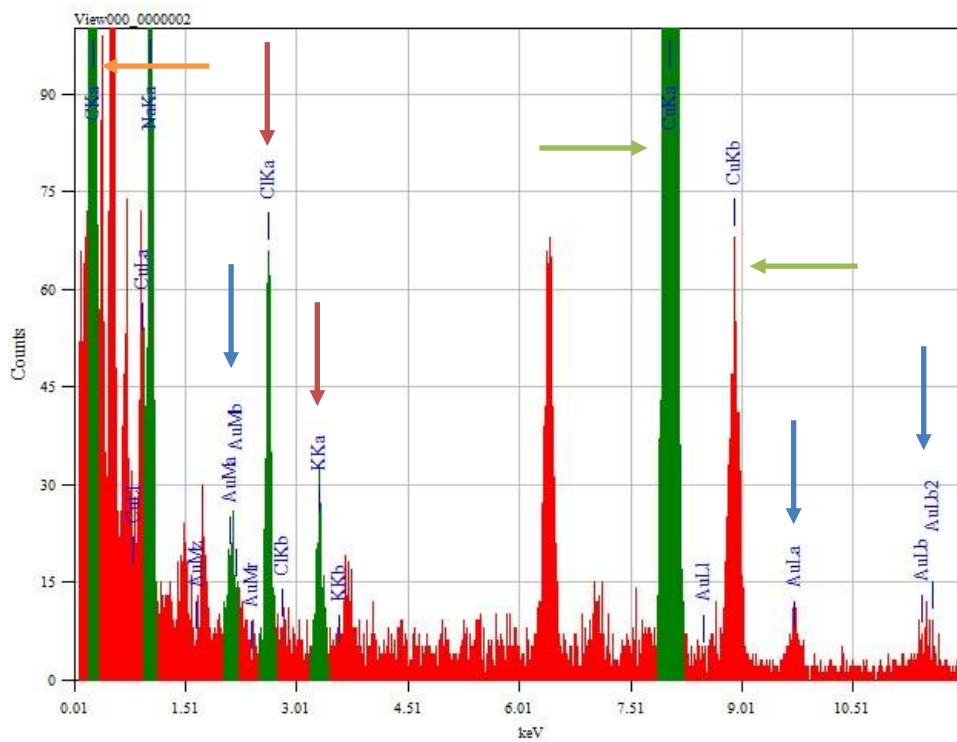


Figure S6.2: EDX spectrum corresponding to Figure 6.9C. Gold peaks are indicated by blue arrows, salt peaks (potassium and chloride) are indicated by red arrows, copper peaks are indicated by green arrows and the carbon peak is indicated by an orange arrow.

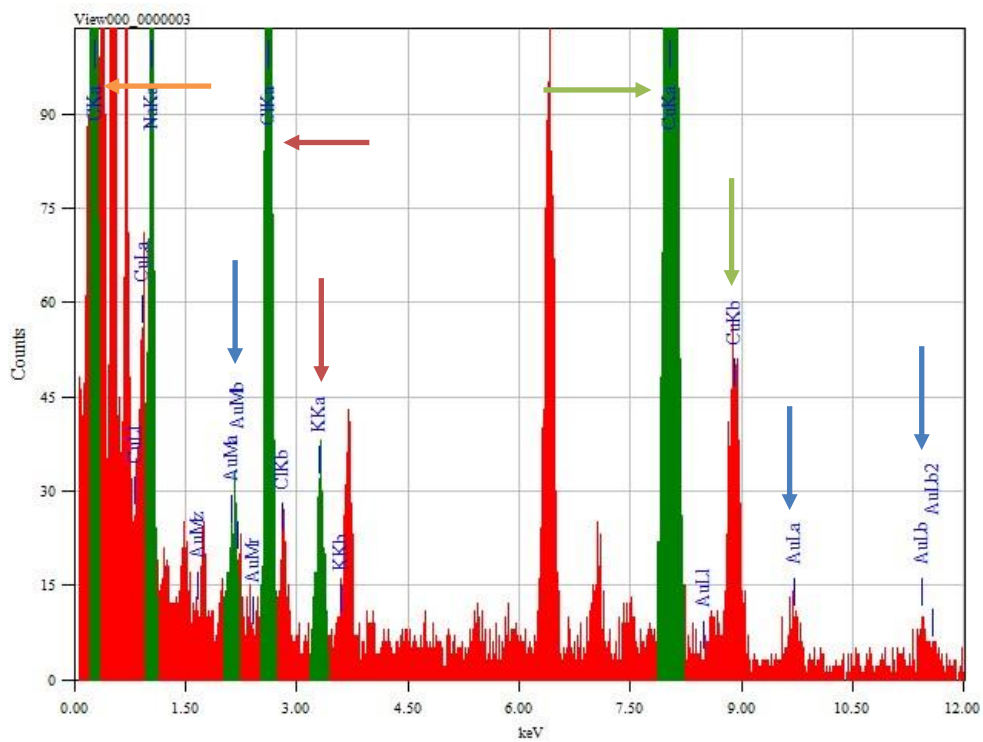


Figure S6.3: EDX spectrum corresponding to Figure 6.9D. Gold peaks are indicated by blue arrows, salt peaks (potassium and chloride) are indicated by red arrows, copper peaks are indicated by green arrows and the carbon peak is indicated by an orange arrow.

Summary:

Aquaporin 2 (AQP2) plays a critical role in maintaining water homeostasis in the human body. For this tightly regulated, vasopressin controlled, mechanism is necessary to ensure proper water balance. A deregulation of this important mechanism causes a disease called nephrogenic diabetes insipidus (NDI), leading to an increased secretion of urine and an increased probability of dehydration. Elucidating the mechanism behind AQP2 trafficking regulation could therefore aid in the cure of this disease. Furthermore, endocytosis and exocytosis are two critical cellular processes which are still not fully understood. The mechanism behind the tight AQP2 endocytosis and exocytosis regulation could therefore shed more light on these important cellular processes.

Since the discovery of AQP2 in the 1990's, AQP2 function and trafficking regulation have been extensively studied and a summary of these findings can be found in **chapter 2**. Although AQP2 has been studied for almost 30 years, the complete mechanism controlling AQP2 trafficking is still not fully understood. Classical methods can still be used to explore the mechanism behind AQP2 transport, of which one new finding was discussed in **chapter 3**. However, to fully understand this complex transporting system, it is necessary to develop new methods.

Recent strides in cryo-EM, makes that this method became more and more suitable to study cellular mechanisms in a high resolution. However, although the imaging possibilities with cryo-EM were greatly enhanced by the development of direct electron detectors and software development, cryo-EM sample preparation methods did not improve much in recent years and is still laborious and difficult to perform. To really use cryo-EM as a more routine lab-experiment, cryo-EM sample preparation techniques need to evolve as well.

Purified proteins are relatively easy to prepare for cryo-EM, due to the relative small volume necessary for cryo-fixation. However, purified proteins lack the complexity of the cell. Preparing complete cells for cryo-EM, and therefore retaining the cellular complexity, is a labour intensive, time-consuming, technically demanding procedure making it difficult to image complex cellular processes (discussed in **chapter 5**). Furthermore, the methods available often lack the possibility to exactly time the moment of fixation, making it difficult to image specific transient mechanisms at specific time points. In order to limit the difficulty of cryo-EM sample preparation for complex biological samples, the thickness of the sample and the sample volume should be reduced as much as possible. This can be achieved by targeting sub-cellular volumes, aspirating this from specific cells and deposition on glow discharged EM-grids. These samples retain the complexity of the cells, can be harvested from cells at specific time points and are thin enough to be vitrified by plunge freezing. The design and use of such a method was discussed in **chapter 5** and **chapter 6**.

In **chapter 2**, AQP2 trafficking regulation mechanisms and the disease NDI are discussed in great detail. AQP2 displays the typical aquaporin fold, spanning the membrane six times, while two half-membrane spanning domains are overlapped once AQP2 folds, forming the typical hourglass shape. However, besides the typical aquaporin fold, AQP2 contains an

exceptionally long C-terminal tail, which is linked to AQP2 trafficking regulation. This C-terminal tail contains four phosphorylation sites, which change their phosphorylative state upon binding of AVP to the vasopressin-2 receptor. Although these phosphorylation sites have been extensively studied and their role in AQP2 trafficking regulation is confirmed, the exact purpose of these phosphorylative changes is still under debate. Results can differ depending on the model organism or the AQP2-mutant used, while for some residues a specific regulation mechanism has yet to be identified.

The same counts for proteins found to control this transportation mechanism or proteins found to interact with AQP2. Although for some proteins their role in this mechanism is relatively clear and well understood, for other proteins their function can differ depending on the model organism studied or their exact role still needs to be elucidated. Based on the data available, a simplified overview of the AQP2 trafficking regulation machinery could be composed and is visualized at the end of **chapter 2**. However, although this figure shows a relatively complex system, the true mechanism behind AQP2 trafficking regulation is much more complex and we are just at the brink of understanding the mechanics completely.

One of the results pointing towards the complexity of this process is discussed in **chapter 3** of this thesis. AQP2 exocytosis has been linked to actin cortex remodelling since 1991. In order to ensure AQP2 apical membrane fusion, the actin cortex, laying just below the apical membrane and acting as an exocytosis and endocytosis barrier, needs to be opened. For this, the actin filaments need to be destabilized, depolymerized and polymerization needs to be locally inhibited. AQP2 interacts directly with actin, as was found in 2008 by using surface plasmon resonance experiments. However, the effect of AQP2 on actin and its effect on actin cortex remodelling remained unknown. **Chapter 3** discusses the actin polymerization inhibiting effect of the AQP2 C-terminus, showing that AQP2 inhibits f-actin formation locally once the actin cortex is opened. Furthermore, AQP2 is able to interact with tropomyosin-5b, leading to the destabilization of actin thin filaments. However, the effect AQP2 has on actin polymerization inhibition is relatively weak as compared to actin polymerization inhibiting peptide Thymosin- β 4. Furthermore, actin cortex remodelling is linked to fluid shear stress (FSS) and the inactivation of RhoA by PKA. This shows that although AQP2 has a direct effect on actin cortex remodelling, the complete cellular process regulating this remodelling is much more complex and a broad variety of different proteins play an integral role in this small part of the complete AQP2 exocytosis pathway. Further research is therefore necessary to understand this small but important step in AQP2 exocytosis completely.

To study AQP2 trafficking regulation, the set-up discussed in **chapter 5** and **chapter 6** can be used. However, in order to specifically target AQP2 bearing vesicles, AQP2 needs to be labelled. AQP2-targeting fluorescent labels can be injected into cells by using hollow cantilevers, but these labels can interfere with AQP2-protein interactions and are therefore not favourable. Furthermore, controlling the phosphorylation state under native conditions is difficult, making it hard to target specific phosphorylation states of AQP2. Therefore, AQP2 bearing fluorescently labelled proteoliposomes can be used to study AQP2 trafficking within

mammalian cells. For this AQP2 needs to be expressed, purified and reconstituted as discussed in **chapter 4**. Overexpression of AQP2 can be achieved in different organisms, of which two were tested. *Sf9* cells are easy to handle and can be used to express a broad range of different AQP2 mutants in a relatively straightforward manner. Furthermore, AQP2 bearing membranes are easy to harvest from *Sf9* cells and an adequate yield of pure protein can be obtained. However, AQP2 expression in *Sf9* cells depends on the viability of the cells, age of the cells and the viral infection efficiency. The obtained yields, although relatively comparable, differ per expression round. Furthermore, the obtained yield is relatively low as compared to other expression systems. The other organism tested was *P. pastoris*, which is easy to handle as well. Purification of AQP2 from *P. pastoris* led to higher yields of pure protein as compared to *Sf9* cells. Moreover, the expression levels of AQP2 were more constant as compared to expression of AQP2 in *Sf9* cells. However, *P. pastoris* lacks the flexibility to produce multiple mutants in a relatively straightforward manner. For each mutant a different *P. pastoris* strain needs to be produced and optimized. Furthermore, *P. pastoris* requires dedicated methods to harvest AQP2 bearing membranes, due to its cell wall. Meaning that although the yields are much higher as compared to *Sf9* cells, purification of AQP2 from *P. pastoris* is a less trivial method.

AQP2 retains its stability once incorporated in a lipid environment, while, in time, it is unstable in detergent. To obtain maximum stability, AQP2 could either be reconstituted into proteoliposomes, or can be purified by incorporation in nanodiscs. Nanodiscs have the advantage that the native lipid environment of AQP2 is retained, leading to maximum stability. However, AQP2 activity can not be measured once incorporated into nanodiscs. Meaning that, although purification of AQP2 bearing nanodiscs in theory results in the most stable protein, the stability of the protein can only be addressed by performing structural studies. Furthermore, although AQP2 incorporation has been visualized by immuno-gold labelling in negative stain electron microscopy, the yield of purified AQP2 was relatively low. A large portion of AQP2 was lost, due to insufficient binding to the nickel beads. Purification conditions should therefore be optimized, to ensure large quantities of AQP2 bearing nanodiscs, followed by structural determination to determine the protein stability. Once this is tested, AQP2 bearing nanodiscs can be used to elucidate the complete structure of the AQP2, without using 2D-crystallization, or to find new AQP2-protein interactions by using co-immuno precipitation experiments.

For AQP2 bearing proteoliposomes, the activity of AQP2 could be measured after purification. The measured water transport capability of AQP2 was in good agreement with previously found activities and therefore shows the stability of this protein after purification and reconstitution. Furthermore, the designed rapid mixing device shows its potential in easy activity measurements. The fact that AQP2 is stable after purification and reconstitution means that AQP2 bearing fluorescently labelled proteoliposomes can be injected into mpkCCD cells to study AQP2 trafficking regulation depending on its phosphorylative state. For this the set-up discussed in **chapter 5** and **chapter 6** needs to be optimized.

In **chapter 5** the development of a new set-up to prepare cryo-EM samples was discussed. The preferred method to prepare samples for cryo-EM is by plunge freezing the sample into a cryogen. For this the sample needs to be thin enough to vitrify. Mammalian cells are generally too thick to plunge freeze into a cryogen without forming ice-crystals, while samples normally used for plunge freezing often lack the desired complexity of cellular contents. In order to obtain subcellular samples, thin enough for plunge freezing, an elaborate set-up is necessary, combining a broad range of different components. To aspirate subcellular volumes, AFM controlled hollow cantilevers connected to a pressure controller are necessary, able to aspirate and dispense sub-picolitre volumes. Furthermore, a plunging system must be located at a close proximity of the AFM, to ensure rapid freezing after aspiration. Evaporation of the sample must be inhibited as much as possible. Therefore, it is necessary to work in a humidity-controlled environment. At the moment, all different components necessary for this set-up are developed and software controlling these components are running. However, most of the components require different software to control, meaning that each component is controlled individually. This individuality increases the chances of human errors and is therefore unfavourable. In the future, one controlling software for all components is necessary to limit the possibility of errors as much as possible. Moreover, although all components are in place now, the use of these components needs to be optimized. The humidity-control indeed limits evaporation to some extent, but the evaporation rate is still too high to inhibit evaporation of sub-picolitre volumes. Optimal humidity and dewpoint control parameters need to be determined experimentally to limit evaporation as much as possible. Furthermore, the plunging system has been used to plunge freeze and image tobacco mosaic virus (TMV). However, the tweezers used are not optimal yet. The relatively deep plunging depth and the relatively wide tweezer arms lead to the formation of an ethane droplet between the tweezer arms due to capillary force after plunging. This ethane droplet freezes once the EM-grid is transferred towards the liquid nitrogen storage box, making it impossible to release the EM-grid from the tweezers after plunging. To ensure proper cryo-EM sample preparation via plunge freezing, the plunging depth and the tweezers used need to be optimized as well.

There is one small, but crucial, part still missing from the set-up, which is the shutter covering the plunging hole during manipulation of the cells. At the moment, this shutter is lacking, leading to leakage of the humidity, impairing the stability of the humidity. During our tests, the plunging hole was covered with parafilm, to ensure proper closing of the humidity chamber. However, during experiments involving cryo-EM sample preparation, this is not possible and the shutter is therefore a necessity. The shutter will be incorporated to the system as soon as possible.

The use of hollow cantilevers was discussed in **chapter 6**. During cryo-EM sample preparation, subcellular volumes are aspirated from targeted cells and dispensed on glow discharged EM-grids. EM-grids are covered by a thin layer of carbon film, which needs to stay intact during dispensing. Furthermore, during aspiration, the hydrophilic-cantilever is penetrating the cellular membrane, which could lead to membrane-cantilever interactions and

a possible rupture of the cellular membrane during retraction, causing cell death. Therefore, cantilevers were coated with a hydrophobic coating (octyltrichlorosilane; OS) and the effect of this coating on cellular contact and EM-grid dispensing was tested. By using this coating, cells could be approached by a cantilever without disturbing them, while the most reproducible EM-grid dispensing was achieved once the EM-grid was glow discharged and the cantilever was coated. Although coated hollow cantilevers have been used to approach and disrupt cells, without inducing cell-cantilever interactions, and hollow cantilevers have been used to dispense volumes at close proximity of targeted cells, the hollow cantilevers have not been used to penetrate cells and dispense or aspirate small volumes into or from these cells. Next experiments should focus on these steps, for these are a necessity for the use of this machinery to produce complex and easy to prepare cryo-EM samples.

Dispensing small volumes on an EM-grid requires that, normally, neglectable forces should be considered. Cantilever-solute interactions and FSS inside the thin cantilever channels could greatly impact the possibility to dispense biological materials. Furthermore, evaporation of the sample is a major hurdle to overcome, for small volumes will evaporate within seconds after dispensing. Evaporation of buffer solute, increases the formation of salt-crystals as was visualized after gold nanoparticles, carrying traces amounts of salts, were dispensed on glow discharged EM-grids, while evaporation of liposome containing volumes induced the formation of fused stacked membranes. Optimization of the humidity control, discussed in **chapter 5**, is therefore a necessity for good EM-sample preparation. Especially because the liquid environment is used as a fixation medium for cryo-EM. In **chapter 6**, dispensing of gold nanoparticles, apoferritin and liposomes was tested. All three samples were successfully dispensed on EM-grids and visualized in the electron microscope. However, no cryo-EM was performed on these dispensed samples yet. The visualization of these particles via (negative stain) electron microscopy shows that it is possible to dispense small volumes of (biological) material on an EM-grid by using this technique. Once the humidity control and the plunging mechanism is optimized, this set-up can be used to produce cryo-EM samples via hollow cantilevers.

In this thesis a part of the AQP2 trafficking mechanism has been studied by using traditional methods, while major steps have been taken to develop a new method to study AQP2 trafficking. Fluorescently labelled AQP2 bearing proteoliposomes have been produced and showed active AQP2 by using a rapid mixing device developed at our department. Furthermore, a set-up able to prepare cryo-EM samples from aspirated subcellular volumes was designed and tested. This set-up needs more optimization but is already able to produce cryo-EM samples by plunge freezing, while the hollow cantilevers have been successfully used to dispense (biological) samples on an EM-grid, while these samples could be analysed by electron microscopy. Moreover, cantilever-cell interactions studies show that targeted cells will not interact with the cantilever once coated with OS. In the near future it will be possible to use this system to aspirate targeted subcellular transient complexes from cells and to study these samples via cryo-EM, leading to a better understanding in specific cellular processes, which are difficult to study at the moment.

Samenvatting:

Aquaporine 2 (AQP2) speelt een zeer grote rol in de controle van de waterhuishouding (water homeostase) in het menselijk lichaam. Een strak gereguleerd, vasopressine gecontroleerd, mechanisme is nodig om ervoor te zorgen dat de waterbalans goed in balans blijft. Wanneer de water homeostase uit balans raakt door een deregulatie van dit belangrijke mechanisme zal een verhoogde secretie van urine plaatsvinden. Deze verhoogde secretie van urine verhoogd de kans op uitdroging. Deze symptomen zijn gelinkt aan de ziekte nefrogene diabetes insipidus (NDI). Door het mechanisme achter de AQP2 transport regulatie te onderzoeken kan er hopelijk een behandeling voor deze ziekte gevonden worden. Daarnaast zijn zowel exocytose en endocytose twee zeer kritische cellulaire mechanismen, welke tot op de dag van vandaag nog niet compleet onderzocht zijn. Het mechanisme achter de strak gereguleerde endocytose en exocytose van AQP2 kan daarom helpen deze processen beter te begrijpen.

AQP2 functie en transportregulatie zijn uitvoerig onderzocht sinds de ontdekking van dit eiwit in de jaren 90. Een samenvatting van de belangrijkste vondsten kan gevonden worden in hoofdstuk 2. Ondanks dat AQP2 al voor 30 jaar onderzocht wordt is het complete mechanisme achter het AQP2 transport nog steeds niet helemaal duidelijk. Klassieke methodes kunnen nog steeds gebruikt worden om nieuwe ontdekkingen te doen met als voorbeeld de ontdekking die besproken is in hoofdstuk 3. Alleen, om dit hele mechanisme compleet te begrijpen, zijn nieuwe onderzoeksmethodes noodzakelijk.

Recente ontwikkelingen in cryo-elektronen microscopie (cryo-EM), hebben het mogelijk gemaakt om cellulaire mechanismen in steeds hogere resoluties te onderzoeken. Echter, ondanks dat de visualisatie technieken enorm verbeterd zijn door de komst van directe elektronen detectoren en door de ontwikkeling van nieuwe software, zijn monster preparatie methodes niet veel ontwikkeld in de laatste jaren. Daarom is het maken van cryo-EM monsters vaak nog een moeilijk en tijdsintensief proces. Om cryo-EM te kunnen gebruiken als een routine experiment zijn er daarom dus nieuwe methodes nodig om cryo-EM monsters te kunnen maken.

Gezuiverde eiwitten kunnen relatief makkelijk gebruikt worden voor cryo-EM, aangezien er maar een relatief klein volume nodig is voor cryo-fixatie. Echter, gezuiverde eiwitten missen de complexiteit van een cel. Het prepareren van complete cellen voor cryo-EM, waarbij dus de cellulaire complexiteit in stand gehouden wordt, kost een hoop tijd en werk waar getraind personeel voor nodig is. Daarom is het relatief ingewikkeld om complexe cellulaire processen in kaart te brengen via cryo-EM (zoals besproken wordt in hoofdstuk 5). Daarnaast missen de huidige methodes de mogelijkheid om een cel te fixeren op een exact gekozen tijdstip, waardoor specifieke, kortdurende processen lastig zijn om te onderzoeken onder een hoge vergroting. Om de cryo-EM monster preparatie te vergemakkelijken voor complexe cellulaire monsters, is het nodig om de dikte van het monster en het monstervolume zoveel mogelijk te reduceren. Dit kan bereikt worden door naar alleen een klein deel van de cel te kijken, in plaats van de complete cel. Om dit te bereiken zijn pipetten nodig die sub-picoliters

aan volume uit een cel kunnen halen en deze kleine volumes kunnen deponeren op een EM-grid (de elektronenmicroscopie monsterhouder). Deze kleine monsters hebben nog steeds de complexiteit van de cel, kunnen op specifieke momenten uit een cel gehaald worden en zijn dun genoeg om te bevriezen via “plunge freezing”. De ontwikkeling en het gebruik van zo’n soort methode wordt besproken in hoofdstuk 5 en 6.

Het AQP2 transportmechanisme en de ziekte NDI zijn gedetailleerd besproken in hoofdstuk 2. AQP2 bezit de typische aquaporine structuur, waarbij het celmembraan 6 keer doorspannen wordt en twee halve membraan domeinen elkaar overlappen zodat een zandloper figuur ontstaat. Echter, ondanks dat AQP2 de typische aquaporine structuur bezit, heeft AQP2 een exceptioneel lange C-terminale staart. Deze C-terminale staart is gelinkt aan AQP2 transport regulatie. De C-terminale staart bevat vier fosforylatie posities, waarvan de fosforylatie status verandert zodra vasopressine (AVP) bindt aan de vasopressine-2 receptor (V2R). Ondanks dat deze fosforylatie posities uitvoerig bestudeerd zijn en het vastgesteld is dat deze posities het transport van AQP2 reguleren, is het exacte doel achter deze veranderingen in fosforylatie status nog steeds niet duidelijk. Resultaten kunnen verschillen, afhankelijk van welk model organisme of AQP2-mutant gebruikt is, terwijl voor enkele posities de rol nog helemaal niet duidelijk is.

Hetzelfde geldt voor eiwitten die gelinkt zijn aan de controle voor dit transportmechanisme. Ondanks dat de rol van sommige eiwitten relatief duidelijk is, is dit niet het geval voor alle gevonden eiwitten. De rol en functie van deze eiwitten in dit proces kan verschillen tussen verschillende model organismen, of een interactie tussen AQP2 en een specifiek eiwit is gevonden, maar de exacte betekenis hiervan is nog niet gevonden.

Een gesimplificeerd overzicht van AQP2 transport regulatie, gebaseerd op de beschikbare data, is te vinden aan het eind van hoofdstuk 2. Echter, ondanks dat dit overzicht een relatief complex systeem visualiseert, is het werkelijke mechanisme nog veel gecompliceerder en staan wij nu nog aan de basis om dit mechanisme compleet te begrijpen.

Een van de resultaten dat wijst naar de complexiteit van dit mechanisme is bediscussieerd in hoofdstuk 3 van deze these. De exocytose van AQP2 is gelinkt aan een herstructurering van de actine cortex. Om ervoor te zorgen dat AQP2 kan fuseren met het celmembraan moet de actine cortex, gelegen net onder het celmembraan met als doel exocytose en endocytose te reguleren, geopend worden. Hiervoor moeten actine filamenten gedestabiliseerd worden, afgebroken worden en de opbouw van actine filamenten moet lokaal gehinderd worden. AQP2 kan een directe interactie aangaan met actine, zoals in 2008 gevonden was. Echter, het effect van AQP2 op actine en het effect van deze interactie op de herstructurering van de actine cortex bleef onbekend. In hoofdstuk 3 wordt aangetoond dat AQP2 in staat is om actine polymerisatie tegen te gaan, wat betekent dat AQP2 in staat is om lokaal de vorming van actine filamenten tegen te gaan nadat deze geopend is. Daarnaast is AQP2 in staat om een interactie aan te gaan met tropomyosine-5b, wat leidt tot destabilisatie van actine filamenten. Echter, het effect van AQP2 op actine polymerisatie inhibitie is relatief zwak wanneer dit effect vergeleken wordt met thymosine- β -4, een eiwit welke bekend staat om zijn actine polymerisatie inhiberende effect. Daarnaast is het herstructureren van de actine cortex ook

gelinkt aan vloeistof schuifspanning en de activatie van RhoA door PKA. Dit laat zien dat ondanks dat AQP2 een direct effect heeft op de herstructurering van de actine cortex, het complete cellulaire proces wat dit proces reguleert is nog vele malen complexer en een breed scala aan verschillende eiwitten speelt een grote rol in dit kleine onderdeel van het AQP2 exocytose mechanisme. Daarom is verder onderzoek nodig om dit kleine, maar belangrijke, proces van AQP2 exocytose te begrijpen.

De set-up, besproken in hoofdstuk 5 en 6, is nodig om AQP2 transport beter te bestuderen. Echter, om AQP2 in de cel te kunnen lokaliseren, moet AQP2 gelabeld worden. Deze labels kunnen in de cel ge-injecteert worden door middel van holle cantilevers, maar het gebruik van deze labels kunnen AQP2-eiwit interacties hinderen en zijn daardoor niet optimaal als methode. Daarnaast is het lastig om de fosforylatie status van AQP2 te controleren onder normale omstandigheden, wat het lastig maakt om AQP2 te bestuderen afhankelijk van zijn specifieke fosforylatie status. Voor dit kunnen fluorescent gekleurde AQP2 dragen proteoliposomen gebruikt worden. Om dit te bereiken moet AQP2 tot expressie gebracht worden in cellen, gezuiverd worden van deze cellen en geconstitueerd in proteoliposomen zoals besproken in hoofdstuk 4. Overexpressie van AQP2 kan bereikt worden in verschillende organismen, waarvan twee getest zijn. *Sf9* cellen zijn makkelijk in de omgang en kunnen vrij eenvoudig gebruikt worden om een breed scala aan verschillende AQP2 mutanten tot expressie te brengen. Daarnaast zijn de AQP2 dragende celmembranen makkelijk te oogsten van *Sf9* cellen en leveren deze cellen een redelijke AQP2 opbrengst. Echter, de expressie van AQP2 in *Sf9* cellen is afhankelijk van de fitheid van de cellen, de leeftijd van de cellen en de virale infectie efficiëntie. De verkregen opbrengsten, ondanks dat ze relatief stabiel zijn, verschillen per expressie ronde en zijn relatief laag in vergelijking met andere expressie methodes. Het andere organisme dat getest is, was *P. pastoris*. *P. pastoris* is ook makkelijk in de omgang en produceert een hogere opbrengst aan AQP2, welke meer constant waren in vergelijking met *Sf9* expressie. Echter, *P. pastoris* is minder flexibel in vergelijking met *Sf9* cellen en de productie van verschillende AQP2 mutanten is daardoor lastiger. Voor elke mutant is een andere *P. pastoris* giststam nodig, welke geproduceerd en geoptimaliseerd moet worden. Daarnaast heeft *P. pastoris* een celmuur welke opengebrouwen moet worden. Hiervoor zijn speciale methodes nodig. Dit betekent dat ondanks dat *P. pastoris* betere opbrengsten genereert in vergelijking met *Sf9* cellen, het een complexere methode is om eiwit mee te produceren en uit te zuiveren.

AQP2 blijft, relatief, stabiel wanneer het gepositioneerd wordt in een dubbele lipiden laag, terwijl AQP2 onstabiel is als het voor lange tijd in een detergent opgelost is. Om maximale stabiliteit te verkrijgen moet AQP2 daarom geïncorporeerd worden in proteoliposomen of gezuiverd worden wanneer het geïncorporeerd is in nanodiscs. Nanodiscs hebben het voordeel dat zij het natuurlijke milieu van het eiwit zo veel mogelijk behouden, wat zal moeten leiden tot maximale stabiliteit. Echter, de activiteit van AQP2 kan niet gemeten worden als AQP2 gelokaliseerd is in deze nanodiscs. Wat betekent dat, ondanks dat AQP2 dragende nanodiscs in theorie de meest stabiele eiwitten oplevert, deze stabiliteit alleen bepaald kan worden wanneer de structuur van AQP2 bepaald wordt. Daarnaast, ondanks dat

de incorporatie van AQP2 in nanodiscs gevisualiseerd is door middel van immuno-goud kleuring en elektronenmicroscopie, de opbrengst van dit gezuiverde AQP2 was relatief laag. Een groot gedeelte van AQP2 was verloren gegaan tijdens de zuivering dankzij onvoldoende binding aan nickel. Daarom moet het zuiveringsprotocol geoptimaliseerd worden zodat een hoog aantal AQP2 dragende nanodiscs gezuiverd kan worden. Deze nanodiscs kunnen dan gebruikt worden voor structurele studies zodat de stabiliteit van het eiwit in deze nanodiscs bepaald kan worden. Zodra dit getest is kunnen AQP2 dragende nanodiscs gebruikt worden om de complete structuur van AQP2 te ontrafelen, zonder gebruik te hoeven maken van 2D kristallisatie, of deze nanodiscs kunnen gebruikt worden om nieuwe AQP2-eiwit interacties te vinden door middel van co-immuno precipitatie experimenten.

Met proteoliposomen kan de activiteit van AQP2 bepaald worden na zuivering. De gemeten watertransport capaciteit van AQP2 was vergelijkbaar met eerder gevonden waarden, wat betekent dat AQP2 stabiel is na de zuivering. Daarnaast is ons zelf ontwikkelde snelle meng machine in staat om op een relatief makkelijke manier de activiteit van AQP2 te meten. Het feit dat AQP2 stabiel is na zuivering en reconstitutie betekent dat AQP2 dragende fluorescent gelabelde proteoliposomen gebruikt kunnen worden voor injectie in muizen nier-cellen, zodat het AQP2 transport, afhankelijk van zijn fosforylatie, onderzocht kan worden. Hiervoor is de set-up nodig, welke besproken is in hoofdstuk 5 en 6.

In hoofdstuk 5 is de ontwikkeling van de set-up besproken voor het prepareren van cryo-EM monsters. De beste methode om cryo-EM monsters te maken is door gebruik te maken van “plunge freezing”, het snel onderdompelen van een monster in vloeibaar ethaan. Om dit te kunnen doen zijn monsters nodig die dun genoeg zijn, zodat deze snel kunnen bevriezen. Zoogdier cellen zijn te dik om te “plunge freezezen” zonder dat er ijskristallen gevormd worden, terwijl monsters die normaal gebruikt worden voor “plunge freezing” vaak de gewenste cellulaire complexiteit missen. Om cellulaire monsters te krijgen, welke dun genoeg zijn voor “plunge freezing”, is er een ingewikkelde set-up nodig. Om sub-cellulaire volumes uit cellen te verkrijgen zijn holle cantilevers nodig, kleine (holle) naalden welke gebruikt worden bij atomic force microscopie (AFM). Deze holle cantilevers kunnen gekoppeld worden aan een drukregulator, wat resulteert in een pipet welke in staat is om femtoliters (10^{-15} L) aan volume te pipeteren. Daarnaast is het nodig dat er een plunging mechanisme dichtbij is zodat geaspireerde monsters meteen bevroren kunnen worden. Verdamping van het monster moet zoveel mogelijk tegengegaan worden. Hiervoor is het nodig dat er in een ruimte gewerkt wordt waarvan de luchtvochtigheid gereguleerd wordt. Op dit moment zijn de verschillende componenten van dit systeem ontwikkeld en geïnstalleerd. Daarnaast is er een software ontwikkeld welke een groot deel van het systeem automatiseert. Echter, verschillende componenten in het systeem worden bestuurd door verschillende software, wat de complexiteit van dit systeem vergroot. In de toekomst is het daarom nodig om alle software te integreren in een programma, waardoor de mogelijkheid om menselijk falen verkleind wordt. Daarnaast, ondanks dat alle componenten aanwezig zijn, moet het gebruik van deze componenten nog geperfectioneerd worden. De luchtvochtigheidsregulator is in staat om de verdamping van het monster tot op zekere hoogte

tegen te gaan. Echter is de verdampingssnelheid nog te hoog om succesvol te kunnen werken met sub-picoliter volumes. Optimale luchtvochtigheid en dauwpunt controle parameters moeten experimenteel geoptimaliseerd worden. Daarnaast is het plunging mechanisme inderdaad in staat om tabak mozaïek virus (TMV) te bevriezen, maar is de pincet nog niet optimaal. De relatief diepe onderdompeling in vloeibaar ethaan en de relatief wijde pincet armen leiden tot de formatie van een ethaan druppel tussen de pincet armen. Deze ethaan druppel bevriest wanneer het EM-grid verplaatst wordt naar de opslag positie in vloeibaar stikstof. Hierdoor is het onmogelijk om het EM-grid van de pincet af te krijgen na het plungen. Om ervoor te zorgen dat goede cryo-EM monsters gemaakt kunnen worden moeten de plunging diepte en de pincet geoptimaliseerd worden. Als laatste mist er een klein, maar belangrijk, onderdeel in deze set-up. Dit onderdeel is de sluiters welke de plunging opening afsluit tijdens de cel manipulatie. Het gebrek aan deze sluiters zorgt ervoor dat de luchtvochtigheid in de set-up onvoldoende gereguleerd kan worden. Tijdens de tests in deze these is deze opening afgesloten door middel van parafilm, wat niet mogelijk is wanneer deze set-up daadwerkelijk in gebruik is. De sluiters is daarom noodzakelijk en zal zo snel mogelijk geïmplementeerd worden.

Het gebruik van holle cantilevers was besproken in hoofdstuk 6. Voor cryo-EM monster preparatie worden sub-cellulaire volumes uit een cel gepipetteerd en geplaatst op een EM-grid. EM-grids bevatten een dunne koolstof laag waarop het monster gedeponeerd wordt. Deze laag moet intact blijven wanneer het monster gepipetteerd wordt op de EM-grid. Daarnaast, tijdens aspiratie penetreert de hydrofiele cantilever het celmembraan, wat zou kunnen leiden tot membraan-cantilever interacties en een mogelijke scheuring van het celmembraan wanneer de cantilever teruggetrokken wordt. Daarom wordt er een speciale hydrofobe laag (octyltrichlorosilane; OS) aangebracht op de cantilevers en het effect van deze laag op de cel en het EM-grid was getest. Door deze laag te gebruiken konden cellen aangeraakt worden zonder cantilever-cel interacties aan te gaan, terwijl de meest reproduceerbare pipeteer resultaten behaald werden wanneer de cantilever hydrofoob was en de EM-grid hydrofiel. Ondanks dat hydrofobe cantilevers gebruikt zijn om cellen te doden, en holle cantilevers gebruikt zijn om volumes te pipetteren in de buurt van cellen, zijn de holle cantilevers nog niet gebruikt om een cel te penetreren en om kleine volumes in de cel te pipetteren of eruit te halen. De volgende experimenten zullen daarom gericht zijn op deze stappen, aangezien deze stappen cruciaal zijn voor het gebruik van deze set-up.

Wanneer kleine volumes gepipetteerd worden op EM-grids, betekent dit dat normaal verwaarloosbare krachten een grotere rol gaan spelen. Interacties tussen de cantilevers en de oplossing die gepipetteerd is en vloeistof schuifspanning binnenin de dunne cantilever kanalen kunnen een grote impact hebben op de mogelijkheid om biologische monsters te pipetteren. Daarnaast, verdamping van het monster is a groot probleem, omdat zeer kleine samples binnen enkele secondes verdampt zullen zijn. Verdamping van buffer vergroot de kans op zoutkristallen formatie, zoals in hoofdstuk 6 gevisualiseerd was toen goud nanodeeltjes gepipetteerd werden op een EM-grid. Daarnaast zorgde verdamping ervoor dat gepipetteerde liposomen fuseerden op het EM-grid. Het is daarom een absolute vereiste dat

de luchtvochtigheid, zoals besproken in hoofdstuk 5, goed gereguleerd wordt. Zeker aangezien het vloeibare milieu gebruikt wordt als fixatie medium voor cryo-EM. In hoofdstuk 6 was het pipetteren van goud nanodeeltjes, apoferritine en liposomen getest. Alle drie de monsters zijn succesvol gepipetteerd op EM-grids en gevisualiseerd in de elektronenmicroscopie. Echter, er is nog geen cryo-EM gedaan met deze samples. Het visualiseren van deze monsters via (negatieve kleuring) elektronenmicroscopie laat zien dat het mogelijk is om picoliter volumes van (biologische) monsters te pipetteren op een EM-grid. Zodra de luchtvochtigheid en het plunging mechanisme geoptimaliseerd zijn, kan deze set-up daarom dus gebruikt worden voor cryo-EM sample preparatie met holle cantilevers. In deze dissertatie is een deel van het AQP2 transportmechanisme bestudeerd door middel van traditionele methodes, terwijl grote stappen gemaakt zijn in de ontwikkeling van een nieuwe methode om AQP2 transport te bestuderen. Fluorescent gelabelde AQP2 dragende proteoliposomen zijn geproduceerd en er is laten zien dat deze proteoliposomen actief AQP2 dragen. Daarnaast is er een set-up ontworpen en ontwikkeld welke in staat is om cryo-EM monsters te maken van geaspireerde sub-cellulaire volumes. Deze set-up heeft meer optimalisatie nodig, maar is op dit moment al in staat om cryo-EM monsters te produceren, terwijl holle cantilevers gebruikt zijn om succesvol (biologische) monsters te pipetteren op EM-grids. Deze samples konden weer gevisualiseerd worden door middel van elektronenmicroscopie. Daarnaast is er laten zien dat cantilever-cel interacties tegengegaan kunnen worden door een hydrofobe laag op de cantilever aan te brengen. In de nabije toekomst zal het mogelijk zijn om dit systeem te gebruiken om sub-cellulaire monsters te aspireren uit cellen en deze te bestuderen via cryo-EM, dit zal leiden tot een beter begrip van specifieke complexe cellulaire processen, welke op dit moment nog onmogelijk zijn om te onderzoeken.

Abbreviations:

A kinase association proteins	AKAP
Aquaporin(-2)	AQP(2)
Arginine vasopressin	AVP
Atomic force microscopy	AFM
Carboxy fluorescein	CF
Dynamic light scattering	DLS
Gold nanoparticles	Au-NPs
Halogenated indolyl- β -galactoside	Bluo-gal
High pressure freezing	HPF
Hours past infection	Hpi
Lilly Laboratories Cell Porcine Kidney cells	LLC-PK1 cells
Madin-Darby Canine Kidney cells	MDCK cells
Mouse polarized kidney cortical collecting duct cells	mpkCCD cells
<i>n</i> -Octyl- β -D-glucopyranoside	OG
Nephrogenic Diabetes Insipidus	NDI
Protein kinase-A	PKA
Size exclusion chromatography	SEC
Soluble <i>N</i> -ethylmaleimide-sensitive factor attachment protein receptors	SNARE
<i>Spodoptera frugiperda</i> cells	Sf9 cells
Thymosin- β 4	TM β 4
Transmission electron microscopy	TEM

Trichloro(octyl)silane	OS
Tropomyosin-5b	Tm5b
Vasopressin-2 receptor	V2R
12-O-tetradecanoylphorbol-13-acetate	TPA

Acknowledgements:

From the first time I learned about the existence of cells and the basic concepts on how they function, I knew I wanted to learn more. It was for this reason that I started with the study Life Science & Technology in 2007. After obtaining my masters in 2012, it was prof.dr. Andreas Engel who took me into his lab and introduced me to the interesting world of Bionanoscience. The research performed at this department opened up a complete new world for me. I really enjoyed seeing such a broad range of different research come together into one department. Either the use of individual biological components to create life (the minimal cell), the development of new techniques to study (cell-)biological principles, a mixture of both or something completely different, all could be found in this department. Furthermore, the researchers working at this department were great as well. Always open to help, to think with you or to share their knowledge to help you succeed.

I therefore want to thank prof.dr. Andreas Engel for the opportunity to work at this department, but also for the opportunity to have my own exciting research. Andreas, you are a smart, kind and enthusiastic man. Everyday you started with a big smile and full of energy. You had answers for all the questions I had, it did not matter whether it was a biological question, or a question related to electron microscopy or atomic force microscopy or even questions unrelated to research. You always had your answers ready and took your time to thoroughly explain everything to me. Your enthusiasm helped me at the moments I was losing mine, while your critical thinking helped me to think critically about my own research. I, therefore, really enjoyed working for you, but also working with you in the past five years. For me, it was a shame that you left our department and I really miss to have you around. Off course, you left for a great purpose (to move back home) and therefore I wish you all the best with your future endeavours in Switzerland. I wish you, your wife Barbara, your children and your many grandchildren all the best.

Also, many thanks to dr. Christophe Danelon for being my co-promotor. You introduced me to the wonderful world of lipids. But besides that, you were a great mentor. You were critical, when you had to be critical. But also knew exactly when to hand out a compliment. Your knowledge in lipids, but also your cell-biological knowledge helped me to find solutions when my own knowledge was lacking. You were always there when I needed you and therefore many thanks. I always enjoyed seeing the work that comes out of your lab. You can be really proud of what have been achieved already, and I believe that in the near future you will achieve many more great things.

I would also like to thank dr. Marie-Eve Aubin-Tam for taking us under her wings. Andreas' group was a small group, but together with Marie-Eve's group we could feel like a much bigger whole. Marie-Eve, I still remember the small group you had when you started, barely able to fill a meeting room to have your weekly meetings. Over the years your group grew exponentially. Now, at the end of my PhD, your group has grown so much that you are barely able to fit everybody into one meeting room. I am grateful that you took our group in, your knowledge and advise really helped me and my research over the past years. I think you should be really proud of what you have achieved here in Delft already, but I also believe that this is just the start. I foresee many more achievements in the (near) future for you.

Many thanks for my defence committee, who gave me some great advice along the way and who have sacrificed their precious time to evaluate my thesis. Prof.dr. Robert Fenton, thank you very much for the great introduction in working with Aquaporin-2 at the start of my PhD and your critical view on my AQP2 research during my PhD. I am really honoured to have

an AQP2 expert in my defence committee. Prof.dr.ir. Abraham Koster, our paths have already crossed during my Masters, and in the past 5 years we have seen each other at many occasions. It was always a pleasure to see the developments in your lab (and seeing the development of NECEN) and to hear the suggestions you had for our research. I am really grateful to have you, a (cryo-)TEM expert in my defence committee. Prof.dr. Urs Staufer, your ground-breaking work with hollow AFM cantilevers laid at the foundation of the development of our set-up. Many thanks for freeing up time to come to my PhD defence. I am really looking forward to hearing your view on this matter. Prof.dr. Marileen Dogterom, I would like to thank you for everything you do in our department. I am really grateful that you are willing to be my reserve-member in the defence committee.

Dr. Arjen Jakobi, besides being in my defence committee, I would like to thank you for “adopting” me into your lab. As you can see in my thesis, we are slowly reaching our end goal and it would be a shame if I had to stop my research before we reached this great goal. Luckily for me, you were as enthusiastic about this research as Andreas and I were and gladly took over. In the short time that I now know you, I have come to know you as a smart and kind man. Even though my knowledge in image processing is limited, you always find the time to clearly explain every detail to me. The same counts for other topics, I can always stop by and get some help. It is really great to see your group slowly expanding, and I am happy I can be a part of this. I wish you all the best in setting up and expanding your own group.

Off course I would also like to thank our close collaborators from 3ME, dr. Murali Ghatkesar and ir. Eleonoor Verlinden. Eleonoor, it was a real pleasure working with you. It was great that I could share our successes with you, while it was also nice to have you by my side when things were not going so smoothly. Your knowledge opened my eyes for questions I would not think of, your kindness and humour made it a pleasure to work with you in the dark surroundings of our lab for 8 hours straight (I would go crazy if I had to endure that by myself) and your hard work brought us where we are today. I wish you all the best with the rest of your PhD and the writing of your thesis. I really believe that you can finish with a nice dissertation and cannot wait to attend your defence. Murali, it was a real pleasure to work with you. Over the years I saw the hard work that you put into this project. Not only in the lab or as a supervisor, but also backstage, arranging the administrative part of this project. I really appreciate your intelligence, your hard work and your careful eye for detail. You are always there for us to help us when we are in need and to think with us to improve our research. I am really happy to see that you completed your tenure track, you really deserved it. I wish you all the best for both you and your wife.

I could not have come so far without the help of Daniel Torres-Gonzalez and Jelle van der Does. Daniel, it was a pleasure working with you. I know working here in Delft was not always easy for you, with the small extensions you received and your constant search for housing. But I am really grateful that you came into our lives. You are a hard-working, kind and overall great guy. Every time I open the software you made, I get a smile on my face. Your eye for detail and determination lead to the development of a great software. I wish you all the best in Spain with your new job, and I hope our paths will cross at some point in the future. Jelle, voor jou zal ik in het Nederlands schrijven. Het is geweldig om te zien hoeveel plezier jij na alle jaren nog steeds in jouw werk hebt. Jouw enthousiasme en oog voor details heeft ertoe geleid dat langzaam, maar zeker onze opstelling functioneel werd. Elk klein detail is uitgedacht, en ik ben vaak nog steeds verbaasd over hoe ingenieus alles in elkaar is gezet. Ik ben enorm blij dat jij betrokken bent geraakt in dit project en dat ik daardoor jou heb leren

kennen. Ik wens jou en je vrouw Desiree al het beste toe. Gelukkig kunnen wij nog enkele maanden met elkaar samen werken.

A special thanks goes out to our collaborators, Patrick Frederix, Paul Laeven, Pascal Huysmans, prof.dr. Peter Peters, Paul Kwant, Edin Sarajlic, Thom Sharp and Hugo Perez Garza. Patrick, many thanks for your introduction in AFM at the start of my PhD and all the AFM help you gave me and Eleonoor in the past years. You were a really great help and we could always contact you, no matter how basic our questions were. Paul L. and Pascal, many thanks for the development of the humidity chamber and the temperature controlled gridholder. It was always a pleasure to have you around in Delft. I really appreciate all the work you have done for us. Peter, many thanks for your advice in the past years and your critical comments. I always enjoyed the work you showed us from your own lab. I wish you all the best. Paul K. it was always a pleasure seeing you during our half yearly meetings and I am glad that you are a part of our project. Edin, although you mainly worked together with Eleonoor and Murali, it was always great to see you. Your cantilevers were a crucial part of our research, while it was always great to see how enthusiastic you were about the progress we made. I wish you all the best. Thom, your research, although seemingly small, was of great help for my thesis. I am thankful I could use the results you obtained in Leiden, showing us some other factors we need to take into account during cryo-EM sample preparations. It was great meeting you.

Also many thanks to the Marie-Eve, Andreas and Arjen lab members and ex-lab members. Roland, Victor, Simon, Vanessa, Dominik, Mihaela, Ewa, Da, Kuang, Lisa, Aurora, Irfan, Chaline, Ramon, Tanja, Cheng, Albert and Fayeze. It was really great working with all of you and getting to know you all during work and after work. I will never forget the game-nights we did. Especially Dixit opened my eyes to the strange ways our minds can think. Roland, many thanks for all your help. Especially for laying the foundation for the software of our system and developing the software for our rapid mixing device. I really enjoyed working with you and wish you all the best for the future. Simon, I never forget the Christmas break we spend behind the electron microscope. Luckily it resulted in a nice paper for you (and for me). Many thanks for the help with the nanodiscs, as you can see it became a small part in my thesis. Also many thanks to your wife Corinne, for helping me with the baculovirus expression at the start of my PhD. This really helped me to kickstart my research. The best of luck to you, your wife and your son Pepijn. Da, it was really nice spending last Christmas break with you at the office during the writing of my thesis. At least I was not alone in the office. I really enjoyed working with you and your (sometimes) original way of thinking. I also really enjoyed the meals your wife prepared, she is a really great cook. I wish you and your wife all the best. Aurora, many thanks for your help with the AFM. It was great to have an AFM expert close by for when we had quick questions. You really helped us a lot and I am very grateful for that. Tanja, although you just started in Arjen's lab, it was really nice to get to know you. I really like your enthusiasm and wish you all the best with the rest of your PhD.

I want to thank Jaqueline Enzlin for her preparation work and her introduction in the *Sf9* culture work. Without your preparation I would not have such a broad range of different AQP2 mutants. Many thanks for that.

Off course I would like to thank the rest of the department as well. Especially Benjamin, Carsten, Mattia, Sascha, Jeremy, Erwin, Mahipal, Yoones, Theo, Behrouz, Misha, Jonás, Richard, Orkide and Marek. It was really great working with all of you (even if I did not mention you or forgot to mention you). You all made working at BN a real pleasure.

A special thanks goes out to the whole secretariat department of Bionanoscience. Without your help, dedication and enthusiasm the department would not run so smoothly. I especially would like to thank Jolijn Leeuwenburgh for all the help you gave me in the past years. I could always come to you for help and you were always there to guide me on my way, no matter how many times I asked you the same questions. Without your help I would have had a difficult time arranging everything. Many thanks for everything.

Although I spend a great amount of time in the lab, I also had a life outside of the lab. I would therefore like to thank all my friends who distracted me from the research I was doing. Max, I always enjoyed the great discussion we had on Friday or Saturday evenings in your apartment. I always left your home with a big smile and a lot to think about. Besides the great discussions, we also had a lot of fun. I will never forget our short holiday in Ireland, our encounter with Maarten van Rossum in Amsterdam or our many evenings in the Surf-in. Joeri, Wessel and Lennart, it was always nice to go out with you guys (and Max). With you, there is never a dull moment and you were always able to put a smile on my face. Lars, I have known you for a great part of my life and I am very grateful for that. I always enjoy hanging out with you and like your original way of thinking. I wish you all the best with your future as a teacher. Christiaan, Steef, Sjoerd and Ian, although we all went our own ways after, and in case of Sjoerd already during, high school, it is nice that we still can find some time in our busy schedules to hang out at least a few times a year. It is really great to see the growth you all made since we went our separate ways. Christiaan, congratulations on your upcoming marriage (the Friday after my defence). I wish you, your wife Marian and your son Tygo all the best. Steef, it is really great to see that you have found a new job. Lots of luck to you. Sjoerd, it is really great that you came back to the Netherlands. You build up a nice life in Deventer. All the best to you. Ian, step-by-step you are working towards your lifetime goal to become a (medical) doctor. I am really happy to see that you are slowly achieving your dream. All the best to you and (your future wife) Anthea.

Off course a special thanks to Yvonne. I admire all the work that you have done and the way you are as a person. You were always genuinely interested in my work, even though you have absolutely no experience in my field. You saw me grow, from being a Bachelor student, towards a Master student and finally to finishing my PhD. Without your continuous support and your “speklapjes” I could not have made it. I am really happy that you are now pursuing your dream of having your own restaurant and although I am (relatively) far away, I will always be there to support you. I wish you and your son Quentin all the best.

None of this I could have achieved without the support of my family. Martijn, my big brother, thank you for being there. I always enjoyed our trips to the different comedians we made. You always have a fine eye to pick out the good ones. I am happy that I can share this humour with you. I am really happy you found a new job, so that you can be closer to your girlfriend Natascha. The best of luck at your new position and the move. Arno, my little brother, I am really happy I can share my passion for Feyenoord with you. The many matches we saw in the past years were a really great distraction from my work. I will never forget the match against Sevilla in the Europe League we witnessed in the stadium, the champions-match against Excelsior (which Feyenoord lost) we saw in the city centre of Rotterdam and the real champions-match we saw the week after (which Feyenoord won, therefore becoming the champions in the Netherlands for the first time in 18 years) in Ahoy. In the past five years you lived in Breda, Spijkenisse, Cork, Brussels, Amsterdam and Haarlem. It is nice to see that you finally found a place where you can stay for a while. I wish you and your girlfriend Kat all the best.

Elke stap die ik heb gezet, heb ik niet kunnen zetten zonder de hulp van mijn ouders. Ik wil daarom mijn vader (Henk) en mijn moeder (Elly) bedanken voor al de hulp die zij mij in mijn leven geboden hebben. Pap, bedankt dat u mij ooit doorgestuurd heeft naar het VWO. Zonder VWO geen universiteit, zonder universiteit geen PhD en zonder PhD geen thesis waarin ik jullie kan bedanken. Die kleine beslissing, op een onbewaakt moment heeft mij gebracht naar waar ik nu ben. Mam, bedankt dat u altijd voor mij klaar gestaan hebt. Ondanks dat het voor u niet altijd duidelijk was waar ik precies mee bezig ben, heeft u altijd achter mij gestaan. U was blij voor me als ik mijn tentamens had gehaald (waar de tentamens over gingen, geen idee), u stimuleerde mij om door te werken als het niet ging en u stond achter mij om mij te steunen met alle keuzes die ik heb gemaakt. Hetzelfde geldt voor u pap. Ook al begreep u niet altijd wat ik aan het doen was, u probeerde het wel altijd te begrijpen. Ik ben heel erg dankbaar voor alle steun die jullie mij hebben gegeven. Ik hoop dat jullie nog een lange tijd van jullie pensioen kunnen genieten.

Ome Aad, tante Wil, tante Anja, Mirella en Sven, jullie ook bedankt voor alle steun die jullie mij en mijn familie in de afgelopen jaren hebben gegeven. Ome Aad en tante Wil, hartelijk dank dat jullie er waren voor mijn ouders tijdens de zware en spannende tijden. Hetzelfde geldt voor tante Anja, Mirella en Sven, jullie zijn er altijd voor ons wanneer wij het het hardst nodig hebben.

Last, I would like to thank my girlfriend Ruby Moll (van Keuk). Seven years ago, I met you at the entrance of the Efteling. Six years ago, we started dating. You were there five years ago when I started my PhD and I was there four years ago when you started your Bachelors. Three years ago, our bunnies came into our lives. Two years ago, we moved towards the edge of Vlaardingingen. One year ago, we could celebrate our five-year anniversary and this year you graduated for your Bachelors' and I am defending my PhD thesis. With every step I took, you were there to support me. Although you never really knew what I was doing, and I never really shared with you what I was doing, you were still there standing by my side. Now I am done. I am at the end of my thesis and I only need to defend. I am really grateful for all the support I received from you in all those years. Now we will go into the next chapter of our lives. You will start your own professional career and I will find the next step to take in my career path. The only thing that matters is that we will have each other for every step that we take. I love you Ruby, with all my heart and thank you for all the support I received from you and all the support you will give me in the future.

I would like to thank God for standing by my side during this journey. He was there when I achieved great results and he was there when everything failed. Thank you for being there for me.

The Lord gives wisdom; from his mouth come knowledge and understanding.

Proverbs 2:6

Curriculum vitae

Joachim Willem Pronk

- 21-03-1989 Born in Spijkenisse, The Netherlands
- 2001-2007 Higher General Secondary Education
Penta college CSG Blaise Pascal, Spijkenisse, The Netherlands
- 2007-2010 Bachelor in Life Science & Technology
Delft University of Technology and University of Leiden, The Netherlands
- 2010-2012 Master in Life Science & Technology
University of Leiden, The Netherlands
- 2013-2018 Ph.D.in Bionanoscience
Title: Aquaporin-2 trafficking: Studying cellular mechanisms with subcellular aspiration and cryo-electron microscopy
Promotor: Prof. Dr. Andreas Engel
Co-promotor: Dr. Christophe Danelon
Department of Bionanoscience
Delft University of Technology, The Netherlands
- Additional:
2011 Radiation protection, expertise level 5B

Publications:

Singh, K.; Ankur, G.; Buchner, A.; Ibis, F.; **Pronk, J.W.**; Tam, D.; Eral, H.B. (2018) A low-cost centrifugal homogenizer for emulsification & mechanical cell lysis. (Submitted).

Pronk, J.W.; Aroankins, T.S.; Fenton, R.A.; Engel, A.H. (2018) Comparing actin polymerization in the presence of C-terminal aquaporin-2 peptides and thymosin- β -4. (Submitted).

Carvalho, V.; **Pronk J.W.**; Engel, A.H. (2018) Characterization of membrane proteins using cryo-electronmicroscopy. (Submitted).

Lindhoud, S.; Carvalho, V.; **Pronk, J.W.**; Aubin-Tam, M.E. (2016) SMA-SH: Modified styrene-maleic acid copolymer for functionalization of lipid nanodiscs. *Biomacromolecules* 17(4):1516-22

Ravelli, R.B.; Kalicharan, R.D.; Avramut, M.C.; Sjollema, K.A.; **Pronk, J.W.**; Dijk, F.; Koster, A.J.; Visser, J.T.; Faas, F.G.; Giepmans, B.N. (2013) Destruction of tissue, cells and organelles in type 1 diabetic rats presented at macromolecular resolution. *Sci Rep* 3:1804